Galaxy physical properties from population model fitting

by

Janine Pforr

THE THESIS IS SUBMITTED IN PARTIAL FULFILMENT OF THE REQUIREMENTS FOR THE AWARD OF THE DEGREE OF DOCTOR OF PHILOSOPHY OF THE UNIVERSITY OF PORTSMOUTH

August 2011

Copyright

To my family.

I would not be who I am without you.

Abstract

In the last two decades astronomers carried out a large number of galaxy surveys tuned towards the study of galaxy formation and evolution. With the ever improving technology, increasing telescope sizes of ground-based telescopes and the development of space-based telescopes it has become possible to detect galaxies at a time when the Universe was only a few hundred million years old. However, for the majority of galaxies a detailed spectroscopic analysis is not possible due to their distance and limited telescope time. Thus, many surveys rely on photometric data alone to help unveil the properties of galaxies.

One of the most important areas of study within galaxy formation and evolution is the analysis of the galaxy stellar population parameters as these can provide us with information about the star formation histories of galaxies and when and possibly how they assembled their mass. A popular approach in the literature is the fitting of synthetic spectral energy distributions inferred from stellar population modelling to the multi-wavelength photometry of galaxies. However, this approach comes with a large number of fitting parameters all of which are essentially user-dependent and will bias the result in one way or another.

The aim of this thesis is to investigate the accuracy and efficiency of spectral energy distribution fitting as derivation technique for the galaxy physical properties, such as age, stellar mass, dust reddening, etc., as a function of the fitting parameters, such as star formation histories, age grids, metallicity, initial mass function, dust reddening, reddening law, filter setup and wavelength coverage and stellar population model, and to find the setup of parameters that recovers the properties best. In particular, we investigate in detail the dependence of the derived properties on the assumed wavelength coverage and exact filter setups. Mock galaxies with known properties serve as test particles for this exercise. The synthetic spectral energy distributions used in this thesis are based on the Maraston (2005) stellar population models. Literature results which investigate similar problems are obtained using the models of Bruzual & Charlot (2003).

Firstly, the fitting is carried out under the assumption that galaxy redshifts are known mimicking surveys for which galaxy redshifts are derived spectroscopically. Then we

study the case in which the redshift is not known and needs to be determined alongside the galaxy physical properties which is the case for most photometric surveys.

In general, we find that - using normal template star formation histories as widely used in the literature - ages and stellar masses of star-forming galaxies are underestimated, reddening and star formation rates are overestimated. This is due to a mismatch in star formation history and the overshining effect. The addition of the rest-frame near-IR appears to be crucial for the derivation of robust results. For aged galaxies with little or no on-going star formation we find that a setup covering a wide range of star formation histories and metallicities works best when the fit is carried out excluding dust reddening. For high redshift star-forming galaxies we find that a new type of star formation history (inverted-τ models which start forming stars at high redshift) recovers stellar masses and star formation rates best. The parameters of truly passive galaxies are much better determined.

In order to ease the comparison of literature data that was analysed with different fitting parameter setups we provide scaling relations for the transformation of stellar masses between different setups. Our results concerning the importance of the wavelength coverage in the fitting are particularly useful for the planning of future surveys and observation proposals.

We apply our findings from the study of mock galaxies to various samples of real galaxies which cover different redshift ranges and galaxy types. We derive the stellar population properties for a sample of star-forming galaxies at $z \sim 2$ from the GOODS-S survey using inverted-τ models (with high formation redshifts) and show that the obtained dust reddening and star formation histories are in excellent agreement with those derived from other methods. We also show how the wrong set of fitting parameters can lead to unrealistically young ages, low stellar masses and high star formation rates which are a pure artefact from the fit.

Furthermore, we study a sample of low redshift, predominantly passive galaxies from the SDSS-III/BOSS survey for which we use the spectral model of Maraston et al. (2009) that is tuned to the needs of this particular type of galaxies. We find that BOSS galaxies are mostly passive, old and massive at each redshift in the range $0 < z < 0.7$. Finally, we complement the study of SDSS-III/BOSS galaxies by deriving stellar masses for the SDSS-I/II galaxies in a similar fashion.

We conclude that the simultaneous derivation of stellar population properties of galaxies from spectral energy distribution fitting is difficult but that these properties can be very well derived provided the right setup and wavelength coverage are used in the fitting. We also conclude that more work is needed to better match star formation histories of aged galaxies with little on-going star formation in order to improve estimates of stellar population parameters.

Preface

The work of this Ph.D. thesis was carried out at the Institute of Cosmology and Gravitation University of Portsmouth, United Kingdom, under the supervision of Dr. Claudia Maraston and Dr. Daniel Thomas. Whilst registered as a candidate for the above degree, I have not been registered for any other research award. The results and conclusions embodied in this thesis are the work of the named candidate and have not been submitted for any other academic award.

The work carried out in Chapter 4 was carried out in collaboration with Claudia Maraston and Chiara Tonini and will be published in Pforr et al. (2012), MNRAS, submitted.

The work carried out in Chapter 5 was carried out in collaboration with Claudia Maraston and Chiara Tonini and will be published in Pforr et al. (2012b, in prep.).

The work carried out in Chapter 6, Section 6.1 was carried out in collaboration with Claudia Maraston, Alvio Renzini, Emanuele Daddi, Mark Dickinson, Andrea Cimatti and Chiara Tonini and is published in Maraston et al. (2010).

The work carried out in Chapter 6, Section 6.2 was carried out in collaboration with Claudia Maraston, Daniel Thomas, Bruno Henriques and David Wake and will be published in Maraston et al. (2012, in prep.).

The work carried out in Chapter 6, Section 6.3 was carried out in collaboration with Claudia Maraston and Daniel Thomas.

Contributions to other works:

Mass and absolute magnitude calculations and model evolutionary tracks for Masters et al. (2011).

Redshift determinations for Afonso et al. (2011).

Mass calculations for Tiret et al. (2011).

Mass calculations for Johansson et al., (2012, in prep.).

Redshift and mass recovery figures for mock star-forming galaxies have been used in several observational proposals for SERVS ancillary data.

Acknowledgements

First I would like to thank my supervisors Dr. Claudia Maraston and Dr. Daniel Thomas for their support and guidance during this PhD and all members (past and present) of the Institute of Cosmology and Gravitation for their help, support, endurance and patience with me. Special thanks goes to Edd who was always there to help with smaller or bigger computer issues and data handling.

I would also like to thank my parents for always letting me follow my dream and their support on the way during the past 28 years.

Of course, a very special thanks goes to my darling. You've always been there and I don't know where I would be without you.

Special thanks goes to M. Bolzonella for providing HyperZ and HyperZspec and support with the fitting code.

This research has been supported by the Marie Curie Excellence Team Grant "Uni-Mass", MEXT-CT-2006-042754, P.I. Claudia Maraston. Numerical computations were carried out on the Sciama High Performance Compute (HPC) cluster which is supported by the ICG, SEPNet and the University of Portsmouth.

Funding for the SDSS and SDSS-II was provided by the Alfred P. Sloan Foundation, the Participating Institutions, the National Science Foundation, the U.S. Department of Energy, the National Aeronautics and Space Administration, the Japanese Monbukagakusho, the Max Planck Society, and the Higher Education Funding Council for England. The SDSS was managed by the Astrophysical Research Consortium for the Participating Institutions.

List of Abbreviations and Acronyms

ACS	Advanced Camera for Surveys
AGB	Asymptotic Giant Branch
AGN	Active Galactic Nucleus/Nuclei
BC03	Bruzual & Charlot (2003)
BOSS	Baryon Oscillation Spectroscopic Survey
CAS	Catalogue Archive Server
CDM	Cold Dark Matter
CMB	Cosmic Microwave Background
COBE	Cosmic Background Explorer
COSMOS	Cosmic Evolution Survey
CSP	Composite Stellar Population
DES	Dark Energy Survey
DR7	Data Release 7
E-AGB	Early Asymptotic Giant Branch
ESA	European Space Agency
GalICS	Galaxies in Cosmological Simulations
GMASS	Galaxy Mass Assembly ultradeep Spectroscopic Survey
GOODS	Great Observatories Origins Deep Survey
Gyr, Myr	Giga year $= 10^9$ years, Mega year $= 10^6$ years
HB	Horizontal Branch
HDF	Hubble Deep Field
HR-diagram	Hertzsprung-Russel-Diagram
HST	Hubble Space Telescope
HUDF	Hubble Ultra Deep Field
IMF	Initial Mass Function
IR	InfraRed
IRAC	Infrared Array Camera
ISAAC	Infrared Spectrometer and Array Camera
JHU	Johns Hopkins University

LMC	Large Magellanic Cloud
LRG	Luminous Red Galaxy
LSST	Large Synoptic Survey Telescope
$M_\odot$	One solar mass
M^*	stellar mass
M98	Maraston (1998)
M05	Maraston (2005)
M06	Maraston et al. (2006)
M09	Maraston et al. (2009)
M10	Maraston et al. (2010)
MIPS	Multiband Imaging Photometer
MPA	Max Planck Institute for Astrophysics
Mpc	Mega parsec
MS	Main Sequence
MW	Milky Way
NASA	National Aeronautics and Space Administration
NIR	Near-InfraRed
PDF	Probability Distribution Function
RGB	Red Giant Branch
PMS	Post Main Sequence
PSF	Point Spread Function
SDSS	Sloan Digital Sky Survey
SED	Spectral Energy Distribution
SERVS	Spitzer Extragalactic Representative Volume Survey
SF	Star Formation
SFH	Star Formation History
SFR	Star Formation Rate
SMC	Small Magellanic Cloud
SMG	Sub-mm Galaxy
S/N	Signal to Noise
SSP	Simple Stellar Population
TP-AGB	Thermally Pulsing Asymptotic Giant Branch
ULIRG	Ultra Luminous Infra Red Galaxy
UV	UltraViolet
VLT	Very Large Telescope
WMAP	Wilkinson Microwave Anisotropy Probe
W09	Wuyts et al. (2009)
2SLAQ	2dFSDSS LRG and QSO

Table of Contents

List of Tables

List of Figures

Chapter 1

Introduction

Ever since Edwin Hubble discovered at the beginning of the 20th century that the galaxy we live in, the Milky Way, is not the only galaxy in the Universe, astronomers try to understand how these massive collections of stars, gas and dust form and evolve with time.

1.1 Galaxies

1.1.1 The nearby Universe

The first attempt by Hubble himself was to classify different types of galaxies[1] according to their outer appearance, their so-called morphology (Fig. 1.1, Hubble, 1926), and to order them. This led him to distinguish two basic types of galaxies, namely early-types or elliptical (E) and late-types or spiral (S) galaxies. Ellipticals show a smooth distribution of stars and a round or elliptical shape. Spiral galaxies are flat disks with clear structure such as spiral arms and dust features. The spiral class is sub-divided into normal spirals and those that have bars in their centre (SB). Later, new types such as irregular galaxies and interacting galaxies were added to the scheme. Although these extended versions of the Hubble Classification Scheme are still in use today, e.g. most famously is the Galaxy Zoo project (Lintott et al., 2008), important physical properties are known to be different in these two basic types of galaxies.

Apart from morphology galaxy types can also be set apart by colour[2], stellar mass, dust content and star formation. Elliptical galaxies are mainly comprised of old stellar populations and appear to not form stars anymore. Old stellar populations consist of old,

[1] Named 'nebulae' in Hubble's time.

[2] Difference of the brightness of a galaxy in different wavelength ranges of the electromagnetic spectrum.

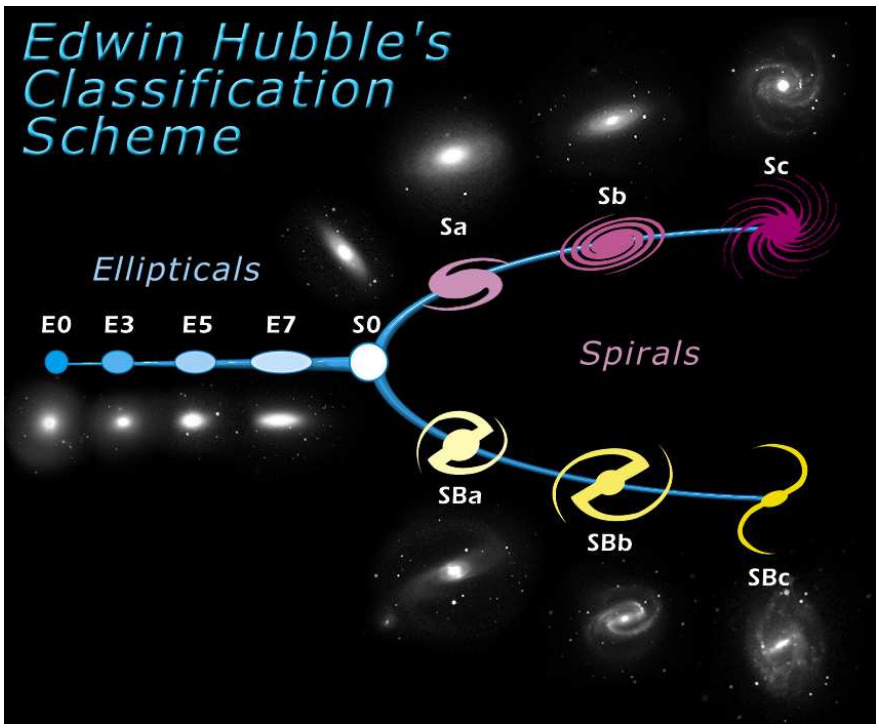

Figure 1.1: Galaxy classification scheme developed by Edwin Hubble (Hubble, 1926) in which galaxies are classified by their morphology into ellipticals (E) and spirals (S). The spirals are further distinguished by the existence of a bar (SB spirals). S0's build the transition between ellipticals and spirals. Because of the diagram's shape it is also called "Hubble's Tuning Fork". Figure taken from $http://hubblesite.org/newscenter/archive/releases/1999/34/image/o/format/large\_web/$.

low-mass stars which have low surface temperatures, consequently their energy emission peaks at long wavelengths; we say they are red in colour and so is the galaxy. Spiral galaxies on the other hand harbour on-going star formation fueled by gas and dust. They are blue in colour because they contain young, high-mass stars which have very hot surface temperatures and are therefore blue. Although spiral galaxies are much more abundant, ellipticals are more massive and thus contain 50-75% of the total stellar mass in the nearby Universe (e.g. Bell et al., 2003). These properties lead to a clear colour bimodality in the local Universe in which massive red galaxies line up along the red sequence whereas blue low-mass galaxies form the blue cloud (Fig. 1.2; Strateva et al., 2001; Kauffmann et al., 2003; Blanton et al., 2003, 2005; Baldry et al., 2004; Balogh et al., 2004). The aim of galaxy evolution studies is to understand the origin of such a separation. Alongside this bimodality many scaling relations have been found for nearby galaxies, for example the correlation between a spiral galaxy's luminosity and its rotation velocity, the so-called Tully-Fisher relation (Tully & Fisher, 1977). A similar correlation exists between luminosity and stellar velocity dispersion for elliptical galaxies (Faber & Jackson, 1976). From observations like these the question arises if what we see locally is

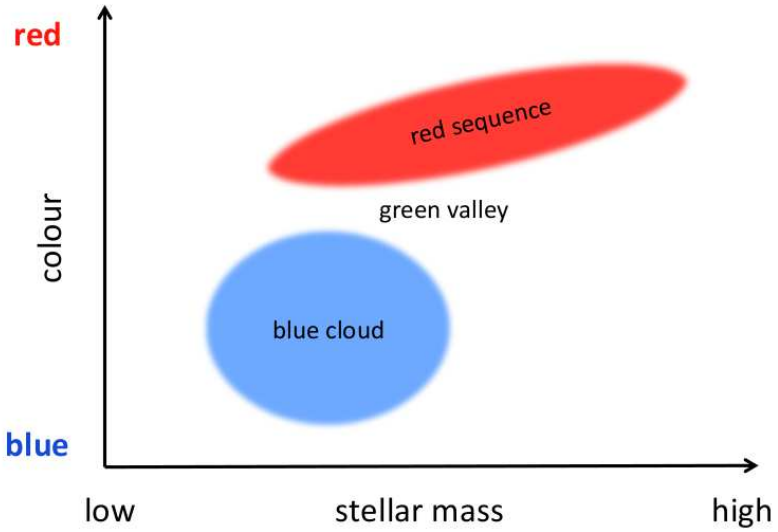

Figure 1.2: Colour-mass (magnitude) diagram illustrating the bimodality of the local galaxy population. Less massive (fainter) star-forming spiral galaxies are predominantly blue in colour and loosely form the 'blue cloud'. Massive (bright) and passive elliptical galaxies are predominantly red in colour and concentrate along the 'red sequence'. Very few galaxies are found in the transition region called 'green valley'.

also valid in the distant Universe. This ultimately urges one to investigate how galaxies form and evolve with time.

1.1.2 The distant Universe

In order to study galaxy formation and evolution one has to extend the study beyond the local Universe into the distance. Thanks to the finite speed of light looking into the distant Universe also means looking back in time. In this way we are able to observe galaxies at different stages in their evolution. However, the further away an object is from us, the fainter and smaller it appears, too. Fig. 1.3 shows the deepest images ever taken of a small part of the night sky - the Hubble Ultra Deep Field (Beckwith et al., 2006)- reaching ~ 13 billion years back in time. Each of the approximately 10,000 light blobs in this picture is a galaxy. For the majority of these galaxies astronomers can only rely on luminosity and colour as means to study their nature. Morphological information remains unresolved and detailed spectroscopic data is too expensive and time consuming to obtain. However, such studies are further complicated by the fact that the Universe is expanding (i.e. all galaxies are moving away from us and distant galaxies move quicker than closer ones, Hubble, 1929). This means that light emitted by distant galaxies gets

stretched out on its way to us. Because of this stretching light appears redder when it is observed compared to when it was emitted, it is *redshifted*. This redshift is a function of the distance and therefore often used as distance indicator. The redshift and its effect on the observed light has to be taken into account when galaxies at various distances are compared to each other.

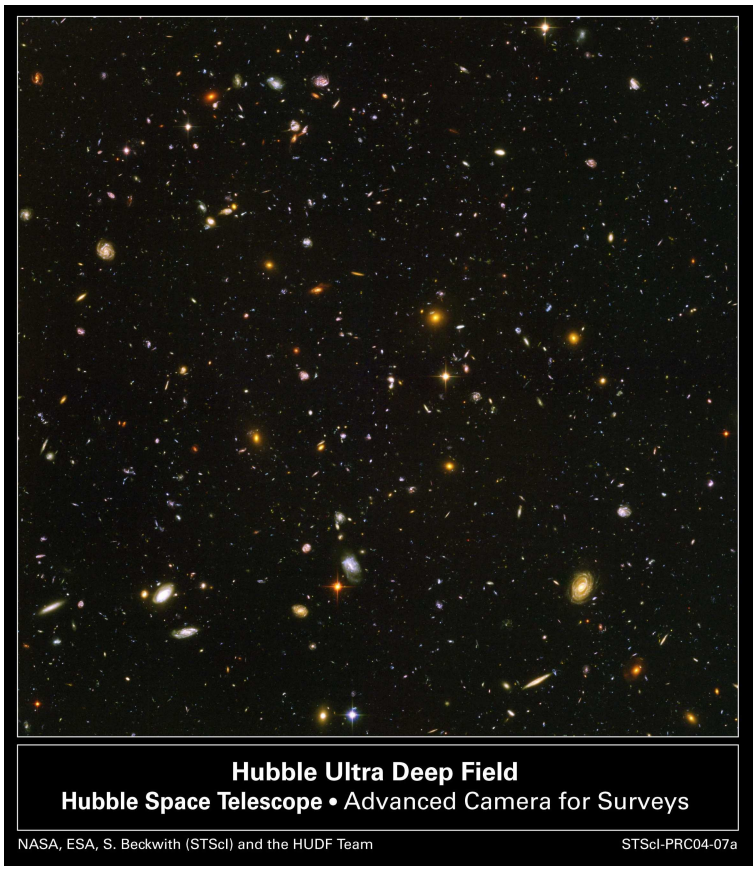

Figure 1.3: Colour composite of the Hubble Ultra Deep Field, deepest image ever taken of a part of the night sky. The image shows more than 10,000 galaxies of all shapes, colours and sizes in an area of 11 $arcmin^2$. Source: $http://hubblesite.org/newscenter/archive/releases/2004/07/$

1.2 Galaxy formation

1.2.1 Structure formation

Is the expansion of the Universe followed back in time one realises that the young Universe must have been smaller and ultimately have started from a singularity. Nowadays it is widely believed that the Universe started with a 'Big Bang' around 13.7 billion years ago and then expanded from this extremely hot and dense state into the Universe we observe today (Fig. 1.4). During this expansion the Universe cooled down. At $\sim 380,000$

years after the Big Bang the initially almost uniform plasma had cooled enough so that matter and radiation decoupled. This point in time is also called the time of recombination because electrons started to combine with nuclei into hydrogen atoms. Since then radiation travels through the Universe nearly undisturbed and has been observed today as the Cosmic Microwave Background (CMB, Penzias & Wilson, 1965) with a temperature of ~ 2.7 Kelvin by satellites such as COBE (Smoot et al., 1991) and WMAP (Bennett et al., 2003). The time of recombination denotes the start of the matter dominated era of the Universe. After this very short time the history of the Universe is dominated by galaxy evolution processes. This thesis focusses on the galaxy-dominated period.

However, not all matter in the Universe is visible. Zwicky (1937) indicated that because of the mismatch between dynamical and luminous mass of Coma cluster galaxies there must be some invisible or 'dark' matter component in the Universe. This was later also found by Rubin et al. (1985) in the rotation curves of spiral galaxies. Since then, the dominating view among astronomers is that galaxies reside in haloes of dark matter. Recent data indicates that the dark matter is about five times more abundant than the baryonic matter (Komatsu et al., 2009). It is this dark matter that creates gravitational potential wells due to tiny primordial density fluctuations, attracts more dark matter to flow into these wells, condenses and clumps into dark matter haloes. Over time these dense regions become even denser and then also attract baryonic matter which, after sufficient cooling,

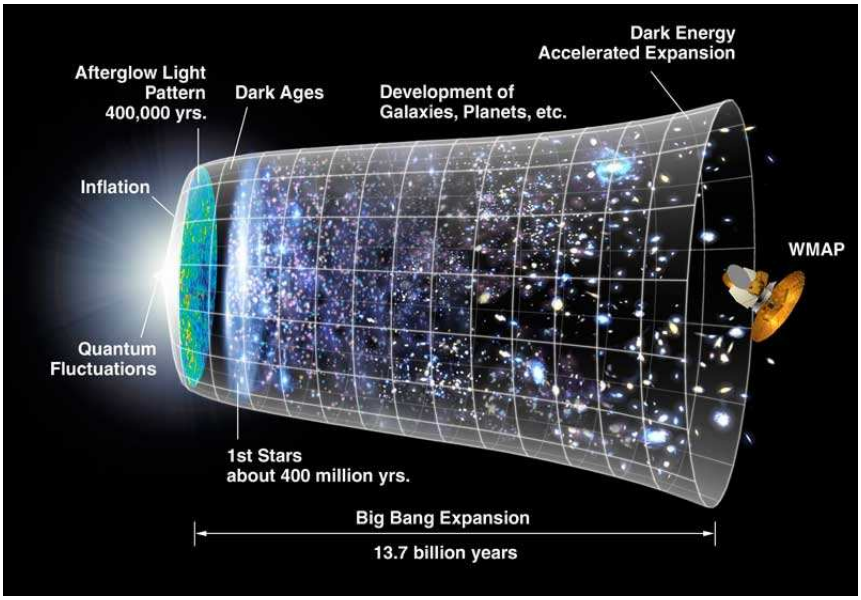

Figure 1.4: History of the Universe according to the Big Bang Theory. The Universe starts in an extremely hot and dense plasma state (Big Bang) and evolves through expansion and cooling eventually allowing structures like galaxies to form. Source: $http://www.astronomynotes.com/cosmolgy/s12.htm$

collapses to form stars and later galaxies. Only after the formation of the first stars did the Universe become transparent as their radiation ionised neutral gas around 400 million years after the Big Bang.
As time progresses, dark matter haloes are held to merge and form the structure of clumps, voids and filaments which are traced by the baryonic matter such as gas and galaxies we see in the late Universe.

The current cosmological model that best describes the formation of structure as observed in today's Universe is a model in which

- 22% of the Universe consists of cold dark matter (CDM), meaning dark matter particles move at classical speeds rather than relativistic (warm) or ultra-relativistic (hot) speeds
- 4% is baryonic matter for which only 0.4% is locked up in stars and 3.6% exists as intergalactic medium
- 74% is made up by dark energy which drives the accelerated expansion of the Universe and is described by a cosmological constant Λ.

This model is called ΛCDM.

1.2.2 Monolithic collapse and hierarchical clustering

As alluded to in the previous section in a ΛCDM cosmological framework structures form hierarchically (Press & Schechter, 1974). This means that small structures form first and grow larger with time because matter gets gravitationally attracted to overdensities. For galaxy formation and evolution this means that gas accumulates until the cloud collapses and stars start to form. This naturally produces disky systems which later turn into ellipticals by merging (Fig. 1.5; Toomre & Toomre, 1972; Toomre, 1977; White & Rees, 1978; Blumenthal et al., 1984).

This opposes the classical scenario of monolithic collapse in which elliptical galaxies form out of quickly collapsing gas clouds at high redshift (and may later turn into spiral galaxies, Eggen, Lynden-Bell & Sandage 1962). The assumption that star formation and assembly of elliptical galaxies happen simultaneously, the short durance of this process and the top-down nature of monolithic collapse (i.e. massive galaxies form first) make it difficult to embed into a ΛCMD framework.

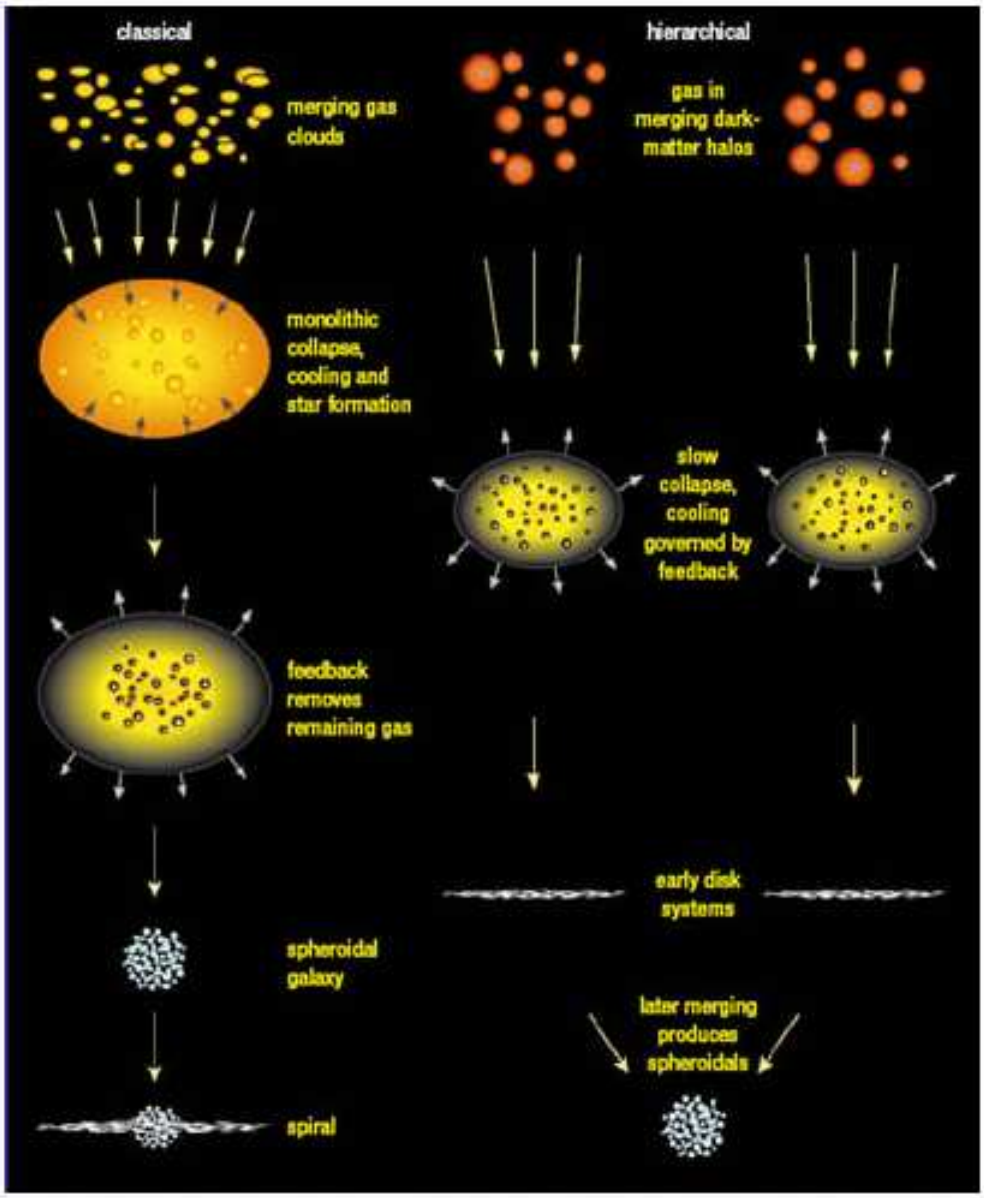

Figure 1.5: Illustrated are the two competing galaxy formation and evolutionary scenarios. In the classical picture (left) elliptical galaxies form out of monolithically collapsing gas clouds and later transform into disk galaxies. The hierarchical clustering scenario on the other hand (right) postulates the formation of disk galaxies out of cooling gas clouds. Elliptical galaxies form later through merging of two disk galaxies. Source: $http://www.jeffstanger.net/Astronomy/galaxyformation.html$

1.2.3 Galaxy formation models

In order to fully understand galaxy formation and evolution processes much effort has been put towards the development of galaxy formation models. The behaviour of dark matter with time has been successfully simulated computationally by Springel et al. (2005). However, following the processes in baryonic matter such as star formation,

feedback, heating and cooling is much more challenging. For this purpose so-called semi-analytic models were developed (Cole et al., 1994; Mo et al., 1998; Somerville et al., 2001; Kauffmann et al., 2003; Hatton et al., 2003; Croton et al., 2006; Bower et al., 2006; De Lucia & Blaizot, 2007; Baugh, 2006; Somerville et al., 2008) which include parametric prescriptions of the physical processes that govern the behaviour of baryonic matter. These processes include gas heating and cooling, star formation, chemical enrichment, feedback from supernovae (SN) and active galactic nuclei (AGN) and dynamical interactions between galaxies such as merging. Since most of these processes are poorly understood the predictive power of these models is reduced. Observations are of great help for constraining the free parameters in such models.

1.2.4 Brief summary of observational results

Crucially, the study of galaxies relies on the investigation of their components, namely stars, gas and dust. The aim is to reconstruct the history of each galaxy to unveil how and when it assembled its mass. Do galaxies predominantly grow in size because of their star formation or is their growth merger-driven? Ultimately, this will help to answer the question whether galaxies form hierarchically or via monolithic collapse.

In recent years, many important results were yield besides the aforementioned scaling relations. It was discovered that red elliptical galaxies preferentially live in high-density environments, such as clusters and groups of galaxies (Oemler, 1974; Davis & Geller, 1976; Dressler, 1980; Aragon-Salamanca et al., 1993; Blanton et al., 2005; Baldry et al., 2006; Lane et al., 2007; van der Wel, 2008). Blue spiral galaxies on the other hand are mainly found in the field (Ellis et al., 2005; Conselice, 2006).

With regard to the evolution of scaling relations with redshift, many studies showed that passive red ellipticals exist already at high redshift and therefore a red sequence is in place since at least ~ 7.5 Gyr ($z \sim 1$; Bell et al., 2004; De Lucia & Blaizot, 2007; Kriek et al., 2008; Williams et al., 2009; Brammer et al., 2009). Furthermore, it has been suggested that the mass in the red sequence is twice as large now compared to $z \sim 1$ (Bell et al., 2004; Borch et al., 2006; Faber et al., 2007; Brown et al., 2008). However, Cimatti, Daddi & Renzini (2006) conclude that this is only the case at the low-mass end. The mass in the blue cloud where actively star-forming galaxies reside on the other hand seems to have stayed nearly constant (Borch et al., 2006; Arnouts et al., 2007; Bell et al., 2007). This suggests that merging and not star formation dominates the growth of mass in galaxies. It also indicates that galaxies from the blue cloud travel towards the red sequence by merging without triggering too much star formation (Faber et al., 2007) or by losing their

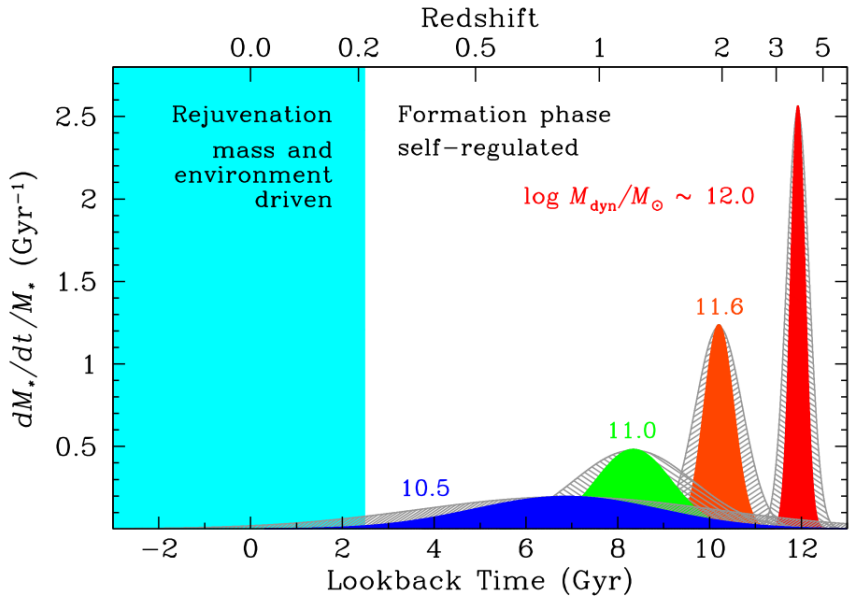

Figure 1.6: Illustration of downsizing by Thomas et al. (2010). Shown is the specific star formation rate (SFR/stellar mass) as function of look-back time for early-type galaxies of different masses (see labels). Grey hatched curves refer to uncertainties in the formation time scales. Time and redshift are connected by adopting $\Omega_M = 0.24$, $\Omega\Lambda = 0.76$, and $H_0 = 73$ km/s/Mpc. The sketched star formation histories refer to the typical formation history averaged over the entire galaxy population (at a given mass) rather than real star formation histories of individual objects which are expected to be burstier and more irregular. Source: *Fig. 9 from Thomas et al. (2010)*.

ability to form stars in other ways. However, this can only work for the least massive galaxies due to chemical evolution. Other studies found passive and already old elliptical galaxies at high redshift ($z \sim 2$) which consequently must have formed (and assembled) their stars at even earlier epochs (Cimatti et al., 2002; Moustakas et al., 2004; Papovich et al., 2005; Treu et al., 2005). These studies at high redshift are consistent with those exploiting so-called galaxy archaeology. In fact, recent studies by, e.g. Thomas et al. (2005, 2010), find a 'down-sizing' trend in galaxy evolution such that the most massive galaxies formed quickly at high redshift while less-massive galaxies continue to form stars over a very long period of time (Fig. 1.6). This is not consistent with hierarchical models and with much late merging. Hence, galaxy evolution is still open.

1.3 From stars to galaxies

As pointed out, the study of galaxies is carried out via the analysis of their components. Most importantly one is interested in the stars that make up a galaxy because it is their

light that we observe. In order to understand galaxies one has to understand stellar evolution first (for reviews on stellar evolution see e.g. Iben Jr., 1967; Renzini & Fusi Pecci, 1988, and references therein). Stellar evolution is driven by nuclear physics as stars burn via nuclear fusion. The hotter and more massive a star is, the brighter it is, too. But this also means a short lifetime. Smaller and cooler stars live orders of magnitudes longer (e.g. Iben, 1967). When stars are sorted into a Hertzsprung-Russell-diagram (HR-diagram, Fig. 1.7, pioneered by E. Hertzsprung and H.N. Russell in 1910, see e.g. Sitterly 1970 for a review) relating surface temperature (spectral class) to stellar luminosity, then we find the cool, faint, low-mass stars in the bottom right corner and the hot, bright, massive stars in the top left corner (Rosenberg, 1910; Russell, 1921). The temperature of a star also determines its colour, with hot stars being blue and cool stars being red. Stars spend most of their lifetime on the main sequence (MS) while they are burning up hydrogen in the core. Once most of the hydrogen is used up, stars move away from the main sequence to the right in the HR-diagram and turn into sub-giants (for post main sequence stellar evolution see e.g. Iben, 1974, and references therein). This marks the transition between hydrogen burning in the core to hydrogen burning in an outer shell while the core consists of helium. Stars now move on to the red giant branch (RGB) where they

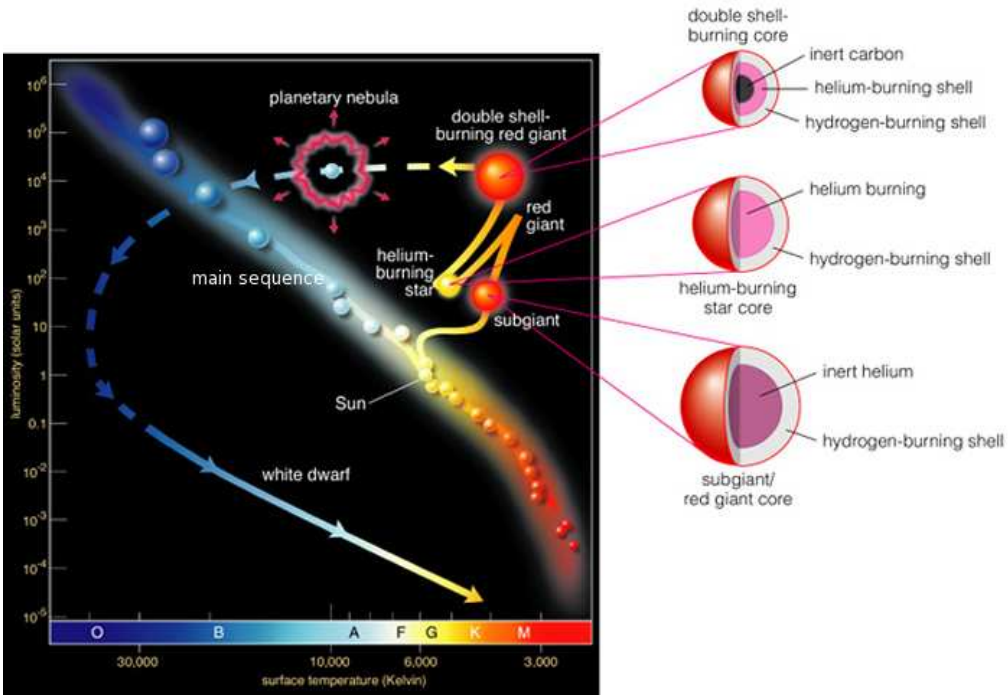

Figure 1.7: Hertzsprung-Russel diagram showing the different evolutionary stages of stellar evolution. The diagram relates surface temperature (and spectral class) of a star to its luminosity. The evolutionary track of the sun is shown as an example of how stars move in the diagram during their evolution. Source: $http://www.bramboroson.com/astro/apr3.html$

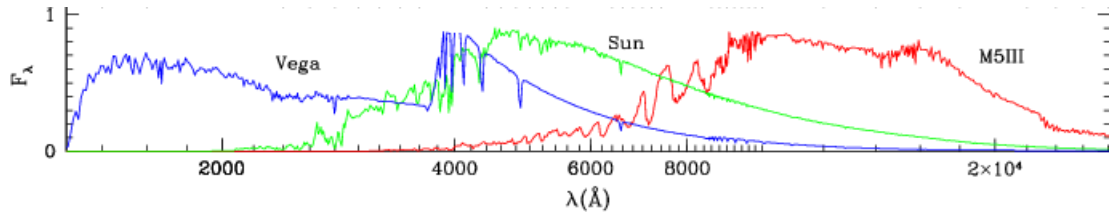

Figure 1.8: Examples for stellar spectra, specifically: Vega (A0V, blue), the Sun (G2V, green), and a M5 giant (red). Fluxes are in arbitrary units. *Adapted from Fig. 3 of Girardi et al. (2002).*

burn hydrogen in a shell. From there they move onto the horizontal branch (HB) where they burn helium in their core (helium burning phase). Once some helium has burnt in the core and a carbon core has formed, helium and hydrogen burn in outer shells. Stars have now moved to the asymptotic giant branch (AGB, e.g Iben Jr. & Renzini, 1983, and references therein). Once stars reached the top of the AGB they expel their outer shell (remnants are called planetary nebulae). They are now very blue thus moving to the left in the HR-diagram. While the helium burning dies off they cool and turn into white dwarfs. Depending on the initial mass of the star the final stage can also be a neutron star (for initial masses between 8 and $60\,M_\odot$) or a black hole (initial masses larger than $60\,M_\odot$).

The spectra of stars depend on surface temperature. Examples for a very young and blue star, our Sun and a red giant star are shown in Fig. 1.8 (Girardi et al., 2002). The spectrum of a galaxy is a superposition of the spectra of all the stars in that galaxy. The age determination of a stellar population exploits the knowledge that stellar lifetimes are anti-correlated with stellar mass. Very massive and blue stars have very short lifetimes while red, lower mass stars live a lot longer. Hence, is a galaxy spectrum mainly red, stars making up that galaxy are mainly old (because all blue stars have died already). Is a galaxy spectrum blue, then stars must have formed recently. The age dating of stellar populations is based purely on nuclear physics and stellar evolution theory and independent of the underlying cosmological model. By exploiting the stellar evolution the integrated spectra of stellar populations as a function of age can be modelled (Tinsley, 1972; Bruzual A. & Charlot, 1993; Maraston, 1998; Bruzual & Charlot, 2003; Maraston, 2005). We will address this in more detail in Chapter 3. These so-called stellar population models are the basic tool of investigation for galaxies.

1.4 Modelling data

Galaxy properties are derived by fitting these stellar population models to data, and several approaches are taken, which have pros and cons (for recent reviews see Walcher et al., 2011; Maraston, 2011a). For our purpose let us briefly distinguish between spectroscopic and photometric methods. While the availability of spectra is mandatory for the determination of detailed chemical abundances, such as chemical abundance ratios, which is accomplished through using selected absorption line indices and comparing to element-ratio sensitive models (e.g. Worthey et al., 1992; Trager et al., 2000; Kuntschner, 2000; Thomas et al., 2005, 2010), the high S/N that is required made this method practical only for a limited number of galaxies at limited redshifts so far. Also popular is the so-called full spectral fitting approach in which population parameters are extracted by fitting the full available spectrum (Heavens et al., 2000; Cid Fernandes et al., 2004; Ocvirk et al., 2006; Panter et al., 2007; Tojeiro et al., 2007, 2009). This also requires high quality and high S/N spectra in order to succeed. These are often limited in wavelength coverage, notoriously time consuming and thus been limited so far in redshift and

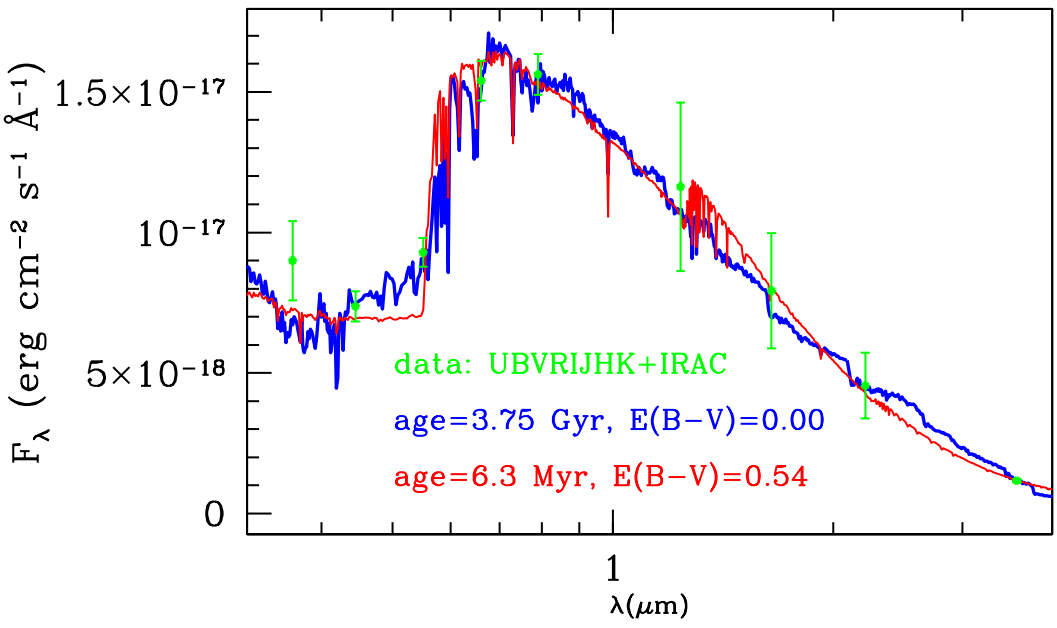

Figure 1.9: Example of broad-band SED-fits of stellar population models (red and blue lines) to data (green points with errorbars). Properties inferred directly from the fit are listed.

to small samples.

Broad-band photometry is the favourite approach at high redshift, because it is relatively cheap and yet - by covering a wide wavelength range as in the modern approach (e.g. The Great Observatories Origins Deep Survey (GOODS) Dickinson et al., 2003) although at a coarser resolution compared to spectroscopy - can be effective in breaking the age-metallicity degeneracy and in providing sensible physical properties for galaxies. It is common to exploit such data in spectral energy distribution fitting and many conclusions on galaxy evolution are based on these results.

Broad-band spectral energy distribution (SED) fitting is the data analysis technique applied throughout this thesis. SED-fitting is based on fitting stellar population models with a variety of different parameters (i.e. ages, dust content, chemical composition) to broad-band photometric data. The resulting best fit among all parameter combinations then gives the stellar population parameters (Chapter 3). Fig. 1.9 shows an example of two such fits with the derived parameters. Clearly, two similarly good fits can yield vastly different stellar population properties. In this case, the age-dust degeneracy is illustrated. This means that a young stellar population in combination with a high-dust content (red curve) and an older stellar population that is dust free (or has very little dust, blue curve) result in similar spectra which cannot be distinguished by the fit.

Over the last two decades numerous galaxy surveys were designed and performed to study galaxy formation and evolution, e.g. CANDELS (Grogin et al., 2011; Koekemoer et al., 2011), COMBO-17 (Wolf et al., 2001), COSMOS (Scoville et al., 2007), DEEP2 (Davis et al., 2003), GMASS (Kurk et al., 2008), GOODS (Dickinson et al., 2003), SDSS (York et al., 2000), SERVS (Lacy et al., 2008), STAGES (Gray et al., 2009). To this end, the determination of the physical properties of galaxies, such as ages, stellar masses, star formation rates (SFRs), star formation mode, dust reddening, metallicity and - when necessary - photometric redshifts possibly as a function of look-back time and environment is crucial. Even for galaxy surveys devoted primarily to Cosmology, such as BOSS (Eisenstein et al., 2011), DES (http://www.darkenergysurvey.org/), LSST (Strauss et al., 2010) and WiggleZ (Blake et al., 2008), galaxy properties need to be accurately determined as galaxies bias the read-out of the cosmological signal (e.g. White et al., 2011).

The interesting question is to assess how well galaxy properties can effectively be recovered with stellar population model fitting and many papers have been devoted to this scope over recent years using real galaxies (e.g. Maraston, 2005; van der Wel et al., 2006; Maraston et al., 2006, and many others).

1.5 Thesis motivation and outline

The aim of this thesis is to understand the systematics and uncertainties involved in the derivation of stellar population properties of galaxies through stellar population model fitting. These are due to the use of different models, parameters, wavelength ranges, etc.. We focus on a popular derivation method - the so-called broad-band spectral energy distribution fitting - which in particular applies to high-redshift galaxies.

The information gained from studies of real galaxies as in e.g. Maraston (2005); van der Wel et al. (2006); Maraston et al. (2006) is useful, but does not yet inform us on which fitting method and parameters provide the correct galaxy properties as a comparison to the true quantities cannot be made for real galaxies. On the other hand, using mock galaxies for which the properties are known a priori allows one to understand the effectiveness of the assumptions made in the fitting, even though there is no guarantee that simulated galaxies have star formation histories similar to real ones in the Universe.

This thesis is organised as follows. In *Chapter 2* we introduce the various data sets that are used throughout this thesis. These include a set of simulated galaxies with known properties which allow us to test the accuracy and robustness of our method for the derivation of stellar population properties. Furthermore, we study several observed galaxy samples covering not only different distance intervals but also different galaxy types. For the analysis of these galaxy samples we use the common approach of spectral energy distribution fitting which is described in detail in *Chapter 3*. *Chapter 4* illustrates the results we obtain with this method for simulated galaxies under the assumption that their redshift is known and can be used as constraint in the fitting. We extensively test the effect of using different setups and parameters in the fit, most of which belong to the most popular ones in the literature. We will show that changes in the fitting setup can have very drastic effects on the derived galaxy population properties. This test is extended in *Chapter 5* to the case in which also redshifts are unknown and need to be derived through fitting as well. Finally, we apply the fitting method to samples of real galaxies of different types and at different distances in *Chapter 6*. We will work our way from distant galaxies to the nearby Universe and span ~ 11.5 billion years in cosmic history. The work of this thesis is summarised and concluded in *Chapter 7*.

Chapter 2

Galaxy data samples

We will begin the work of this thesis by introducing the data samples used throughout this thesis in this chapter. In the Introduction we already pointed out that many galaxy surveys aimed at galaxy formation and evolution have been undertaken in the last two decades. However, for our purpose we need galaxies for which we know the true properties so that we can compare our results in absolute and not just relative terms. Therefore, we start by describing the mock galaxies which are extracted from a semi-analytic galaxy formation model and which we use as test particles to analyse the robustness of the derived stellar population properties in Chapters 4 and 5. After that we introduce three samples of real galaxies which cover different redshift ranges and galaxy types. Specifically these are 95 high redshift, star-forming galaxies from the GOODS-S survey, $\sim 430,000$ mostly passive and massive galaxies from the SDSS-III/BOSS survey and $\sim 750,000$ low redshift galaxies from the SDSS-I/II legacy survey. Data from the SDSS-III survey are available to us through the University of Portsmouth's full membership in SDSS-III.

2.1 Mock galaxies

2.1.1 Star-forming galaxies from a semi-analytic model

We extract model galaxies from the hybrid hierarchical model GalICS (Galaxies in Cosmological Simulations, Hatton et al., 2003). This uses dark matter merger trees obtained with an N-body simulation covering the redshift range $0 = z \lesssim 35$. Baryonic physics is implemented semi-analytically following standard recipes (for details about GalICS see Hatton et al. 2003 and for a review see Baugh, 2006). The latter includes gas cooling, star formation, chemical enrichment, feedback from supernovae and AGN and treats the

dynamical interactions of galaxies in clusters and groups, such as tidal stripping, dynamical friction and mergers.

The mass distribution inside each single galaxy is governed by its evolution. Cooling of hot gas into the dark matter potential wells forms disks where star formation occurs depending on the mass of the available cold gas and on the galaxy dynamical time[1] with the star formation efficiency as a free parameter. Secular evolution in disks and mergers produces bulges at the centres of disks. They are characterised by a Hernquist density profile, and they do not benefit from gas cooling, which always forms disks. Therefore, star formation can occur in bulges only from gas expelled from supernovae or infalling into the bulge during a merger event or from the disk following disk instabilities. In this case a starburst component is activated at the centre of the bulge, which carries the mass of the newly produced stars, and has a geometry similar to that of the bulge but with a smaller radius. Subsequent cooling of gas will produce a disk around the bulge, but will not directly add mass to the bulge itself.

For each galaxy and its components (disk, bulge, burst) separately the code produces rest-frame spectral energy distributions. We use the GalICS version in which these are based on the Salpeter IMF (Salpeter, 1955) Maraston (2005, hereafter M05) stellar population models (Tonini et al., 2009, 2010). We then apply dust reddening to the total spectra. Following Tonini et al. (2010), we adopt a Calzetti et al. (2000) extinction curve (see Fig. 3.3) and a colour-excess $E(B-V)$ proportional to the galaxy star formation rate, parameterised as

$$E(B-V) = 0.33 \cdot (log(SFR) - 2) + 1/3 \tag{2.1}$$

and $E(B-V) = 0$ for SFRs less than $10\,M_{\odot}$/yr. This parameterisation is based on the reddening derived for a sample of real star-forming galaxies at $z \sim 2$ in the GOODS fields (Daddi et al., 2007, M10, Section 6.1). We do not randomise the inclination of disk galaxies (which reduces the dust effect in face-on objects) but we redden the spectrum by the total amount of extinction calculated for each galaxy, therefore considering the maximal reddening for each object.

As in Tonini et al. (2010) the mock catalogues are built by redshifting the (unreddened and reddened) spectra in each simulation time step to the corresponding redshift value, obtaining the observer's frame spectra. We then filter the spectra with a chosen set of broad-band filters (see Fig. 3.2) to obtain the observer's frame broad-band magnitudes.

[1] The time it takes a particle located at the half-mass radius to reach either the opposite side of the galaxy (for a disk) or its center (for a bulge, Hatton et al., 2003)

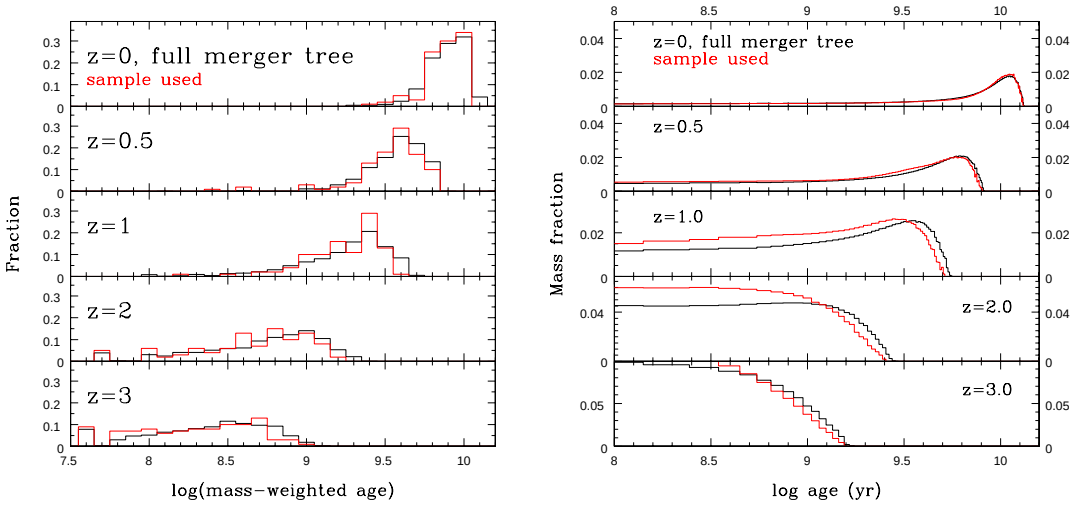

Figure 2.1: *Left:* Mass-weighted ages of mock star-forming galaxies at redshifts 0, 0.5, 1, 2 and 3 for the entire merger tree (black) and the sub-sample used in this thesis (red). *Right:* Age distribution. Note the different scales on the y axes.

Finally, we scatter the magnitudes with Gaussian errors with three σ errorbars typical of those of the COSMOS survey (Capak et al., 2007) for mock galaxies at redshifts ≤ 1 and those of the GOODS star-forming objects (Giavalisco et al., 2004) for mock galaxies at redshift ≥ 2 (~ 0.05 and 0.1 mag, respectively). From one merger tree[2] we use a sample 100 mock galaxies at each of the five redshifts $z = 0$, 0.5, 1, 2 and 3, respectively. For simplicity we chose the first 100 galaxies at each redshift. Within GalICS the order of galaxies depends on the order of the haloes they reside in. This order depends on the halos position in the simulation volume but is not specific with regard to mass for example. Since haloes as well as galaxies merge over time and new haloes and galaxies form this subsample still represents the merger tree adequately (see also Figs. 2.1-2.4) just in a smaller volume. [3] The fitting method is described in Section 3.

The stellar population properties of the mock galaxies of the full merger tree are shown in conjunction with those of the 100 galaxy sample used in this thesis in Figs. 2.1-2.4. The mass-weighted ages of galaxies at $z \sim 0$, 0.5 and 1 are confined around a few Gyr (Fig. 2.1, left). However, star formation is never completely shut off in semi-analytic models such that low redshift objects contain a small fraction of populations that are much younger than the mass-weighted age. This is shown in Fig. 2.1, right hand panel. Therefore, the intrinsic stellar populations of these galaxies cover a much broader age

[2]The full merger tree consists of 1811, 2003, 2118, 1760 and 1195 galaxies at $z = 0$, 0.5, 1, 2 and 3, respectively.

[3]We also verified that our conclusions remain unchanged when using the entire merger tree at each redshift in the analysis.

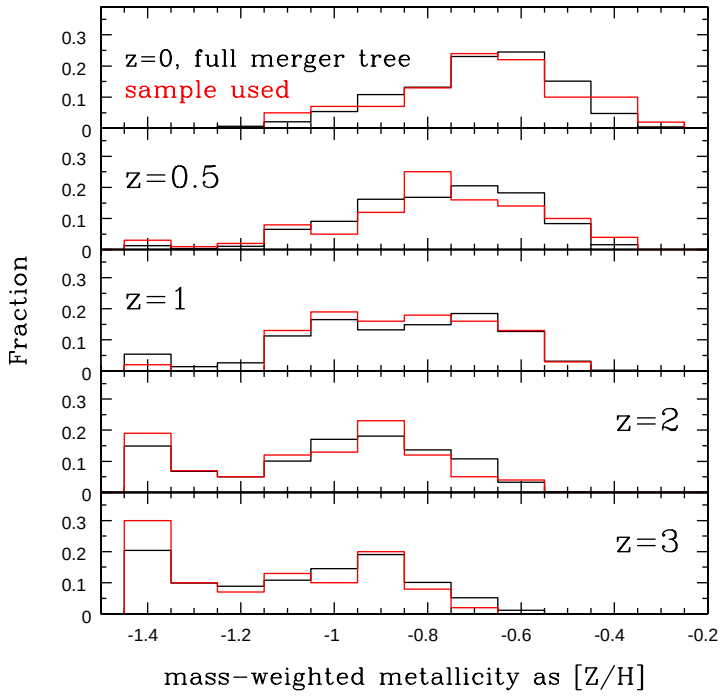

Figure 2.2: Mass-weighted metallicities of the mock star-forming galaxies at redshifts 0, 0.5, 1, 2 and 3 for the entire merger tree (black) and the sub-sample used in this thesis (red).

range than those at higher redshift. This will have consequences on the capability of simple composite models to recover the actual properties of these galaxies (see Chapters 4 and 5). Mass-weighted metallicities increase with redshift, but hardly reach half-solar metallicity by $z \sim 0$ (Fig. 2.2). Note, that the latest formed populations have indeed solar and super-solar metallicities but their contribution to the total stellar mass is very small. At high redshift, the mass-weighted ages of most galaxies are younger than 1 Gyr, and much more similar to each other with respect to those at low redshift. As expected, metallicities are lower.

As a further illustration we show the typical star formation histories of galaxies at redshift 0.5 and 2 in Fig. 2.3. Galaxies at redshift 2 show predominantly increasing star formation rate while for most galaxies at redshift 0.5 the star formation rate decreases with time. Finally, star formation rates are shown as a function of stellar mass in Fig. 2.4. The number of low mass objects decreases towards $z = 0.5$. Most objects have very low star formation rates.

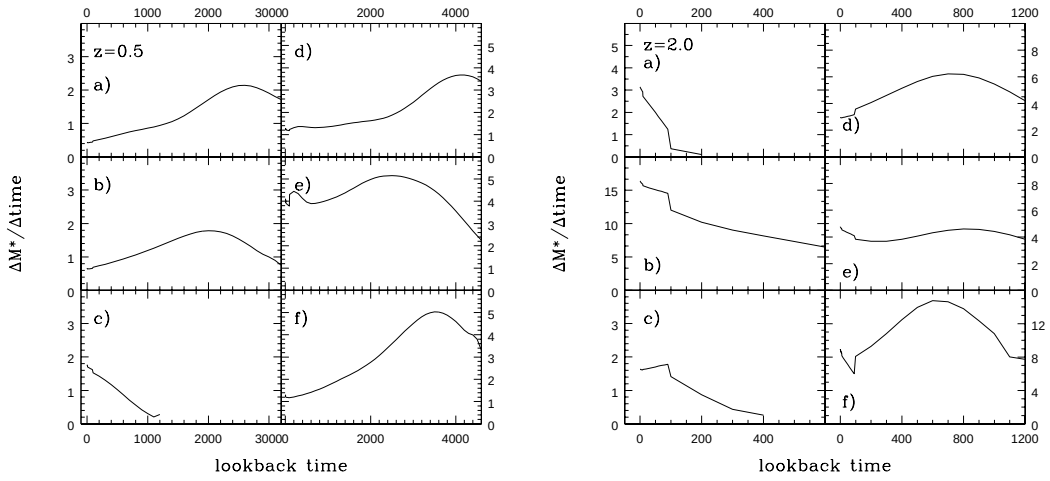

Figure 2.3: Selection of star formation histories of semi-analytic galaxies at $z = 0.5$ (left) and 2 (right). The zeropoint of the lookback time lies at the given redshift. Galaxy star formation rates at $z = 2$ increase, while those at $z = 0.5$ predominantly decline. Galaxies at redshift 2 are younger than those at redshift 0.5 (see Fig. 2.1).

It is important to notice that - from the stellar population properties point of view - galaxies at $z = 2$ and 3 and galaxies at $z = 0.5$ and 1 are similar, and with regard to various assumptions in the fitting. The wavelength coverage is obviously redshift sensitive and conclusions may be different.
Note that we do not show the $z \sim 0$ objects further because they are more easily accessed by other diagnostic methods such as spectroscopy, and we shall study them in a separate publication.

2.1.2 Passive galaxies

Star formation in the semi-analytic model is never completely shut off. In order to study the case of truly passive and old galaxies, we consider a set of solar metallicity, Salpeter IMF, simple stellar populations of M05 and place them at the various redshifts. The ages of the mock passive galaxies range from 1 to 7 Gyr at $z = 0.5$ and from 1 to 1.5 Gyr at $z = 3$. Stellar masses vary between $10^{10.5}$ and $10^{12}\,M_{\odot}$ in steps of 0.25 dex[4]. Internal reddening was not added to these passive galaxies.

[4]In total these are 56, 42, 21 and 14 galaxies at redshift 0.5, 1, 2 and 3, respectively.

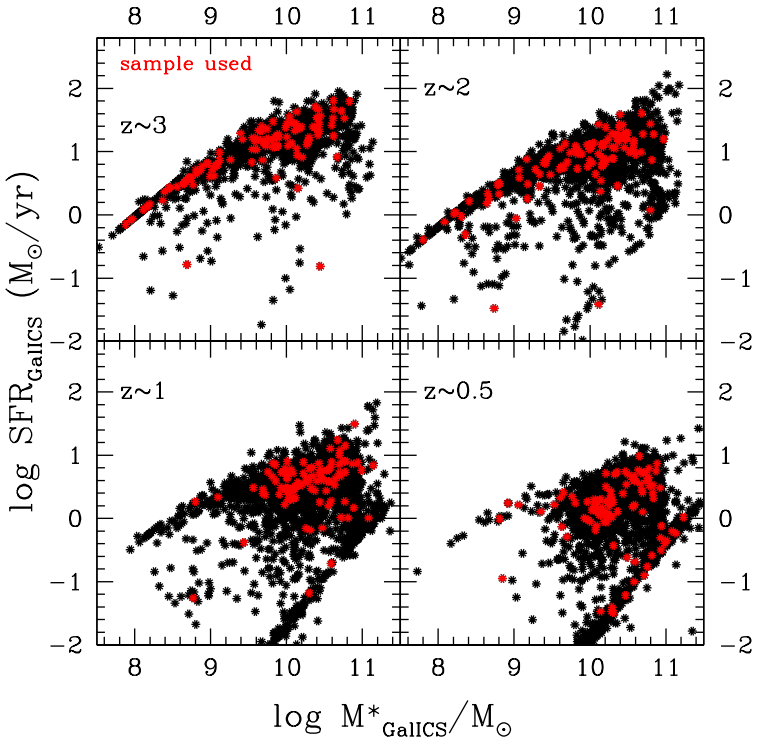

Figure 2.4: Stellar masses and star formation rates of mock star-forming galaxies at redshifts 0.5, 1, 2 and 3 for the entire merger tree (black dots). The sub-sample used in this thesis is marked in red. The build-up of the red sequence towards lower redshift is visible in the bottom right of each panel.

2.2 Star-forming galaxies in GOODS-South

2.2.1 GOODS - The Great Observatories Origins Deep Survey

The Great Observatories Origins Deep Survey (GOODS[5], Dickinson et al., 2003) combines very deep observations carried out with NASA's great observatories - namely the Spitzer Space Telescope, the Hubble Space Telescope (HST) and the Chandra X-ray Satellite - ESA's Herschel Telescope and XMM-Newton and ground-based telescopes to enable the study of galaxy formation and evolution at early cosmic times. Observations cover a wide wavelength range from the optical (HST+ground-based data) via the infrared (Spitzer, Herschel) to the X-ray (Chandra, XMM-Newton) regime of two fields covering a total area of $\sim 320\,arcmin^2$. The northern field (GOODS-North) is centred on the Hubble Deep Field North at 12h 36min 55s, +62° 14min 15s. The southern field (GOODS-South) is centred on the Chandra Deep Field South at 3h 32m 30s, -27° 48min 20s. Photometric observations are complemented by ground-based spectroscopic data.

[5]http://www.stsci.edu/science/goods/

In the next section we describe the sample of galaxies from the southern field which we study in detail in Chapter 6, Section 6.1.

2.2.2 Galaxy sample selection

We use a sample of 96 galaxies in the GOODS-South (Giavalisco et al., 2004) field from Daddi et al. (2007). These galaxies were selected via the BzK diagram[6] (Daddi et al., 2004) to be star-forming, as confirmed by the detection in deep Spitzer+MIPS data at 24μm for $> 90\%$ of the galaxies in the sample. We include only objects with accurately determined spectroscopic redshifts at $z > 1.4$, which were derived from a variety of surveys (see Daddi et al., 2007, for references), including notably ultra-deep spectroscopy from the GMASS (Galaxy Mass Assembly ultradeep Spectroscopic Survey) project[7](Kurk et al., 2009) and from the GOODS survey at the Very Large Telescope (Vanzella et al., 2008; Popesso et al., 2009). Galaxies in the resulting sample lie in the range $1.4 \leq z \leq 2.9$.

The multicolour photometry was obtained using the four bands HST+ACS data in the optical (Giavalisco et al., 2004), the JHK bands in the near-IR from VLT+ISAAC observations (Retzlaff et al., 2010) and from Spitzer+IRAC (Dickinson et al., *in prep.*). We used PSF-matched images to build photometric catalogues from B to K. The IRAC photometry was measured over $4''$ diameter apertures and corrected to total magnitudes using corrections appropriate for point sources, and matched to the K-band using total K-band magnitudes as a comparison. This is the same procedure that was used for the GOODS-S catalogues presented by Cimatti et al. (2008) and Daddi et al. (2007). In summary, all SED-fits in Chapter 6, Section 6.1 make use of the following bands: $BVizJHK$ plus the Spitzer/IRAC channels 1, 2 and 3.

Besides satisfying the BzK criterion, the sample of galaxies used in this thesis is subject to the additional selection imposed by the various spectroscopic surveys mentioned above. Fig. 2.5 shows the distribution functions of the mass, SFR, and reddening, as derived by Daddi et al. (2007), separately for the full $K_{\rm Vega} < 22$ sample in the GOODS-South field, and for the sub-sample of 96 objects with spectroscopic redshifts. The sample used here is somewhat biased towards higher masses, SFRs, and extinctions, but by and large for all three quantities it covers a major fraction of the range exhibited by the full sample. This can also be appreciated by inspecting Fig. 2.6, where the 96 galaxies used

[6]Star-forming galaxies at $z \geq 1.4$ are selected with $BzK = (z-K)_{AB} - (B-z)_{AB} > -0.2$, passive galaxies in the same redshift range are selected with $BzK < -0.2$ and $(z-K)_{AB} > 2.5$.

[7]http://www.arcetri.astro.it/$\sim$ cimatti/gmass/gmass.html

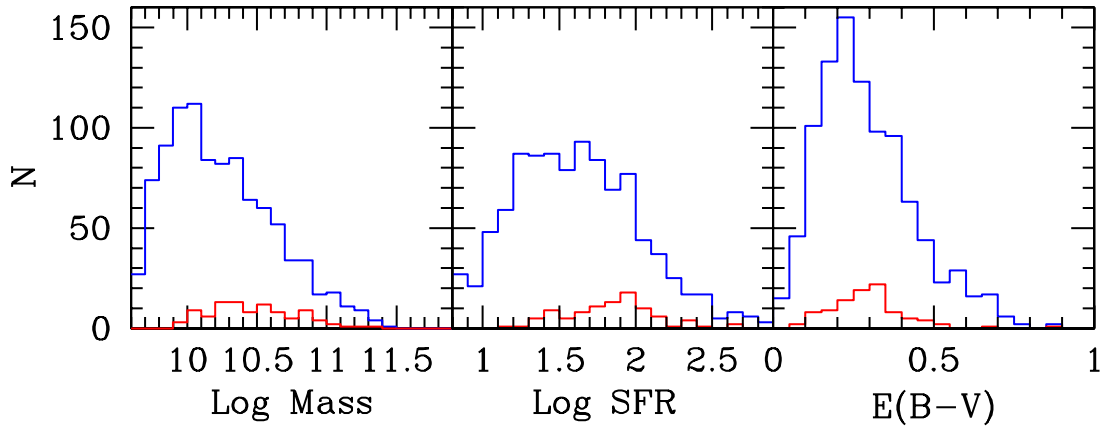

Figure 2.5: The distribution functions of the stellar mass, SFR, and reddening of BzK galaxies in the GOODS-South sample as from Daddi et al. (2007), separately for the full sample and for the sub-sample with spectroscopic redshifts which is used in this thesis.

in the present study are compared to the whole sample in Daddi et al. (2007). Therefore, we consider that the conclusions drawn from this spectroscopic sample should hold for the full sample, perhaps with the exclusion of some low-mass, low-SFR objects.

This database allows the sampling of galaxy SEDs up to the rest-frame K-band. The SEDs over the whole wavelength range from the rest-frame UV to the K-band will be analysed in Chapter 6, Section 6.1.

2.3 Luminous galaxies in the Baryon Oscillation Spectroscopic Survey

2.3.1 BOSS - The Baryon Oscillation Spectroscopic Survey

The Baryon Oscillation Spectroscopic Survey (BOSS[8], Eisenstein et al., 2011) is one of the four surveys comprised within the Sloan Digital Sky Survey (SDSS) III. SDSS-III/BOSS (hereafter BOSS) contains two simultaneous spectroscopic surveys[9] itself:

- one designed to map 1.5 million luminous galaxies over the last ~ 6 Gyr (out to a redshift of $z \approx 0.7$)
- and one targeting $150,000$ quasars between redshift 2.2 and 4 in order to observe the Lyman-α forest

[8] http://www.sdss3.org/surveys/boss.php
[9] excluding ancillary projects

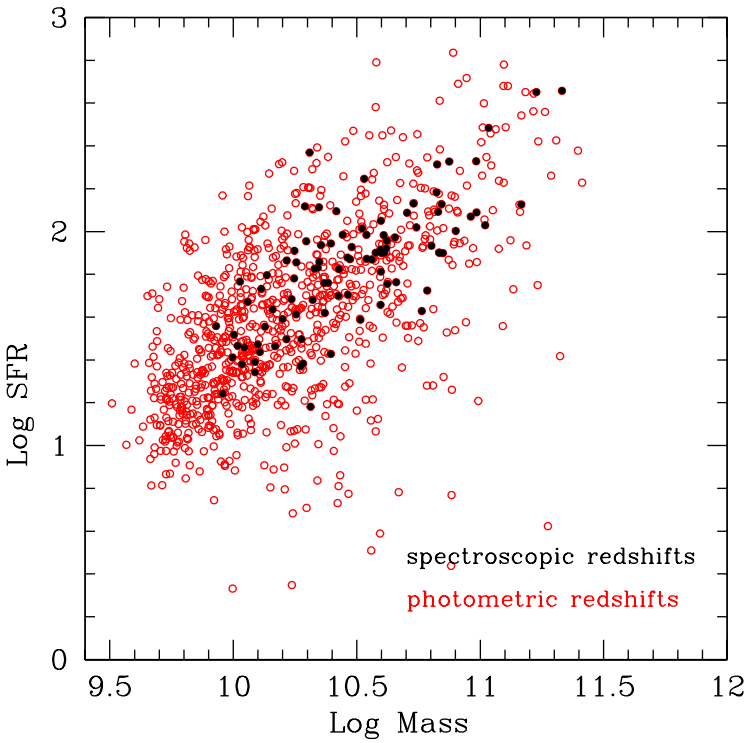

Figure 2.6: The SFR vs. stellar mass of star-forming BzK-selected galaxies in the GOODS-South field (from Daddi et al., 2007). The sub-sample with spectroscopic redshifts is indicated and represents the set of galaxies for which various SED-fits are attempted in this thesis. The SFRs are in $M_{\odot}$/yr and masses in $M_{\odot}$ units.

BOSS, when finished, will cover an area of over $10,000\,deg^2$ (Fig. 2.7). The survey aims at measuring the baryon acoustic oscillation signature[10] in the correlation function of galaxies and the quasar Lyman-α forest with unprecedented accuracy to improve constraints on the accelerated expansion of the Universe.

BOSS is carried out over 5 years (Fall 2009 - Summer 2014). Besides the above mentioned survey aim BOSS data can be exploited for a variety of other science. These include (among others) constraints on clustering growth rates (White, Song & Percival, 2009) via redshift space distortions, evolution of matter clustering using weak lensing, constraints on the mass profiles of early-type galaxies from strong lensing (Bolton et al., 2008; Koopmans et al., 2009), constraints on the evolution and clustering of quasars,

[10]Baryon Acoustic Oscillations (BAO) are the imprint of propagating sound waves in the early Universe on today's baryonic matter distribution. In the early Universe sound waves of baryons and photons propagated together. When matter (baryons) and radiation (photons) decoupled at the time of recombination the baryonic sound wave signal was frozen into the matter distribution (creating overdensities) while the photon sound wave continued to travel. The characteristic length scale of the imprinted baryonic sound waves is 150 Mpc (measured for example by Cole et al., 2005; Eisenstein et al., 2005; Percival et al., 2010).

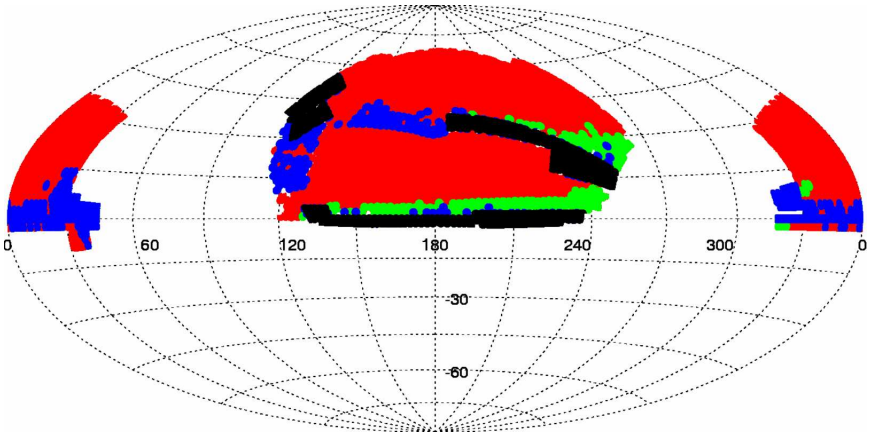

Figure 2.7: BOSS survey footprint. Each colour presents a superset, in the sense that it contains the area of the colour before. Black refers to the first semester of data, green to the data taken already, blue to the projected survey covered till the summer shutdown and red to the final sky coverage of the survey. *Credit: Cameron McBride*.

etc.. Most importantly for this thesis, however, is the possibility to study the evolution of massive galaxies between $0 \leq z \leq 0.7$. In the following, we focus on this part of BOSS only.

2.3.2 Galaxy Target Selection

The galaxy sample used in this thesis is a subsample of all objects targeted in BOSS and covers observed galaxy data up to 22 July 2011. The galaxy target selection is carried out via colour and apparent magnitude cuts using SDSS imaging (Fukugita et al., 1996; Stoughton et al., 2002) in $ugriz$ filter bands (see Fig. 3.2). For this all apparent magnitudes are based on SDSS *cmodel* magnitudes. When apparent magnitudes are combined to a colour then SDSS *model* magnitudes[11] are used following the recommendations on the SDSS webpage[12]. Specifically, for BOSS there are separate selection criteria for low (LOZ cut) and higher redshift ($CMASS$ cut) galaxies following the approach of Eisenstein et al. (2001) for the selection of luminous red galaxies (LRGs) in the SDSS-I/II survey. Both selection criteria make use of the following 3 colour definitions:

- $c_{||} = 0.7 \times (g - r) + 1.2 \times (r - i - 0.18)$ (Cannon et al., 2006)
- $c_{\perp} = (r - i) - ((g - r)/4) - 0.18$ (Eisenstein et al., 2001)
- $d_{\perp} = (r - i) - (g - r)/8$

[11] Magnitude definitions are given in Chapter 3.
[12] http://www.sdss.org/dr7/algorithms/photometry.html

The focus lies on the three photometric bands gri to help decode a galaxy's redshift and nature (i.e. passive or star-forming galaxy and age of the galaxy). Most important for this are location and strength of the 4000 Å break. The 4000 Å break wanders through these three filter bands with increasing redshift (see Fig. 3.2 for a guideline on the positions of the 4000 Å break at various redshifts). For galaxies with $0.1 < z < 0.4$ the 4000 Å break falls into g-band, hence $g - r$ is a good redshift tracer for low redshift galaxies (redshift increases with redder $g - r$). For galaxies with $0.4 < z < 0.7$ the 4000 Å break lies in r-band causing $r - i$ colours to be red. Finally, for galaxies with $z > 0.7$ the 4000 Å lies in i-band. In the $g - r$ vs. $r - i$ colour-colour plane the evolutionary tracks for star-forming and passive galaxies overlap for $z < 0.4$ such that bluer (star-forming) galaxies with a higher redshift and redder (passive) galaxies with a lower redshift occupy the same space in the diagram (compare Fig. 2 in Eisenstein et al. 2001). The tracks separate for $z > 0.4$ such that passive (redder) galaxies show redder $r - i$ for increasing redshift at nearly constant $g - r$ of ~ 1.7 while for star-forming galaxies $g - r$ remains bluer due to a weaker 4000 Å break and on-going star formation. Because $d_\perp$ is dominated by the contribution of $r - i$ a line of constant $d_\perp$ is almost horizontal in the $g - r$ vs $r - i$ colour-colour plane (compare Fig. 2.9). Thus one can effectively select galaxies according to redshift for $z > 0.4$. Star-forming and passive galaxies can then be separated using for example $c_{||}$. At low redshift $c_{||}$ and $c_\perp$ help to disentangle star-forming from passive galaxies (by exploiting the rotated coordinate system of $g - r$ and $r - i$, for definition and details see Eisenstein et al. 2001).

Based on the colour definitions listed above, BOSS galaxies fulfilling the following criteria pass the LOZ cut (also Cut I):

- $r < 13.6 + c_{||}/0.3$
- $|c_\perp| < 0.2$
- $16 < r < 19.5$

Requirements for passing the $CMASS$ cut (also Cut II) are:

- $17.5 < i < 19.9$
- $d_\perp > 0.55$
- $i < 19.86 + 1.60 \times (d_\perp - 0.80)$ (sliding cut)

The LOZ selection is aimed at luminous, massive galaxies in the redshift range between 0.2 and 0.4 using $c_\perp$ and $c_{||}$. The $CMASS$ cut is designed to select galaxies with redshifts between 0.4 and 0.7 by restricting $d_\perp > 0.55$. Additionally, the cut in apparent

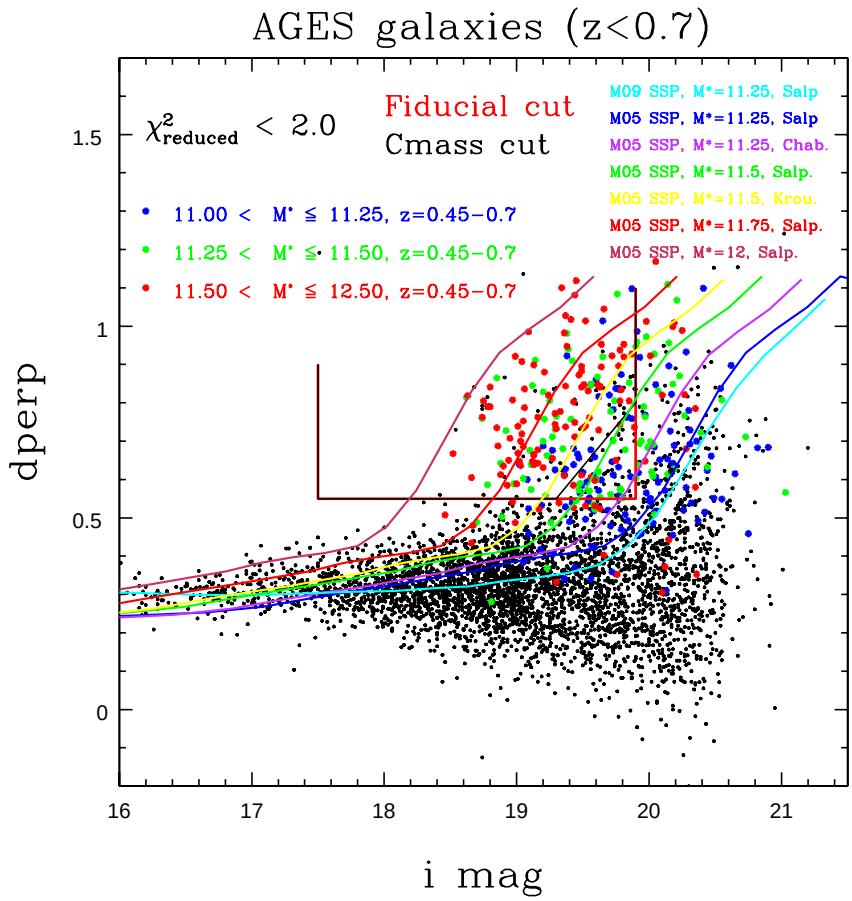

Figure 2.8: $d_\perp$-colour i-band magnitude diagram illustrating the BOSS $CMASS$ target selection. Everything within the indicated boxed region is selected via the $CMASS$ cut. A sample of AGES (Kochanek et al., 2004) galaxies for which we derived stellar masses from SED-fitting are colour-coded by stellar mass and redshift. Only fits with sufficiently low χ^2_ν are shown. Illustrated are also the evolutionary tracks of passively evolving galaxies as a function of stellar mass and stellar population model: Salpeter IMF M09 SSP of $log\, M^* = 11.25$ (cyan), Salpeter IMF M05 SSP of $log\, M^* = 11.25$ (blue), Chabrier IMF M05 SSP of $log\, M^* = 11.25$ (purple), Salpeter IMF M05 SSP of $log\, M^* = 11.5$ (green), Kroupa IMF M05 SSP of $log\, M^* = 11.5$ (yellow), Salpeter IMF M05 SSP of $log\, M^* = 11.75$ (red) and of mass $log\, M^* = 12$ (dark red). All M05 SSPs are of solar metallicity, the M09 SSP is 97% solar metallicity and 3% metal-poor (see Chapter 3 for details). These tracks start at $z \approx 0.7$ such that at $z = 0$ an age of ~ 13 Gyr is reached.

i-band magnitude and the sliding cut aim at selecting galaxies with roughly constant stellar mass (see also Eisenstein et al., 2011; White et al., 2011). In order to achieve a selection of nearly constant mass the evolutionary track of a passively evolving galaxy of a given mass based on the Maraston et al. (2009) stellar population model served as guide (solid lines in Fig. 2.8). In particular, we tested how the slope of the sliding cut in Fig. 2.8 changes with model parameters, such as IMF and stellar population model. In order

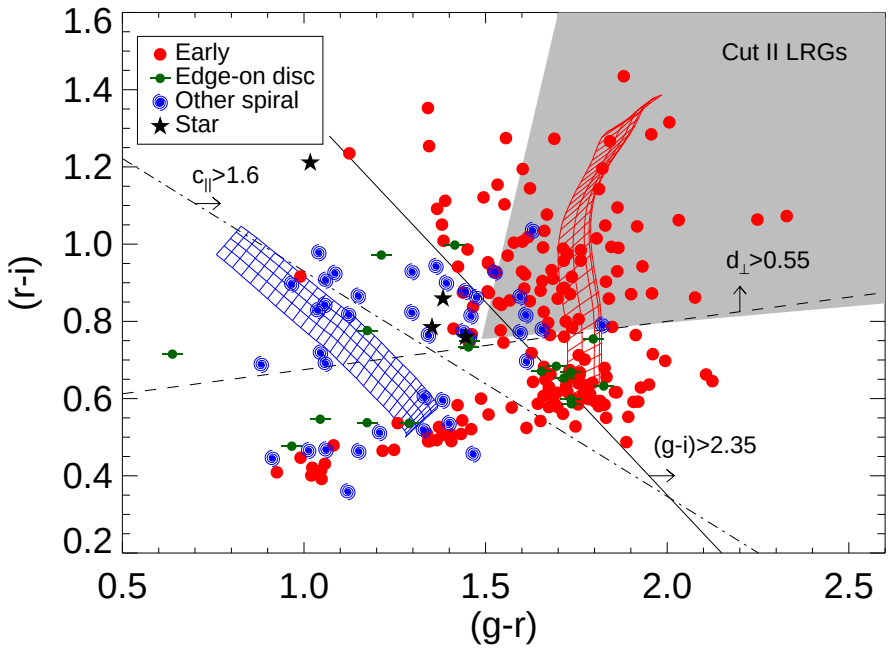

Figure 2.9: *Fig. 4 of Masters et al. (2011)* of the $g-r$ vs $r-i$ colours for a sub-sample of BOSS galaxies for which COSMOS HST imaging is available. Symbols are encoded by galaxy morphology - early-types (red dots), late-types (blue spirals), stars (black stars) and edge-on spirals (green). The dashed line represents $d_{\perp} = 0.55$, the colour selection criterium for $CMASS$ galaxies. Galaxies above this line are selected as $CMASS$. The solid line illustrates a colour cut with $g - i = 2.35$ which divides early and late-type galaxies in the BOSS $CMASS$ cut. The dot-dashed line shows the $c_{||} > 1.6$ colour cut which defines LRGs in the 2SLAQ survey (Cannon et al., 2006). The grey-shaded region shows the Cut II LRG sample used in Eisenstein et al. (2001) in SDSS-I/II. Red and blue grids illustrate the tracks of theoretical models for passive (red) and constantly star-forming (blue) galaxies in a redshift range of $0.4 < z < 0.7$. The grid shows steps of 0.01 in redshift and 1 Gyr in age ranging from 4 to 8 Gyr.

to confirm the constant mass assumption we determined stellar masses via SED-fitting of a sample of AGES (Kochanek et al., 2004) galaxies covering the same redshift range as BOSS. These tests contributed to the adjustment of the slope of the sliding cut as listed above.

Because the BOSS galaxy target selection does not contain a strong restriction on the $g - r$ colour all types of galaxies (early-type/red and late-type/blue) are selected as long as they are massive. For example, for galaxies at $z > 0.4$ the observed $g - r$ colour is close to the rest-frame $u - g$ colour and thus a blue $g - r$ colour reflects star formation and a red $g - r$ colour a passive nature. However, we already pointed out in the Introduction that early-type galaxies are generally more massive than late-type galaxies.

Consequently, the majority of galaxies in BOSS is expected to be early-type. This is confirmed for $CMASS$ galaxies in Fig. 2.9 which shows a sub-sample of BOSS galaxies imaged with HST in the COSMOS field enabling morphological classification (Masters et al., 2011). About 75% of the galaxies in this sub-sample are of early-type. In particular, Masters et al. (2011) find that a colour cut placed at $g - i = 2.35$ works very well in dividing $CMASS$ galaxies by morphology.

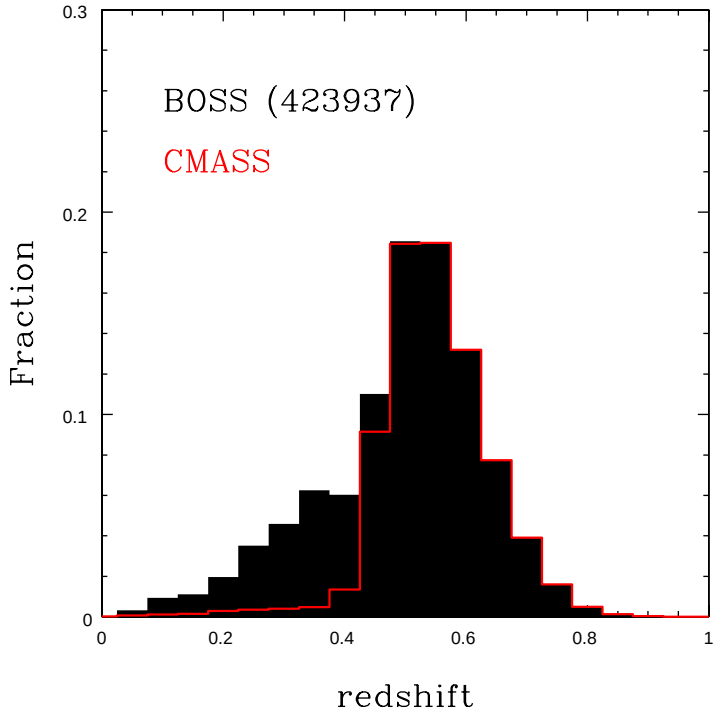

Figure 2.10: Redshift distribution of a subsample of BOSS main sample galaxies observed by 22 July 2011 (total number of 423,937 galaxies) used in this thesis. The red histogram marks the redshift distribution of the $CMASS$ galaxies within that sample (total number of 323,920 galaxies). As expected galaxies above $z = 0.5$ are selected via the $CMASS$ cut.

In order to select the cleanest sample of galaxies we additionally require the following SDSS-internal data flags to be true:

- $specprimary = 1$ (defines a unique sample of objects, only primary observation of object is used, repeats are excluded)
- classified as GALAXY
- $z\_warning = 0$ (ensures a reliable redshift estimate)

Redshifts were determined through the SDSS pipeline (Stoughton et al., 2002). The redshift distribution of the BOSS galaxies used in this thesis is shown for the total and for the $CMASS$ selection separately in Fig. 2.10.

The galaxy targeting algorithm of BOSS is described in more detail in Padmanabhan et al., (*in prep.*). Details about the BOSS data can be found in the DR8 overview paper (Aihara et al., 2011) and about SDSS itself in the next section.

2.4 Galaxies in the Sloan Digital Sky Survey Data Release 7

2.4.1 SDSS - The Sloan Digital Sky Survey

The Sloan Digital Sky Survey (SDSS[13], York et al., 2000) is the largest galaxy, quasar and star survey undertaken so far. SDSS started in 2000. The initial survey (now called SDSS-I) finished in 2005 and was continued for another three years (called SDSS-II). SDSS-III is the third iteration of SDSS, running from 2008 to 2014, and comprises the BOSS survey which we introduced in the previous section. The area mapped by SDSS (entire survey) photometrically in $ugriz$ filter bands and spectroscopical follow-up covers more than one quarter of the entire sky, mostly in the northern hemisphere. Data collected by the SDSS survey is released publicly once a year. The latest data release before the start of SDSS-III is the Data Release 7 (hereafter DR7, Abazajian et al., 2009) which contains images, spectra, imaging catalogues and redshifts. The imaging and spectroscopic footprint are shown in Fig. 2.11.

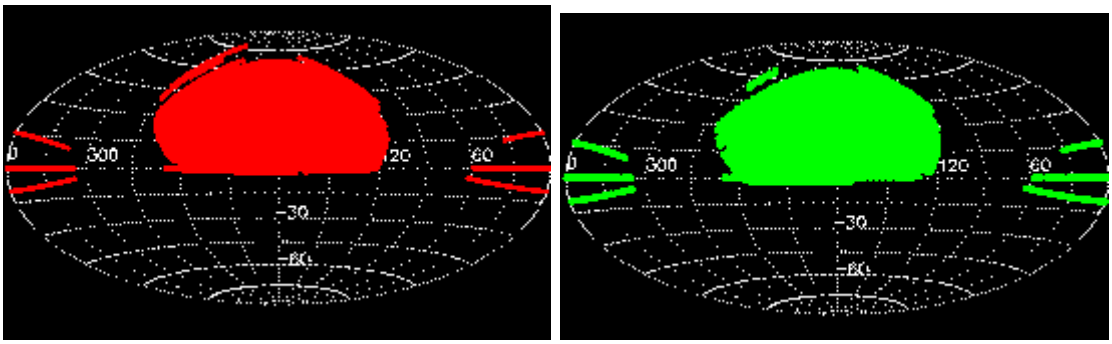

Figure 2.11: SDSS DR7 survey footprint. *Left:* Imaging footprint. *Right:* Spectroscopic footprint. *Source:* $http://www.sdss.org/dr7/coverage/index.html$

[13] http://www.sdss.org/

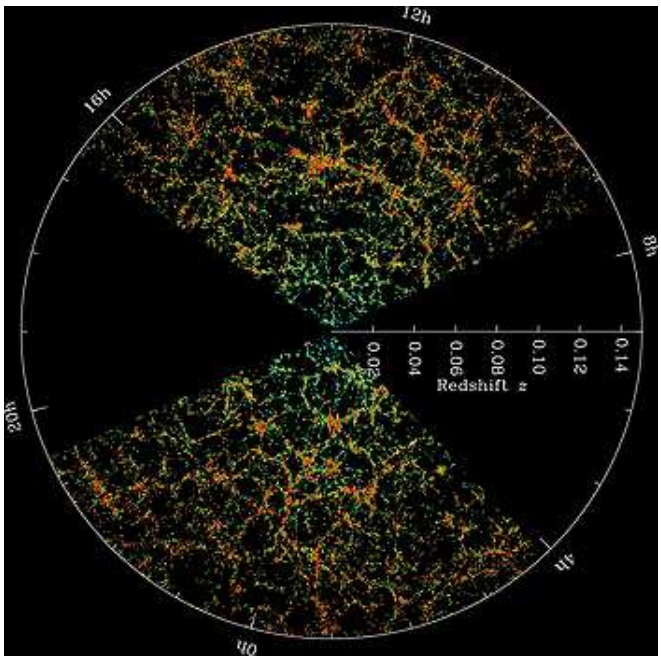

Figure 2.12: Large scale structure with SDSS DR7. *Source:* $http://www.sdss.org/legacy/index.html$

SDSS DR7 data contains spectra of more than 930,000 galaxies, 120,000 quasars and 225,000 stars. Observations (imaging and spectroscopy) were carried out with the Sloan telescope (Gunn et al., 2006) at Apache Point Observatory, New Mexico, using a mirror of 2.5 m and specialised instruments (CCD camera, Gunn et al. 1998, and multi-object fibre spectrographs, Uomoto et al. 1999). All data is analysed via the automated survey pipeline which encompasses image reduction (sky subtraction, flatfielding, image defect corrections), coordinate measurements and shape and flux measurements (Stoughton et al., 2002). Fluxes are transferred to magnitudes as described in Chapter 3. Extinction corrections for galactic extinction are provided using the Schlegel, Finkbeiner & Davis (1998) dust maps. By mapping such a large number of objects spectroscopically a 3-dimensional map of the local Universe (out to redshift ~ 0.15) was be obtained (Fig. 2.12) which shows the large scale structure in form of overdensities, filaments and voids which we described in the Introduction.

2.4.2 Galaxy sample selection

In this thesis we use a sub-sample of the DR7 data. Via the Catalogue Archive Server (CAS[14]) we assemble the photometry and spectroscopic redshifts from the *PhotoPrimary* and *SpecObjAll* tables for objects that are contained in both tables (identified by

[14]http://cas.sdss.org/astrodr7/en/

the spectroscopic object ID), which are classified as galaxies ($specclass = 2$) and for which redshifts are reliable ($z\_warning = 0$). The redshift distribution of the sample of galaxies used in this thesis is shown in Fig. 2.13.

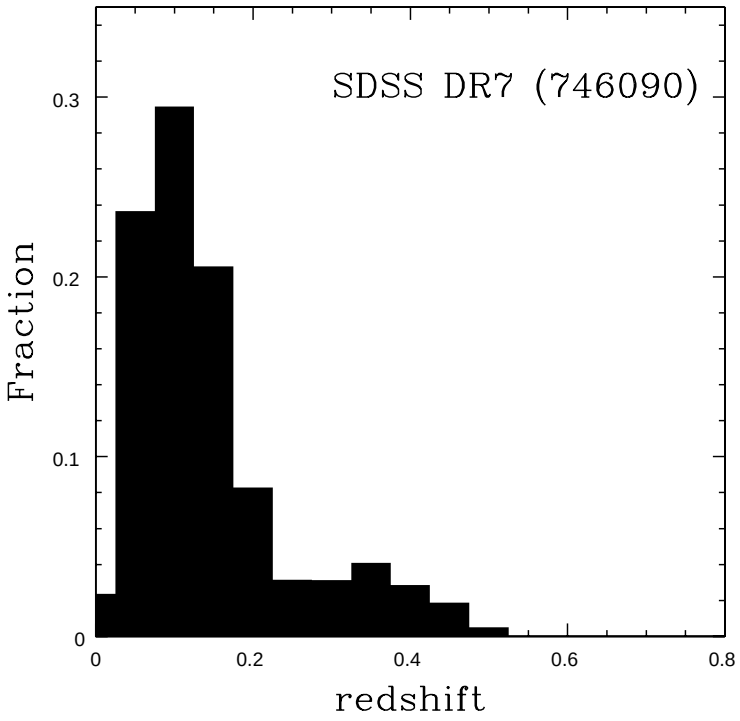

Figure 2.13: Redshift distribution of DR7 galaxies analysed in this thesis. See text for details about the selection criteria for this data sample.

Chapter 3

Spectral energy distribution fitting

In the previous chapter we introduced the data samples that are analysed in this thesis. In this chapter we focus on the method that is applied throughout this thesis to derive the stellar population properties of these galaxies. Firstly, we introduce the concepts of redshift and magnitudes. Then we summarise the variety of methods that are used in the literature to decode the stellar content of galaxies. Finally, we turn our attention to the method employed in this thesis - the spectral energy distribution (SED) fitting by describing the fitting code and model templates used in detail.

3.1 Redshift

We briefly described the Doppler Effect in the Introduction. The Doppler Effect describes how the emitted light of a galaxy that moves away from us is stretched out on its way to us and causes the galaxy to appear redder when it is observed - the light is redshifted. Redshift is then defined as

$$z = \frac{\lambda_{obs} - \lambda_{emit}}{\lambda_{emit}} \tag{3.1}$$

where λ_{obs} is the observed wavelength and λ_{emit} is the emitted wavelength. In a cosmological framework redshift is caused by the expansion of the Universe and is therefore a function of the object's distance from us (Hubble, 1929).

Redshifts can be measured in two different ways - spectroscopically and photometrically. Spectroscopic redshifts are obtained from the comparison between the position of observed (redshifted) spectral features, such as breaks, absorption and emission lines, in the spectra of galaxies and their rest-frame (unredshifted) position. Redshifts are determined most accurately spectroscopically but this method relies crucially on the S/N of the spectra. Thus the fainter and more distant a galaxy is, the more time consuming and

difficult it is to get a good quality spectrum. Moreover, the most commonly used spectral features to determine spectroscopic redshifts move out of the observable region at $z \sim 1.5$, leaving observers with little reference lines for the redshift determination (see Renzini & Daddi, 2009, for a summary).

Thus, in order to obtain larger samples and probe the high-redshift regime redshifts are more commonly determined photometrically. This method relies on the identification of strong spectral features, such as the Lyman-break at 912 Å and the 4000 Å break, and the overall spectral shape, the SED. Photometric redshifts are determined either via *template fitting* or *empirical training sets*. A variety of codes for the determination of photometric redshifts are publicly available to carry out this task (e.g., Benítez 2000, *HyperZ* by Bolzonella, Miralles & Pelló 2000, ANNZ by Firth, Lahav & Somerville 2003, IMPZ by Babbedge et al. 2004, LePhare by Ilbert et al. 2006, ZEBRA by Feldmann et al. 2006, EAZY by Brammer et al. 2008, GalMC by Acquaviva, Gawiser & Guaita 2011). Template fitting compares model SEDs to the data and the SED with the best fit determines the redshift (pioneered by Baum, 1962). We will explore this method in more detail in Section 3.3. Empirical training set techniques rely on a large set of galaxies with known colours and spectroscopic redshifts from which a relation between observed colour and redshift is inferred and then used to obtain redshifts for galaxies for which only colour information is available (Connolly et al., 1995; Brunner et al., 1997; Wang et al., 1998).

3.2 Magnitudes

Besides observing a spectrum, information about the shape of a galaxy's SED can also be obtained via photometry by observing a galaxy in specific confined regions (so called filter bands, see Fig. 3.2) of the electromagnetic spectrum. The flux of an object in a specific filter band can then be transformed into the so-called apparent magnitude of the object in that filter band. The apparent magnitude (m) in a filter band is defined as

$$m_{Vega} = -2.5 \times log \frac{\int F_\nu \times S_\nu \times d\nu}{\int F_\nu(Vega) \times S_\nu \times d\nu} \tag{3.2}$$

where ν is frequency, F_ν is the flux of the object in ergs/s/cm^2/Hz, S_ν is the instrumental response (filter band transmission curve, CCD and telescope) and $F_\nu(Vega)$ is the flux of the star Vega in ergs/s/cm^2/Hz. This magnitude system was chosen such that the apparent magnitudes of the reference star Vega are zero in all filter bands. An alternative magnitude system is the AB system (Oke, 1974) in which an object with constant flux

(i.e. a flat energy distribution) has the same apparent magnitude in all filters and therefore all colours are zero. AB magnitudes are defined as

$$m_{AB} = -2.5 \times log \int F_\nu \times S_\nu \times d\nu - 48.6. \tag{3.3}$$

Conversions from one magnitude system to the other are obtained via the AB magnitudes of Vega. In both systems smaller values for magnitudes correspond to brighter objects. The origin of the magnitude definition stems from the historic classification of stars into six equally spaced classes of brightness (1^{st} magnitude as the brightest class, 6^{th} magnitude as the faintest class which includes stars that are just bright enough to still be visible with the naked eye) as defined by Greek astronomers. The transformation from flux into magnitudes follows the suggestion of Pogson (1856) such that 5 magnitudes difference relate to a factor of 100 in flux. The colour of an object is simply defined as the difference of the magnitudes in two filter bands.

Since apparent magnitudes depend on the distance of the object from us, another definition of brightness is needed to ease the direct comparison between objects at various distances. Thus absolute magnitudes are defined as the apparent magnitude an object would have at a standard distance of 10 pc. With the inverse square law connecting fluxes and distances[1] we can then express the absolute magnitude as function of the apparent magnitude as

$$M = m + 2.5 \times log(\frac{f}{F}) - A - K - e \tag{3.4}$$

$$= m - 5 \times log(d) + 5 - A - K - e. \tag{3.5}$$

The factor A corrects for the interstellar extinction. Light travelling through our own galaxy is affected by the interstellar medium (gas and dust) such that light is scattered and absorbed. How strong this effect is depends on its wavelength, e.g. blue wavelengths are scattered more than red wavelengths. K (the K-correction, e.g. Hogg et al. 2002) corrects for redshift effects between the true distance d of the object and the standard distance of 10 pc. e describes the evolutionary correction. Additionally to the K-correction one has to account for the evolution in galaxy colour with time, i.e. the fact that galaxies at higher redshifts are younger than those at lower redshifts. Both the K- correction and the evolutionary correction are determined through stellar population models.

[1] $f = (\frac{D}{d})^2 F$ where f is the flux that would be observed if the object were at distance d and F is the flux of the object if it is at distance D (=10 pc for absolute magnitudes).

SDSS magnitudes

Within the SDSS survey a different definition of magnitude was chosen in order to accommodate fainter objects with low S/N ratios and possible negative fluxes after pipeline processing (Lupton et al., 1999). In this definition the logarithm is replaced by an inverse hyperbolic sine such that

$$m = \frac{-2.5}{\ln(10)} \times (\mathrm{asinh}(\frac{\mathrm{f}}{\mathrm{f_0}}/2\mathrm{b}) + \ln(\mathrm{b})) \tag{3.6}$$

where b is a softening parameter which reflects the typical one sigma noise of the sky in an PSF aperture at 1" seeing and f_0 is the flux of an object with the classical magnitude of zero. b ($\sim 10^{-10}$) is dimensionless and measured relative to f_0. Above a flux of $10 \times f_0$ (~ 22 mag) the classical and 'asinh magnitude' differ by less than 1% [2].

In order to measure the total flux (and magnitude) of galaxies in a specific filter band as accurately as possible the surface brightness profile has to be modelled. In the SDSS survey two profiles are employed for this. Firstly, the intensity I as a function of radius r for an exponential profile is defined as

$$I(r) = I_e \times \exp(-1.68(\frac{r}{r_e})) \tag{3.7}$$

and secondly, for a De Vaucouleurs (de Vaucouleurs, 1948) profile as

$$I(r) = I_e \times \exp(-7.67(\frac{r}{r_e})^{\frac{1}{4}}) \tag{3.8}$$

where r_e is the effective radius and I_e the surface brightness at r_e. The flux for the so-called *model magnitudes* is then determined via the best fit of the two surface brightness profile fits to the 2-dimensional image for each object in the r filter band. The flux in every other band is obtained by using the best fit model from the r-band fit and only allowing the amplitude to vary. Thus the flux in each band is measured through apertures of similar size which enables an unbiased estimate of colours. The flux for the so-called *cmodel magnitudes* is determined from the linear combination of the two profile fits in each band. In the following we will use *model magnitudes* for colour-measurements and *cmodel magnitudes* for absolute brightness measurements when dealing with BOSS or SDSS data[3].

[2] See $http://www.sdss.org/dr7/algorithms/fluxcal.html\#asinh\_table$ for values of b and magnitude limits.

[3] More details about the different magnitude definitions within SDSS can be found at $http://www.sdss.org/dr7/algorithms/photometry.html$.

3.3 SED-fitting with *HyperZ* and *HyperZspec*

Recent reviews by Walcher et al. (2011) and Maraston (2011a) give overviews of different methods for the derivation of stellar population properties of galaxies and their pros and cons. In this section, we describe the SED-fitting method based on template fitting which is employed throughout this thesis to determine the stellar population properties of galaxies. The SED-fitting in this thesis is carried out using the *HyperZ* and *HyperZspec* codes of Bolzonella et al. (2000). We start by introducing the general method and the workflow within *HyperZ* and *HyperZspec*, and then describe the variety of fitting parameters.

3.3.1 χ^2 minimisation

SED-fitting is based on the comparison between theoretical (or empirical) template spectra and observed broad-band magnitudes. We use *HyperZ* (Bolzonella et al., 2000) and a modified version of the code in which redshift can be fixed at its spectroscopic value for each object, called *HyperZspec* (M. Bolzonella, private communication). The fitting method is based on a χ^2 minimisation. χ^2 is defined as

$$\chi^2 = \sum_{i=1}^{N_{filters}} \left[\frac{F_{obs,i} - b \times F_{temp,i}}{\sigma_i}\right]^2 \tag{3.9}$$

in which $F_{obs,i}$ and $F_{temp,i}$ are the observed and template fluxes in filter i, σ_i is the photometric uncertainty and b is a normalisation factor. The reduced χ^2_ν is defined as

$$\chi^2_\nu = \frac{\chi^2}{\nu} \tag{3.10}$$

with ν as the number of degrees of freedom. The χ^2_ν is computed for each combination of fitting parameters (see Section 3.3.4) and for templates covering a broad range of star formation modes, ages and metallicities. The combination of parameters that provides the minimum χ^2_ν is the best-fit solution.

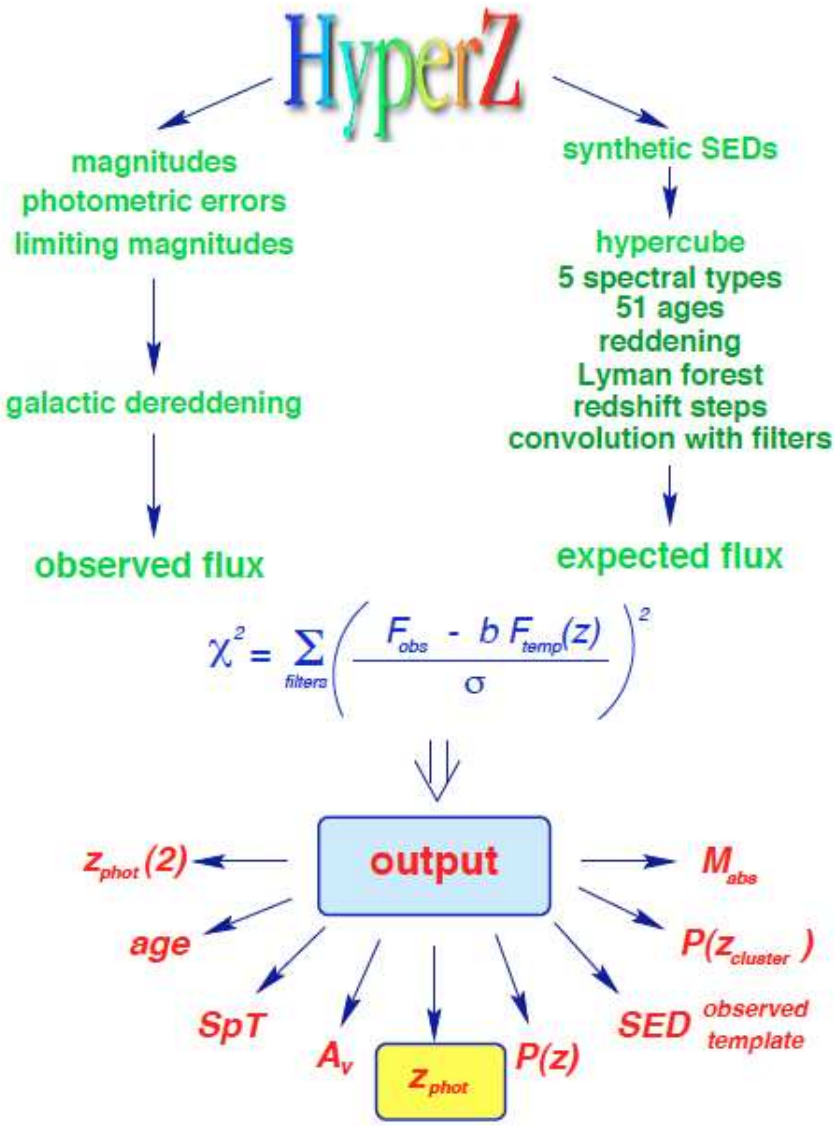

Figure 3.1: Illustration of the workflow within the *HyperZ*-code (Bolzonella et al., 2000). *Source: Fig. 6 from HyperZ-manual. (http://webast.ast.obs-mip.fr/hyperz/manual.html)*

3.3.2 Fitting procedure

In order to derive the χ^2_ν several steps have to be taken first. On the one hand, observed spectral energy distributions provided by the user in the form of broad-band filter magnitudes are treated in the following way:

- Observed apparent magnitudes, errors on magnitudes, limiting magnitudes (of the survey) and filter curves are read in.
- Observed apparent magnitudes get corrected for galactic reddening $E(B-V)$ (if required) following the reddening law of Allen (1976) for the Milky Way.

- These are then translated into fluxes (F_{obs}).

On the other hand, fluxes (F_{temp}) in the required filter bands for the synthetic SEDs (described in Section 3.4) as provided by the user (we discuss the template SEDs used in this thesis in Section 3.4) are yield by the following steps:

- Template SEDs are read in.
- Internal dust reddening is applied to each template SED following one of six reddening laws (see next section) covering the required, user-defined range in reddening in the user-defined step size.
- Lyman-α forest absorption is added to each template SED following the prescription by Madau (1995).
- Then each SED is redshifted to every redshift within the user-defined range according to the user-defined redshift step. In *HyperZspec* each SED is only redshifted to the spectroscopic redshift for each object.
- Then the obtained SED is convolved with each filter band provided for the observations.

Then the χ^2_ν is computed as defined in Eqs. 3.9 and 3.10. The best fit solution yields the galaxy age, star formation law, metallicity and dust reddening. When *HyperZ* is used instead of *HyperZspec* then the photometric redshift, confidence levels for the redshift and the photometric redshift of the secondary solution are given as well. The workflow is illustrated in Fig. 3.1. An example for such a fit is shown in Fig. 1.9 in which two best fits to the same multi-wavelength data points using different fitting setups are presented. Furthermore, Fig. 1.9 illustrates the degeneracies, such as the age-dust degeneracy, one has to overcome in order to obtain robust results.

3.3.3 Filter curves

Although the *HyperZ*-package includes a variety of filter curves we chose to use our own response curves as input throughout this thesis to ensure consistency with the simulations and the SDSS data. Some of them are illustrated in Fig. 3.2. The upper panel of filter response curves refers to the filters used for the simulated galaxies ranging from the rest-frame optical to the far-IR. The bottom panel shows the SDSS filter curves for $ugriz$.

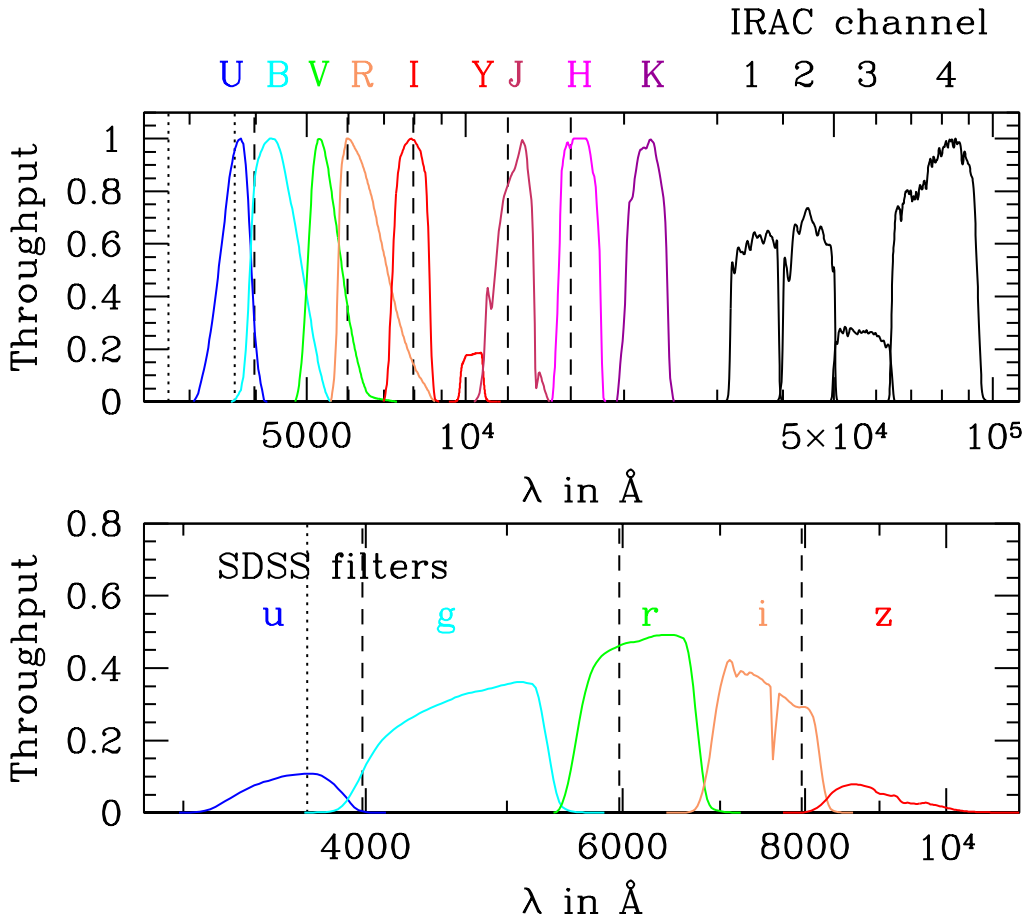

Figure 3.2: Filter curves used for data and fitting in this thesis. The filter curves for UBVRIJHK and IRAC channel 4 are normalised to a throughput of 1 at the peak throughput. All other filter curves are not normalised. Dashed black lines show the position of the 4000 Å break at $z = 0, 0.5, 1, 2$ and 3, from left to right, respectively. Dotted black lines show the position of the Lyman-break (912 Å rest-frame) at redshift 2 and 3 from left to right, respectively.

3.3.4 Fitting parameters

In this section we address the number of free parameters within the two fitting codes available to the user. We start with the free parameter unique to *HyperZ*, photometric redshift, and then cover the parameters which can be changed in both codes. Examples for parameter files as used in Chapter 4 and 5 are given in Appendix A.

As redshift is a free parameter in *HyperZ*, not only the range of redshift can be defined but also the stepsize. The given stepsize will internally be refined by a factor of 10 around the minimum χ^2_ν. In this thesis redshifts between 0 and 6 in steps of 0.05 are considered

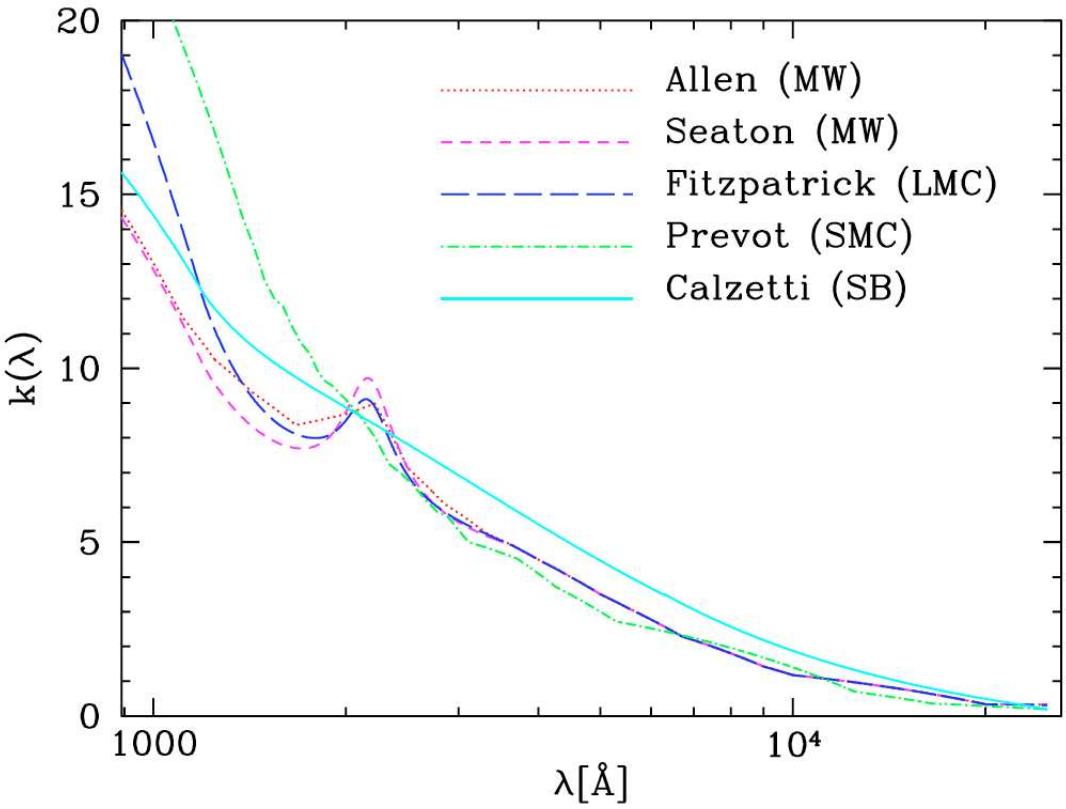

Figure 3.3: Reddening laws used in *HyperZ* and *HyperZspec*. Each reddening law is normalised to $k(B) - k(V) = 1$. *Source: Fig. 4 from HyperZ manual.*

when fits are carried out with *HyperZ*.

HyperZ and *HyperZspec* provide various empirically-derived laws to treat galaxy internal reddening. These are

- Milky Way (MW) by Allen (1976)
- MW by Seaton (1979)
- Large Magellanic Cloud by Fitzpatrick (1986)
- Small Magellanic Cloud by Prevot et al. (1984)
- Calzetti's law for local starburst galaxies (Calzetti et al., 2000)
- no reddening.

The different laws (apart from the no reddening option) are shown in Fig. 3.3. The user is able to choose not only the type of reddening law but also the range and stepsize for the

reddening in form of the visual attenuation A_V. A_V is then translated into a dust-screen model via

$$f_{obs} = f_{intrinsic}(\lambda) \times 10^{-0.4 \times A_\lambda} \tag{3.11}$$

with f_{obs} as the observed flux, $f_{intrinsic}$ as the intrinsic flux of the object without dust attenuation and

$$A_\lambda = k(\lambda) \times E(B-V) \tag{3.12}$$

$$E(B-V) = A_V / R_V \tag{3.13}$$

where $E(B-V)$ is the colour excess and R_V takes values of 2.72 (for the SMC law), 3.1 (for MW laws and LMC law) and 4.05 (for the Calzetti law). When dust reddening is included in the fit, we let A_V vary from 0 to 3 mag in steps of 0.2 mag. We carry out fits for all reddening laws and then choose the best fit among them. The remaining free parameters are all encoded within the user-specific template set. These are age, star formation mode, metallicity, initial mass function (IMF) and stellar population model. We will discuss these in the next section.

3.4 Model templates

Since the properties of galaxies are determined by using the observed light emitted by the stars within each galaxy, one can compare the data to either empirical spectra of galaxies or to model spectra. By default two sets of templates are included in the *HyperZ* code package. One set comprises the empirical templates of Coleman, Wu & Weedman (1980) which are based on local galaxies of early and late-type galaxies. The drawback when working with local galaxy spectra as templates is that although they might represent the local galaxy population very well, they could be a complete mismatch to the galaxy population at higher redshift because of their restricted parameter range. Furthermore, galaxies at higher redshift will be younger. The other template set is based on the synthetic stellar population models of Bruzual A. & Charlot (1993). The advantage of model spectra is that they can be created within a large range of parameters.

In recent years, a variety of different stellar population models are used in the literature (Bruzual A. & Charlot, 1993; Maraston, 1998; Bruzual & Charlot, 2003; Maraston, 2005, Charlot & Bruzual, 2007, in prep.). Most commonly used are the models of Bruzual & Charlot (2003, hereafter BC03) and Maraston (2005, hereafter M05). The basis for these model spectra are simple stellar populations (SSPs), consisting of chemically homogeneous and coeval stars of different stellar masses distributed according to an initial mass

function (IMF). The templates used in this thesis are based on the simple stellar population models of M05 which we describe in more detail in the next section.

3.4.1 Simple stellar populations by Maraston 2005

The light emitted by a SSP at different ages can be computed using two approaches - the *Isochrone Synthesis* (Charlot & Bruzual, 1991; Bruzual A. & Charlot, 1993; Bruzual & Charlot, 2003) and the *Fuel Consumption Theorem* (Renzini & Buzzoni, 1986; Maraston, 1998, 2005). SSPs of M05 make use of the latter. The Isochrone Synthesis is based on the integration of the flux contributions along a single isochrone for all masses under the assumption of an IMF. The integration covers all mass bins from a lower limit to an upper limit in mass given by the isochrone itself. This usually covers the stellar evolutionary phases up to the early asymptotic giant branch (E-AGB) whereas later stellar evolutionary phases are added using other recipes (e.g. Charlot & Bruzual, 1991). Including the contribution of all stellar evolutionary phases is difficult because of persisting uncertainties in stellar evolution, e.g. mass loss during some of the phases. Therefore M05 models only make use of the Isochrone Synthesis for the luminosity contribution of main sequence (MS) stars using the stellar evolutionary tracks of Cassisi et al. (1997), Cassisi et al. (1997) and Cassisi et al. (2000, hereafter Cassisi tracks), those of Schaller et al. (1992), Meynet et al. (1994, hereafter Geneva tracks) for very young SSPs and those of Girardi et al. (2000, hereafter Padova tracks) for the highest metallicity.

For post-main sequence (PMS) stars the Fuel Consumption Theorem is used. Here, the luminosity contribution of each stellar evolutionary phase is calculated by the amount of hydrogen and/or helium, the so-called fuel, burned by nuclear fusion within the stars. The fuel of each phase is directly proportional to the contribution of the stellar evolutionary phase to the total luminosity. Furthermore, the Fuel Consumption Theorem provides analytical relations between the main sequence and post-main sequence stellar evolution. Thus, including later and short-lived stages of stellar evolution, such as the thermally-pulsing asymptotic giant branch (TP-AGB) phase, is easier than with the Isochrone Synthesis. Bolometric luminosities are then converted into spectral energy distributions using transformations between colours/spectra and bolometric corrections (Maraston, 1998, M05).

The contributions of various stellar evolutionary phases to the total luminosity is shown in Fig. 3.4 for various filter bands and stellar population ages. In optical filter bands (UBV-bands) the main sequence is the largest contributor at all ages. Stars in the TP-AGB phase dominate the luminosity in the near-IR (K-band) for ages around 1 Gyr where this phase

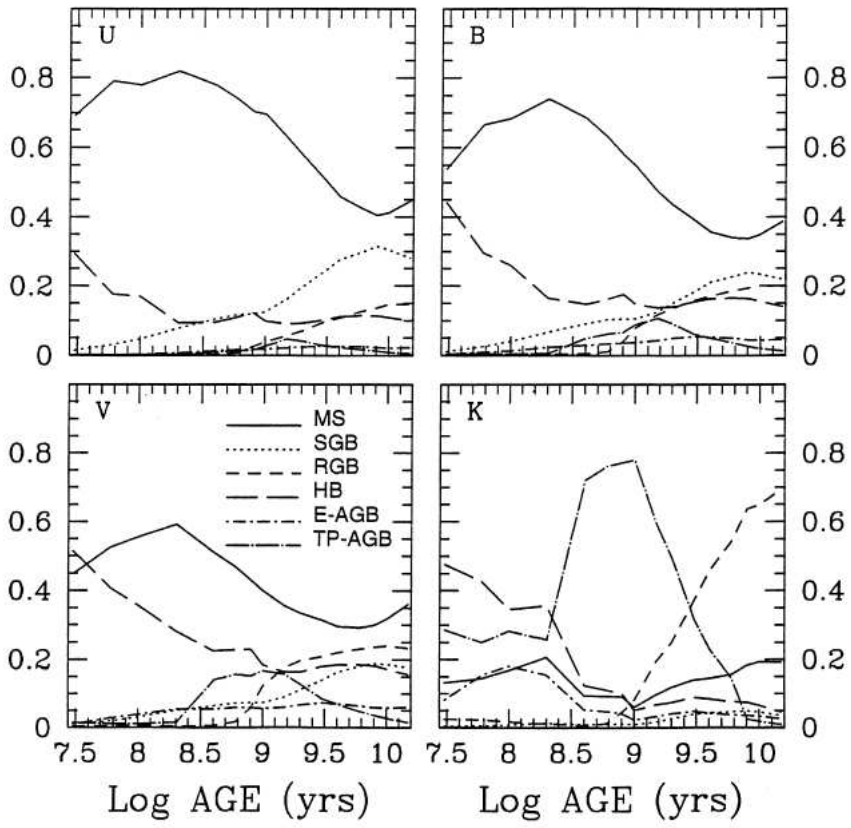

Figure 3.4: Contributions of various stellar evolutionary phases to the luminosity as L_{phase}/L_{total} (y-axis) in various filter bands (U to K from top right to bottom left) as a function of stellar population age. The stellar phases are distinguished by line type. *Source: Fig. 11 from Maraston (1998).*

contributes up to 80% (and up to 40% to the total bolometric luminosity). Thus accurate modelling and calibration of this phase is crucial. M05 calibrate their models using globular cluster data because globular clusters closest resemble simple stellar populations.

Naturally, galaxies contain more than one simple stellar population due to e.g. longer lasting and on-going star formation or starbursts triggered by galaxy interactions. Thus, depending on the star formation history of a galaxy, stellar populations of various ages and stars in all stages of stellar evolution can be present at any redshift. Hence, the inclusion of the most luminous stellar phases although their duration might be short, such as the TP-AGB phase, in the models is crucial for the fitting of galaxies in order to obtain robust results.

M05 explore also the effect of various metallicities in the models. Metallicity (Z) describes the proportion of an object's elements which are heavier than hydrogen and helium, e.g. the metallicity of the sun is $Z_{\odot} = 0.02$ because the sun is made up mostly

of hydrogen and helium. Heavier elements are then referred to as *metals*. In summary, M05 find that SSP luminosities decrease with increasing metallicity because the amount of fuel is smaller and the opacity higher. This also means that the M^*/L-ratio (mass-to-light ratio) decreases with decreasing metallicity.

The effect of different initial mass functions (IMF) on the stellar population models manifests itself in the varying number of high and low-mass (short and long-lived) stars contributing to a SSP because the IMF defines the mass distribution of stars in a newly formed SSP. The simplest parametrisation of the IMF is in form of a power law with exponent x such that the number of stars decreases with increasing mass. The most commonly used IMF is a Salpeter (1955) IMF with slope $x = 1.35$. More recent efforts and measurements of the IMF in the Milky Way suggest a turnover at lower masses (around 1 $M_\odot$) which can be modelled with a broken power law (Kroupa, 2001; Chabrier, 2003). M98 showed that integrated colours remain nearly independent of the IMF slope in the optical. In the near-IR and for old ages, dwarf-dominated IMFs (steeper slope than Salpeter, $x = 2.5$) show redder colours than a Salpeter IMF because of the larger number of long-living low-mass stars. M^*/L-ratios are affected by the choice of IMF such that the M^*/L-ratio is lowest for a Salpeter IMF. Dwarf-dominated and top-heavy IMFs (flatter slope than Salpeter) have larger M^*/L-ratios because of larger numbers of low-mass stars and heavy remnants, respectively. An IMF described by a broken power law such that the number of low-mass stars is decreased in comparison to a Salpeter IMF has a smaller M^*/L-ratio at older ages. Since the IMF is a free choice in population synthesis models, we adopt the most commonly used IMFs in the literature (Salpeter, Kroupa and Chabrier) in combination with the M05 SSPs throughout this thesis and show their effect on the derived galaxy properties (Chapters 4, 5 and 6).

However, many parts of stellar evolution that affect the broad-band colours of the SED and that are therefore important for studies of galaxies with the help of stellar population models are not yet fully understood and still discussed in the literature. The most important ones are stellar mass loss, convective overshooting and the mixing length. Mass loss in PMS phases is poorly understood because mass loss has not yet been related to basic stellar parameters. Hence, stellar tracks cannot predict mass loss and one has to use parametrisations and rely on calibrations with data. M05 adopt an empirical prescription for the mass loss during the RGB phase and an efficiency parameter depending on age and metallicity. They found good agreement with MW globular cluster data (Maraston & Thomas, 2000; Maraston et al., 2003).
The stellar tracks adopted in M05 do not contain convective overshooting. This is motivated by results from Ferraro et al. (2004) for Large Magellanic Cloud globular clusters.

The main effect of convective overshooting is a slowed down evolution. For example, the onset of the RGB is delayed by 0.3 Gyr in comparison to the classical tracks without overshooting (compare also Fig. 7 in M05) which results in a SSP that is 40% more luminous around 1 Gyr.
Finally, the mixing length parameter, which describes the efficiency of the convective energy transfer in stars and thus affects stellar effective temperatures, needs calibration with observations because its connection with other stellar parameters is unknown. The Cassisi tracks which are used in the M05 models adopt a mixing length such that the mixing length decreases with metallicity (Salaris & Cassisi, 1996). In the Padova tracks the mixing length parameter for solar metallicity is assumed for all metallicities resulting in a cooler RGB at higher metallicities and a warmer RGB at lower metallicities compared to the Cassisi tracks (see Fig. 9 in M05).
Overall M05 find that the differences between stellar population models in the literature are larger than those between different stellar tracks in their code.

In the following section we will discuss the differences between various stellar population models.

3.4.2 Differences between M05 and BC03

In the last decade most comparisons between observed galaxy data and model spectra were carried out using models that were based on the SSPs of Bruzual A. & Charlot (1993) and more recently those of Bruzual & Charlot (2003, hereafter BC03). In this section we point out differences between these stellar population models and the models of M05 which we described in the previous section and which we use throughout this thesis.

The main differences between the BC03 and M05 models are:

- the approach to compute the light emitted by a SSP - Isochrone Synthesis for BC03 models, Fuel Consumption Theorem for M05 models
- contribution of the TP-AGB phase - not included in BC03 models, included in M05 models
- the stellar evolutionary tracks - Padova tracks including overshooting for BC03 models, Cassisi tracks without overshooting for M05 models.

We already discussed the effects of the different stellar tracks as analysed by M05 in the previous section. In summary, stellar evolution is delayed when Padova tracks are used

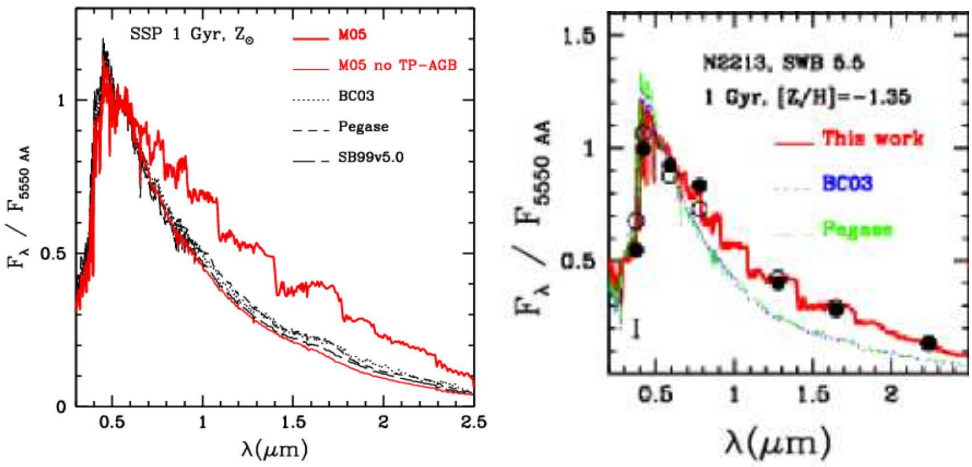

Figure 3.5: *Left:* SEDs of 1 Gyr old, solar metallicity SSPs from different stellar population models. Shown are as red thick solid line the M05 model including the TP-AGB treatment, as red thin solid line the M05 model without the TP-AGB, as black dotted line the BC03 model, as dashed line the Pegase (Fioc & Rocca-Volmerange, 1997) model and as long-dashed, short-dashed line the Starburst99 model (Vázquez & Leitherer, 2005). *Source: Fig. 18 from Maraston (2005). Right:* SED-fit to Magellanic Cloud globular cluster data (black dots) with various stellar population models: M05 in red, BC03 in blue, Pegase in green. Open circles reflect predicted broad-band magnitudes from the M05 model. *Source: Adapted Fig. 19 from Maraston (2005).*

such that stars remain on the MS for longer and the onset of the RGB phase occurs later. Furthermore the different mixing lengths assumed in the stellar tracks of Padova result in a warmer/cooler RGB at lower/higher metallicity for the BC03 models. This is the dominating effect for old stellar populations.

Most importantly, however, is the inclusion of the TP-AGB phase which, as elucidated in the previous section, has a significant impact on the luminosity at near-IR wavelengths although only for a limited age range between $\sim$ 0.2 and 2 Gyr. Fig. 3.5 shows the SED of a 1 Gyr, solar metallicity SSP of different stellar population models. The difference between models including the TP-AGB phase (M05, red thick solid line) and those without proper treatment of the TP-AGB phase (BC03, Fioc & Rocca-Volmerange 1997, Vázquez & Leitherer 2005[4], dotted and dashed lines, respectively, and M05 without TP-AGB as red thin solid line) is striking. Particularly, models with the TP-AGB treatment are much brighter in the rest-frame near-IR ($\lambda \geq 1\mu$m). M05 fitted their SSPs to globular clusters in the Magellanic Clouds and found good agreement. An example is shown on the right-hand side of Fig. 3.5.

The difference between the stellar population models also manifests itself in the M^*/L-ratio, especially in the rest-frame near-IR (K-band in Fig. 3.6). Here the M^*/L is larger

[4]All of these three models use Padova tracks.

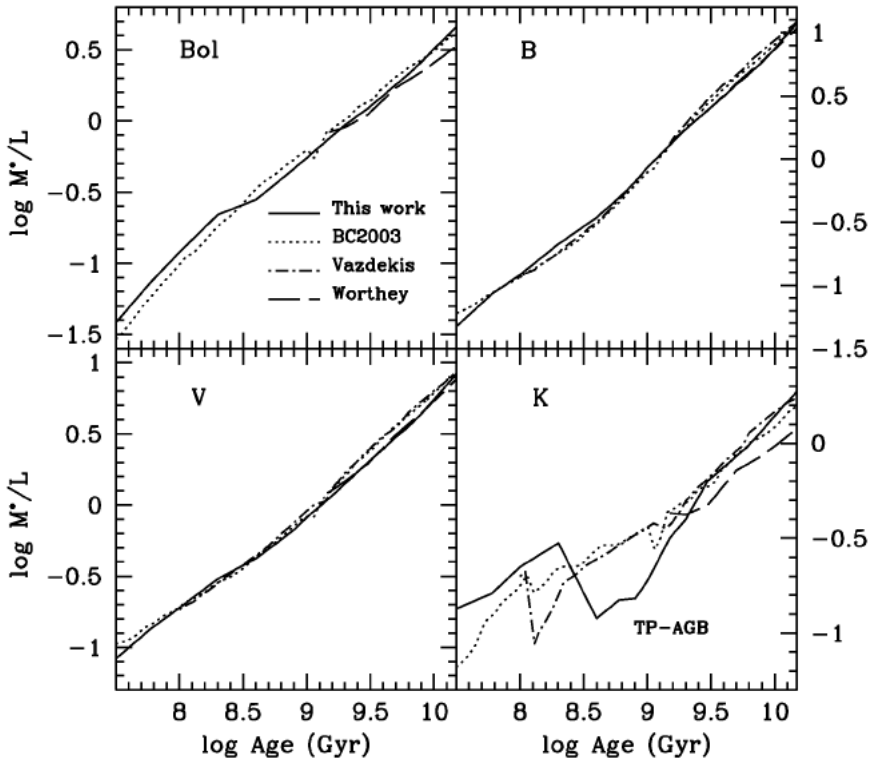

Figure 3.6: Mass-to-light (M^*/L)-ratios for a solar metallicity, Salpeter IMF SSP in various filter bands (bolometric luminosity and luminosity in BVK-bands, top right to bottom left, respectively) as a function of stellar population age and stellar population model (distinguished by line type). *Source: Fig. 24 from Maraston (2005).*

for BC03 models for ages in which the TP-AGB dominates because this phase is lacking in the models. At older ages the M^*/L is smaller because of the cooler RGB. The bolometric M^*/L-ratios of BC03 models are generally higher than those of the M05 models for intermediate and old ages due to the later onset of the RGB in the Padova tracks.

Since globular clusters are the closest counterparts of SSPs they are useful to test SSP models. Galaxies, however, as described above, may require more complex star formation histories which we will focus on in the next section.

3.4.3 Composite stellar populations

On the basis of a simple stellar population (or a set thereof), models with more complex star formation histories than a single burst can be created. Such models are referred to as composite stellar population (CSP) models. Basically any star formation history (SFH) can be created by adding up SSPs of different ages. The most commonly used SFHs besides the single burst scenario are exponentially declining star formation rates

motivated by the use with local elliptical galaxies. Exponentially declining SFRs are parametrised as

$$\mathrm{SFR} = A \times \exp^{-(t-t_0)/\tau} \tag{3.14}$$

where SFR starts at a cosmic time t_0 and $A = \mathrm{SFR}(t = t_0)$. For a galaxy at cosmic time t the age derived from the best fit is then defined as $t - t_0$, i.e. the time elapsed since the beginning of star formation. Constant SFRs can be expressed using very large values of τ (> 20 Gyr). Maraston et al. (2006, hereafter M06) also used models with truncated SFRs, meaning constant star formation for a certain time period which is then shut off.

It has recently been suggested that the SFHs of high redshift galaxies might show an increase in SFR rather than a steady decline (Cimatti et al., 2008; Renzini, 2009; González et al., 2010; Maraston et al., 2010). For this purpose M10 (Chapter 6, Section 6.1) introduced composite stellar populations with exponentially increasing SFR expressed equivalent to Eq. 3.14 as

$$\mathrm{SFR} = A \times \exp^{+(t-t_0)/\tau}\,. \tag{3.15}$$

We further motivate and use these templates in Chapter 4 and Chapter 6, Section 6.1.

Several codes are available to us for the production of composite stellar population (CSP) models. Firstly, the private code of M05 with which several CSP models, in particular τ and inverted-τ models, were created. These are publicly available in the form of simple ASCII files at *http://www.icg.port.ac.uk/∼maraston/*. We transformed these into the format required by *HyperZ* using codes developed by M05.[5] Secondly, the routine *csp_galaxev* in the *galaxev*-code package by BC03 is the most popular choice in the literature because, once installed, the routine is ready-to use with any input SSPs (as long as they are provided in the same format as the BC03 SSPs) to create CSPs. In each case, the convolution integral of the SSP with the SFH is calculated requiring the interpolation of the SEDs at each age. This can, when not carried out carefully, be a significant source for error. Most CSP templates used in this thesis (apart from those used in Chapter 6) have been processed via the *csp_galaxev* routine for consistency with the literature. Due to the availability of both codes, of M05 and BC03, for creating CSPs we are in the unique position to investigate the more technical aspect of the importance and impact of the SFH-code on the derivation of the galaxy physical properties. Results are summarised in Appendix E.

[5]These models are available upon request.

3.4.4 Models for luminous red galaxies

So far the stellar population models described were based on spectra of theoretical stellar libraries and stellar atmospheres (Lejeune et al., 1997). More recent efforts have been undertaken to introduce empirical stellar libraries into the models (Maraston et al. 2009, Maraston et al. 2009, hereafter M09, and Maraston & Strömbäck 2011, *in press*). For this exercise a number of empirical libraries are available (Pickles, 1998; Le Borgne et al., 2003; Sánchez-Blázquez et al., 2006; Prugniel et al., 2007) which differ in wavelength coverage, resolution and metallicity coverage.

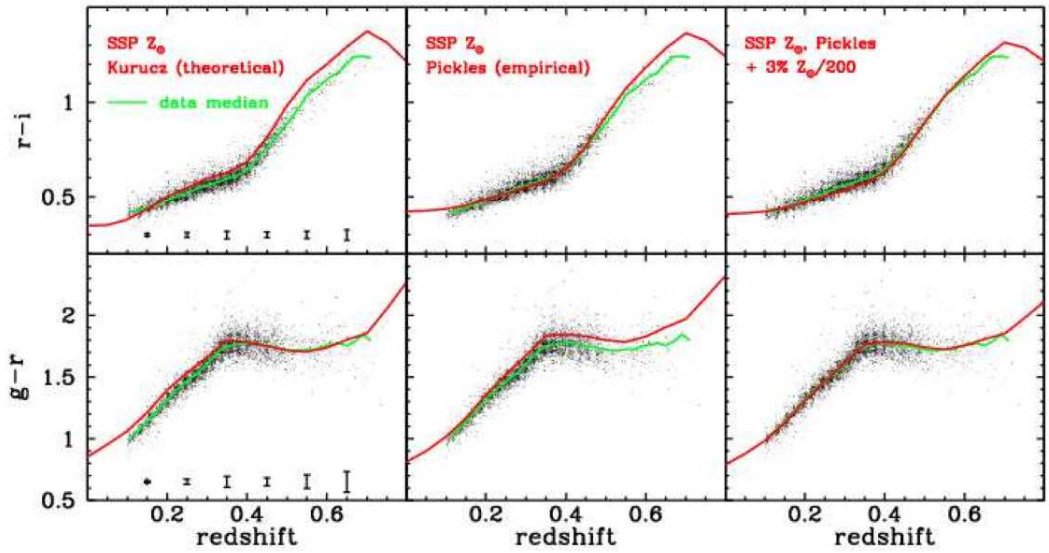

Figure 3.7: $(r-i)$ and $(g-r)$ colours of SDSS-II LRGS as function of redshift and stellar population model. Black dots reflect a subsample of the SDSS-II LRGs as selected by M09, green lines refer to the data median. Red lines show the predicted colour evolution of the stellar population model which is $\sim$ 12 Gyr old at $z = 0$. *Left:* Standard solar metallicity M05 SSP. *Middle:* Same as left but for Pickles (1998) library. *Right:* Same as middle but with added metal-poor component. *Source: Fig. 1 from Maraston et al. (2009).*

In the framework of this thesis we make use of the stellar population model of M09 which is tuned for the use with LRGs such as the BOSS data sample (Chapter 2). M09 found that using the Pickles (1998) stellar library, chosen for its wide wavelength coverage, for a solar metallicity SSP with added small percentage (3% in mass) of old, metal-poor stars solves the long-standing problem of matching the colours of LRGs over a wide redshift range (Eisenstein et al., 2001; Wake et al., 2006; Cool et al., 2008). In particular, the use of empirical spectra improves the match of $(r-i)$ and $(g-r)$ at low redshift (Fig. 3.7) because of a higher flux in the empirical spectra around 6000 Å. The inclusion of the metal-poor component then rectifies the mismatch at higher redshift where colours need

to be bluer. M09 found the combination of empirical library and metal-poor component to match the colours best. Other possibilities such as a small percentage of young stars could be excluded.

We make use of this model for the BOSS data set in Chapter 6, Section 6.2. We follow the assumption of M09 that these galaxies are old and started forming stars around redshift 5 as suggested by studies of local galaxies (Kauffmann et al., 2003; Nelan et al., 2005; Thomas et al., 2005; Bernardi et al., 2006; Jimenez et al., 2007).

3.4.5 Structure of the template spectra

As indicated previously, *HyperZ*[6] (and *HyperZspec*) require input template spectra in a specific format which is inherent in the format of the BC03 SSPs. Most importantly for our purpose is that the template spectra contain the SED (of SSPs or CSPs) at 221 ages from 0 to 20 Gyr, equally spaced in logarithmic space. The age is defined as the time passed since the onset of star formation, which is therefore the age of the oldest stellar population present in the template. However, in the fit we only consider ages that are younger than the age of the Universe at the given redshift and for the given cosmology. At each age step the SED is given in 1221 flux points ranging from 90 Å to 160μm.

3.4.6 Template setups

Throughout this thesis we employ a number of fitting setups which are inspired by M06 and M10 and contain various combinations of the above introduced SSPs and CSPs. We will describe the template setups used for the data sets analysed in this thesis (Chapter 2) in more detail at the beginning of each corresponding chapter.

3.5 Derivation of stellar masses and star formation rates from the best fit

The best fit provides us with some stellar population parameters directly. These are the redshift (in the case of *HyperZ*), the age since onset of star formation, the star formation mode, the amount of dust reddening and the dust law, metallicity and of course the quality of the fit. However, the two properties one is most interested in are stellar mass

[6]More recent versions of *HyperZ* provided by R. Pelló at $http : //www.ast.obs - mip.fr/users/roser/hyperz/$ are adapted to the ASCII format of the original M05 templates. However, these versions are not used here as the version of *HyperZ* and *HyperZspec* provided to us privately by M. Bolzonella contain special features optimised for our work.

and star formation rate. These can be obtained indirectly from the best fit by using the normalisation (expressed as scale factor A in Eqs. 3.14 and 3.15 and as b in *HyperZ* and *HyperZspec*) between template and observed SED. For a template that is normalised to one $M_{\odot}$ we can calculate the stellar mass (in units of $M_{\odot}$) following Daddi et al. (2005) and M06 as

$$M^* = 4\pi \times (D_{lum} \times 3.086 \times 10^{24})^2 \times b/L_{\odot} \tag{3.16}$$

with the luminosity of the sun $L_{\odot} = 3.426 \times 10^{33}$ erg/s and the luminosity distance (expressed in cm using the conversion factor 3.086×10^{24}) defined as

$$D_{lum} = D_A \times (1+z)^2 \tag{3.17}$$

in which D_A is the angular diameter distance, i.e. the ratio between the object's actual size and its angular size as viewed from Earth. The stellar mass in Eq. 3.16 is in essence derived by multiplying the M^*/L-ratio of the sun with the luminosity of the observed galaxy (as derived from the SED-fit) where the distance of the object from the observer is accounted for by $4\pi \times (D_{lum}^2)$ and the difference between the flux of the object and the solar flux is expressed in b, the normalisation derived from the fit. The SFR then follows according to the star formation mode, i.e for exponentially declining models from Eq. 3.14, where t is the cosmic time corresponding to the observed redshift of each galaxy.

However, when the code of BC03 is used in order to obtain composite stellar populations, then the different normalisation of the templates (e.g. stellar mass tends to unity as time tends to infinity) has to be taken care of in the calculation of the stellar masses.

3.5.1 Mass loss

The calculation of stellar mass as presented in Eq. 3.16 yields the *total* stellar mass in which mass loss due to stellar evolution, i.e. stars die and leave remnants of lower mass, is not accounted for. Thus stellar masses calculated this way are in principle overestimated. However, this mass loss can be accounted for by multiplying the obtained mass with a correction factor for the according age and metallicity (and IMF) of the best fit stellar population model. Both M05 and BC03 provide tables with the correction factors [7]. The *corrected* stellar mass then reflects the mass in stars still alive plus the mass in remnants. For the mock galaxies we do not correct the stellar mass in this way, as the stellar mass given by the galaxy formation model does not include mass loss. The stellar masses of the GOODS-S galaxies are not corrected for stellar mass loss (see Section 6.1), for those of BOSS and SDSS galaxies we account for mass loss.

[7] For BC03 models these are provided by the *csp_galaxev* routine in form of the *.4color files.

Chapter 4

Recovering stellar population properties of mock galaxies at fixed redshift

In this chapter we explore the dependence of galaxy stellar population properties that are derived from broad-band spectral energy distribution fitting - such as age, stellar mass, dust reddening, etc. - on a variety of parameters, such as star formation histories, age grid, metallicity, initial mass function (IMF), dust reddening and reddening law, filter setup and wavelength coverage. The mock galaxies described in Chapter 2 are used as test particles. Here, we show that - for star-forming galaxies - galaxy ages, masses and reddening, can be well determined *simultaneously* only when one uses the right setup and wavelength coverage, in other words when one can identify the correct star formation history. This is the case for *inverted-*τ models at high-z, for which we find that the mass recovery (at fixed IMF) is as good as ~ 0.04 dex. However, since the right star formation history is normally unknown, we quantify the offsets generated by adopting standard fitting setups. Stellar masses are generally underestimated, which directly results from underestimating the age. For mixed setups with a variety of star formation histories the median mass recovery at $z \sim 2-3$ is as decent as ~ 0.1 dex (at fixed IMF), albeit with large scatter. The situation worsens towards lower redshifts, because of the variety of possible star formation histories and ages. At $z \sim 0.5$ the stellar mass can be underestimated by as much as ~ 0.6 dex (at fixed IMF). A practical trick to improve upon this figure is to exclude reddening from the fitting parameters, as this helps to avoid unrealistically young and dusty solutions. Stellar masses still tend to be underestimated, but by a smaller amount (~ 0.3 dex at $z \sim 0.5$). Reddening and the star formation rate should then be determined via a separate fitting. Not surprisingly, the recovery of properties is substantially better for passive galaxies, for which e.g. the mass can be

underestimated by only ~ 0.01 dex (at fixed IMF) using a setup including metallicity effects. In all cases, the recovery of physical parameters is crucially dependent on the wavelength coverage adopted in the fitting such that a coverage from the rest-frame UV to the rest-frame near-IR appears to be optimal. We also quantify the effect of narrowing the wavelength coverage or adding and removing filter bands, which can be useful for planning observational surveys. Finally, we provide simple scaling relations that allow the transformation of stellar masses obtained using different template and fitting setups and stellar population models.

The chapter is organised as follows. The different fitting setups are described in Section 4.2. Results and discussion are presented in Sections 4.3 and 4.4. The comparison of our results with the literature is carried out in Section 4.8. In Section 4.9 we provide the scaling relations. We summarise our work in Section 4.10.

Throughout this chapter we use a standard cosmology of $H_0 = 71.9$ km/s/Mpc, $\Omega_\Lambda = 0.742$ and $\Omega_M = 0.258$ as used in GalICS (see Hatton et al., 2003) and magnitudes in the Vega system.

The work in this chapter was carried out in collaboration with C. Maraston and C. Tonini. The contents of this chapter are published in Pforr, Maraston & Tonini (2012, submitted to MNRAS). Since the publication was still in the referee process at the time of submission of this thesis the contents of Pforr, Maraston & Tonini (2012, submitted to MNRAS) might be slightly different from the contents of this chapter.

4.1 Background

The interesting question is to assess how well galaxy properties can effectively be recovered with SED-fitting, and many papers have been devoted to this scope over recent years. The first papers that addressed the dependency of the derived galaxy properties at high redshift on the input stellar population models are Maraston (2005, hereafter M05), van der Wel et al. (2006) and Maraston et al. (2006, hereafter M06). These works consistently found that stellar ages and masses, of observed objects are - not surprisingly - a function of the stellar evolution pattern adopted in the models used to derive them (for a review see Maraston, 2011b). This information is useful, but does not yet inform us on which fitting method provides the correct galaxy parameters. On the other hand, using mock galaxies for which the properties are known a priori allows one to understand the effectiveness of the assumptions made in the fitting, even though there is no guarantee

that simulated galaxies have star formation histories similar to the real ones in the Universe. In addition, different parameters can be recovered with different accuracies. For example it is well known that stellar masses are generally better recovered than ages and SFRs (Papovich et al., 2001; Pozzetti et al., 2007; Bolzonella et al., 2010; Lee et al., 2009; Maraston et al., 2010).

In recent years there have been several works in this direction. Longhetti & Saracco (2009), Wuyts et al. (2009) and Lee et al. (2009) address the dependency of the results on fitting parameters using simulated galaxies. Longhetti & Saracco (2009) study the dependence of stellar mass estimates on a variety of models and their parameters like age, metallicity, IMF and star formation history (SFH) for early-type galaxies at $1 < z < 2$. They assume different stellar population synthesis codes for stellar evolution modelling (Bruzual & Charlot, 2003, hereafter BC03; M05; and various others). They simulate early-type galaxies using BC03 stellar population models assuming exponentially declining star formation rates (with timescale τ). Furthermore, they superimposed second star bursts with a smaller value of τ at later epochs. They find that stellar masses can not be recovered better than a factor of 2-3, at fixed known IMF.

Wuyts et al. (2009) use mock galaxies from a hydrodynamical merger simulation based on BC03 models. They simulate all types of galaxies, but focus on a small redshift interval between 1.5 and 3 and also do not explore metallicity effects. They conclude that properties of spheroidal galaxies (which means galaxies with little star-formation) are generally well reproduced, whereas those of star-forming galaxies suffer from large uncertainties.

Lee et al. (2009) focus on mock Lyman break galaxies at $z \sim 3.4$, 4 and 5 based on BC03 stellar population models. They find that masses and SFRs tend to be underestimated and mean ages overestimated. They attribute these effects to the difference in SFH between the mocks and the τ-model template used in the fitting. Furthermore, Lee et al. (2009) show that a large wavelength coverage from optical to rest-frame near-IR is required to best recover the input physical parameters.

In this chapter we follow the same approach as these works. We perform our investigation by using both mock star-forming as well as passive galaxies, for which the physical properties - age, metallicity, reddening, mass and star formation rate - are well defined. We then treat these mocks as observed data and SED-fit them with several different setups. The comparison between input properties and those derived from the fitting allows us to understand and quantify the robustness of the derived properties as a function of the

fitting parameters.

Our work is complementary to these earlier works on several aspects. Firstly, it relies on the M05 stellar population models both as ingredient of the fitting and of the mock galaxies, but also explores the case of using different stellar population models in the mocks and in the fitting. Also, a wider redshift span is considered, down to redshift 0.5, and a larger set of parameters in terms of metallicity and reddening prescriptions. Moreover, a detailed exploration of the effects of wavelength coverage and photometric filters is performed. This latter analysis aims at providing a practical guide for planning observational surveys and proposals. Finally, we provide scaling relations between properties obtained with different fitting setups and population models, which will help unifying results obtained from different data sets and using different modelling.

This work complements a recent paper Maraston et al. (2010, hereafter M10, Chapter 6, Section 6.1) in which we focussed on real $z \sim 2$ star-forming galaxies from the GOODS survey and studied how well - or how bad - star formation histories that are typically adopted for the fitting templates are able to recover the galaxy star formation rates, stellar masses and reddening. One of the main conclusions of this work is that - because of the overshining effect from massive stars even if present in small proportions - essentially no star formation history is able to provide an accurate determination of star formation rates, reddening and masses if the age is left as a free parameter in the fit. This happens because the fit tries to match the light from the most massive stars, which is best accomplished with a low age. As a main conclusion a template was found that was able to recover the galaxy properties very well, which is an exponentially increasing star formation - that we named *inverted-*τ models as opposite to the usually assumed declining star formation or τ-model but with two important priors, namely

- i) that the starting of star formation was at a much earlier epoch with respect to the time of observation ($z \sim 5$)
- ii) that the typical timescale for star formation (τ) could not be too short, namely $\tau > 0.3$ Gyr.

This conclusion is able to provide information on the actual star formation mode of high redshift star-forming galaxies, which triggers a lot of astrophysical consequences.

In this chapter we do not pursue the aim at unveiling the galaxy star formation mode. Rather, we quantify the galaxy property offsets that are obtained with usually adopted templates, expanding upon the investigation of M10 (Section 6.1) by exploring a wider

parameter space in terms of reddening, metallicity, etc..

For real passive galaxies at $z \sim 2$, M06 found that a fitting setup including a wide range in metallicities, star formation histories and reddening laws was optimal as the derived best-fitting star formation histories were able to match the observed strength of the Mg_{2800} line-strength in the galaxy spectra, which was regarded as a test independent of the photometric SED-fitting. In the present work we test the same fitting setup on mock passive galaxies and we reach similar conclusions.

4.2 Spectral Energy Distribution Fitting

We introduced the method of SED-fitting in Chapter 3. What fitting setup and compilation of template spectra is used in the fitting is basically an arbitrary choice. In the following subsections, we describe the variety of template and fitting setups that we use to obtain the stellar population properties of the mock galaxies introduced in Section 2.

4.2.1 Model Template Setups

Wide template setup

We adopt a mixed template setup as in Maraston et al. (2006, hereafter wide setup) as default setup. It consists of 32 types of theoretical spectra which cover a wide range of star formation histories - specifically:

- i) SSP (single starburst)
- ii) exponentially declining SFR (so-called τ-model with $\tau = 0.1, 0.3$ and 1 Gyr)
- iii) truncated SFR (constant star formation for a time t with $t = 0.1, 0.3$ and 1 Gyr, no star formation afterwards)
- iv) constant SFR

and metallicities of $\frac{1}{5}\,Z_{\odot}$, $\frac{1}{2}\,Z_{\odot}$, $Z_{\odot}$ and $2\,Z_{\odot}$. A Salpeter IMF is assumed, consistent with the mock galaxies, but we also use templates for different IMFs in the following.

Despite the increase in CPU time that is required to fit data with the wide setup, it was found by M06 that this approach gives the most accurate results for the sample of passive galaxies in their study. For example, as an independent constraint, they find that predictions for the Mg_{UV} line strength from the best SED-fit agree very well with the observed

Table 4.1: Overview of all fits carried out with various template and filter setups for simulated galaxies at redshift 0.5, 1, 2 and 3. Fits that involve constraining or rebinning the age grid were only carried out for mock star-forming galaxies. Fits with inverted-τ models as a function of wavelength dependence were only carried out for mock star-forming galaxies at $z = 2$.

Template Setup	UBVRI JHK IRAC	UBVRI IRAC	UBVRI JHK	UBVRI JH	UBVRI J	UBVRI	BVRI JHK IRAC	VRI JHK IRAC	RI JHK IRAC	u'g'r'i'z'	UBVRI Y JHK IRAC	BRIK
wide setup	x	x	x	x	x	x	x	x	x	x	x	x
wide, age rebin	x	-	x	-	-	-	-	-	-	-	-	-
wide, age ≥ 0.1 Gyr	x	-	-	-	-	-	-	-	-	-	-	-
wide, $Z = 0.004$	x	-	-	-	-	-	-	-	-	-	-	-
wide, $Z = 0.01$	x	-	-	-	-	-	-	-	-	-	-	-
wide, $Z = 0.02$	x	-	-	-	-	-	-	-	-	-	-	-
wide, $Z = 0.04$	x	-	-	-	-	-	-	-	-	-	-	-
wide, Kroupa	x	-	-	-	-	-	-	-	-	-	-	-
wide, Chabrier	x	-	-	-	-	-	-	-	-	-	-	-
wide, top-heavy	x	-	-	-	-	-	-	-	-	-	-	-
only-τ	x	-	x	-	-	-	-	-	-	-	-	-
inverted-τ	x	x	x	x	x	x	x	x	x	x	x	x
only SSPs	x	-	-	-	-	-	-	-	-	-	-	-
solar SSP	x	-	-	-	-	-	-	-	-	-	-	-
wide, BC03	x	-	x	-	-	x	-	-	-	-	-	-

line strengths in the GOODS-S sample (Daddi et al., 2005). However, as well known, passive galaxies are much easier to fit than star-forming ones and also metallicity effects are more evident in passive spectra. Hence, the result of M06 may not be confirmed for other classes of galaxies.

In order to study the effect of metallicity, we also obtain best fit solutions using the wide setup in mono-metallicity form. Furthermore, we retrieve separate solutions for the full setup in combination with different reddening laws to reveal their effect on the fitting.

We also consider an identical setup based on BC03 models (hereafter BC03 setup). It is well known that these models mostly differ from the M05 models in the energetics of the TP-AGB and at the young ages (Maraston, 2011a, and Section 3.4). From this

viewpoint, these two stellar population models represent two extremes which enclose other ones, e.g. Charlot & Bruzual (CB07), (e.g. Cimatti et al., 2008; Conroy et al., 2009). As BC03 models are widely used in the literature using them for the same set of mock galaxies allows us to provide scaling relations which help translating the results obtained with BC03 models to M05 models and vice-versa. Results are summarised in Appendix B.

Only-τ setup

Exponentially declining SFH or τ-type models are a common choice in the literature (e.g. Papovich et al., 2001; Shapley et al., 2005; Pozzetti et al., 2007). In M10 (Section 6.1) we showed that for real star-forming galaxies as well as mock star-forming galaxies at $z = 2$ τ-models do not provide a good approximation of the star formation histories.
Here, we try to quantify the effect of this mismatch by adopting a template setup which contains τ-models (only-τ setup, with $\tau = 0.01, 0.05, 0.1, 0.2, 0.5, 1, 2$ and 5 Gyr) and constant star formation, solar metallicity and a Salpeter IMF as in Shapley et al. (2005) (but based on M05). Furthermore, Shapley et al. (2005) used a Calzetti type reddening law and models from BC03. We explore these templates by exploiting various reddening laws.

Inverted-τ models

Exponentially increasing SFHs (so-called *inverted*-τ models) were explored for the first time in SED-fitting in M10 (Section 6.1). It was found there that - with priors on the galaxy formation redshift and the typical τ - these models were the only ones able to recover the SFR and the reddening that was determined from independent indicators such as far-IR luminosities or the UV-corrected slope. In M10 we also used a set of mocks from this chapter and show that the same setup also gave excellent results on the SFR-mass-relation of semi-analytic galaxies.
In this chapter we extend the test to mocks at other redshifts, using the same assumptions, namely a formation redshift of ~ 5, which translates into ~ 1 Gyr age models for fitting $z \sim 3$ galaxies and ~ 4 Gyr age models for $z < 2$.

Age Grids

We also investigate intrinsic properties of the templates themselves, in particular the age grid. Templates normally get rebinned from 221 to 51 values in age within the *Hyper-Zspec*-code. The original age grid is equally spaced in logarithmic space. Hence, the rebinning has a larger effect on younger ages. The latest version of the code considers

221 ages without rebinning. In both cases minimum and maximum age are $100,000$ yrs and 20 Gyr, respectively. We adopt the finer age grid of 221 ages as default and test the effects of using the wide setup with a rebinned age grid.

Furthermore, we study the effect of excluding very young ages in the fitting by limiting the minimum age to 20 Myr and 100 Myr. We showed in M10 (Section 6.1) that solutions obtained with the exclusion of the youngest ages are less biased by very young and bright stellar populations that dominate the emitted light, thus disabling their outshining effect. Similar minimum age constraints are applied by Bolzonella et al. (2010) and Wuyts et al. (2009) in order to exclude very young solutions and to improve the mass estimate. Bolzonella et al. (2010) verified this through tests with simulations.

Age grids are only varied for mock star-forming galaxies as these are affected by outshining; our mock passive galaxies are by definition devoid of this[1].

Varying the IMF

A further interesting question to address is the sensitivity of the SED-fit to IMF choices as the IMF is a free parameter in population synthesis models. Commonly a conversion factor between Salpeter and other IMFs is assumed to convert stellar masses and other quantities, for example masses obtained with a Kroupa IMF are smaller by a factor of ~ 1.6 when compared to Salpeter (M06). Here, we have the opportunity to assess whether a simple scaling is sufficient. We use the wide setup with templates based on a variety of different IMFs, namely Salpeter, Kroupa (Kroupa, 2001), Chabrier (Chabrier, 2003) and a top- heavy IMF (with slope $x \sim 0$). For the Chabrier and top-heavy IMFs we adopt the slopes as given in van Dokkum (2008).

4.2.2 Wavelength range included in the fitting

Which wavelength coverage is required in order to gain robust results from SED-fitting? How many broad-band filters should be used? These are key questions in galaxy evolution studies especially for the planning of galaxy surveys and observational proposals and for understanding the reliability of the results. In order to answer these questions we carry out a comprehensive test of various filter setups and their performance in recovering the galaxy physical properties. M06 discuss the importance of including the rest-frame near-IR in the fitting (illustrated in their Figure 9). Kannappan & Gawiser (2007) also

[1] We have verified that a minimum age constraint of 0.1 Gyr has no effect on the final results for the mock passive galaxies.

point out the dependency of stellar mass estimates on filter type and wavelength coverage. Shapley et al. (2005) on the other hand conclude that the near-IR does not carry additional information with respect to a fitting carried out in the optical, using BC03 population models. van der Wel et al. (2006) even conclude - in combination with the M05 stellar population models - that including the near-IR could even be damaging the results.

The light of a galaxy is a superposition of the light emitted by its stellar populations and the wavelength range in which a single stellar population emits most of its light changes with age. Hence, by sampling the entire spectrum there is generally a better hope to trace all different stellar populations in a galaxy whereas restricting the filter set to certain wavelengths may result in overemphasising the contributions of specific populations. In order to better understand the extent of this effect, we explored the following filters sets:

- UBVRI JHK IRAC (3.6, 4.5, 5.8 μm), UBVRI JHK, UBVRI JH, UBVRI J, UBVRI
- UBVRI IRAC
- BVRI JHK IRAC, VRI JHK IRAC, RI JHK IRAC
- u' g' r' i' z' (SDSS) [$z = 0.5$]
- UBVRI *Y* JHK IRAC
- BRIK

Obviously, the assumption that all mock galaxies are detected in all filter bands is an idealised case. In particular, the majority the mock passive galaxies at $z \geq 2$ would not be detected in filter bands bluer than V (I for log $M^* \sim 10.5$) in even the deepest surveys, such as e.g. GOODS (Giavalisco et al., 2004), because of their old age and SFH. However, this case is addressed when filter setups that omit the bluest filter bands are used in the fitting.

4.2.3 Photometric uncertainties

In order to quantify the effect of photometric uncertainties we use two different catalogues of the same 100 galaxies[2] at $z = 0.5$. One catalogue contains the magnitudes that were scattered with Gaussian errors as described in Section 2.1 the other the true magnitudes without this scatter. For both we derive the stellar population properties with the exact same method using our default setup and no reddening in the SED-fitting. The exclusion of reddening in the catalogues and fitting allows us to single out the effect of

[2] without dust reddening

the photometric uncertainties without being affected by the age-dust degeneracy.

The influence of photometric uncertainties for the sample of mock passive galaxies is determined in the same way but using only a solar metallicity SSP as template to provide the exact match in star formation history to the mock passive galaxies.

4.3 Results for star-forming galaxies

In this section we compare the galaxy properties derived from SED-fitting of mock galaxies to the true values. The comparison is performed as a function of template setup (star formation history, metallicity, age grid, IMF, stellar population model[3]), filter set and wavelength coverage, and reddening law. For the semi-analytic galaxies, we first produced mock catalogues without dust reddening to better single out the contributions of the multiple stellar populations building up the galaxies. For these unreddened galaxies we also do not consider reddening in the fitting. In the following, we refer to this as the 'case without reddening' or the 'unreddened case'. Although ignoring the existence of dust when simulating star-forming galaxies is an unrealistic case it provides an insight into the impact of the age-dust degeneracy. The procedure is then repeated including dust reddening, both in the mock catalogue and the fitting. For the mock passive galaxies no internal dust reddening has been included, but both the cases of including and excluding reddening in the fitting are studied. Table 4.1 gives an overview of all fits that were carried out.

In order to evaluate the optimal template and filter sets - intended as the one for which fitted and input properties are closest - we define a quality estimator *Q* similar to a χ^2:

$$Q = \sqrt{\sum_i (\Delta)^2} \tag{4.1}$$

with

$$\Delta = x_{i,fitting} - x_{i,input}, \tag{4.2}$$

i being the number of objects and *x* representing age, metallicity, reddening, stellar mass or SFR, respectively. The optimal value of *Q* and Δ is zero.

A first indicator of the individual performances of the various template setups is the χ^2_ν of the best fit. We show results for the mock star-forming galaxies at $z = 2$ in Fig. 4.1

[3] see Appendix B

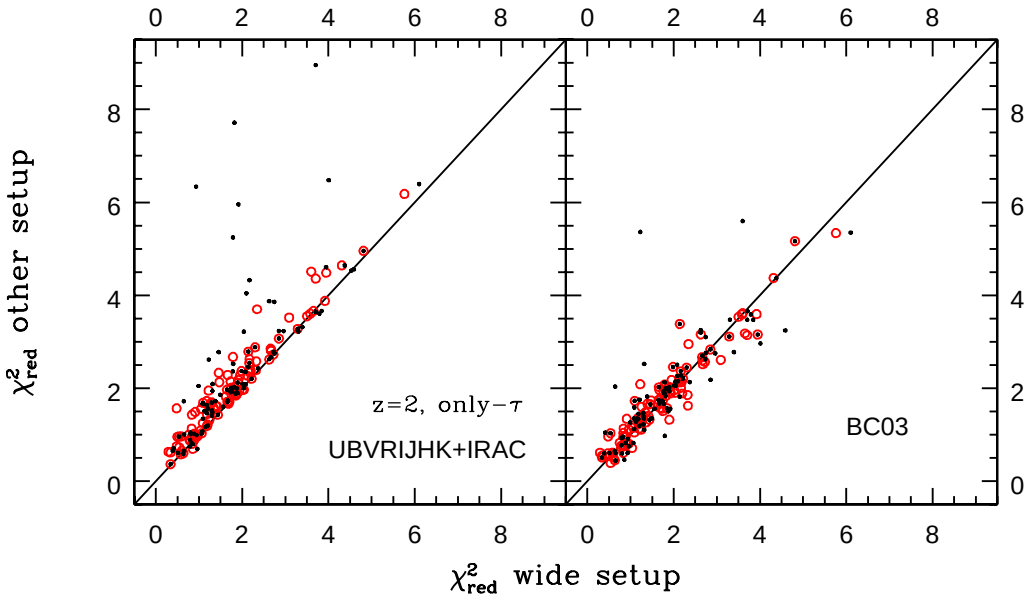

Figure 4.1: Minimum χ^2_ν of best fits with alternative setups in comparison to the wide setup, using UBVRIJHK+IRAC bands for mock star-forming galaxies at redshift 2. Black symbols show the unreddened case (internal dust reddening is not included in the mock galaxies and the fitting is carried out without dust reddening). Red symbols show the case with dust reddening. The same results are found at all other redshifts.

as an example. For nearly all objects the wide setup provides a better χ^2_ν in comparison to the only-τ setup due to the wider template library with regard to metallicity and star formation histories. However, we showed in M10 (Section 6.1) that models with the smallest χ^2_ν are not necessarily a better physical solution. This is further confirmed here by the fact that a BC03-based setup shows a better χ^2_ν in some cases although the mock galaxies are based on the M05 models and therefore their SED is intrinsically different.[4]. This example highlights again how misleading the mere consideration of the minimum χ^2_ν can be.

In the following we focus on the ability of different template setups and wavelength coverage to recover the age, metallicity, SFH, reddening and stellar mass.

[4]We summarise the results for fits with the BC03-setup to M05-based mock star-forming galaxies in Appendix B and vice versa in Appendix C.

4.3.1 Age

The comparison of fitted ages with the intrinsic ages allows us to identify which *age* (mass-weighted age, luminosity-weighted age[5], age of the oldest population) is actually recovered by the fit. As discussed in M10 (Section 6.1), by definition, the age parameter t of the templates and the fitting denotes the age of the oldest population that is present, as it marks the starting of star formation (see M10 and Section 6.1 for details). However, as one fits the integrated luminosity the true age is difficult to extract, particularly for galaxies with extended star formation due to the overshining effect. For example, it is known that fitting single-burst models to data give 'luminosity-weighted' quantities, which mostly reflect the properties of the most luminous generation.

In Fig. 4.2 we show the comparison for the wide and only-τ setups at redshift 0.5 and 2. We find that ages derived for dust-free spectra agree best with mass-weighted ages, particularly at high redshift. This is a somewhat new conclusion, and suggests that the use of composite templates allows to obtain ages that are closer to the mass-weighted ones than to the luminosity-weighted ones. The youngest fitted ages ($\lesssim 10^8$ yr) are underestimated most. At high redshift fitted ages are similarly comparable to the oldest ages while most are underestimated for the oldest galaxies (at $z = 0.5$). V-band luminosity-weighted ages are predominantly overestimated for objects with higher SFRs (at $z = 2$) and predominantly underestimated for objects with little star formation (at $z = 0.5$), the latter is due to the overshining. Since the range of available ages in the fitting narrows towards higher redshift, differences in best fit age between template setups and between recovered and true age decrease towards higher redshift, particularly for ages $\geq 10^8$ yr.

For the reddened case, the age-dust degeneracy is strong and causes ages to be underestimated (by up to nearly 3 dex in the worst cases). The effect is less severe at higher redshift because of the smaller available age range. Here, only the youngest ages (below 10^8 yr) are underestimated. For young and dusty star-forming galaxies (those at high redshift) the reason is twofold. Firstly, a small contribution stems from the age-metallicity degeneracy. Template metallicities are much higher than mock galaxy metallicities (compare Fig. 2.2). Thus, bluer colours are reproduced by younger ages. Secondly and dominating, template SFHs do not match those of the semi-analytic galaxies resulting in the overestimation of some mass-weighted ages (at $z = 2$).

[5] Ages are weighted by the V-band luminosity of the corresponding SSP models. We also considered the bolometric luminosity. Overall, the latter provides younger ages in comparison to the V-band luminosity weighted ages, but the overall trends are similar.

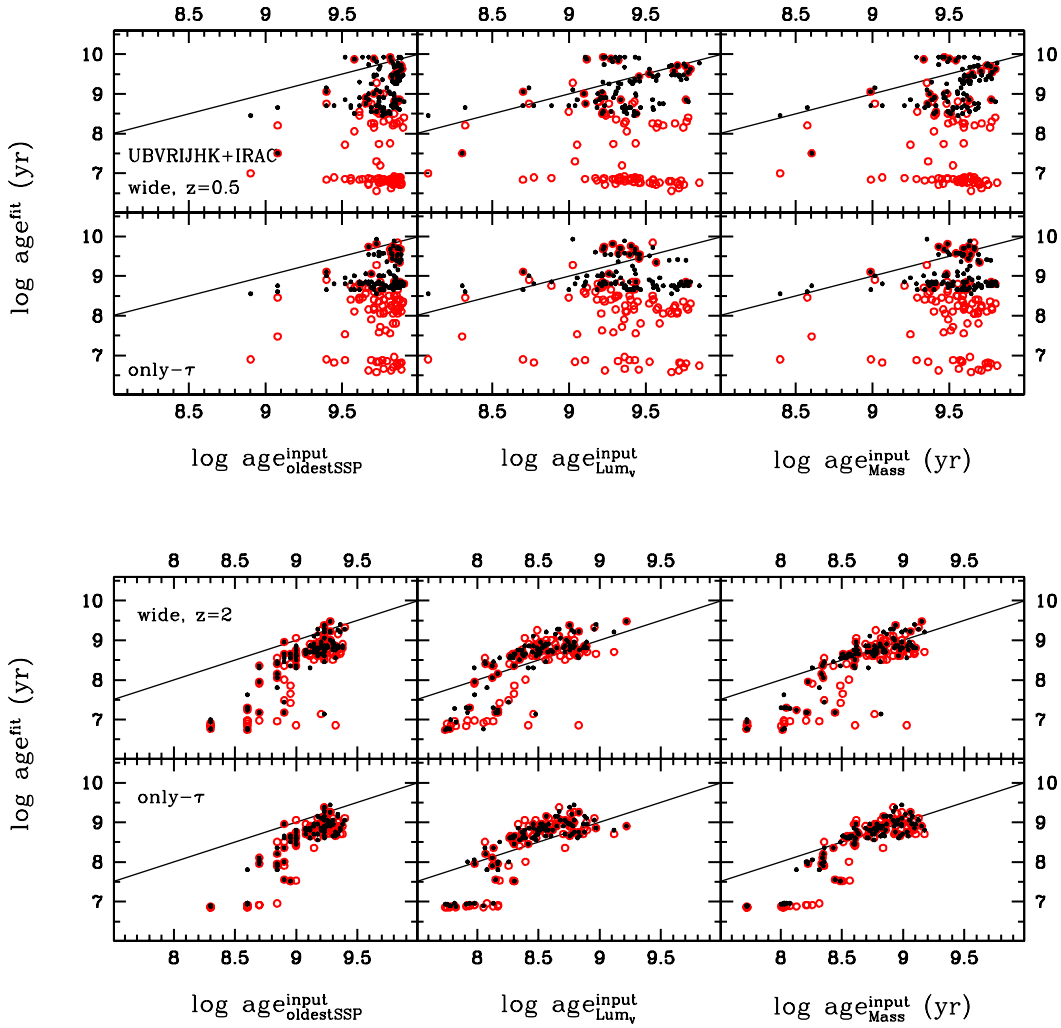

Figure 4.2: Best fit ages (y-axis) compared to input ages (x-axis) of mock star-forming galaxies for the wide and only-τ setups at redshift 0.5 and 2 (top and bottom panels, respectively). Symbols as in Fig. 4.1. *Left:* Comparison with the age of the oldest population. *Middle:* comparison with V-band luminosity-weighted ages. *Right:* Comparison with mass-weighted ages.

For older galaxies with little on-going star formation (those at low redshift) and in the reddened case very young ages ($< 10^8$ yr) and a large amount of dust are obtained with the SSP component included in the wide template setup. The fit is clearly fooled by the overshining in combination with the age-dust degeneracy (see Renzini, 2006, for a detailed description of this degeneracy and its effects). Semi-analytic galaxies at $z \leq 1$ are hardly reddened due to their low SFRs (see Section 2.1). Allowing for dust reddening in the fit drives the ages to younger values since the addition of dust mimics redder colours (see also Fig. 4.6, this effect is less strong for $z = 2$ and 3 as the simulated

galaxies are dust reddened). With the only-τ setup most of these objects are fitted with significantly less dust, longer τ, higher metallicity and older ages. Very young ages from the only-τ setup are due to the SFH and metallicity mismatch. In general, the age determination is better at high redshift. Deviations at low redshift are large because of on-going star formation and the wide age range covered by the stellar populations in a single galaxy (Fig. 2.1).

In order to single out the effect of metallicity on the derived ages, we used mono-metallicity template setups, keeping the variety of star formation histories and IMF of the wide setup. Overall, the effect is small and therefore, it is not shown here. When

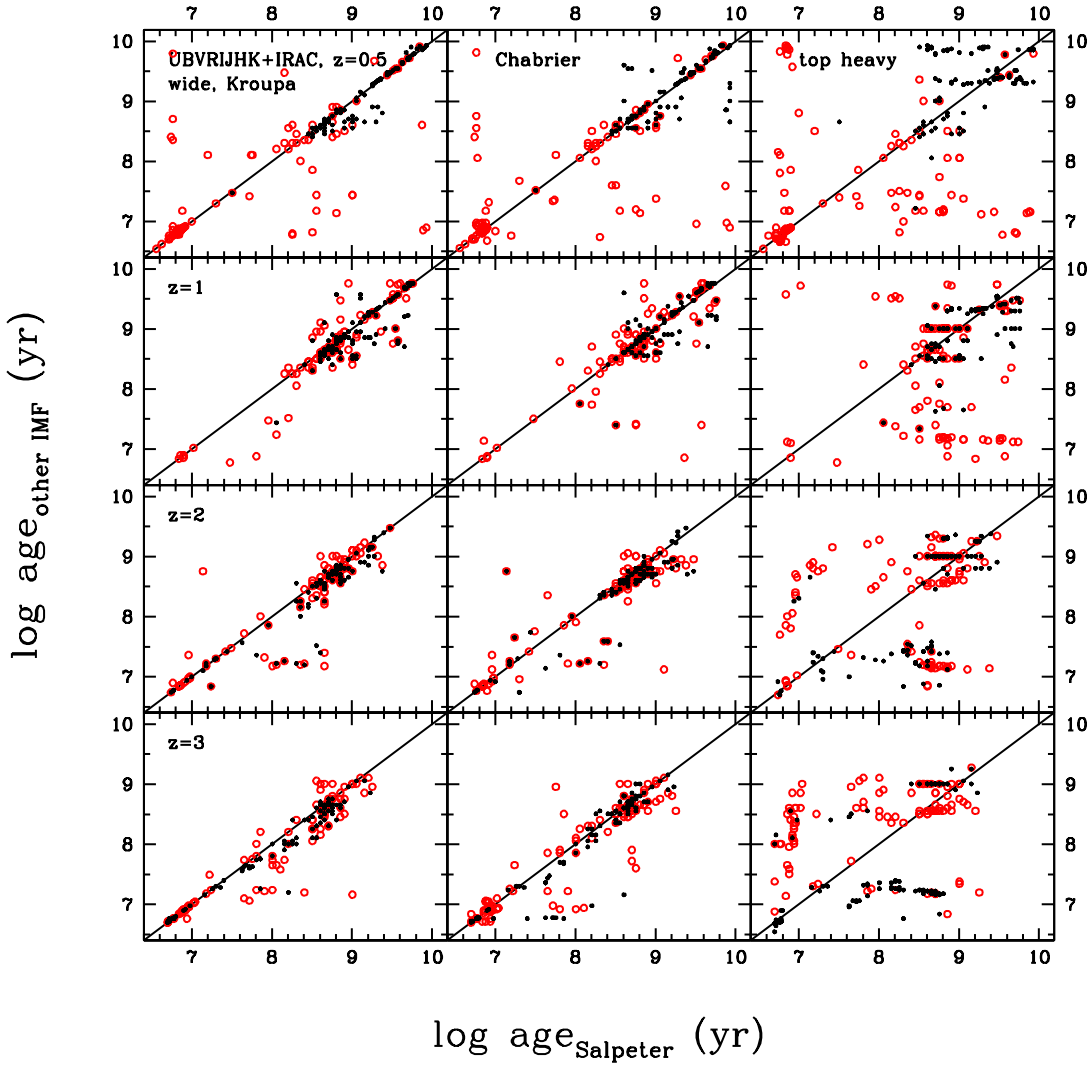

Figure 4.3: Comparison of ages derived from SED-fitting with templates of different IMFs. Symbols as in Fig. 4.1.

reddening is switched off the effect is very clear: when the template metallicity is high, sub-solar metallicity galaxies are fitted with a younger age to compensate this mismatch. When reddening is introduced into the procedure, the age-dust degeneracy partly compensates metallicity effects. Only when the metallicity is overestimated the most, the number of objects with a younger best fit age increases significantly, particularly for the metal poorest objects (at high redshift).

We now investigate how the differences in the model-SED due to different IMFs affect the derived best fit ages. These differ substantially between the various IMFs (Fig. 4.3), especially for a top-heavy IMF. Again, the case without reddening helps understanding the effect. At $z = 3$ and 2 top-heavy IMF models give systematically older ages than Salpeter IMF models. The excess of massive stars and thus UV light for very young ages of the top-heavy IMF models is compensated by on older age. The same is true at low-redshift where ages for a top-heavy IMF are systematically older than ages for a Salpeter IMF. Ages derived with a Chabrier and Kroupa IMF are much closer to those derived with Salpeter. At intermediate ages (i.e. in the intermediate stellar mass range) the SED of a Kroupa and Chabrier IMF is slightly redder because of the effect on the evolutionary flux. This is compensated by younger ages. When reddening is included scatter increases, particularly at low redshift, due to the age-dust degeneracy. At high redshift ages obtained with top-heavy IMF templates are now much older than those of Salpeter IMF templates (and the fitted reddening is higher).

Finally, we study the dependence of the derived ages on the adopted wavelength range in the fitting which is shown for the unreddened case in Fig. 4.4 for a few common filter sets. Since the emission of stellar populations of different ages peaks at different wavelengths one expects that a narrow wavelength range in the fit biases the result towards particular ages. In the unreddened case the effects are small for the oldest galaxies ($z = 0.5$). Excluding IRAC filters and using only optical wavelengths in the fitting makes derived ages somewhat older. For higher redshift and intrinsically younger objects the opposite is the case. The more the wavelength coverage is focussed towards the rest-frame UV, the younger the derived ages. Neglecting blue filter bands has a slightly rejuvenating effect for the oldest galaxies, for younger ones ($z \sim 2$) the effect is smaller because the rest-frame UV is excluded and underlying older stellar populations are emphasised in the fit. The inclusion of reddening has little impact on the general dependence of derived ages on wavelength coverage and is therefore not shown. At low redshift, however, the age-dust degeneracy dominates.

In summary, fitted ages compare best to mass-weighted ages and not to luminosity-weighted ages, as widely believed. The difficulty in recovering the oldest age remains which is mostly related to mismatches in the star formation history. In conclusion and perhaps not surprisingly, SSPs or τ-models with low τ's should not be used when dealing with star-forming objects. Since using mono-metallicity template setups has a very small effect on the derived ages compared to using a wide set of metallicities because age effects dominate over metallicity effects in star-forming galaxies, it is sufficient to use mono-metallicity template setups for star-forming galaxies. The choice of IMF affects ages such that the wrong IMF can be compensated by a different age. The largest effects are seen for the IMF that is most discrepant (top-heavy IMF here) to the input IMF. The wavelength coverage plays a crucial role in the determination of ages such that a restriction in wavelength coverage results in younger ages at high redshift. At low redshift ages are underestimated due to the age-dust degeneracy and the wrong SFH. Because of

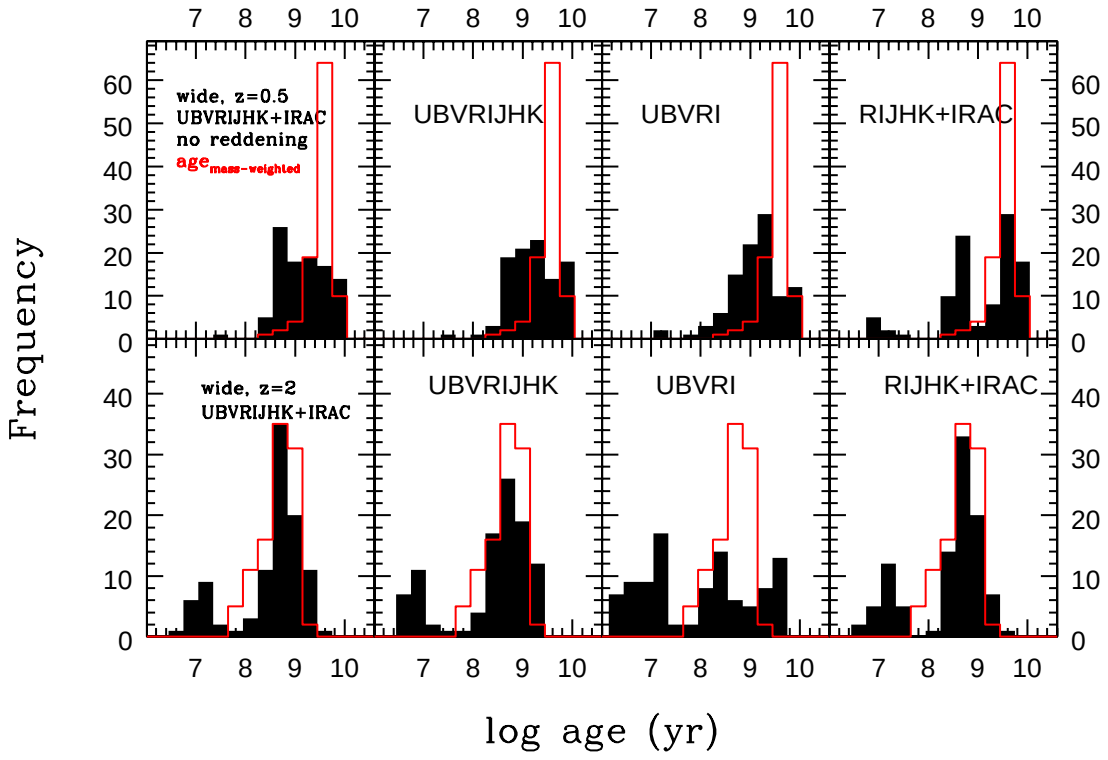

Figure 4.4: Ages derived from SED-fitting as a function of wavelength for redshift 0.5 and 2 in the case without dust reddening. The red histogram shows the distribution of the mass-weighted age.

the mismatched SFH the derived age resembles the real one, e.g. the oldest population present, in hardly any case.

4.3.2 Metallicity

We know that most template metallicities are too high compared to input metallicities. Consequently, metallicity is overestimated for most objects, particularly at high redshift (Fig. 4.5). This is the case even when reddening is switched off and demonstrates the age-metallicity degeneracy. The highest metallicity templates of the wide setup are mainly chosen when reddening is allowed in the fit because of the added degeneracy with dust. These are best fit with a young and short starburst (SSPs or small values of τ) and larger amounts of reddening. In a statistic sense the fit is sensitive to the metallicity, such that the number of best fit templates with low metallicities is higher at high redshift. The opposite is the case for high metallicities.

The derived metallicities depend only little on the wavelength coverage, therefore we do not show it. The lack in wavelength coverage affects the most when only optical filter

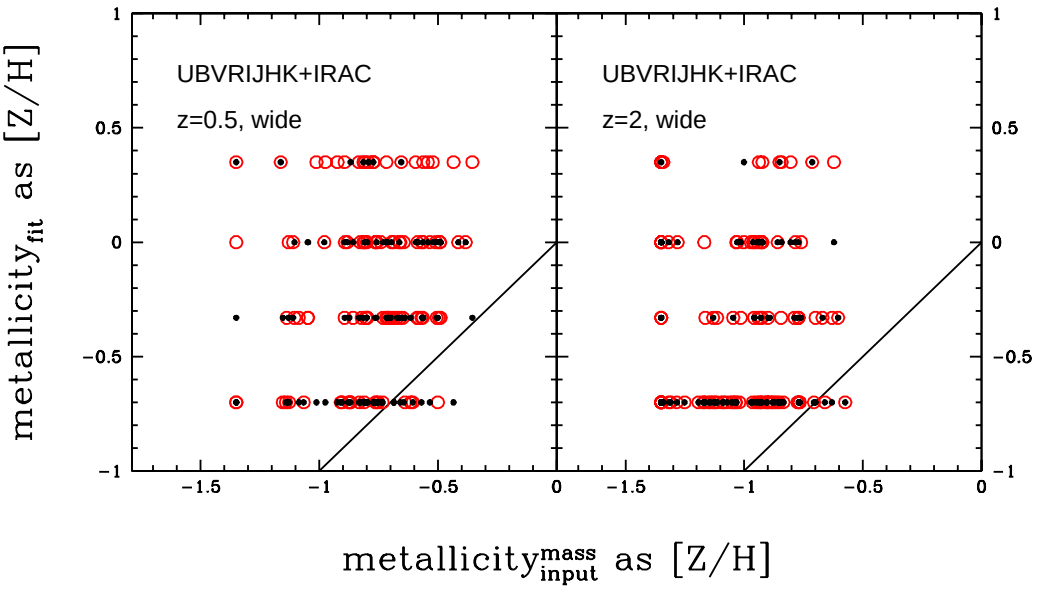

Figure 4.5: Comparison between recovered and mass-weighted metallicity of mock star-forming galaxies at redshift 0.5 and 2 for the wide setup. Black and red symbols refer to the cases without and with dust reddening, respectively. Template metallicities are -0.7, -0.33, 0 and 0.35 (from a fifth solar metallicity to twice solar metallicity). The line of equality is shown.

bands are used such that most galaxies are best fitted with the highest metallicity templates.

Overall, for star-forming galaxies, metallicities are poorly recovered because ages are poorly recovered, i.e. ages are underestimated and metallicities are overestimated, which in turn is driven by the poor match of the SFH and the overshining effect.

4.3.3 E(B-V)

We present the comparison between derived and input reddening for the wide setup and illustrate the age-dust degeneracy in Fig. 4.6. The reddening is very well recovered at $z \geq 2$ for the wide and inverted-τ setups. The only-τ setup provides slightly larger reddening values. This is the same result that M10 (Section 6.1) found for real $z \sim 2$ star-forming galaxies. They showed that dust reddening obtained from a fit with inverted-τ models agrees best with those derived from the rest-frame UV (compare their Figs. 16 and 20). At $z < 2$ on the other hand reddening is heavily overestimated for all setups. Accordingly, we find that fitted ages are younger at low redshift in the case with reddening compared to the case without reddening. When reddening is overestimated by $E(B-V) \sim 0.4 - 1.2$ ages are lower by up to ~ 3 dex at redshift 0.5. This difference decreases towards redshift 3 where ages are also older than in the unreddened case (lower panel in Fig. 4.6).

Because the ability to recover reddening depends only little on the wavelength coverage, we only summarise the main points: 1) the exclusion of near-IR filter bands has almost no effect because dust reddening absorbs light predominantly at rest-frame UV wavelengths. 2) For that reason the exclusion of the bluest filter bands has the largest effect on the derived reddening, such that reddening is even more overestimated at low redshift and underestimated at high redshift.

Compared to the full age grid shown in Fig. 4.6 a cap on minimum age reduces the overestimation in $E(B-V)$ from maximal $\Delta E(B-V) = 1.1$ to 0.45 at $z = 0.5$ for all template setups. The maximum age difference is now ~ 2 dex at the lowest redshifts. At higher redshift the minimum age restriction improves the derived reddening only little and ages differ less between cases with and without reddening. Rebinning of the age grid does not improve the recovery of reddening at any redshift.

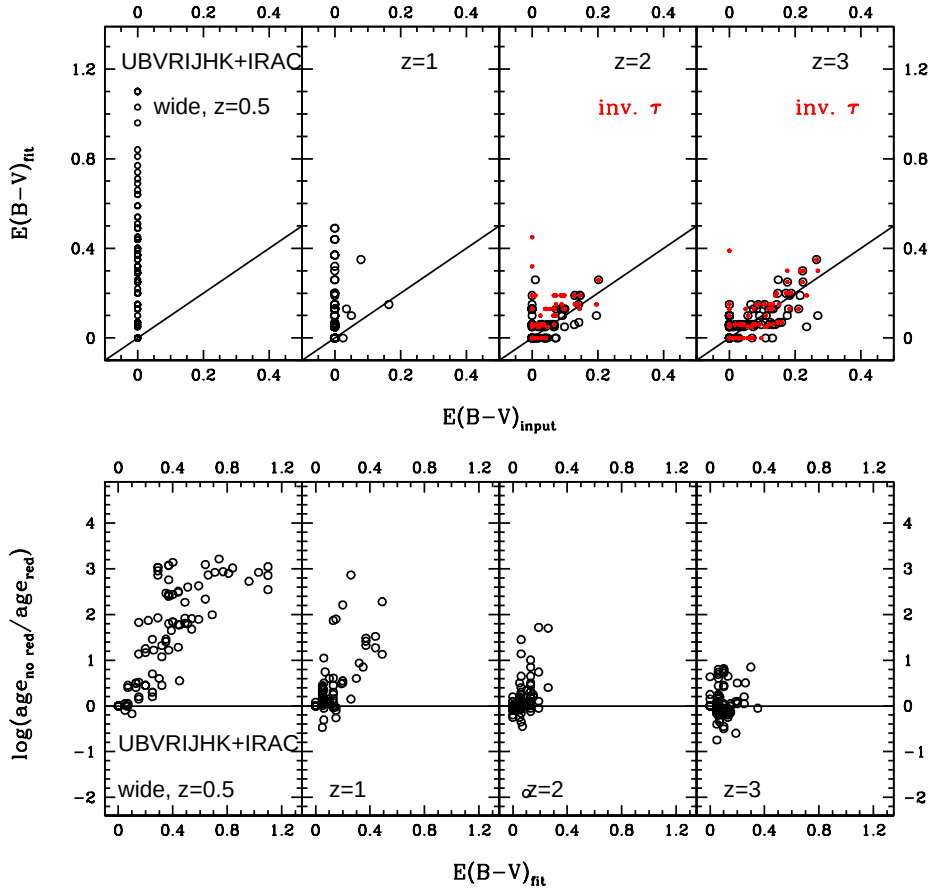

Figure 4.6: *Upper panel:* Difference between derived and input $E(B-V)$ as a function of redshift (0.5, 1, 2 and 3, respectively, from left to right) for the wide setup (black open circles) and for the inverted-τ model (red dots, redshift 2 and 3). *Lower panel:* Difference in derived ages with and without internal reddening as a function of fitted reddening.

Metallicity has only a small effect on the derived reddening, hence, we do not show it. $E(B-V)$ is slightly more overestimated at high redshift for the highest metallicity template setup. Overall, the scatter is increased.

In summary, reddening for both inverted-τ and wide setups is well recovered for galaxies that are dust reddened. This depends little on wavelength coverage, metallicity and age. For intrinsically dust-free galaxies (those at $z = 0.5$), reddening is heavily overestimated and ages are underestimated because of the age-dust degeneracy.

4.3.4 Stellar Mass

The choice of template setup also affects the mass recovery (Fig. 4.7). With the wide template setup the mass recovery at redshift 2 and 3 is very good, particularly for masses between 10^{10} and $10^{11} M_{\odot}$. Masses are underestimated for lower-mass galaxies. These are small disks with increasing SFHs like the ones shown in panel a) of Fig. 2.3 left-hand side. Indeed, their mass can be perfectly recovered using the inverted-τ models (bottom

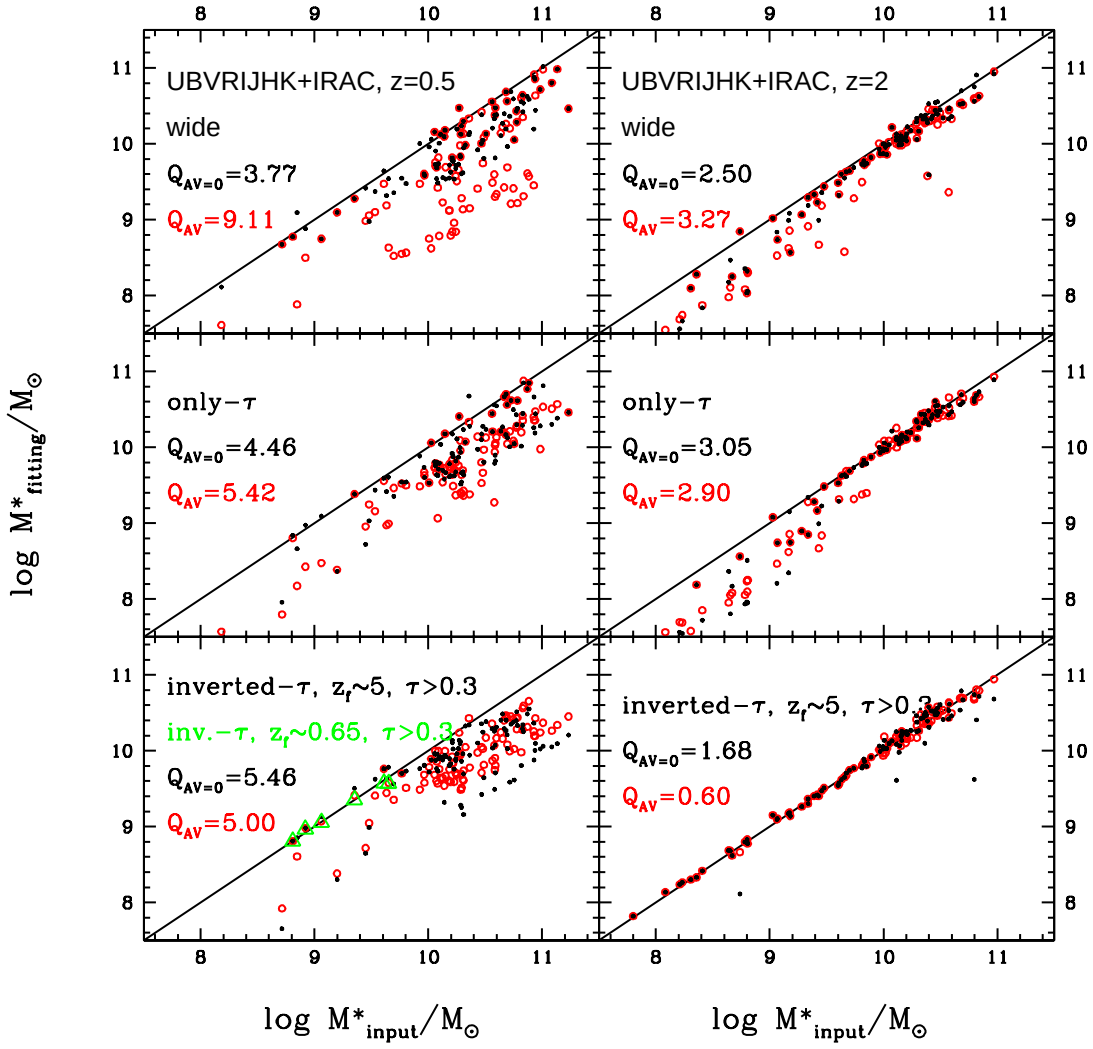

Figure 4.7: Stellar mass recovery at redshift 0.5 and 2 as a function of template setup, namely from top to bottom: wide, only-τ, inverted-τ. Red circles refer to cases with reddening, black dots to no reddening. Quality factors are given for the entire mass range for reddened and unreddened cases, respectively. Green triangles show the mass estimate for the youngest objects at $z = 0.5$ with increasing SFH (see Fig. 2.3) when an inverted-τ model of age 1.1 Gyr is used in the fitting.

panel in Fig. 4.7). Including dust affects the result only little. For older galaxies with little on-going star formation ($z = 0.5$) on the other hand, masses are underestimated. When dust is included, this effect is mostly due to the age-dust degeneracy, whereas without reddening a different set of degeneracies dominates. Firstly, no available SFH provides a real match to the mock SFHs. As seen in Fig. 2.3 the typical SFH at low redshift is bimodal in the sense that star formation decreases after an initial period of increasing star formation. On-going star formation causes overshining, thus hiding most of the old underlying populations. This has the largest effect at redshift 0.5 because the age distribution of the stellar populations building up a particular galaxy is much wider (see Fig. 4.2). Secondly, template metallicities are discrete and for the bulk of stellar populations of about half the objects still too metal rich (compare Fig. 2.2 and Fig. 4.5). The blue colour of a galaxy is matched by a template of low metallicity in combination with a longer star formation time scale and an older age, or a higher metallicity, shorter star formation time scale and a younger age. The latter leads to underestimate the mass. SSPs are the main cause for very young ages and consequently very low stellar masses in the wide template setup. Masses are underestimated by up to 0.8 dex.

It is important to note that - if instead of picking up the best fit for those objects for which the mass is underestimated, one would average over neighbouring solutions (in the range of $\chi^2_\nu + 1$) - their mass estimate could be improved by up to 0.4 dex. Although masses are significantly improved for some of these objects, carrying out the procedure for all objects only results in an average improvement of 0.06 dex in the unreddened case and 0.18 dex when dust reddening is included.

An only-τ setup can recover stellar masses at high redshift similarly well in the high-mass range, and due to the different star formation history, similarly badly in the low-mass range. For older galaxies with little on-going star formation at low redshift masses are underestimated. However, this setup including reddening performs slightly better than the wide setup.

At all redshifts masses are better recovered when the mock star-forming galaxies are unreddened, because there is no age-dust degeneracy (Fig. 4.7). At $z = 0.5$ masses are recovered within -0.8 dex and $+0.3$ dex for all template setups. When reddening is included the SED-recovered stellar masses are underestimated by up to ~ 1.6 dex for the least dust reddened and oldest galaxies in our sample. This stems from underestimating the age due to the age-dust degeneracy (Fig. 4.2).

The mass recovery improves with overall decreasing galaxy ages and age spread, for all setups which perform in a very similar way for $z \geq 1$. Masses larger than $10^{9.5}\,M_{\odot}$ are very well recovered for all template setups. Masses lower than $10^{9.5}\,M_{\odot}$ are underestimated by ~ -0.7 dex at $z = 3$.

Here, it is important to note that the mock galaxies have SFRs of at most around $30 M_{\odot}$/yr (see Fig. 2.4), whereas real galaxies can have higher star formation rates (e.g. Daddi et al., 2007). Hence, these conclusions may not be extended to real galaxies, and indeed in M10 (Section 6.1) we showed that for $z \sim 2$ star-forming galaxies with higher SFRs, an only-τ setup underestimates the age, hence underestimates the stellar mass and overestimates the star formation rate. In M10 (Section 6.1) we have also verified that an inverted-τ-type star formation history with high formation redshift is best for the derivation of physical properties such as reddening and SFR and for the mock galaxies of this work for stellar mass (their Fig. 24). Here we reinforce the result by a starring mass recovery for mock galaxies at redshift 2 and 3 (Fig. 4.7 bottom right) with inverted-τ models.

Obviously, the same models with the same priors do not allow a good mass recovery for older galaxies at lower redshifts because they do not trace their correct SFH. However, if we change priors and use inverted-τ models with formation redshift (i.e. age) closer to the age of the oldest population, thus simulating objects like the one shown in the bottom-left of Fig. 2.3, the stellar mass is recovered very well (green triangles in Fig. 4.7). However, the SFHs of real galaxies are not known and a distinction between objects of increasing and decreasing SFR cannot be made prior to the fitting. A focussed investigation on these models and on how to apply them to different redshifts and types of galaxies is postponed to a dedicated paper.

Nowadays, in order to simulate more realistic star formation histories, several authors adopt a two-component template, such that a second burst at an arbitrary time is superimposed on an underlying exponentially declining star formation history (Papovich et al., 2001; Gallazzi et al., 2005; Salim et al., 2007; Pozzetti et al., 2007; Walcher et al., 2008; Muzzin et al., 2009; Noll et al., 2009). In this way, the stellar mass can be maximised. Pozzetti et al. (2007) report an up to 40% increase in stellar mass using two-component models over models with simpler SFHs. This composite model maybe a much better choice at low redshifts.

In Fig. 4.8 we show the mass recovery as a function of the metallicity adopted in the templates. For star-forming galaxies in the dust free case the lowest metallicity setup performs best at each redshift. The true mass is still underestimated by a median of

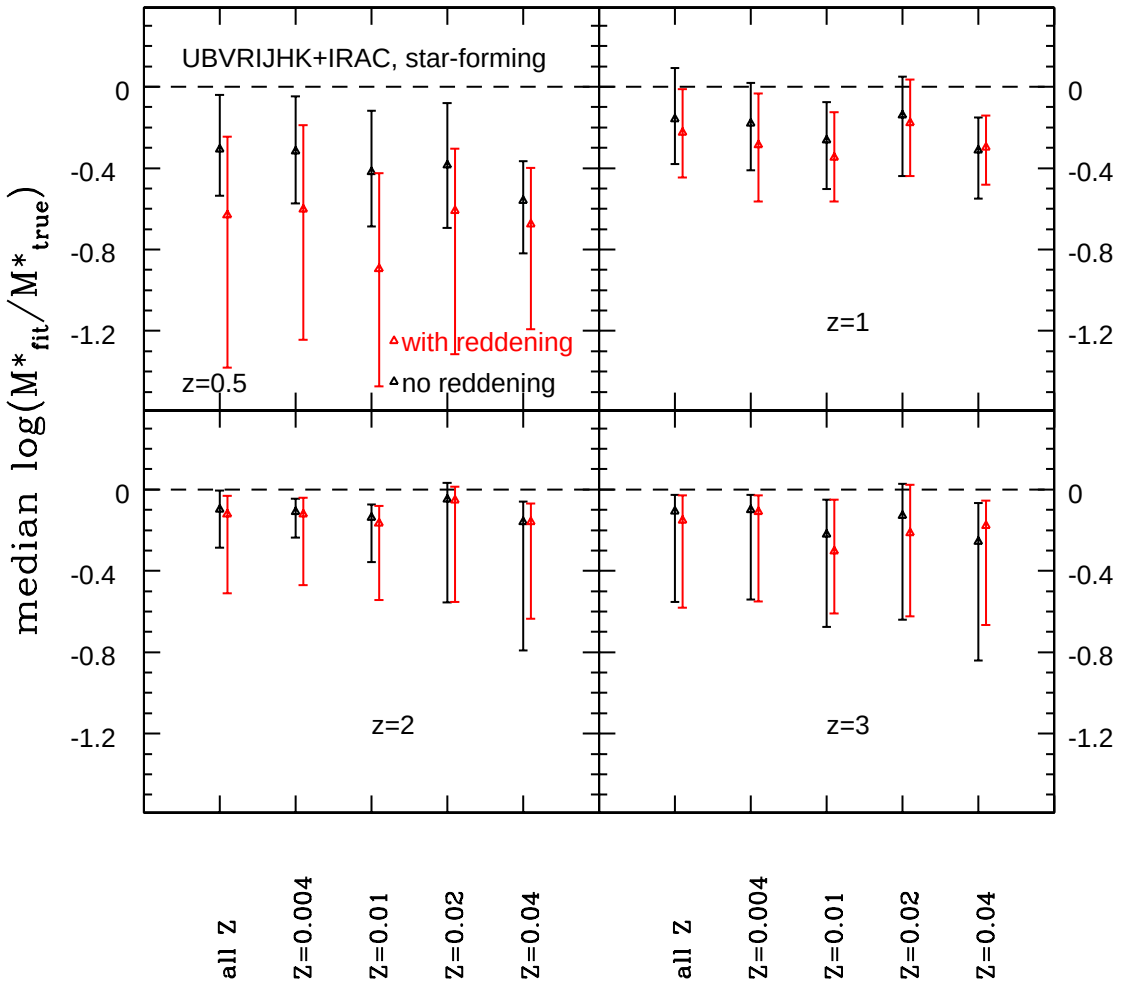

Figure 4.8: Median recovered stellar mass of mock star-forming galaxies for mono-metallicity wide setups as a function of redshift, hence galaxy age (upper left to lower right). Metallicity in each panel increases from left to right. Red and black triangles refer to cases with and without reddening, respectively. Error bars reflect 68% confidence levels.

$0.3 - 0.1$ dex. The mass recovery becomes worse with increasing metallicity because metallicities are too high compared to the mock (see Fig. 2.2). This is distorted when reddening is included and masses are now underestimated by a median $0.6 - 0.1$ dex. Overall, as already concluded by Bolzonella et al. (2010), the differences between different metallicity setups are small. Consequently, fitting with a mono-metallicity template setup is sufficient for star-forming objects even when the metallicity is wrong.

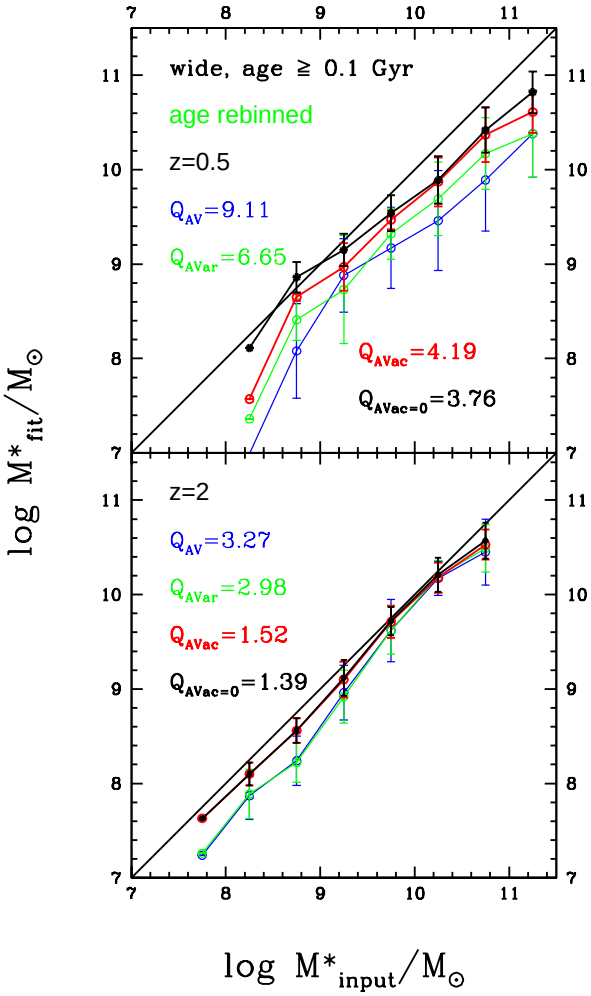

Figure 4.9: Average recovered stellar mass in given input mass bin (binsize 0.5 dex) for the wide setup with a minimum age of 0.1 Gyr and a rebinned age grid. Red points and lines represent the reddened case, black stands for the unreddened case, blue thin lines show recovered masses obtained with the full age grid including reddening, green thin lines refer to a setup with rebinned age grid and reddening. Errorbars are one standard deviation. Quality factors are given for the entire mass range.

Since the age-dust degeneracy is the main reason for underestimated ages which in turn cause underestimated masses we quantify the effect of putting a prior on the minimum age of templates in the wide setup or choosing a coarser age grid. An age restriction is often applied in the literature (Bolzonella et al., 2010; Wuyts et al., 2009) and we have also explored its effect in M10 (Section 6.1), though there we could conclude that this trick is not sufficient to ensure a correct derivation of galaxy properties and - especially - does not allow to make progress in understanding galaxy evolution. We found that among the explored age grids, a minimum age of 0.1 Gyr improves the mass estimate the most

(Fig. 4.9)[6]. The resulting regulation of both the overshining and the age-dust degeneracy is particularly effective for the oldest galaxies (at low redshift) and in the reddened case. Here, the improvement is 0.4 dex on average, but can be much larger for single objects. Especially, at $z > 1$ stellar masses are remarkably well recovered with this artificial age constraint. Hence, if one is merely interested in estimating the stellar mass setting an artificial age constraint appears to be a good idea. We found that switching off reddening and applying a minimum age cut has similar effects.

The difference in the stellar mass recovery when one uses an incorrect IMF is small (Fig. 4.10). Cases for different IMFs differ the most at $z = 0.5$ for the reddened case - a clear effect of the age-dust degeneracy. A top-heavy IMF - the most discrepant to a Salpeter IMF - fails to reproduce the correct stellar mass (Fig. 4.11). At each redshift we find a large scatter around the true masses. However, there is no clear offset between these IMFs[7] (even without dust) for galaxies with little star formation, unlike commonly assumed in the literature. This demonstrates that other free parameters in the fitting, such as age and SFH are able to compensate for the wrong IMF. For young galaxies with high star formation an offset exists. Bolzonella et al. (2010) state statistical differences of stellar mass between the various IMFs as $log\, M^*_{Salpeter} \simeq log\, M^*_x + y$ with $y = 0.23$ and 0.19 for Chabrier and Kroupa IMF (x), respectively, but acknowledge that the best fit value for other parameters can significantly differ. We list our scaling relations in section 4.9.

Although Figs. 4.10 and 4.11 show that the choice of the IMF is felt in the fit and the correct IMF recovers masses best, the right IMF cannot be identified by choosing the fit with the minimum χ^2_ν among all solutions. In fact, very often even a top-heavy IMF is picked. This confirms again that the minimum χ^2_ν does not necessarily provide the best physical solution and confirms the notion that picking up the IMF from SED-fits is virtually impossible.

We focus now on the effect of the assumed wavelength coverage in the fitting, on stellar masses for the wide setup at each redshift and the inverted-τ models at redshift 2 (Figs. 4.12 and 4.13). The dependence on wavelength coverage is weak for old galaxies with little on-going star formation at $z = 0.5$ - masses are similarly underestimated for each filter setup[8]. This is obviously driven by the overshining and the wrong SFH which the filter setup cannot help rectifying. For $z > 1$, where galaxies are younger and the SFR

[6] We have also explored larger minimum ages - 0.5, 1 and 5 Gyr - for $z = 0.5$ star-forming galaxies and found that these have a negative effect on the mass estimate.

[7] For verification we used the entire merger tree, but in Fig. 4.11 only show the sample of 100 galaxies.

[8] Note that excluding SSPs in the fitting setup improves the mass estimate in the reddened case by ~ 0.2 dex for the various filter setups. In the unreddened case the improvement is not significant.

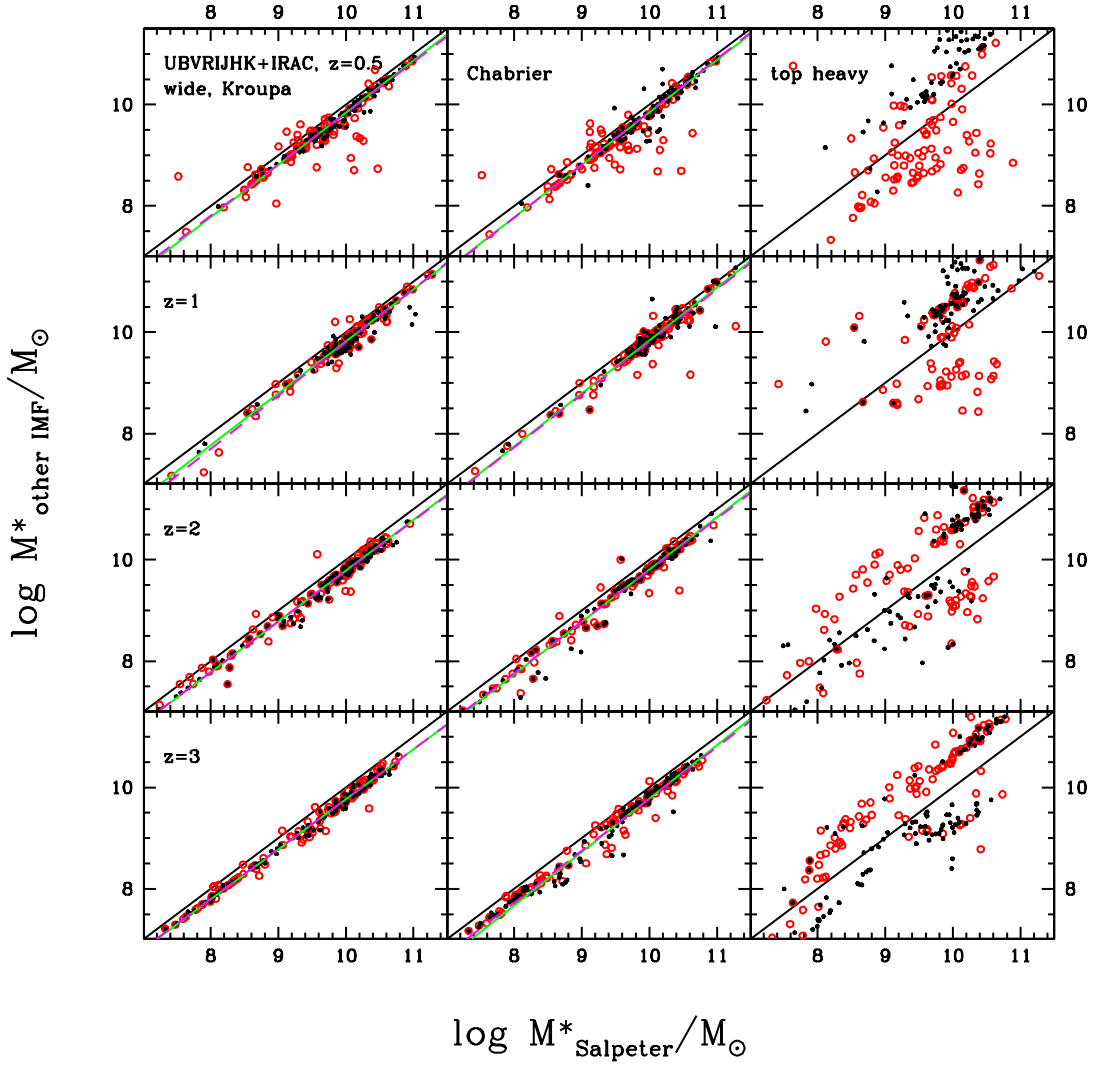

Figure 4.10: Stellar masses of mock star-forming galaxies derived using templates with IMFs different from the input Salpeter IMF. Red marks solutions obtained with reddening, black the unreddened case. Green solid lines represent fits to the unreddened case, magenta dashed lines fits to the reddened case. There is little difference between them (see also tables 4.3 and 4.4). For obtaining scaling relations we used the entire merger tree for the linear fits. The coefficients of the fits are provided in section 4.9.

is higher, we find that the broader the wavelength coverage, the better the mass recovery, particularly when reddening is involved. When red filter bands are excluded in the fit, masses are underestimated by up to 2 dex. The coverage of the rest-frame near-IR appears to be crucial - as concluded in M06. The same conclusion was reached by Kannappan & Gawiser (2007); Bolzonella et al. (2010) and Lee et al. (2009). Shapley et al. (2005),van der Wel et al. (2006) conclude the opposite. Muzzin et al. (2009) merely find an improvement in the confidence levels for the derived parameters when including

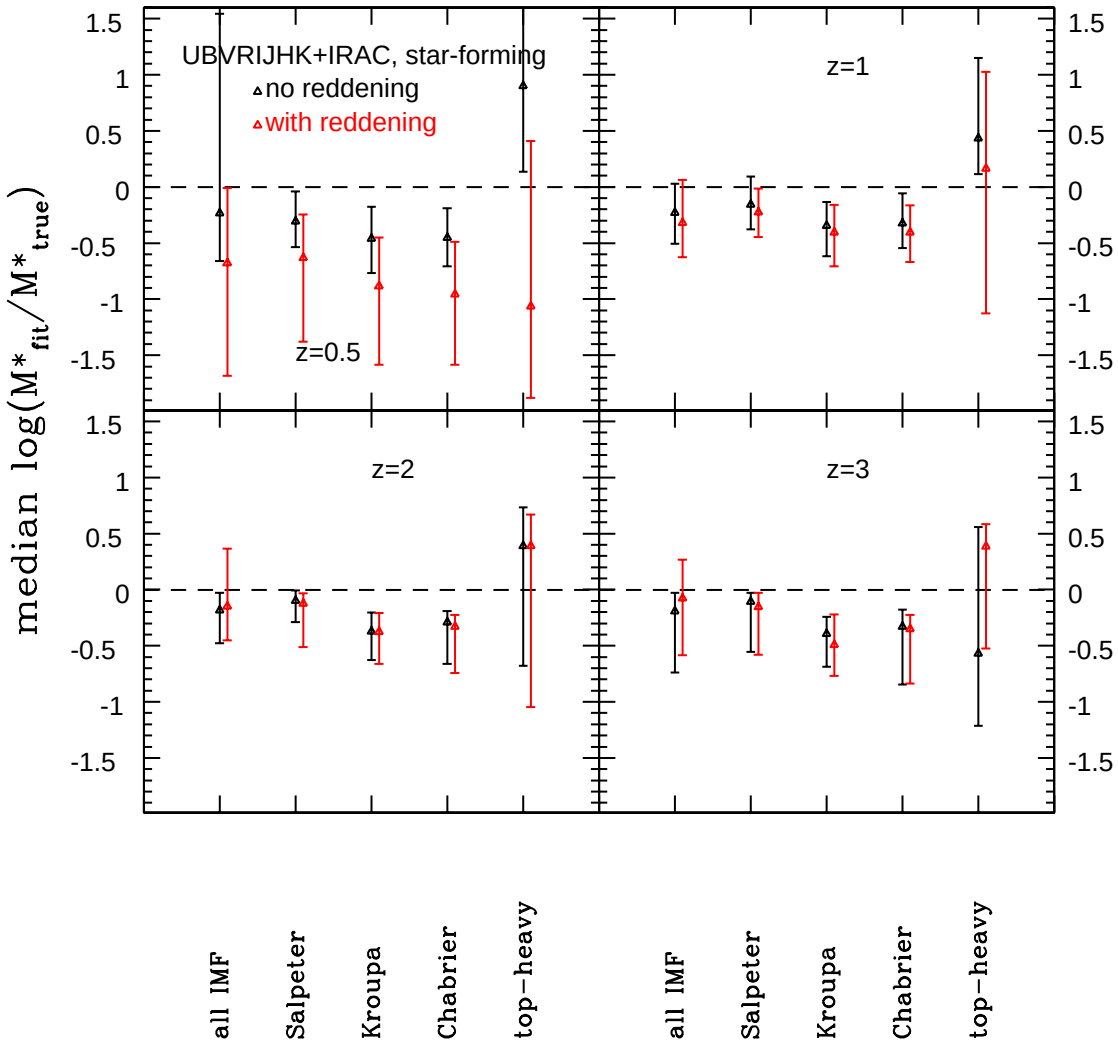

Figure 4.11: Median stellar mass recovery as a function of redshift and IMF (wide template setup and UBVRIJHK+IRAC wavelength coverage for each). 68% confidence levels are shown as error bars. Redshift increases from the top left to the bottom right. Red and black mark solutions obtained with and without reddening, respectively.

the rest-frame near-IR. Pozzetti et al. (2007) (for $z > 1$) and Walcher et al. (2008) (for $z < 1.2$) find that the lack of near-IR filter bands (observed-frame) in the fit leads to larger stellar masses compared to estimates which included them. We find a decrease instead. We assign this different behaviour to the differences in stellar population model and SFHs used in the fitting setup. For $z \geq 2$ we find that excluding filter bands covering the rest-frame UV allows one to recover stellar masses on average equally as well as the full filter set. Whereas the near-IR contains information from older, less luminous stellar populations and allows us to get a robust estimate on stellar mass, the UV contains mostly information about younger, more recently formed stellar populations. Hence, for

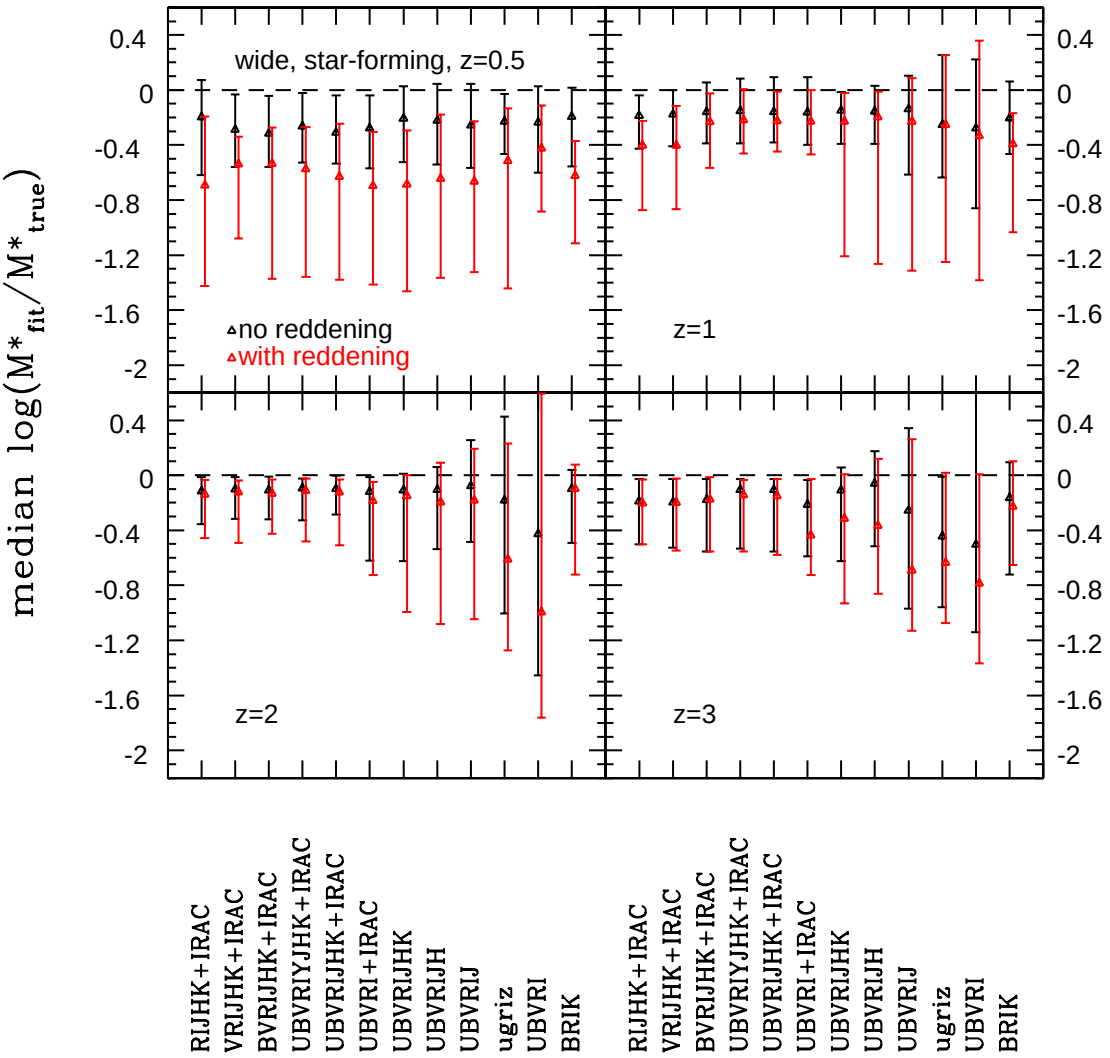

Figure 4.12: Stellar mass recovery (median) of star-forming galaxies as a function of wavelength coverage and filter set at redshifts 0.5, 1, 2 and 3, for the wide template setup. The filter setup is varied from left to right in each panel, redshift increases from top left to bottom right. Red represents reddened solutions, black unreddened ones. 68% confidence levels for each setup are shown.

a good stellar mass recovery, the bluest filter bands are less important and may even be damaging. Clearly, a filter setup that only covers the rest-frame UV is useless for the mass recovery of high redshift galaxies. Remarkably, the combination of optical (BRI) and only one near-IR filter (K) recovers masses reasonably well. This could be useful for economising the request of telescope time. The inclusion of a further filter band (Y with $\lambda_{eff} \sim 10,000$ Å) does not improve the stellar mass estimate independently of redshift and reddening. In general, the mass recovery at redshifts $z \geq 1$ is extremely good, provided one uses a filter set that covers the rest-frame near-IR because this helps to pick the

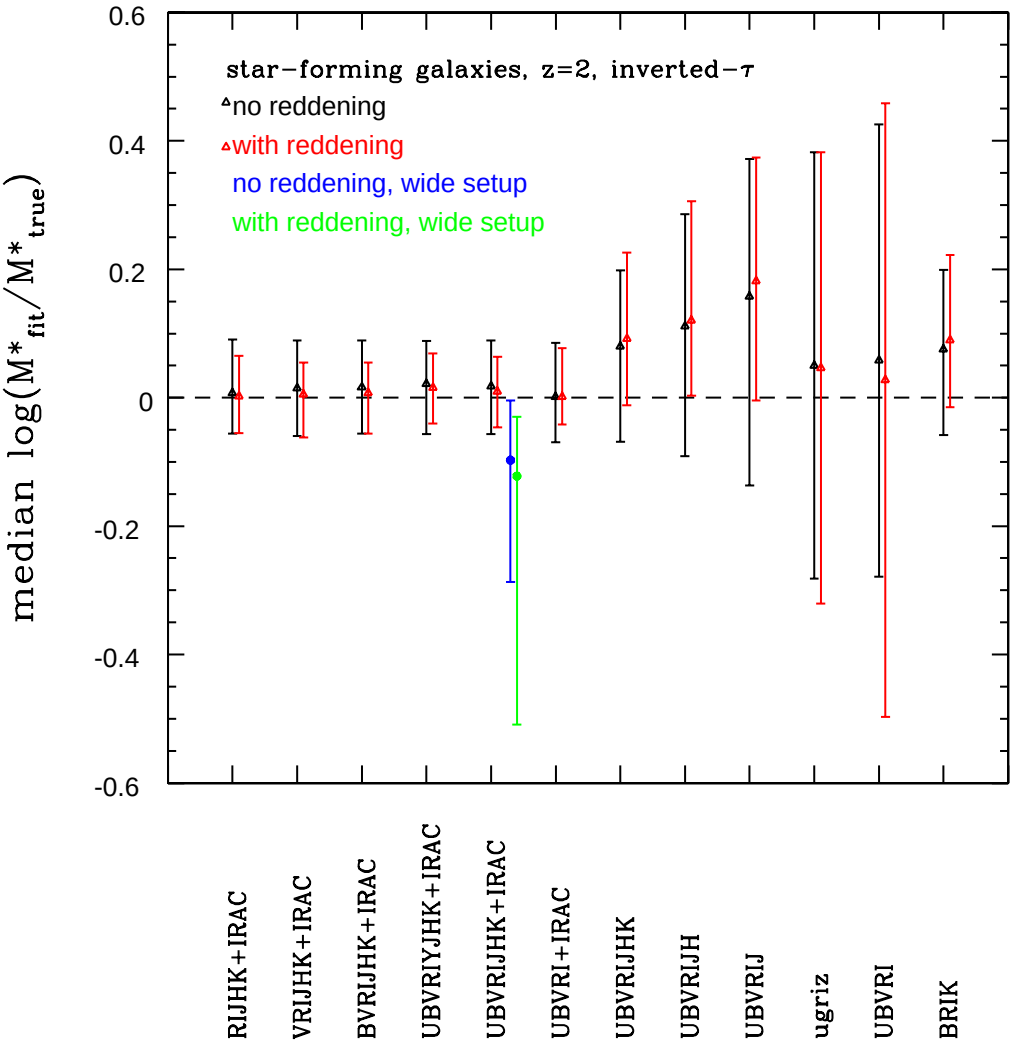

Figure 4.13: Median differences between true and recovered stellar mass as function of wavelength coverage and filter set for the inverted-τ templates at redshift 2. The blue and green symbols refer to the mass recovery obtained with the wide setup without and with reddening, respectively.

right star formation history (see M05).

In M10 (Section 6.1) we showed that inverted-τ models recover the stellar masses of high redshift star-forming galaxies best. We show here (Fig. 4.13) that this is robust against variations in filter setup because this model is less dependent on age. Only for the most restricted wavelength ranges and those without rest-frame near-IR a significant scatter around the true masses is found.

As a summary of this whole section, the stellar masses of old galaxies with little residual star formation are usually underestimated because ages are underestimated which in turn is due to a mismatch in SFH between template and galaxy and the overshining effect. This effect is worse when dust reddening is included because of the age-dust degeneracy. This depends only very little on metallicity and wavelength coverage. An artificial age constraint improves the mass estimation. The masses of young galaxies with high star formation are slightly underestimated when age is a free parameter in the fit. Masses are perfectly recovered with inverted-τ templates with proper priors on formation epochs and τ, as shown in M10 (Section 6.1). Dust reddening and metallicity affect the whole result very little. Masses are increasingly underestimated for narrower wavelength coverages when the wide setup is used. Here, the rest-frame near-IR is crucial for a robust mass estimate. Masses derived using inverted-τ models are less sensitive to wavelength coverage. Overall, a wide wavelength coverage also implies a smaller scatter. The SED-fit and the mass estimate is sensitive to the choice of IMF of the fitting template, but the correct IMF cannot be identified by means of the overall minimum χ^2_ν.

4.3.5 Star formation history and star formation rate

Fig. 4.14 shows that - similarly to stellar masses - SFRs agree very well with input SFRs only when reddening is switched off. This is nearly independent of template setup. When reddening is involved, however, SFR are drastically overestimated at $z \leq 1$. As was shown in M10 (Section 6.1), such very high star formation rates in combination with low stellar masses are a pure artefact of SED-fitting. The inverted-τ setup allows for the best estimates. The wide setup reproduces the SFR best at $z = 1$ but this may just be due to the particular composition of the mock galaxies at these redshifts. At redshift 3 for the wide and only-τ setup SFRs are also underestimated at the high SFR end because of SFH mismatches. Low SFRs are overestimated for the same reason. The inverted-τ setup can recover the SFRs well for objects with increasing SFH. In M10 (Section 6.1) we showed that SFRs derived from inverted$-\tau$ models are in excellent agreement with those derived with the UV-corrected-slope method for high-redshift star-forming galaxies in the GOODS-S sample (see Fig. 19 in M10). Note that in M10 (Section 6.1) we used only the Calzetti reddening law in the fit while in this chapter we show SFRs that are derived with all reddening laws which results in small differences in SFR for some objects.

The accuracy with which one estimates SFRs also profits from the constraint in age and the limited age-dust degeneracy. Particularly, low star formation rates are overestimated less at $z = 0.5$ (Fig. 4.15). Only allowing ages larger than 0.1 Gyr gives the best result,

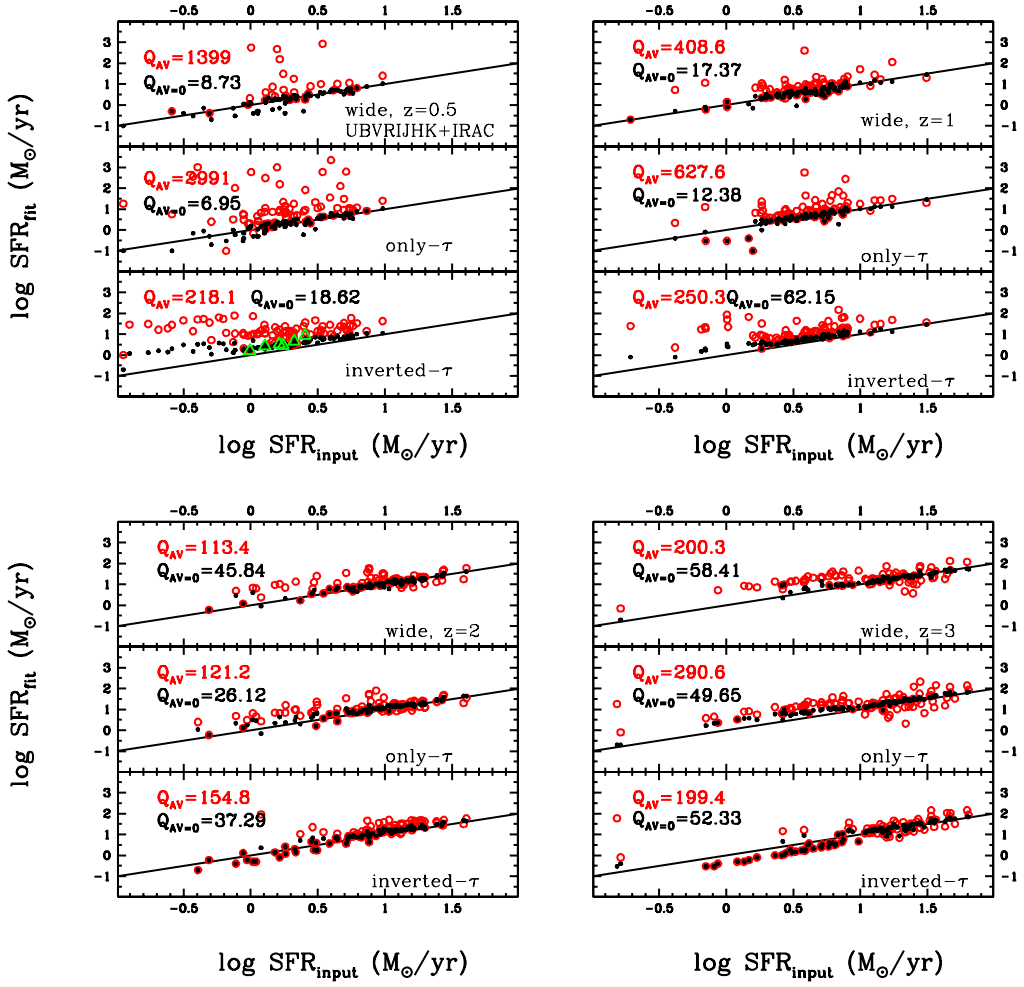

Figure 4.14: The recovery of SFR as a function of template setup, namely wide, only-τ and inverted-τ from top to bottom. Redshift increases from top left to bottom right. Red circles refer to cases with reddening, black dots to no reddening. Quality factors are given for the entire SFR range for reddened and unreddened case, respectively. Green triangles show the SFR estimate for the youngest objects at $z = 0.5$ with increasing SFH when an inverted-τ model of age 1.1 Gyr is used in the fitting. These are the same objects as in Fig. 4.7. Objects with SFR$= 0$ are not shown. SFR$= 0$ indicates that the best fit solution is an SSP or a truncated SF model with an age larger than the truncation time.

although some degree of overestimation is still present. Simply rebinning the age grid, however, does not work, SFRs are even more overestimated. At higher redshift the improvement is less than at $z = 0.5$. Again a rebinned age grid performs worse and leads to underestimation of the highest SFRs. The effect on stellar mass and SFR caused by the age constraint is the same for each template setup (excluding the inverted-τ setup

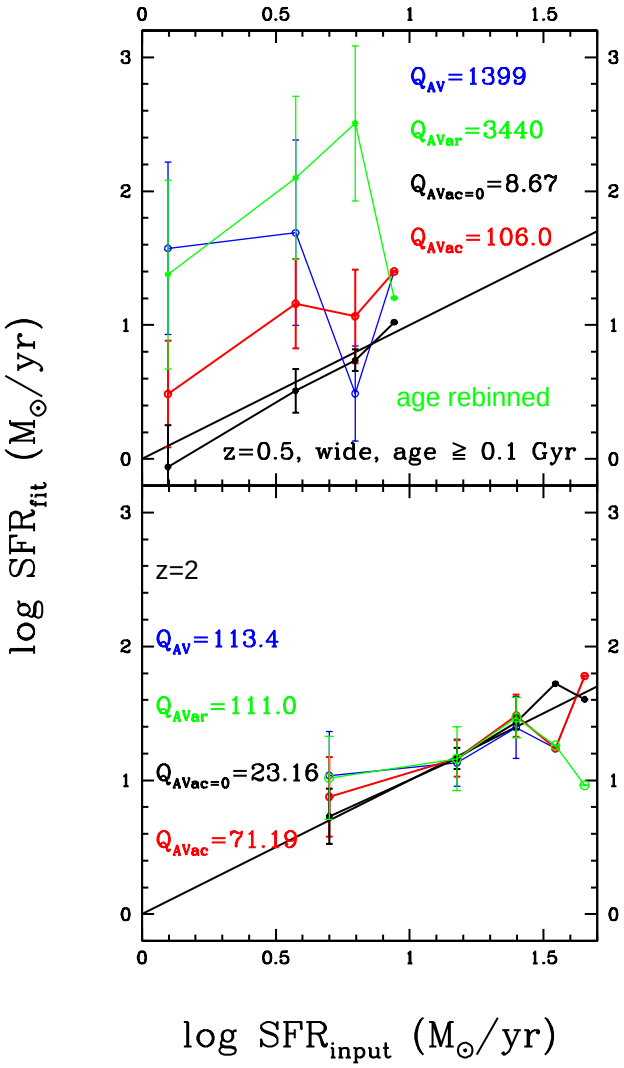

Figure 4.15: Averaged recovered SFRs (y-axis) compared to known binned SFRs (x-axis) as a function of age grid. Representatively, we show results for redshift 0.5 and 2 only. Red dots and lines represent solutions with reddening, black ones those without reddening, both when the minimum age is 0.1 Gyr. Blue thin lines show the SFR recovery with a wide setup and reddening. Green lines refer to a wide setup with rebinned age grid and reddening in the fit. Binsizes vary from $2.5\,M_{\odot}$/yr to $20\,M_{\odot}$/yr from $z = 0.5$ to $z = 3$. Errorbars are one standard deviation. Quality factors are given for the entire SFR range for reddened and unreddened cases, respectively.

because its age is fixed).

SFR estimates using templates with a Kroupa or a Chabrier IMF instead of a Salpeter IMF show qualitatively the same behaviour (in the case with reddening). In the unreddened case SFRs are predicted correctly from fits with these three IMFs. In Fig. 4.16 we

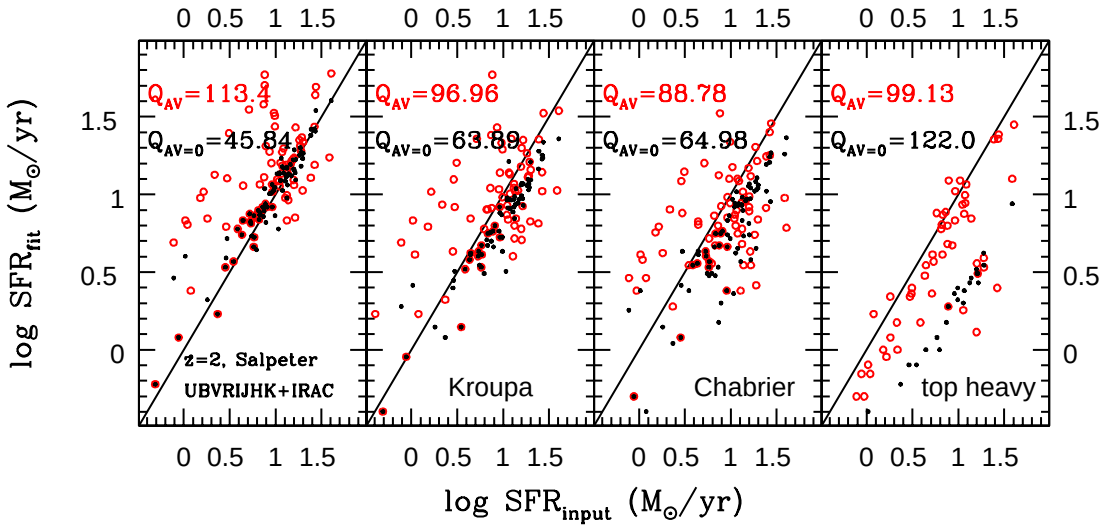

Figure 4.16: SFR recovery as a function of template IMF at redshift 2. Colours are the same as in Fig. 4.28. SFR$=0$ cases are not shown in this plot.

show the star formation rates derived with a Salpeter, Kroupa, Chabrier and top-heavy IMF for redshift 2 galaxies as an example. SFRs for a top-heavy IMF are generally lower than SFRs for a Salpeter IMF and also lower than the true value. This leads to a clear offset in the no reddening case, independently of redshift. When reddening is included, SFRs increase as the age decreases.

Fig. 4.17 demonstrates the effect of wavelength coverage (or lack thereof) on the determination of the star formation rate. SFRs are generally well recovered in the unreddened case partly because of compensating effects. Deviations from this are due to a lack in wavelength coverage (RIJHK+IRAC at $z = 3$). In the reddened case SFRs are overestimated at almost all redshifts. While the mass recovery is nearly insensitive to the neglection of blue filter bands, the SFR estimate is hampered. This is not surprising since the most recently formed stars dominate the light emission in the UV which therefore plays an important role in the estimation of SFRs. At $z = 3$ SFRs are also underestimated at the high end. In the reddened case, SFRs are best recovered with filter setups that cover the broadest wavelength range, while in the unreddened case a dependence with wavelength coverage is negligible. We show the derived SFRs from inverted-τ models in Fig. 4.18 for a selection of filter setups. Similarly to the mass derivation, the

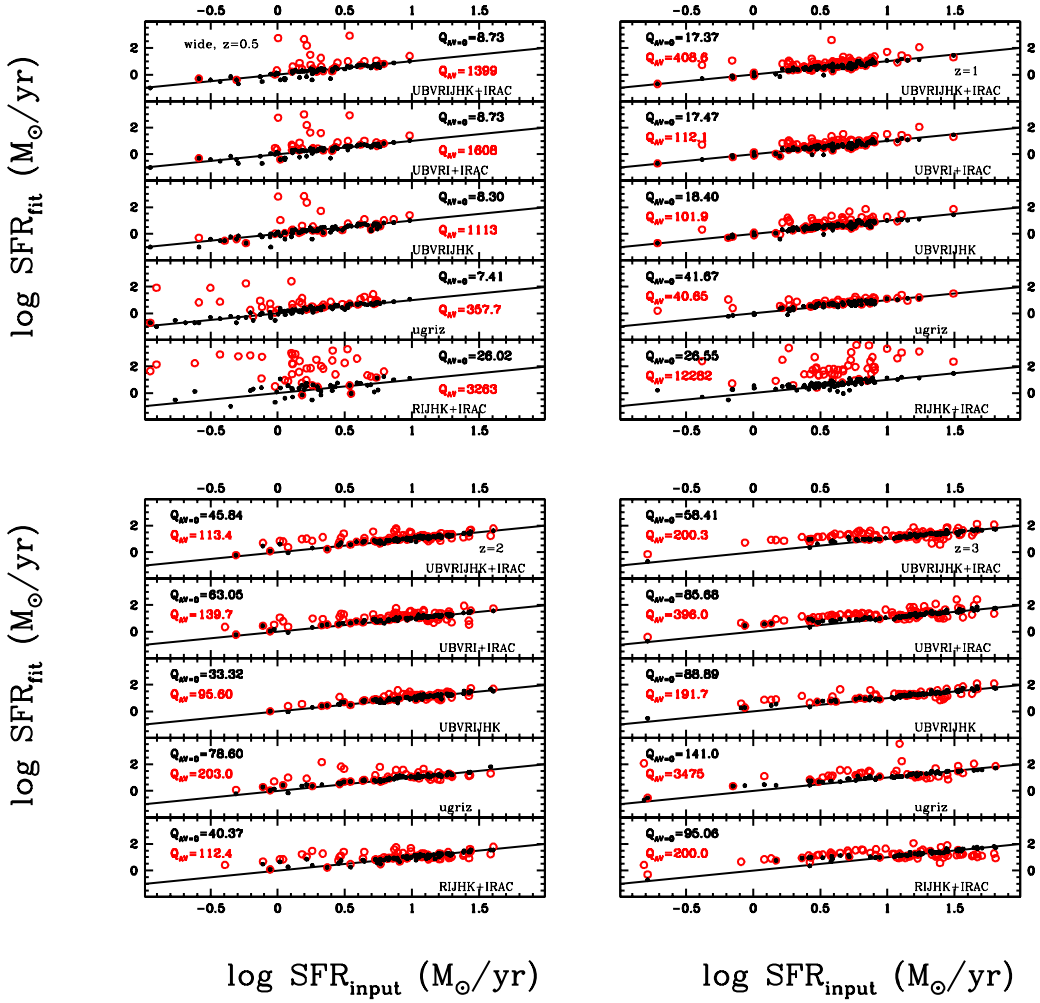

Figure 4.17: SFR recovery as a function of wavelength coverage and redshift (increasing from top left to bottom right). The filter setup is varied from top to bottom in each panel. Objects with SFR$= 0$ are best fit with a SSP or a truncated model with age larger than the truncation time and are not shown in this plot. Red circles refer to the reddened case, black dots to the unreddened case.

SFR estimates do not differ much with filter setup and wavelength coverage. SFRs are very well reproduced in the unreddened case. In the reddened case, SFRs are overestimated for all filter setups when SFHs between mock galaxy and template does not match.

As already concluded in M10 (Section 6.1), the SFR determination is driven by the correct SFH. The good SFR recovery in the unreddened case at $z = 0.5$ despite the mismatch in SFH is due to compensating effects with underestimated ages and stellar masses. This again reinforces our conclusion, that the *simultaneous* recovery of mass, age, SFR, etc.

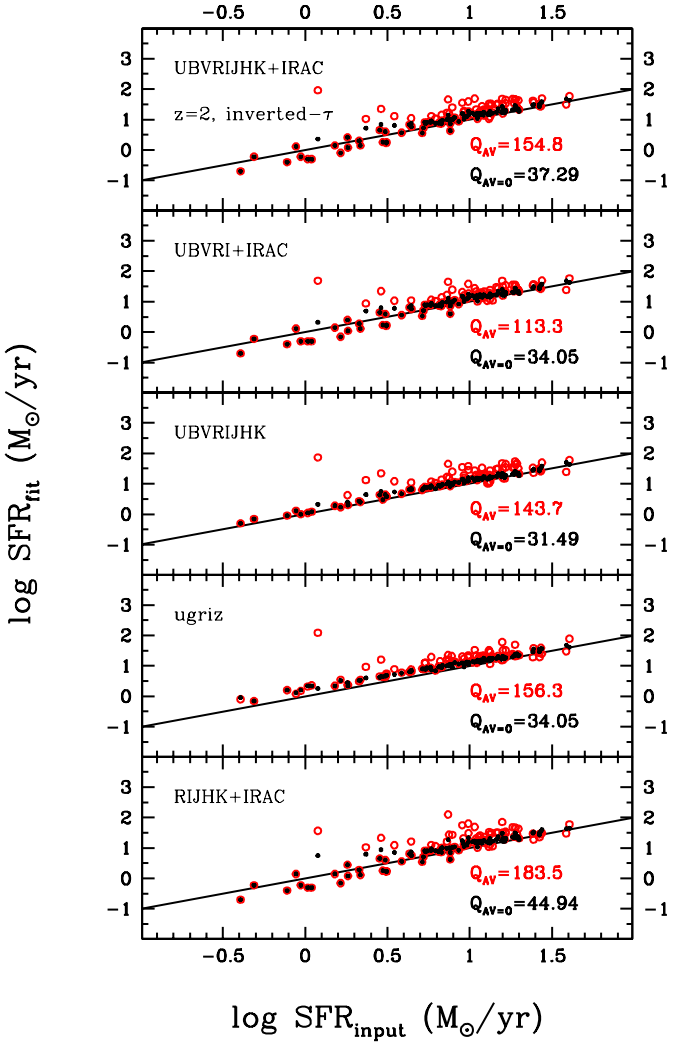

Figure 4.18: SFR recovery using inverted-τ models for mock star-forming galaxies at redshift 2 as a function of wavelength coverage. The filter setup is varied from top to bottom. Red circles are with reddening, black dots are without reddening.

for galaxies from SED-fitting is not possible without knowing the exact star formation history.

4.4 Results for passive galaxies

4.4.1 Age

Fig. 4.19 shows the age recovery of mock passive galaxies as a function of template setup for wide, only-τ, only SSPs (but all four metallicities) and only solar SSP template setups.

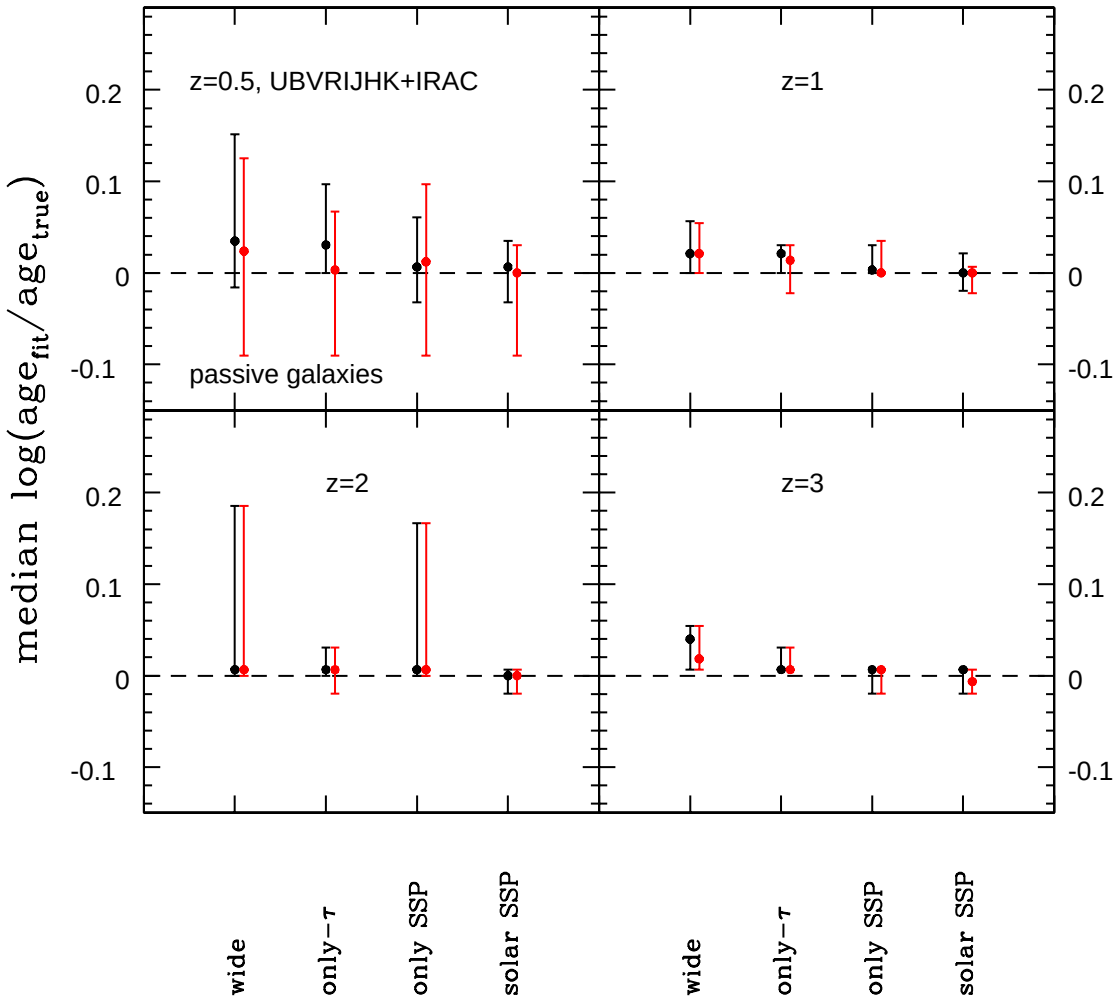

Figure 4.19: Median recovery of age for mock passive galaxies as a function of redshift and template setup. Black and red symbols refer to the cases without and with reddening, respectively. 68% confidence levels are shown.

Overall, the age determination is much better than was the case for star-forming galaxies (Fig. 4.2). A wider range of star formation histories and metallicities in the fitting leads to generally overestimated ages in the unreddened case at redshifts 0.5 and 1 with the mismatched SFH as the biggest driving factor. Overall, the age recovery improves with templates with the correct metallicity (i.e. only-τ and solar SSP). Additionally, matching the SFH correctly recovers the age best. Small deviations from the true age still occur when fitting with the correct template for two reasons: 1) a slight mismatch in age between template age grid and galaxy age[9] and 2) photometric uncertainties. Since the

[9]For ages of 1 and 1.5 Gyr the closest matching age of the template age grids are 1.015 Gyr and 1.434 Gyr.

choice of SFH is limited in the only-τ setup and the metallicity is the correct one, short τ's which resemble a SSP closest are chosen. The longer period of star formation is then compensated by an older age. Within the wide setup a variety of SFHs exists besides the correct solution of a solar metallicity SSP. Both τ and truncated models closely resemble a SSP as long as the timescale τ for star formation or truncation time t are short enough compared to the age. The differences between them are smaller than the imposed photometric uncertainties. Furthermore, a wider variety of metallicities is available. Thus, it is not surprising that the age-metallicity degeneracy and a degeneracy between age and SFH cause the average recovered age to be slightly older than for the only-τ setup and that the dispersion is larger. The median offset in age for the wide setup is maximally ~ 0.04 dex. Comparing results for the only-SSP and solar-SSP setups - thus using the correct SFH - enables us to isolate the effect of the age-metallicity degeneracy. This is small on the median, but the scatter induced by using wrong metallicities is much larger. Similarly to the mock star-forming galaxies, including reddening in the fit has the largest effect for the oldest galaxies ($z = 0.5$) due to the age-dust degeneracy. But overall, the effect of reddening is small.

Another way to decouple metallicity from SFH effects is to use mono-metallicity wide setups for which we show the results in Fig. 4.20. Obviously, ages derived with a solar metallicity setup are best recovered. The remaining scatter of $0.05 - 0.1$ dex stems from the SFH mismatch. Template setups with sub-solar metallicity overestimate the age to compensate their bluer colour. For the lowest metallicity, every galaxy is fit with the maximum age possible at the given redshift (or close to that age) in order to compensate the underestimated metallicity. In addition, all χ^2_ν are larger than 2, most are larger than 10, and fits are getting worse towards higher redshift. Clearly, neither age nor SFH can compensate such a large discrepancy in metallicity. The situation is reversed for super-solar metallicity templates. At low redshift the scatter is largest because the covered age range is wider. Ages around 1 Gyr are very well defined by the TP-AGB emission, older ages are more difficult to distinguish because of little evolution in the colours during the RGB-dominated epoch. The introduction of reddening has the largest impact at low redshift. Particularly at $z = 1$ the age-dust degeneracy partly compensates and reverses the effect of the age-metallicity degeneracy and causes an underestimation in age. At high redshift, reddening has no impact. Most importantly Fig. 4.20 shows that even when using all metallicities ages and metallicities are very well recovered. This means that when we do not know the metallicity it is better to use a wide range for it, as concluded in M06.

Mismatches in the IMF have rather small effects for the mock passive galaxies which is why we do not show it. Ages derived with different IMFs are similarly well recovered

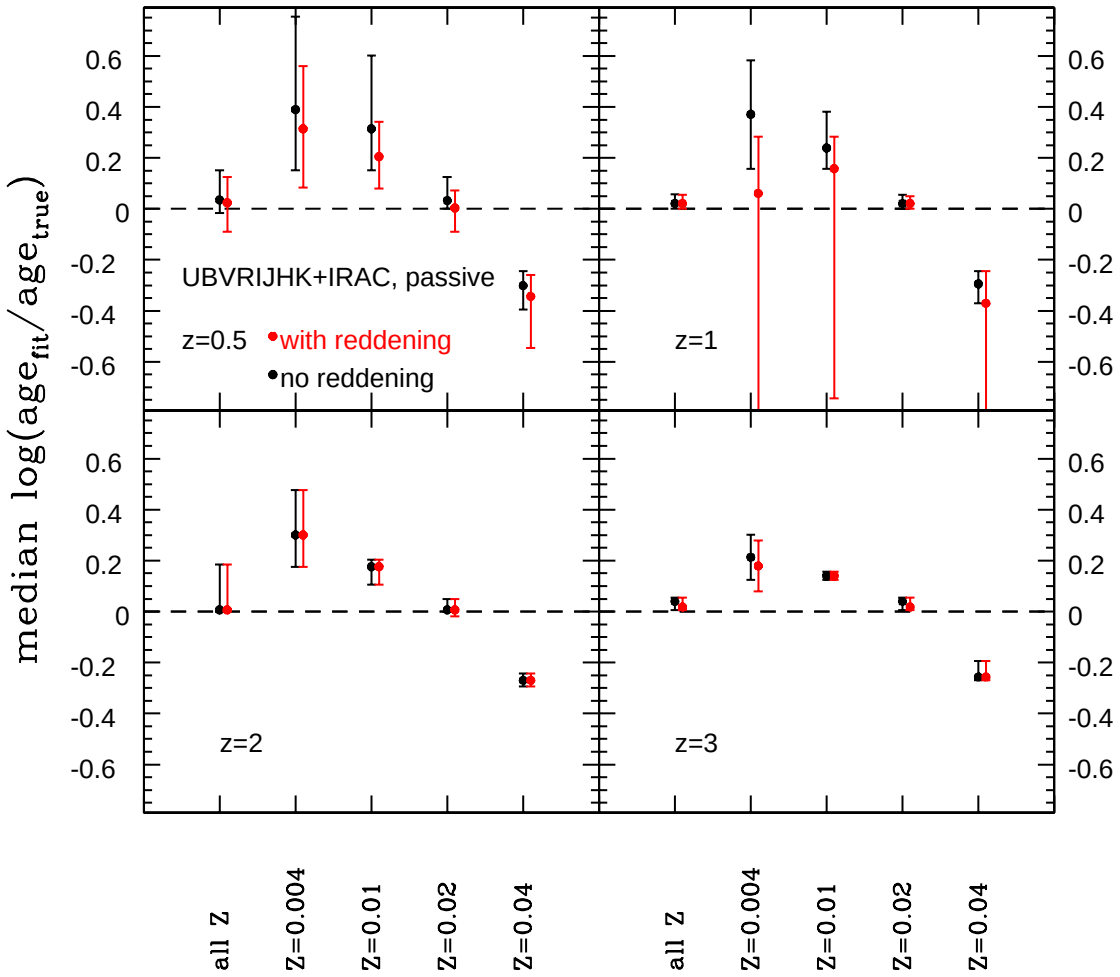

Figure 4.20: Median deviation of fitted age from true age of mock passive galaxies as a function of redshift and metallicity. Black dots and 68% confidence levels refer to the unreddened case, red to the case that includes reddening in the fit.

and do not show an offset between each other because differences in SED-shape due to the IMF are small for intermediate-mass stars, hence intermediate and old ages. The scatter increases for the oldest galaxies. The effect of reddening is negligible.

We investigate the wavelength dependence of the derived ages using a wide setup in Fig. 4.21. Median ages are recovered within ± 0.1 dex in the unreddened case with little dependence on the wavelength coverage at low redshift. At higher redshift filter setups that do not cover the rest-frame near-IR and the red part of the optical generate a larger scatter. As already mentioned, the mock passive galaxies at these redshifts are $1 - 2$ Gyr

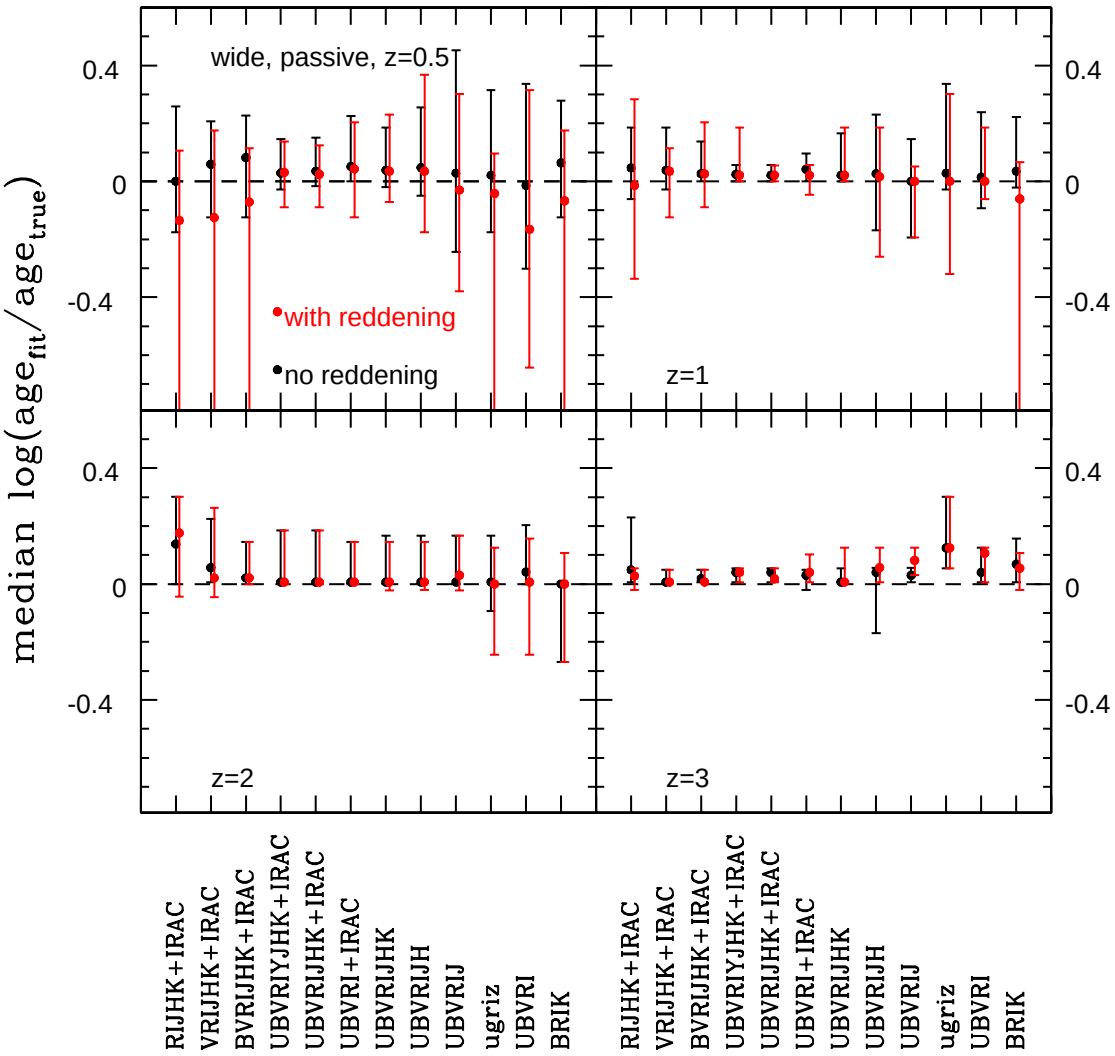

Figure 4.21: Median deviation of fitted age from true ages of mock passive galaxies as a function of wavelength coverage at redshifts from 0.5 to 3 using the wide setup. Black dots and 68% confidence levels refer to the unreddened case, red to the case that includes reddening in the fit.

old, the age range in which the near-IR is dominated by the TP-AGB emission. Without this crucial information, the fit is more prone to degeneracies between age, metallicity and SFH. Interestingly, a filter setup containing only four filter bands but including the near-IR and thus sampling the SED shape over a wider wavelength range, performs in most cases equally as good as other filter sets. The lack of rest-frame UV data at $z = 2$ and 3, causes ages to be overestimated because of star formation history mismatches. The inclusion of reddening in the fit has its biggest impact at low redshift. Here the age-dust-degeneracy causes a large scatter and an on average underestimated age for shorter wavelength coverages. Particularly, the large scatter shows that the age recovery fails

when the information of the blue and reddest filter bands is missing. Overall, ages are best derived with the full wavelength coverage. Compared to star-forming galaxies, ages of passive galaxies can be better determined in the fit due to a well-defined 4000 Å break and the absence of multiple generations.

In summary, mismatches in SFHs are contributing the most to an offset in the derived ages. Thus the best SFHs for passive galaxies are SSPs and exponentially declining SFRs. As metallicity can be recovered (see also section 4.4.2), SED templates should cover a range in metallicities. Ages are best determined using the full wavelength coverage. Note that a *ugriz* filter setup at $z \sim 0.5$ performs well, albeit with larger scatter, which is mostly due to the low number of objects. This is an important finding as we are obtaining galaxy properties (stellar masses in particular) of BOSS (Baryon Oscillation Spectroscopic Survey) galaxies using this setup (Maraston et al. *in prep.*, Section 6.2).

4.4.2 Metallicity

For nearly passive objects at $z \sim 2$, M06 found that metallicity plays an important role in allowing a robust determination of the stellar population parameters. We confirm this result in section 4.4.1. Although a wide choice of metallicities is provided, the fit closely recovers the true metallicity for most objects (Fig. 4.22). When reddening is introduced, the age-dust-metallicity degeneracy affects mostly the oldest galaxies (at low redshift).

Derived metallicities depend on the wavelength coverage in the fitting such that at low redshift a lack of rest-frame near-IR and red optical coverage causes metallicities to be overestimated in more cases, clearly, by compensating underestimated ages. The rest-frame near-IR is crucial in breaking the age-metallicity degeneracy as already concluded in M06. When blue filter bands are excluded metallicities are underestimated for a few more objects. These effects are smaller at higher redshift. Including reddening results in underestimation of metallicity for more objects when the wavelength coverage is restricted. Again the effect is largest at low redshift.

In conclusion, for nearly passive and aged galaxies it is important to fit with a wide choice of metallicities because metallicity can be recovered. The best template setup for metallicity recovery is the wide setup. The broadest wavelength coverage results in the best metallicity estimates.

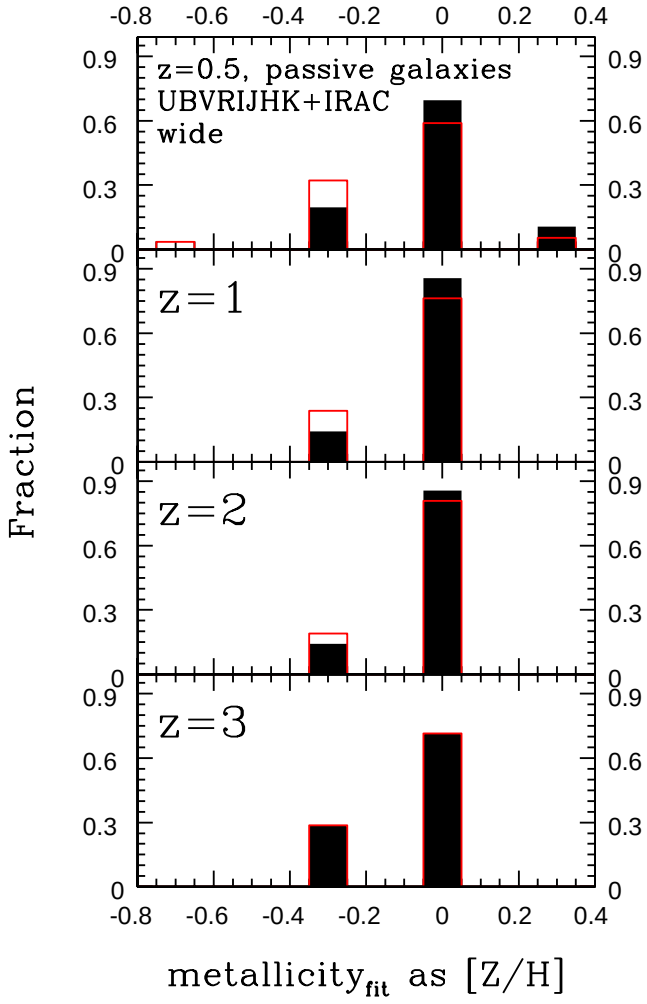

Figure 4.22: Recovered metallicities of mock passive galaxies at redshifts from 0.5 to 3. Black and red are without and with reddening, respectively.

4.4.3 E(B-V)

Since we did not add reddening to the passive galaxies, any reddening resulting from the fitting procedure is overestimated. But generally, the reddening is correctly identified for most objects (Fig. 4.23). Independently of template setup, the largest effect is found at low redshift where the age-dust degeneracy is more efficient as the allowed age range is larger.

More objects are wrongly identified to be reddened as wavelength coverage decreases (in both red and blue wavelength) but the effect is small.

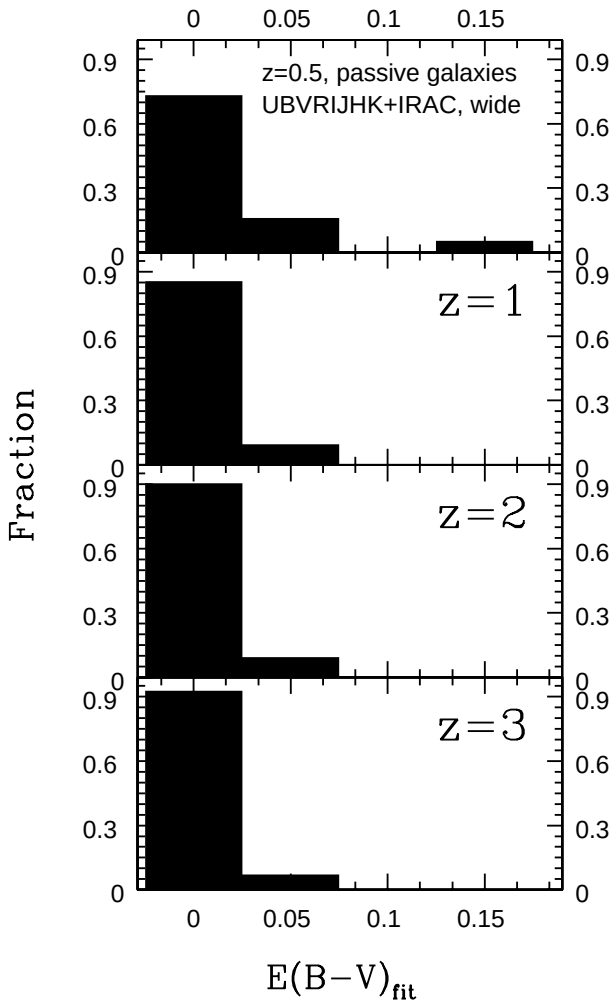

Figure 4.23: Recovered $E(B-V)$ of mock passive galaxies at redshifts from 0.5 to 3.

4.4.4 Stellar Mass

The mass recovery for the mock passive galaxies is very good (Fig. 4.24) and the median offset in mass is maximally $\pm \sim 0.02$ dex for all template setups. As usual, differences between the reddened and unreddened case are small. Scatter is largest at low redshift. Deviations from the true stellar mass for the wide setup are due to degeneracies between star formation histories, metallicity, age and dust (when included in the fit). Offsets in stellar mass even when using the correct template are caused by a slight mismatch in age between template and galaxy for the youngest ages and photometric uncertainties (see also sections 4.4.1 and 4.7, respectively). When fitting with the solar metallicity SSP these small age mismatches cannot be compensated by a different choice of metallicity and SFH (or dust at high redshift). The contribution of dust increases the errors on the derived ages at low redshift because of the age-dust degeneracy. Clearly, in the other

template setups the mass is corrected by the choice of an incorrect metallicity and/or SFH and, in the reddened case, dust.

Metallicity effects are further explored in Fig. 4.25. Stellar masses follow the same trend with metallicity as ages (compare to Fig. 4.20). For lower metallicities for which ages are overestimated, stellar masses are larger. For higher metallicities masses are smaller. In the unreddened case, masses derived from the lowest metallicity template are

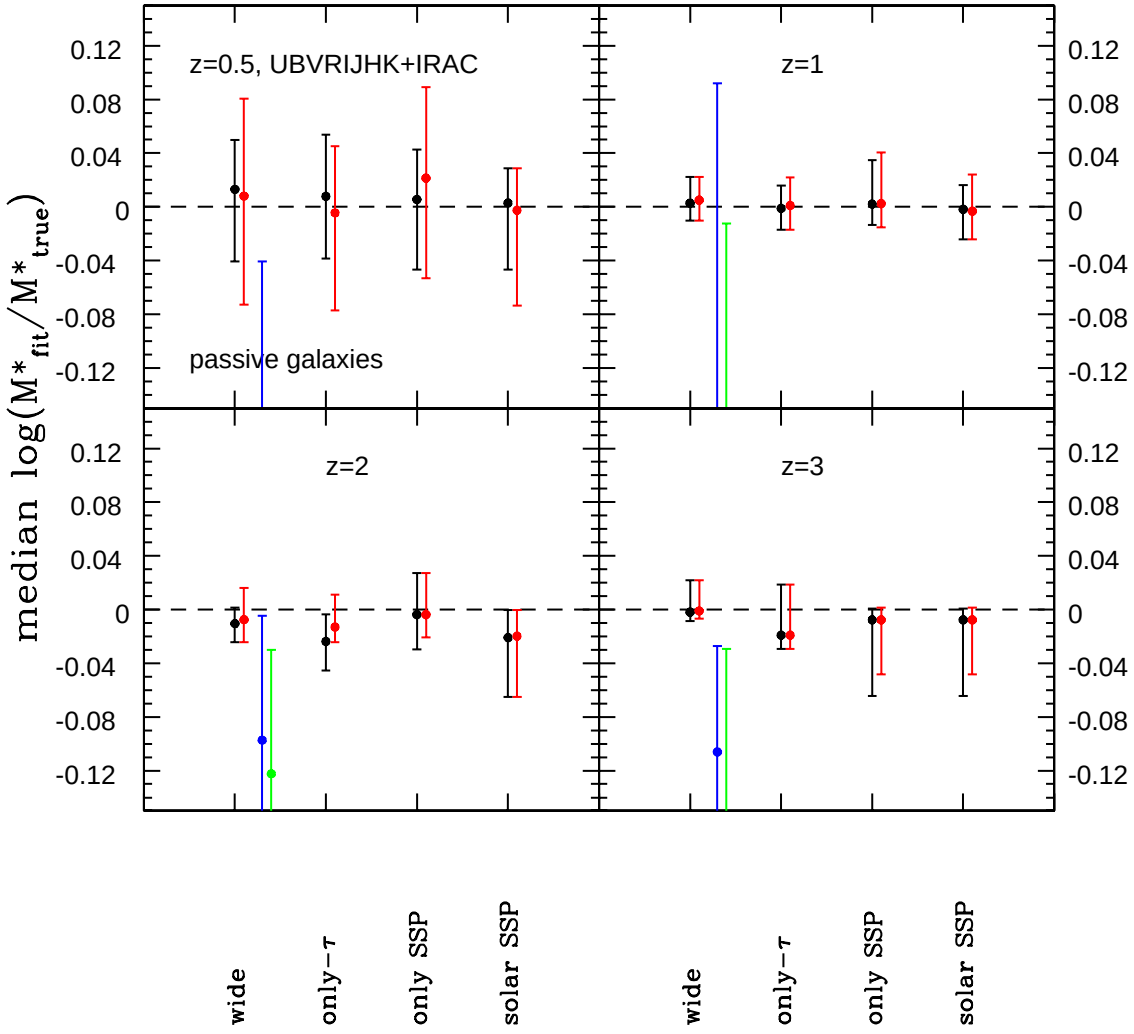

Figure 4.24: Median mass recovery of mock passive galaxies for different template setups as a function of redshift. Red dots and 68% confidence levels refer to the inclusion of reddening in the fitting, black symbols to the unreddened case. The blue and green symbols refer to the mass recovery of mock star-forming galaxies obtained with the wide setup without and with reddening, respectively (compare also points for 'all Z' in Fig. 4.8).

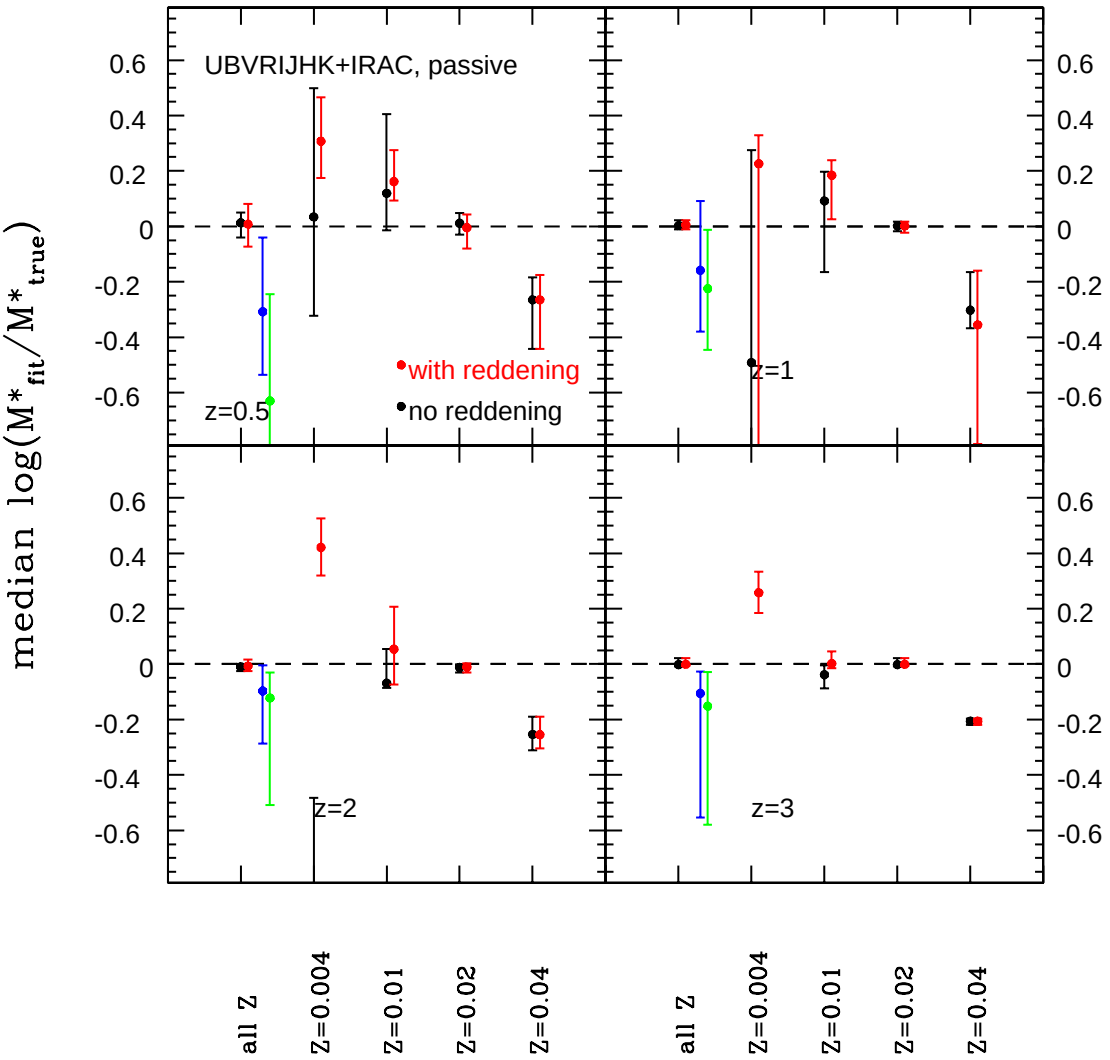

Figure 4.25: Median recovered stellar mass with 68% confidence levels for mono-metallicity wide setups as a function of redshift and therefore galaxy age (upper left to lower right). Metallicity in each panel increases from left to right. The input metallicity is solar. The missing points at Z=0.004 without reddening lie at $-1.51^{+1.03}_{-0.68}$ at $z = 2$ and at $-3.31^{+0.47}_{-0.54}$ at $z = 3$. Symbols are the same as in Fig. 4.24.

significantly underestimated as a direct consequence of the metallicity mismatch and its effect as described in Section 4.4.1. This shortcoming in metallicity can only be partly compensated by age and not at all by SFH (which would just make the SED even bluer). At $z > 0.5$ the fit with the lowest metallicity setup fails completely ($\chi^2_\nu > 50$) and masses are not recovered. Adding dust improves the fits since some of the required red colour of the observed SED can be compensated by dust but ages are still overestimated. This results in overestimated masses.

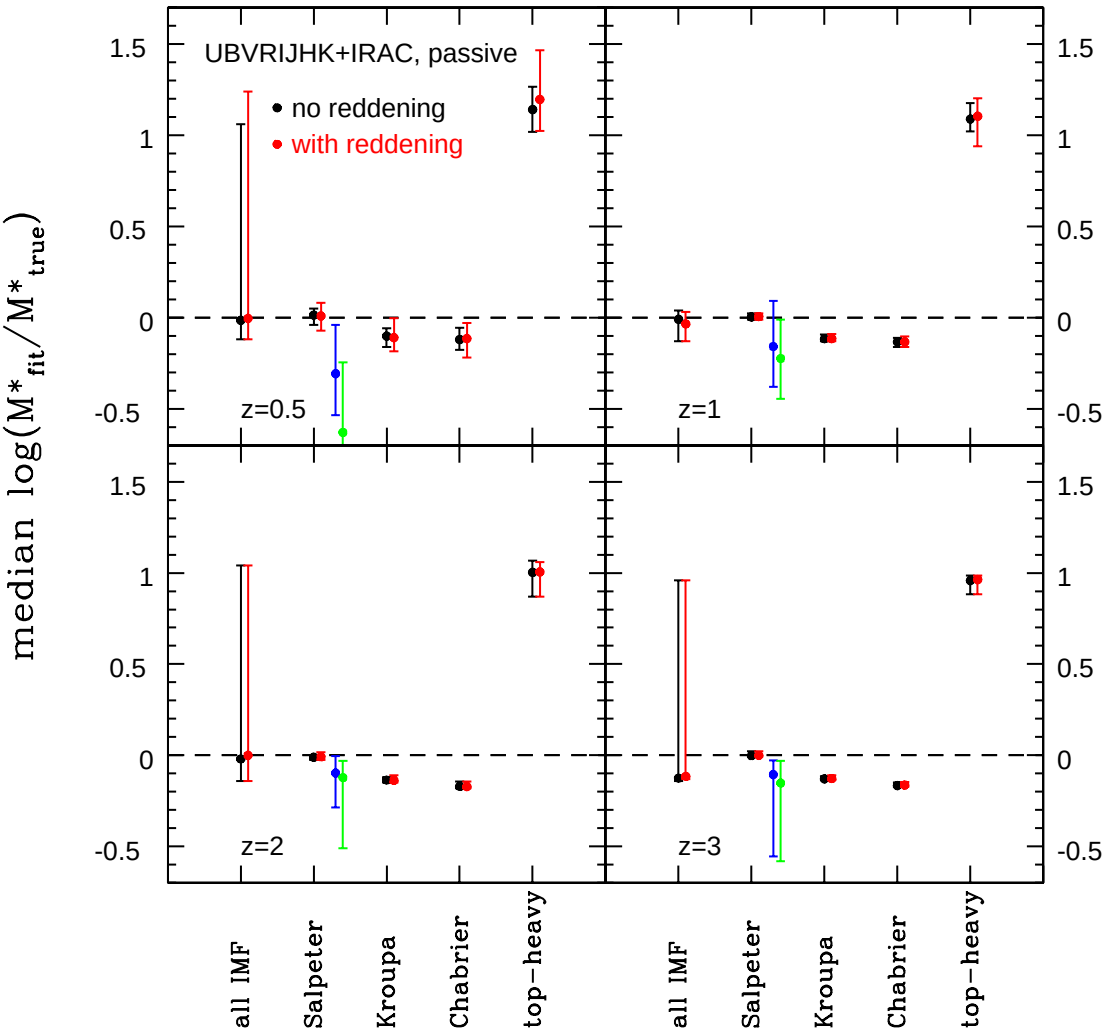

Figure 4.26: Median stellar mass recovery as a function of the IMF assumed in the fitting template for a wide template setup and UBVRIJHK+IRAC wavelength coverage. The input IMF is Salpeter. Errorbars are 68% confidence levels. Redshift increases from the top left to the bottom right. Symbols are the same as in Fig. 4.24.

Stellar masses of mock passive galaxies are best determined with a template setup based on the same IMF used as input, namely a Salpeter IMF (Fig. 4.26)[10]. Although ages derived with a Kroupa and Chabrier IMF template setup are very similar to those for the Salpeter setup, stellar masses are systematically underestimated by $\sim 0.1 - 0.2$ dex. The stellar masses obtained with a top-heavy IMF template setup on the other hand are largely overestimated (by ~ 1 dex on average). These differences can be explained with the different mass-to-light ratios (M^*/L) for the various IMFs. As show in Maraston

[10]The inclusion of dust reddening in the fitting has very little impact on these results and merely increases the scatter at lower redshift.

(1998) bottom-light IMFs have lighter M^*/L because of a lower amount of dwarf M stars whereas a top-heavy IMF is heavier because of the large amount of massive remnants. It is encouraging that the choice of IMF is felt in the fit, but an identification of the correct IMF based on the minimum χ^2_ν is not possible as shown in Fig. 4.26. The large scatter stems mainly from the top-heavy IMF. Unfortunately, no comparison can be made with the true stellar mass for real galaxies.

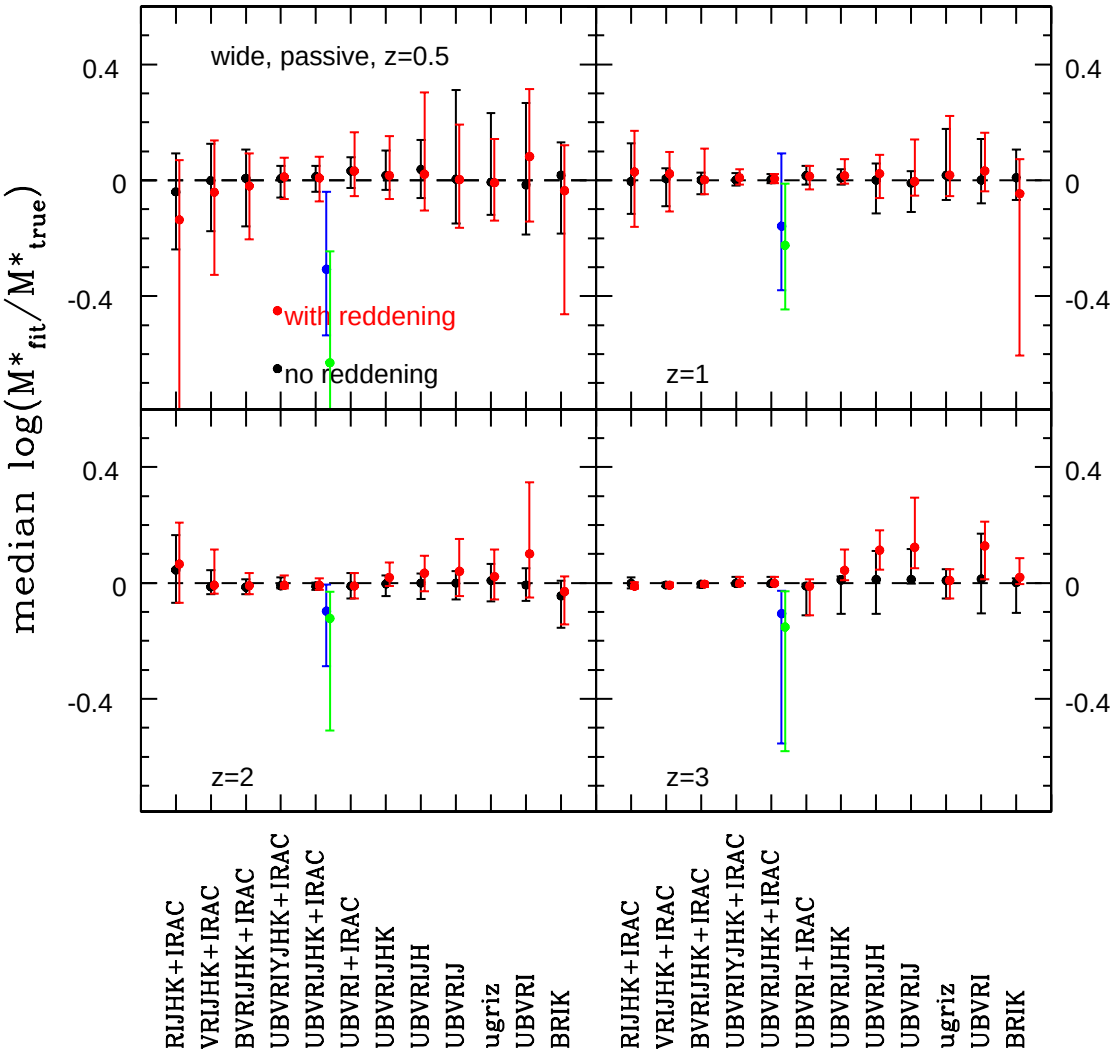

Figure 4.27: Median differences between true and recovered stellar mass as function of photometric filters used in the model fitting, at redshifts 0.5, 1, 2 and 3. The filter setup is varied from left to right in each panel, redshift increases from the top left to the bottom right. Given are the 68% confidence levels for each setup. Symbols are the same as in Fig. 4.24.

The median stellar mass recovery of passive galaxies depends little on the wavelength coverage used in the fit, but the scatter increases when fewer filter bands are used in the fitting (Fig. 4.27). Masses are best recovered with the full wavelength coverage when the rest-frame near-IR is included. Stellar masses are recovered within 0.05 dex when reddening is not included in the fit. Similar to the ages, the inclusion of reddening affects the most at low redshift where masses are underestimated for filter setups lacking blue filter bands. Towards higher redshift the exclusion of the rest-frame near-IR wavelengths in the fit introduces larger errors in the mass estimation. The information stored in the rest-frame near-IR is crucial in order to recover the right stellar mass.

In summary, stellar masses of passive galaxies can be recovered within ~ 0.02 dex for a wide coverage in metallicities, SFHs and wavelength and the exclusion of reddening in the fitting. Restricting the template setup in metallicity has the strongest effect on the mass estimate. The dependence on wavelength coverage is small though not negligible and the scatter decreases when the rest-frame near-IR is included.

4.5 Measuring the strength of the latest starburst

As widely discussed in M10 (Section 6.1) and Section 4.3, a young stellar population overshines underlying older populations. Naturally, the question arises whether the derived stellar population properties reflect those of the latest burst. For this purpose we simulated passive galaxies located at redshift 1 that consist of a large percentage of an old stellar population and a low percentage of a younger population, both with solar metallicity. The old component is 5 Gyr old, for the young component we take ages of 1 Myr, 10 Myr, 100 Myr and 1 Gyr. We combine old and young components as 99 and 1 % and 90 and 10 %. Each galaxy has a total mass of $10^{11}\ M_{\odot}$. Thus, recovered stellar masses of $10^{10}\ M_{\odot}$ and $10^{9}\ M_{\odot}$ would reflect the mass of the burst. Ages of ~ 4.5 (for 10% young) and ~ 4.95 Gyr (for 1% young) would reflect the mass-weighted age of the galaxies. The fitting is carried out using the broadest wavelength coverage and a wide setup. Results for stellar mass and age are listed in Table 4.2.

Clearly, even just one percent of a relatively younger stellar population with respect to the dominant one has the power to hide $30 - 40$% of the stellar mass locked up in old stars. When the population is just 1 Myr old it even hides nearly 99%. For these ages, the fit renders precisely the mass of the burst. When reddening is allowed in the fit, an age of 10 Myr is already young enough to hide nearly 99% of the remaining old stellar population. In both cases is the mass of the burst recovered within ~ 0.3 dex rather than the

Table 4.2: Derived ages and stellar masses for a $10^{11} M_{\odot}$ galaxy composed of a 5 Gyr old population and a low percentage - 1 or 10% - of a younger population. Burst characteristics are listed in the first column, while the second and third columns list the derived ages and masses.

Burst no reddening	derived age	derived M^* $[M_{\odot}]$
1% 1Gyr	3.75 Gyr	10.85
1% 100Myr	4.5 Gyr	10.86
1% 10Myr	4.5 Gyr	10.74
1% 1Myr	15 Myr	9.23
10% 1Gyr	2.75 Gyr	10.83
10% 100Myr	404 Myr	10.42
10% 10Myr	8.7 Myr	9.91
10% 1Myr	6.6 Myr	9.93
Burst + reddening	derived age	derived M^* $[M_{\odot}]$
1% 1Gyr	3.5 Gyr	10.90
1% 100Myr	4.5 Gyr	10.86
1% 10Myr	7.9 Myr	9.28
1% 1Myr	13.8 Myr	9.30
10% 1Gyr	2.75 Gyr	10.83
10% 100Myr	6.3 Myr	9.69
10% 10Myr	8.7 Myr	9.91
10% 1Myr	6.6 Myr	9.93

mass of the entire galaxy. The situation is very similar when the latest stellar population contributes 10%. The recovered mass is closer to the burst mass for the youngest bursts. Ages are very close to the age of the young component. When reddening is involved, the age-dust degeneracy even causes the recovered mass and age to be lower than those of the burst component which clearly is a mere artefact stemming from the many degeneracies. Derived ages and masses are closest to that of the old population when the young population is 1 Gyr old. Thus, a wide age gap between old and young stars is the biggest challenge in the fitting. This explains the worse recovery of the physical properties of the mock star-forming galaxies at $z = 0.5$. Serra & Trager (2007) found in a similar exercise that the stellar ages inferred from Lick-indices measurements of two-component composite stellar populations are driven by the younger less massive component.

4.6 Reddening laws

In this section we explore the dependence of the fitting result on the adopted reddening law. The question is: Can a better overall result be achieved by considering several reddening laws or is using just one - which makes the fit faster - sufficient?

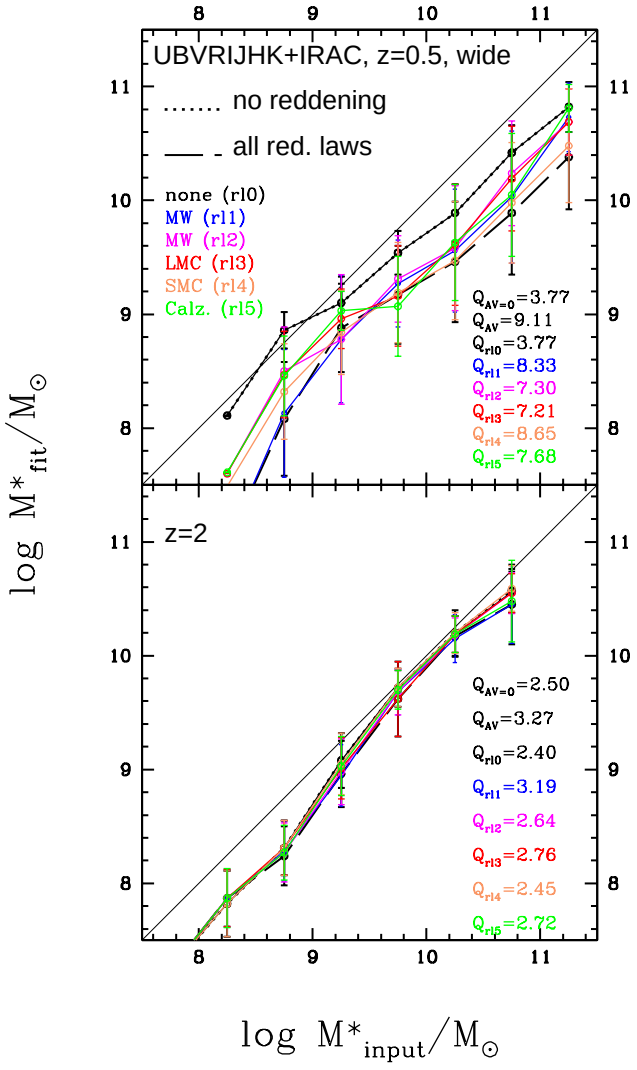

Figure 4.28: Average mass recovery as a function of reddening law at redshift 0.5 and 2. The dotted black line shows the mass recovery when no reddening is used in either spectra or fitting. The dashed thick black line shows the result when the best fit out of all reddening laws is chosen for each object. The coloured thin lines represent the results applying only one reddening law on the reddened spectra. Errorbars show one standard deviation.

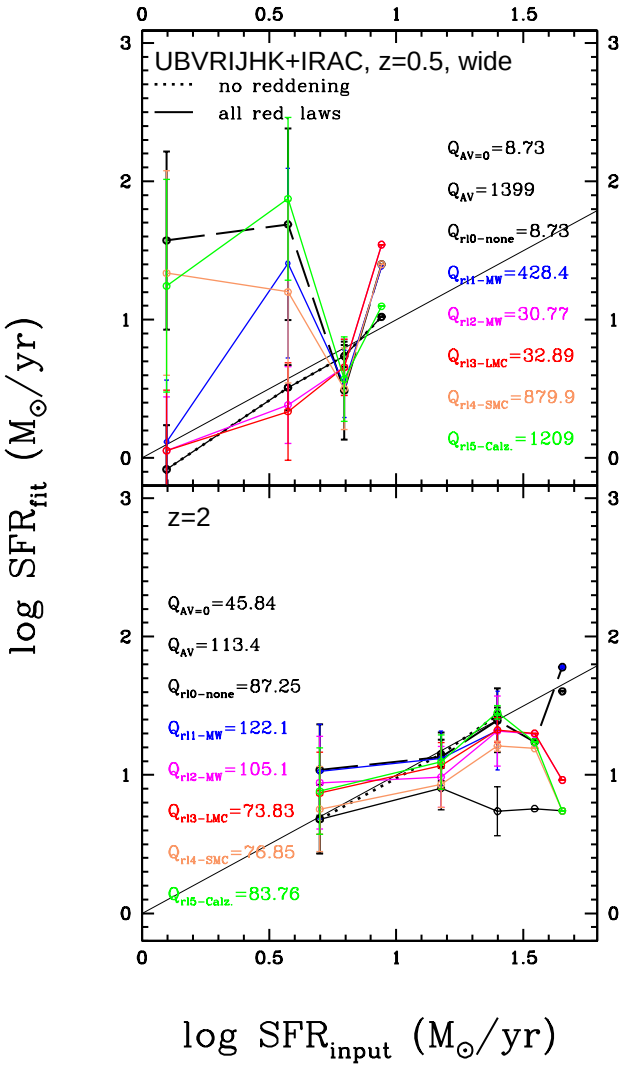

Figure 4.29: Average SFR recovery as a function of reddening law at each redshift where redshift increases from the top left to the bottom right. We show solutions for a wide setup only. Colours and lines are the same as in Fig. 4.28. Note that the data point at the highest SFR at $z = 0.5$ and the two points at the highest SFR at $z = 2$ consist of only one object each and are merely shown for completeness. Errorbars show one standard deviation.

Since we do not add dust reddening to passive galaxies, we investigate the case only for star-forming galaxies. Naively one would expect the Calzetti reddening law to provide the best fit and most accurate result for all reddened objects since the reddening prescription for the semi-analytic galaxies is based on it (Section 2.1). We find that the best mass estimate is achieved when no reddening is used in the fitting. This is also true at higher redshift where galaxies are dust reddened.

The largest difference in mass recovery between the reddening laws occurs at $z = 0.5$ where there is little reddening anyway (Fig. 4.28). The MW law by Allen and the SMC law give the worst mass recovery. This is also reflected in the results for the best fit among all reddening laws. In particular, the SMC reddening curve is much steeper and higher than the Calzetti law (compare Fig. 7 in Bolzonella et al., 2000, and Fig. 3.3 in Chapter 3). On average, the exact type of reddening law is less important at high redshift but variations in the quality factors imply larger effects for individual objects. Papovich et al. (2001); Förster Schreiber et al. (2004); Pozzetti et al. (2007); Muzzin et al. (2009) and Muzzin et al. (2009, b) also found the effect of different extinction laws on stellar masses to be small.

SFRs on the other hand are much more sensitive to the type of reddening law (Fig. 4.29). We can summarise this in two points:

- When the reddening is a fitting parameter and galaxies are dust reddened, the fitting code is able to pick out the right reddening law for most objects, the Calzetti law in our case. Fitting without reddening leads to underestimated SFRs.
- When galaxies have little reddening ($z = 0.5$ case) and reddening is a free parameter in the fit, the age-dust degeneracy causes SFRs to be overestimated. SFRs are best recovered with no reddening in the fit in this case.

In conclusion, stellar masses are best derived without reddening in the fitting at each redshift when the SFHs cannot be matched. For the best SFR estimate on the other hand all reddening laws should be used in the fitting for high redshift, dust reddened objects. For objects without dust reddening, SFRs are best obtained without reddening in the fitting. These conclusions stress again that the simultaneous recovery of masses and SFRs is very difficult and can be achieved only when the assumed SFH is the correct one, as we found at $z = 2$ with inverted-τ models and a proper parameter selection (M10, Section 6.1).

4.7 The effect of photometric uncertainties

Comparing the results obtained when using original magnitudes and those scattered using a Gaussian error[11] in the fit enables us to study the effect of photometric uncertainties. In order to single out this effect we only consider the case without dust reddening. We focus on the older galaxies with little or no on-going star formation (mocks at $z = 0.5$) for which we find the largest deviations between true and recovered stellar population

[11] Original magnitudes were scattered with their three σ photometric errors.

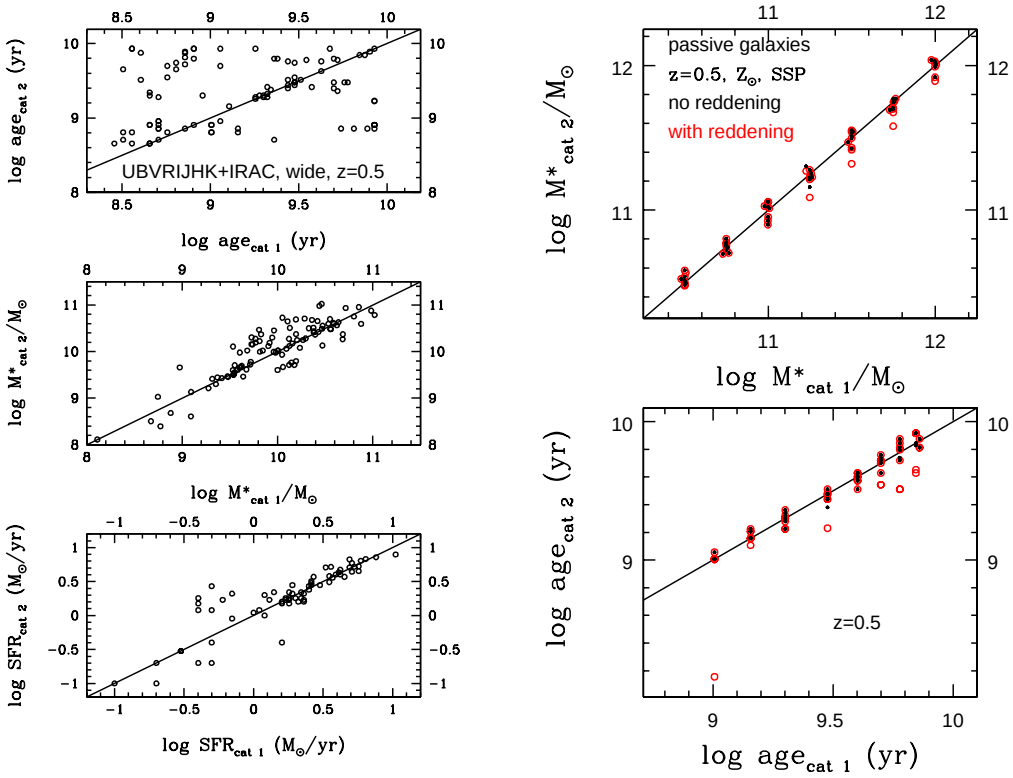

Figure 4.30: *Left:* Effect of photometric uncertainties for mock star-forming galaxies at $z = 0.5$ for a wide template setup and broad wavelength coverage in the fit. From top to bottom: ages, stellar masses and star formation rates, respectively. *Right:* The same for mock passive galaxies. Red and black symbols refer to the cases with and without reddening in the fit. We show galaxies at redshift 0.5 because for these the differences from the true values are largest.

properties. Star-forming galaxies are fit with the wide setup. Passive galaxies are fit with a solar metallicity SSP only.

Fig. 4.30 (top left) shows that ages can be very discrepant, reaching 1.5 dex difference. Masses differ on average by 0.08 ± 0.27 dex and up to ~ 0.7 dex (Fig. 4.30, middle left). The overall trend of underestimating the masses of older galaxies with little on-going star formation remains unaffected by the photometric uncertainties. The mean difference between the derived SFRs is small for the highest SFRs (see Fig. 4.30, bottom left). At the low SFR end deviations are larger (up to 1 dex).

Fig. 4.27 and Fig. 4.30 (right) show that for passive galaxies the effect is small. The largest deviations in stellar mass are found at $z = 0.5$ amounting to maximal ~ 0.2 dex. The inclusion of reddening is negligible. Ages are more affected in the reddening case,

particularly at the youngest and oldest ages, because of the age-dust degeneracy. Older ages are hard to distinguish from each other in the fitting as the spectra are very similar.

4.8 Literature comparison

Other works in the literature exist on this topic. Wuyts et al. (2009, hereafter W09) address the efficiency of SED-fitting for a smoothed particle hydrodynamical merger simulation of two disk galaxies before (disk phase), during (merger phase with triggered star formation) and after the merging (spheroid phase) spanning a total time of 2 Gyr, but not fixed to a particular redshift. They construct the SEDs at various snapshots in time for different viewing angles, place them at redshifts between 1.5 and 2.9 and study the effects of SFH, dust attenuation, metallicity and AGN contribution on the recovery of age, reddening ($E(B-V)$), visual attenuation (A_V), stellar mass and SFR. Their SED-fitting uses solar metallicity templates for three SFHs, namely SSP, constant SFR and a τ-model with $\tau = 0.3$ Gyr. The templates are based on a Salpeter IMF and BC03 stellar population synthesis code. A_V varies between 0 and 4 in steps of 0.2 but is only applied to the constant SFR and τ-model template. Ages are constrained to be larger than 50 Myr and younger than the age of the Universe. The fitting is carried out with *HyperZ* and a Calzetti reddening law.

Our semi-analytic mock galaxies show considerable star formation for $z \geq 1$ and thus compare to the disk (and merger phase) of W09[12]. For this we predominantly consider the wide setup with age constraint and the inverted-τ setup (both with reddening). We compare the results of the wide setup without reddening for our mock passive galaxies for $z \leq 1$ to their spheroid phase. For the purpose of comparison, we define Δ as the difference between recovered and true value[13] analogue to W09. Negative values of Δ correspond to underestimation of the according quantity, positive values to overestimation. As true age for the mock star-forming galaxies we assume the mass-weighted age. We list our median values for Δ together with those of W09 in Table D.1.

W09 find slight overestimation of ages in the disk phase and underestimation in the merger phase. The ages we derive are underestimated at $z = 1$ and 2 and overestimated at $z = 3$ for the wide setup with age constraint. Ages are more underestimated towards lower redshift due to the wide range in population ages comprised within those galaxies (compare Fig. 2.1). W09 seem to determine better ages as they consider only

[12] We do not distinguish our mock galaxies in disks and mergers although they might have undergone a merging event shortly before we observe them.

[13] logarithmic values for age, mass and SFR

a small age-range, no metallicity effects and set an age constraint. We do not compare the age for the inverted-τ models as those have a constant age which is more comparable to the oldest age. While $E(B-V)$ is underestimated in all phases in W09, our derived reddening values are overestimated at lower redshift and very well recovered at higher redshifts. Our scatter is smaller than that of W09 at all redshifts for the two setups. Stellar masses at $z \geq 2$ are equally underestimated as in W09's disk and merger phase. Our mass estimate for $z \geq 2$ improves if we only consider objects in the same mass range as W09 (log $M^* > 9.8$). However, masses are best recovered with the inverted-τ setup where they show almost no offset with smaller scatter. The median stellar mass offset is larger for galaxies at redshift 1. In both disk and merger phase W09 underestimate the SFRs. We overestimate the SFRs at intermediate redshifts. At $z = 3$ the median offset in SFR is small. Our scatter is somewhat smaller than that of W09.

Since we did not put reddening onto the mock passive galaxies, we only compare the fit values for the stellar masses, ages and SFRs with W09. Even in the case with reddening, a value of $E(B-V) = 0$ is correctly recovered for most objects. Both ages and stellar masses are slightly overestimated in our case, while they are underestimated in W09. However, in each case, offsets and scatter are very small. This confirms that stellar masses of passive galaxies can be much better determined by SED-fitting than those of star-forming galaxies. While W09's reddening and SFRs are underestimated in the spheroid phase, both quantities are very well recovered for our passive galaxies. We assign this to the fact that the passive galaxies we simulated are single bursts while galaxies in the spheroid phase in W09 are clearly precessed by considerable star formation and thus still suffer from overshining.

For a direct comparison we reproduce Fig. 8 of W09 for the basic trends and correlations between these physical properties of galaxies and show our results for mock star-forming galaxies in Fig. D.1. As in W09, in summary, those correlations are:

- 1) Age and stellar mass show a strong correlation, i.e. an underestimation in age will lead to an underestimation in mass and vice versa.
- 2) This is anti-correlated with dust reddening, the so called age-dust degeneracy.
- 3) It is also anti-correlated with metallicity, the so called age-metallicity degeneracy.
- 4) SFR and dust reddening are tightly correlated, consequently age and SFR are anti-correlated.

Furthermore, we find evolution in these with redshift. Ages and stellar masses are increasingly underestimated whereas reddening and SFRs are increasingly overestimated towards low redshift. We also list median values with 68% confidence levels of the difference between derived and true age, mass, SFR and $E(B-V)$, together with those of Wuyts et al. (2009) in Table D.1.

Lee et al. (2009) focus on the robustness of the derivation of physical parameters of Lyman break galaxies at redshifts ~ 3.4, 4.0 and 5.0 (U-, B-, and V-dropouts, respectively). They create mock galaxies from a semi-analytical model using BC03 stellar population models with a Chabrier IMF and apply the Lyman break selection criterium to identify star-forming objects at high redshift. Their SED-fitting employs Chabrier IMF BC03 templates with three metallicities (0.2, 0.4 and $1 Z_{\odot}$) and exponentially declining SFRs with $\tau = 0.2 - 15$ Gyr. The Calzetti law is used for dust extinction. They find that the means of the intrinsic and reproduced mass distributions differ between 19 and 25% (for U- and V- dropouts, respectively), such that recovered masses are underestimated. The corresponding difference for our $z = 3$ objects is ~ 17% (or 0.08 dex) using the wide setup with reddening and ~ 15% (or 0.07 dex) when the minimum age is 0.1 Gyr. For the inverted-τ setup the difference between the means of true and recovered stellar mass distributions is < 1% (0.004 dex).

Lee et al. (2009) also report larger discrepancies for mean age and SFR in comparison to the true values, mean SFRs (averaged over 100 Myr) are underestimated by ~ 62% and mass-weighted mean ages are overestimated by about a factor of 2. They assign this behaviour to two effects: the mismatch between real and template SFHs and the overshining effect of a young stellar population. Furthermore, they acknowledge the influence of the age-dust degeneracy on the derived SFRs. Lee et al. (2009) try to solve the SFH mismatch in using two-component templates consisting of two time-separate burst of star formation with different values of τ. However, we have shown in M10 (Section 6.1) and the previous sections that using inverted-τ models recovers the mass for mock star-forming galaxies at $z = 2$ and 3 perfectly. SFRs are slightly overestimated and show a larger scatter at the low SFR end where the exponentially increasing SFH of the template is not matched by the simulated galaxies. Based on the SFHs of the mock star-forming galaxies as shown in Fig. 2.3 we believe that the best model to recover the masses and SFRs of star-forming objects at $z > 3$ is the inverted-τ template (using appropriate formation redshifts and ages). Because of the fixed age, the overshining by young components is ignored in the fit. Derived ages will therefore always be older than input luminosity- or mass-weighted ages and compare better to the oldest age.

Longhetti & Saracco (2009) study the systematics involved in the mass estimates from SED-fitting of mock early-type galaxies between redshift 1 and 2. They simulate early-type galaxies with Salpeter IMF solar metallicity BC03 models of exponentially declining SFH ($\tau = 0.6$ Gyr) and ages between 1.7 and 4.2 Gyr. Furthermore, they add secondary bursts at different times with mass fractions of 5 and 20% and star formation time scale of $\tau = 0.1$ Gyr. Dust obscuration is considered to be $A_V = 0$, 0.2 and 0.5 using the Calzetti law. SED-fits are performed using *HyperZ* and solar metallicity τ- models of BC03 with $\tau = 0.1, 0.3, 0.6, 1.0$ Gyr. They also test the effects of using different stellar population models. Longhetti & Saracco (2009) conclude that overall stellar masses of early-type galaxies cannot be estimated better than within a factor of $2 - 3$ of the true value at fixed known IMF. We find that the stellar masses of the mock passive galaxies in our work at $z = 1$ can be recovered within a factor of ~ 1.05 (~ 0.02 dex) at known IMF. Including uncertainties on the IMF (but only considering among Kroupa, Chabrier and Salpeter) masses are recovered within 0.2 dex. Our result is better probably just because we have really zero on-going star formation in our passive galaxies while Longhetti & Saracco (2009) by considering a τ-model and second bursts keep a small amount of star formation, which confuses the derived properties for the reasons we amply discussed above.

Lastly, Bolzonella et al. (2010) find a typical total uncertainty caused by different choices of reddening law, metallicities, SFHs and stellar population models in stellar mass estimates of $\sigma \simeq 0.2$ dex.

4.9 Homogenising derived properties via scaling relations

For many purposes, combining results from different authors and data sets is required. In this case, homogeneity of the analysis method is essential. However, different models, templates, IMFs and fitting procedures are used in the literature and we have demonstrated in the previous sections their impact on the results. Here, we have the opportunity to obtain 'scaling relations' which allow the transformation of the derived physical properties from one set of fitting parameters to another. Based on the previous sections we have derived such relations for stellar mass for a variety of parameter choices using a least squares fit. They are listed in table 4.3 for star-forming galaxies and in table 4.4 for passive galaxies. In order to gain statistical robustness we use results for the entire merger tree. Some examples are shown in Fig. 4.10 as solid green and dashed magenta lines.

Table 4.3: Scaling relations for mock star-forming galaxies in the form of $log\, M^*_{wideSalpeter} = a_1 + a_2 * x$ where x stands for $log\, M^*$ of the various fitting setups. The coefficients a_1 and a_2 represent the unreddened case, b_1 and b_2 represent the reddened case.

redshift	x	a_1	a_2	b_1	b_2
0.50	wide Chabrier	0.4814	0.9666	0.5559	0.9581
1.00	wide Chabrier	0.5913	0.9563	0.5826	0.9601
2.00	wide Chabrier	0.5125	0.9673	0.3675	0.9831
3.00	wide Chabrier	0.7223	0.9485	0.4631	0.9755
0.50	wide Kroupa	0.4445	0.9707	0.2827	0.9882
1.00	wide Kroupa	0.4244	0.9754	0.6725	0.9515
2.00	wide Kroupa	0.2409	0.9973	0.1958	1.0024
3.00	wide Kroupa	0.1042	1.0136	0.0840	1.0151
0.50	wide $Z_\odot$	0.8464	0.9292	-0.9575	1.0978
1.00	wide $Z_\odot$	-0.0264	1.0077	-0.5233	1.0531
2.00	wide $Z_\odot$	0.7532	0.9225	0.5159	0.9452
3.00	wide $Z_\odot$	0.6843	0.9314	0.4773	0.9514
0.50	only-τ	1.0651	0.9057	-2.8838	1.2630
1.00	only-τ	-0.1275	1.0171	-0.8565	1.0844
2.00	only-τ	0.5824	0.9383	0.4459	0.9510
3.00	only-τ	0.8008	0.9197	0.4467	0.9554
0.50	wide BC03	-0.0349	0.9887	0.0385	0.9611
1.00	wide BC03	0.0887	0.9675	-0.2077	0.9939
2.00	wide BC03	0.9366	0.8855	0.8272	0.8947
3.00	wide BC03	1.0761	0.8785	0.7205	0.9101
0.50	BC03 only-τ	0.2524	0.9617	-2.4432	1.1980
1.00	BC03 only-τ	0.2369	0.9487	-0.1809	0.9906
2.00	BC03 only-τ	1.2843	0.8480	1.1366	0.8613
3.00	BC03 only-τ	1.3341	0.8523	1.0544	0.8759

Note that these relations provide information only about statistical differences, the difference in stellar mass between various fitting setups for a single object can significantly deviate from this.

Table 4.4: Scaling relations for passive galaxies in the form of $log\, M^*_{wideSalpeter} = a_1 + a_2 * x$ where x stands for $log\, M^*$ of the various fitting setups. The coefficients a_1 and a_2 represent the unreddened case, b_1 and b_2 represent the reddened case.

redshift	x	a_1	a_2	b_1	b_2
0.50	wide Chabrier	0.0243	1.0095	0.3167	0.9821
1.00	wide Chabrier	0.0913	1.0042	0.1660	0.9974
2.00	wide Chabrier	0.1477	1.0007	0.2017	0.9960
3.00	wide Chabrier	0.1612	1.0001	0.1615	1.0001
0.50	wide Kroupa	-0.0188	1.0124	0.0795	1.0022
1.00	wide Kroupa	0.0785	1.0035	-0.7200	1.0731
2.00	wide Kroupa	0.1289	0.9996	0.1785	0.9952
3.00	wide Kroupa	0.1217	1.0004	0.1214	1.0005
0.50	wide $Z_\odot$	0.1568	0.9865	-0.1059	1.0129
1.00	wide $Z_\odot$	0.0227	0.9983	-0.0418	1.0051
2.00	wide $Z_\odot$	0.0773	0.9941	-0.0145	1.0022
3.00	wide $Z_\odot$	0.0006	0.9999	0.0003	1.0000
0.50	only-τ	-0.0161	1.0012	-0.2548	1.0261
1.00	only-τ	0.0442	0.9966	-1.0724	1.0948
2.00	only-τ	0.0592	0.9963	0.0013	1.0005
3.00	only-τ	-0.0512	1.0060	-0.0336	1.0046
0.50	SSPs	-0.0401	1.0043	0.0877	0.9914
1.00	SSPs	-0.0498	1.0039	0.3950	0.9628
2.00	SSPs	0.2261	0.9792	0.2829	0.9744
3.00	SSPs	0.0685	0.9956	0.0715	0.9952
0.50	wide BC03	0.7390	0.9240	0.8017	0.9245
1.00	wide BC03	1.3682	0.8783	-0.6348	1.0528
2.00	wide BC03	7.7711	0.4620	0.0007	0.9854
3.00	wide BC03	8.8104	0.6450	0.0241	0.9793

4.10 Summary and conclusions

We analyse the problem of recovering galaxy stellar population properties - such as ages, star formation rates, stellar masses - through broad-band spectral energy distribution fitting as a function of the various parameters of the fit, namely: star formation history, metallicity, age grid, the initial mass function, reddening law, wavelength coverage and filter setup used in the fitting. This is a crucial question in galaxy formation and evolution as most conjectures that are derived from data are fully based on the galaxy properties that are obtained through this method. As test particles we use mock galaxies whose properties are known and well defined. We consider both star-forming and passive galaxies and a large redshift range, from 0.5 to 3. Mock star-forming galaxies are taken from a semi-analytical galaxy formation model (GalICS) which uses as input the same stellar population model (by Maraston 2005) used for the fitting templates, but we also experiment with other stellar population models for both the fitting and the semi-analytic galaxies (results for this are fully discussed in the Appendix). Mock passive galaxies are simulated using solar metallicity simple stellar populations. We then treat the mocks as real observed galaxies, i.e. we obtain their observed-frame magnitudes, apply SED-fitting with various templates and compare the properties derived from the fitting to their true values.

This work complements an earlier paper (Maraston et al., 2010, Section 6.1) where we discuss the problem of deriving star formation rates and masses for real $z \sim 2$ star-forming galaxies right at the peak of the cosmic star formation rate. There we found that the adopted star formation history affects the results, as well as the priors that are set on the galaxy formation ages. This happens because the age parameter becomes very poorly constrained for galaxies with on-going star formation, due to the overshining of an older generation by the youngest stars, even when these make up just a few percent of the total stellar mass. As a main result of that paper we put forward a star formation history that allows a very good determination of star formation rates and masses of star-forming galaxies. This is an exponentially-increasing star formation with high formation redshift and a star formation timescale $\tau \sim 0.4$ Gyr. We also find that normally adopted τ-models underestimate the stellar mass and overestimate the star formation rates. In this chapter we quantify these various offsets using simulated galaxies.

Our results for mock star-forming galaxies can be summarised as follows:

- The match between template and real SFH is crucial for a *simultaneous* determination of the galaxy physical parameters. For example, at high redshift - when the

galaxy ages span a confined range - stellar masses are very reasonably determined - within 0.1 dex - with a variety of template choices. However, this comes as a compensating effect of other properties being underestimated/overestimated.

- When there is a SFH mismatch, the direction is typically at underestimating ages and stellar masses and overestimating reddening and SFRs, both due to overshining from the youngest stellar generations and the age-dust degeneracy. We quantify these effects as functions of adopted fitting setup.
- Inverted-τ models with the exact same prescriptions as in M10 (Section 6.1) allow for a virtually perfect mass and SFR determination of $z \sim 2-3$ galaxies.
- When galaxies are older and have residual star formation, as is the case for the semi-analytic galaxies at lower redshifts, the larger age span and the age-dust degeneracy cause the mass (and the age) to be severely underestimated (by up to 0.7 dex) using standard templates composed of a variety of star formation histories.
- An efficient trick to reduce this effect is to switch off reddening in the fit as this helps avoiding unrealistically young and dusty solutions. Reddening and star formation rates should then be obtained through a separate fit.
- A similar effect is obtained by constraining the minimum age in the fitting as already done in the literature.
- Ages derived from the best fit are best compared to mass-weighted ages. They are generally underestimated.
- Metallicity effects play a secondary role.
- The exact type of reddening law can be correctly identified when dust reddening is present in the galaxies even if at high redshift differences in stellar mass arising from the use of various reddening laws are negligible.
- Photometric uncertainties alone produce an uncertainty of on average 0.08 dex in stellar mass and SFR and of 0.07 dex in age.
- At all redshifts, a wavelength coverage from the rest-frame UV to the rest-frame near-IR allows to obtain the most robust results.

For mock passive galaxies we can summarise our results to:

- The stellar masses of passive galaxies can be very well recovered. The dispersion from the true value amounts on average to less than 0.05 dex.

- Metallicity effects become important for aged passive galaxies and using various metallicities in the fitting appears to be the most secure option.
- The effect from photometric errors alone on the ages and stellar masses is ~ 0.2 dex.
- The wavelength dependence of the best fit ages for old passive galaxies is smaller than in the case of star-forming galaxies, but the scatter is substantially reduced by including the rest-frame near-IR in the fit.

We conclude that the stellar population parameters of star-forming and passive galaxies can be reasonably well determined provided one uses the right setup and wavelength coverage. Although degeneracies between age, dust and metallicity can have a significant effect, the mismatch between template and real SFH dominates at low redshift. Because of this and the larger spread in stellar ages the stellar population properties of galaxies at low redshift are recovered worse than those at high redshift. Based on our extensive study we conclude that at $z = 0.5$ and 1 stellar population parameters are best recovered with a wide setup, setting a minimum age of 0.1 Gyr in the fitting and excluding reddening from the fitting parameters. This solution is acceptable, though not optimal, and future work will be devoted in envisaging a good analytical description for this type of galaxies. For $z \geq 2 - 3$ inverted-τ models give the best results for both mass and star formation rates.

In all cases, the coverage of UV to near-IR rest-frame wavelengths in the fitting is crucial, but in some cases it is possible to find alternative filter band setups that can give reasonable results. We quantify these effects which will be useful for the planning of surveys and observational proposals.

Finally, due to the variety of assumptions made in the literature regarding fitting methods, stellar population models and adopted filters, caution is required when comparing SED-fitting results between different studies (Lee et al., 2009). In order to ease these comparisons we provide scaling relations for the stellar mass that allow transformation from one set of fitting parameters and population models to another.

Chapter 5

Recovering stellar population properties of mock galaxies with redshift as a free parameter

In this chapter we explore the dependence of galaxy stellar population properties that are derived from broad-band spectral energy distribution fitting on a variety of parameters, such as star formation histories, age grid, metallicity, IMF, dust reddening and reddening law, filter setup and wavelength coverage when redshift is also a free parameter in the fit. In general, in this chapter we want to study whether one can obtain reasonable estimates of photometric redshifts and stellar population properties *at once*. Again, the mock galaxies described in Chapter 2 and used in Chapter 4 serve as test particles. This also gives us the opportunity to directly compare to the case when redshift is known for these galaxies. We show that for high redshift star-forming galaxies when using a broad wavelength coverage (including the Lyman and the 4000 Å break) and a wide template setup in the fit, photometric redshifts, stellar masses and reddening can be determined *simultaneously*. Masses are then similarly well recovered (median ~ 0.2 dex) as at fixed redshift using the same fitting setup. At low redshift masses are better recovered than in the fixed redshift case, such that the median recovered stellar mass improves by up to 0.3 dex (at fixed IMF) whereas the uncertainty in the redshift accuracy increases by only ~ 0.05 dex. However, a failure in redshift recovery also means a failure in mass recovery. Masses are still generally underestimated because of mismatches in SFH and degeneracies between redshift, age and dust, particularly at low redshift, which also cause underestimated ages and overestimated reddening. Again at low redshift, the best way to determine stellar masses is to fit without reddening. Masses are then underestimated by only ~ 0.1 dex whereas redshifts are similarly well recovered. As in the fixed redshift case (Chapter 4) we quantify the offsets generated by adopting standard fitting setups. Not surprisingly,

the recovery of properties is substantially better for passive galaxies, for which e.g. the mass is recovered only slightly worse than at fixed redshift (underestimated by ~ 0.02 dex instead of ~ 0.01 dex, at fixed IMF) using a setup including metallicity effects. In all cases, the recovery of physical parameters is crucially dependent on the wavelength coverage adopted in the fitting because the redshift recovery depends on the wavelength coverage. Redshifts are best recovered for a wavelength coverage from the rest-frame UV to the rest-frame near-IR which includes the Lyman and 4000 Å break. As in the fixed redshift case we quantify the effect of narrowing the wavelength coverage or adding and removing filter bands and provide simple scaling relations that allow the transformation of stellar masses obtained using different template and fitting setups and stellar population models.

This chapter is organised as follows. We recap the different fitting setups and parameters in Section 5.2. Results for star-forming galaxies are shown and discussed in Section 5.3, those for passive galaxies in Section 5.4. The comparison of our results with the literature is carried out in Section 5.8. In Section 5.9 we provide scaling relations that can be used for homogenising data sets. Section 5.10 gives a summary of the work in this chapter.

Throughout this chapter we use a standard cosmology of $H_0 = 71.9$ km/s/Mpc, $\Omega_\Lambda = 0.742$ and $\Omega_M = 0.258$ as used in GalICS (see Hatton et al., 2003) and magnitudes in the Vega system.

The work in this chapter was carried out in collaboration with C. Maraston and C. Tonini. The contents of this chapter will be published in Pforr, Maraston & Tonini (2012b, in prep.). Since the publication was still in preparation and has not undergone the referee process at the time of submission of this thesis the contents of Pforr, Maraston & Tonini (2012b, in prep.) might be slightly different from the contents of this chapter.

5.1 Background

In the previous chapter we studied the recovery of galaxy properties of mock galaxies with known redshift. We compared our work to recent studies by Longhetti & Saracco (2009), Wuyts et al. (2009) and Lee et al. (2009) who address the uncertainties of the derivation of physical parameters and their dependency on the fitting parameters using simulated galaxies (Section 4.8). In this chapter we extend our study by assuming that redshift is not known and needs to be determined alongside the stellar population parameters in the fit. Lee et al. (2009) and Wuyts et al. (2009) include photometric redshifts in

their investigation and we will compare our results with theirs. In particular, Lee et al. (2009) find that when redshift is free their stellar masses are underestimated more than at fixed redshift. SFRs are slightly better determined, particularly at the highest redshifts. Mean ages are younger than at fixed redshift but still overestimated overall. Furthermore, their recovered redshifts are on average underestimated slightly. In general, when redshift is underestimated then ages and masses are underestimated and SFRs are overestimated. Furthermore, Lee et al. (2009) show that a large wavelength coverage from optical to rest-frame near-IR is required to best recover the input physical parameters. Bolzonella et al. (2000) already showed this for the determination of photometric redshifts when testing their code *HyperZ*. They also showed that the redshifts of old and passive galaxies are determined better than those of younger ones.

Wuyts et al. (2009) investigate the effects of photometric redshift and its uncertainties by deriving the redshift first and then all other parameters in a separate fit in which the derived redshift is used as fixed value. They find that errors on the derived properties expressed as 68% confidence levels broaden by a few percent. For the most dust reddened objects they find a mass increase of 0.05 dex compared to the fixed redshift case. Reddening is then somewhat lower.

As in Chapter 4, here we complement the literature work by using the M05 stellar population models and also a wider redshift range and galaxy type.

In the previous chapter (Chapter 4, see also Pforr et al., *submitted*), we used mock galaxies with known physical properties - age, metallicity, reddening, mass and star formation rate (for details see Chapter 2, Section 2.1). We studied the robustness of the results as a function of various fitting setups by comparing the derived properties to the input properties of mock galaxies. Here, we use the same mock galaxies (star-forming and passive), treat them in the same way and explore the same fitting setups.

However, in Chapter 4 spectroscopic redshifts were available and used in the fit. In this chapter, we focus on investigating the effects of various assumptions for wavelength coverage, star formation history, dust reddening, metallicity and IMF on the derivation of galaxy physical properties when also the redshift is a *free* parameter.

5.2 SED-fitting setups

The SED-fitting is carried out in the same way as described in Maraston et al. (2006) and in Chapter 4. A detailed description of the method is given in Chapter 3. In this chapter we employ the *HyperZ* code instead of *HyperZspec*. Again the best fit solution is obtained by means of minimising χ^2_ν. Template setups and fitting parameters are introduced in detail in Chapter 4, Section 4.2. In this section we recap them.

5.2.1 Model Template Setups

We employ the same template setups as in Chapter 4, Section 4.2. These are:

- wide template setup (default: Salpeter IMF, full age grid, 4 metallicities)
- mono-metallicity wide template setups
- wide template setup based on Kroupa, Chabrier and top-heavy IMF
- wide template setup with different age grids (rebinned, minimum age of 0.1 Gyr)[1]
- wide template setup based on BC03 models (Results for this are summarised in Appendix B.)
- only-τ template setup

We do not consider the inverted-τ setup. Indeed, these models are not expected to be very effective in determining the redshift because of their fixed age.

5.2.2 Wavelength range included in the fit

In Chapter 4 we addressed the importance of the wavelength coverage adopted in the fit. We established that a broad wavelength coverage is needed in order to obtain the most robust results in agreement with the findings of M06 and Kannappan & Gawiser (2007). The wavelength coverage is of even greater importance when redshift needs to be determined because the fit relies on the correct identification of the position of important spectral features from which the redshift can be inferred when compared to their rest-frame position in the spectrum (see Chapter 3 for a detailed description). Therefore, a broad wavelength coverage appears to be important as already pointed out by Bolzonella

[1] Age grids are only varied for mock star-forming galaxies as these are affected by the overshining; mock passive galaxies are by definition devoid of this.

et al. (2000). With an accurate redshift we can then hope to be able to accurately determine galaxy physical properties such as stellar masses. Moreover, up-coming surveys such as the Dark Energy Survey (DES) rely on accurate photometric redshifts.

We carry out a comprehensive test of various filter setups and their performance in recovering the galaxy physical properties to answer these questions. For this we use the same filter setups as in Chapter 4, Section 4.2.2.

5.2.3 Photometric uncertainties

We quantify the effect of photometric uncertainties on the derived physical properties by comparing results for original magnitudes and those scattered with Gaussian errors of the mock galaxies[2] at redshift 0.5 in the same way as described in Section 4.2.3.

5.3 Results for star-forming galaxies

In this section we compare the results derived from SED-fitting to the true values for mock star-forming galaxies as a function of template setup (star formation history, metallicity, age grid, IMF, stellar population model[3]), filter set and wavelength coverage and reddening law as we did in Chapter 4. Differences to the results in the previous chapter will be caused by the additional degree of freedom in the fitting due to the unknown redshift. Throughout this section we will compare our results to those obtained for mock star-forming galaxies with known redshift in Chapter 4, Section 4.3.

As before we start by leaving dust reddening out of the procedure (both in the fitting and the mock galaxies, referred to as 'unreddened case' or 'case without reddening') for understanding the contributions of multiple stellar populations in the galaxies and their degeneracies with redshift. We then repeat the exercise including dust reddening. Table 4.1 gives an overview of all fits that were carried out for redshifts 0.5, 1, 2 and 3. As defined in the previous chapter we will use the quality estimator Q to evaluate the performance of the various fitting setups and parameters.

We have shown in M10 (Section 6.1) and Chapter 4 that models with the smallest χ^2_ν do not necessarily provide the best physical solution. For this reason we abstain from showing any comparisons of χ^2_ν but focus instead on the effects of different template setups and wavelength coverage on the recovered redshifts, ages, metallicities, SFHs, reddening

[2] without dust reddening
[3] see Appendix B

and stellar masses. Additionally to the previous chapter, we also have the opportunity to see how the derivation of other properties depends on the derived redshift.

5.3.1 Photometric redshift

In this section, we study the redshift recovery for mock star-forming galaxies (Figs. 5.1-5.4). Firstly, we show the effect of template setup in Fig. 5.1. Overall, the differences in redshift recovery between template setups are small. On average, redshifts are recovered correctly within $\sigma = \sqrt{(\sum (z - z_{mean})^2)/N} \sim 0.1$. The highest redshifts are recovered best. Those for which $z_{true} = 2$ redshifts are overestimated and show larger scatter ($\sigma \sim 0.15$). For the only-τ setup we find more outliers for $z_{true} = 2$ objects in the unreddened case. For these, recovered redshifts are mainly below 1 and best fits have very short star formation time scales ($\tau \leq 0.05$) and young ages. Indeed, they belong to the youngest objects at this redshift. In the wide setup these are fitted with slightly older ages, lower metallicity and even shorter star formation time scales (namely SSPs). Including modest amounts of reddening reduces the outlier fraction and improves the redshift recovery with the only-τ setup. For the wide setup, differences arising from the inclusion of dust reddening are small. Since the galaxies at $z \geq 2$ are intrinsically young and inhabit significant star formation they lack a distinct 4000 Å break. At $z = 2$ the chosen filter set does not comprise the Lyman-limit (at 912 Å rest-frame). Hence, two important features aiding the redshift determination are missing, making the process of obtaining redshifts for galaxies in this redshift range very difficult. Galaxies with redshifts around 2 lie in the so-called redshift desert where the redshift determination is challenging even with spectroscopic methods due to the lack of spectral lines in the optical (e.g. Bunker 1999; Glazebrook & the GDDS team 2003; Steidel et al. 2004 for attempts on filling the redshift desert and for a recent review see Renzini & Daddi 2009). At $z = 3$ the Lyman-limit falls into the range of the U filter and thus significantly helps in determining the redshift.

Unlike for the mass recovery, excluding SSPs from the fit does not help to improve the redshift recovery at low redshift. At high redshift, the scatter is somewhat smaller.

From these results we conclude that a wide setup is best for the redshift determination at low redshift. At high redshift, the only-tau setup (including reddening) is better and also more economic due to a smaller number of fitting templates.

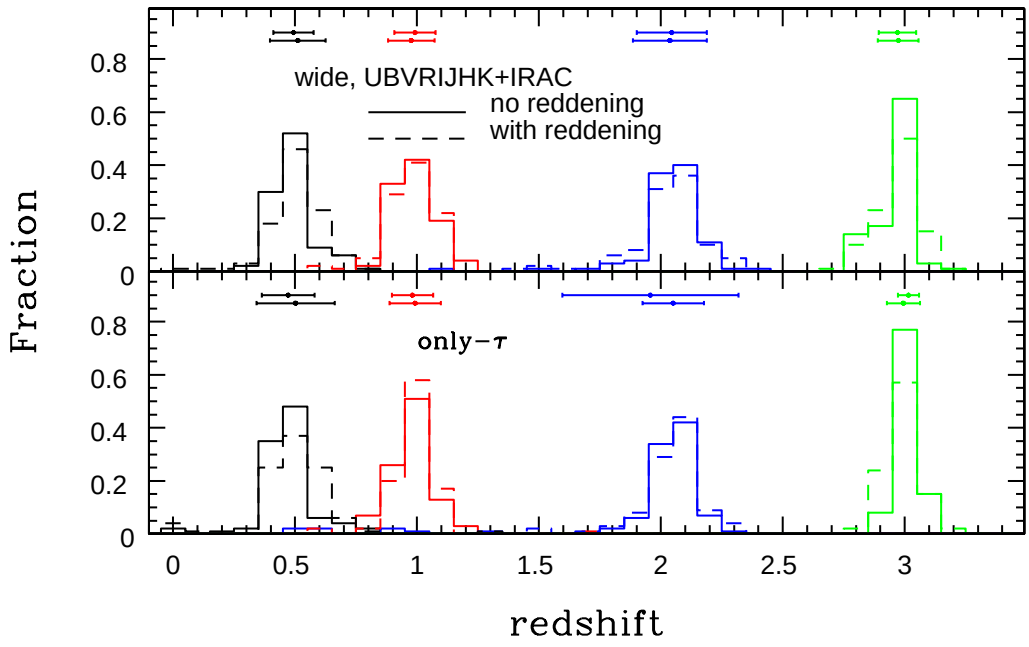

Figure 5.1: Redshift recovery for mock star-forming galaxies as a function of template setup, namely wide (top) and only-τ (bottom) using a broad wavelength coverage (UBVRIJHK+IRAC). Solid lines refer to the case without reddening, dashed lines to the reddened case. Input redshifts are colour-coded as black for $z = 0.5$, red for $z = 1$, blue for $z = 2$ and green for $z = 3$, respectively. For each redshift we show the mean redshift. Errorbars are one standard deviation (unreddened case in upper row, reddened case in lower row).

In the next step we investigate the effect of metallicity on the redshift determination by using the wide setup in mono-metallicity form. Although metallicity effects are small (Fig. 5.2), redshifts are best determined with the lowest metallicity setup because the metallicities of mock star-forming galaxies are predominantly sub-solar (compare Fig. 2.2). At every metallicity, the redshift recovery is best for $z = 3$ objects, because of the above named reason. The redshift recovery is worst for $z = 2$ objects and in particular for the highest metallicity setup. Reddening has the largest impact at low redshift where it helps to rectify metallicity effects, but only a small effect overall. Note how well redshift is recovered at $z = 0.5$ with reddening in spite of large offsets for the stellar mass (compare Fig. 5.10).

Fig. 5.3 illustrates the dependence of redshift determination on the IMF of the templates. Redshifts are best recovered with Salpeter IMF templates. Results for a Chabrier and Kroupa IMF are very similar. Templates with a top-heavy IMF perform worst. The

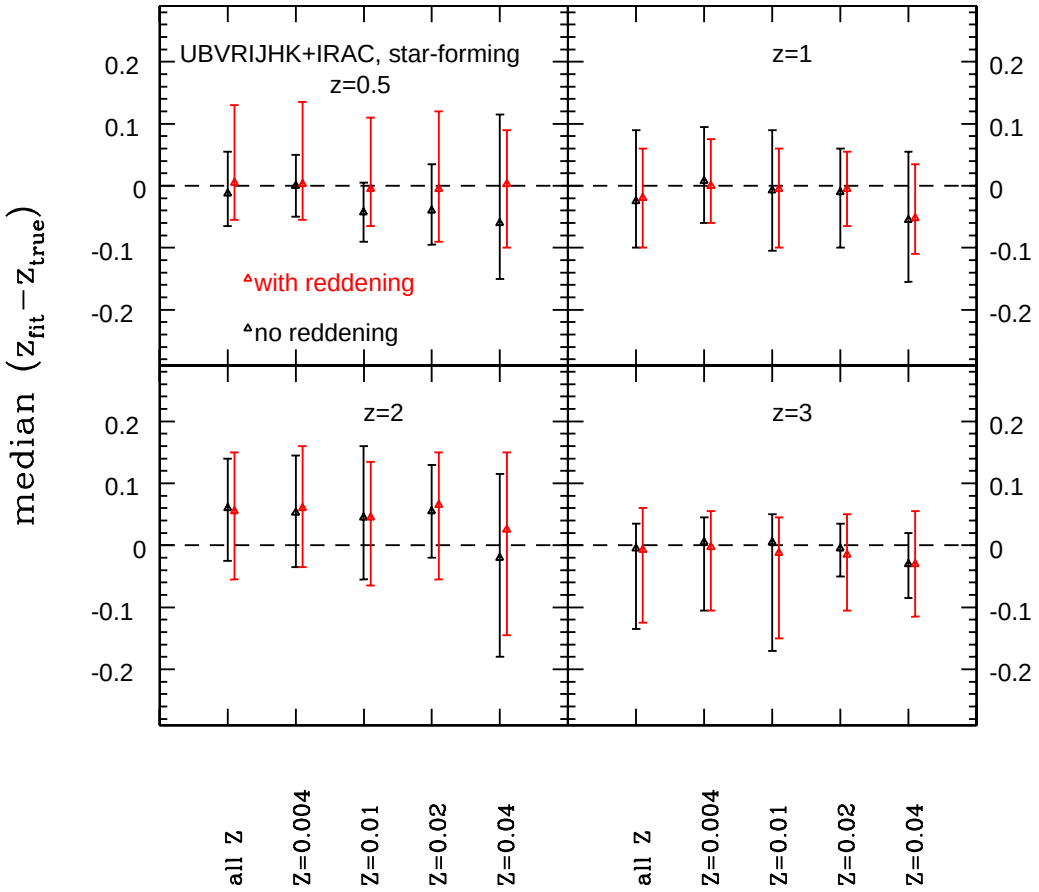

Figure 5.2: Median redshift recovery for mock star-forming galaxies as a function of metallicity (increasing from left to right in each panel) using a broad wavelength coverage (UBVRIJHK+IRAC). Black symbols refer to the case without reddening, red to the reddened case. Errorbars are 68% confidence levels.

right IMF cannot be identified by the fit as already concluded in Chapter 4. About 30% of the objects at each redshift are associated with a top-heavy IMF instead of Salpeter. The effect of adding reddening is again small. For the top-heavy IMF redshift estimates at $z = 3$ are improved such that underestimated redshifts are cured by choosing larger amounts of dust reddening. This is clearly due to the significantly bluer SED of the top-heavy IMF at young ages. For Chabrier and Kroupa IMF redshift estimates at $z = 1$ are improved when reddening is involved.

Finally, in Fig. 5.4 we show the dependence of the redshift recovery on the wavelength coverage adopted in the fitting. The largest effects are seen for filter setups that do not

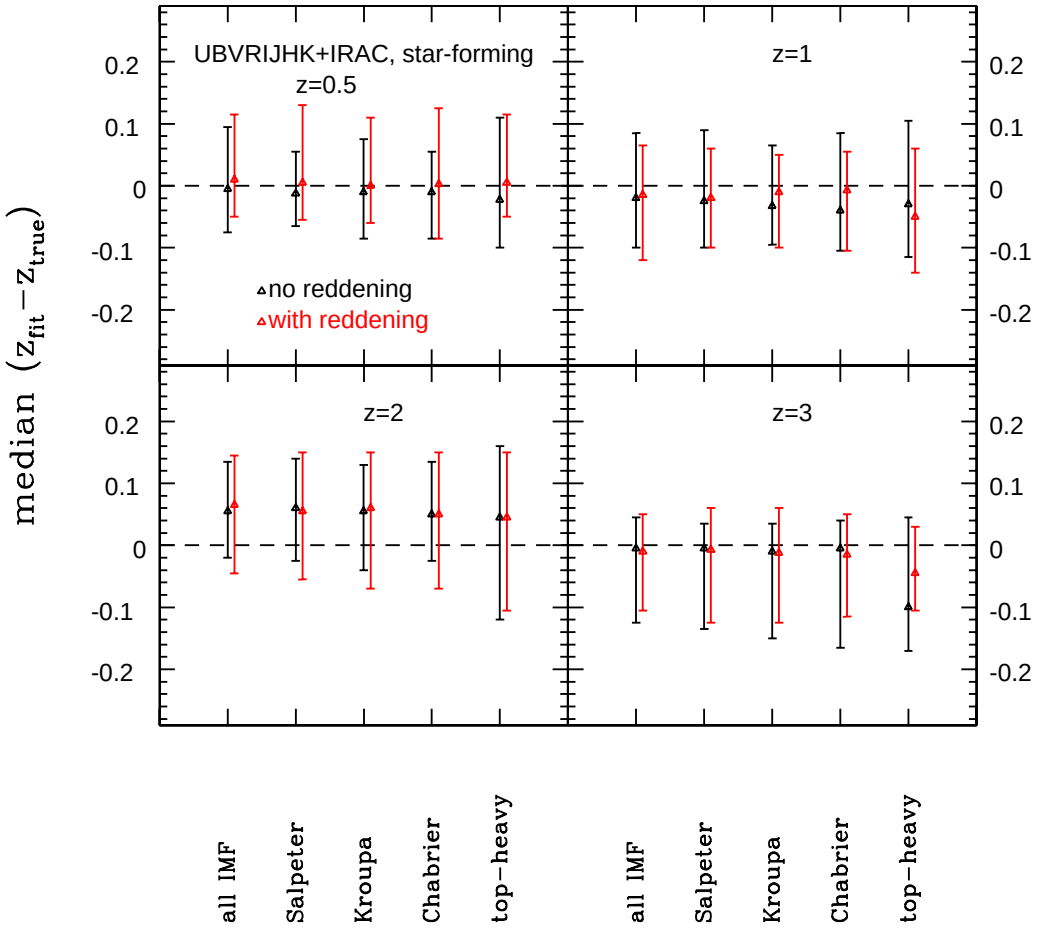

Figure 5.3: Median redshift recovery for mock star-forming galaxies as a function of IMF using a broad wavelength coverage (UBVRIJHK+IRAC) and a wide setup. Symbols as in Fig. 5.2.

comprise the rest-frame near-IR and the red optical resulting in larger scatter and overestimated redshifts at $z = 0.5$ and 1. Clearly the old age of the objects is not sufficiently constrained in the fit and gets compensated with a higher redshift. At $z = 2$ and 3, redshifts are underestimated because the use of sole optical filter bands excludes the 4000 Å break. At redshift 3 at least the Lyman-limit is covered by the filters. Additionally, the galaxies' young ages and restricted age range in the fitting helps the redshift recovery. Omitting blue filter bands in the fitting has little effect at low redshift because the 4000 Å break is still included (in R band at $z = 0.5$ and I band at $z = 1$, compare Fig. 3.2). At redshift 2 redshifts are overestimated with these filter setups because the rest-frame wavelength covered by these filters contains information about the Lyman-absorption between Lyman-α (1216 Å) and the Lyman-limit (912 Å) although missing the Lyman-limit itself.

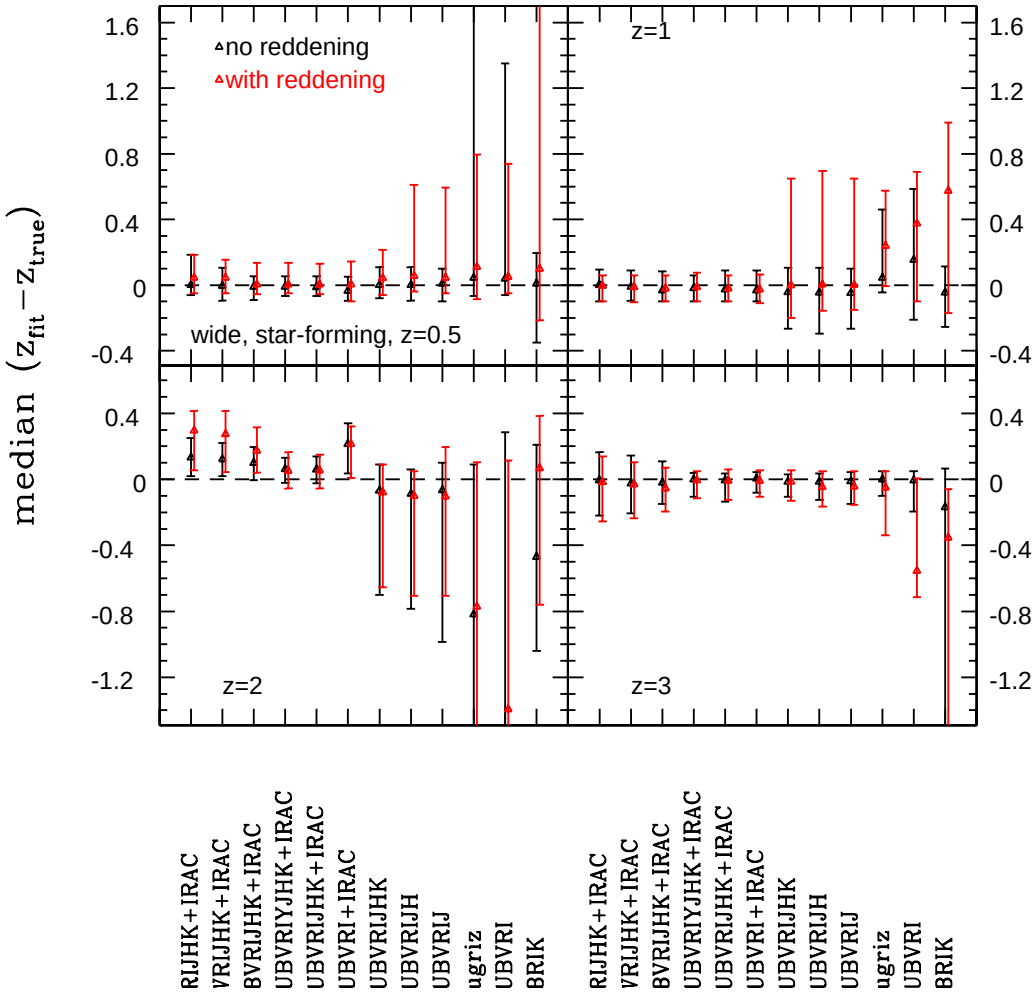

Figure 5.4: Redshift recovery (median) for mock star-forming galaxies as function of wavelength coverage using a wide template setup. Redshift increases from top left to bottom right. Red symbols refer to the case with reddening, black to the unreddened case. Errorbars reflect 68% confidence levels.

For redshift 3 objects only the scatter increases. Furthermore, a filter setup missing out on the near-IR filter bands JHK, means excluding the 4000 Å break at $z = 2$. For $z = 3$ this is less harmful because the Lyman-limit is still covered. Including reddening does not alter these trends much but the scatter increases. At redshift 1 redshifts are overestimated for the most restricted wavelength coverages.

In Chapter 4 we demonstrated that degeneracies between age, dust and metallicity are the largest obstacles against obtaining robust stellar population properties from the fitting because all of them have the ability to make the SED redder. Here, we have an additional degeneracy due to the unconstrained redshift. We show the correlation of redshift

recovery with derived reddening and age in Fig. 5.5 for the wide setup and the broadest wavelength coverage. There is no correlation between redshift recovery and reddening. Fig. 5.1 already revealed that there is little difference in the redshift recovery between the reddened and unreddened case. However, in the unreddened case the redshift recovery is clearly anti-correlated with the fitted age at the lowest redshifts. For younger ages redshifts are overestimated, for older ages they are underestimated. At $z = 2$ the connection loosens up and at $z = 3$ it turns into a weak correlation, such that for the youngest ages redshifts are also underestimated. Here, young ages and lower redshifts (and low metallicities) try to compensate shortcomings in the star formation history (SSPs) which does not reflect the true star formation history of these objects (i.e. rising star formation). We concluded in Chapter 4 already that SSPs should not be used in the fitting due to their negative effect on the stellar mass recovery. However, for the redshift recovery the exclusion of SSPs has a negligible effect at low redshift and only the scatter is decreased

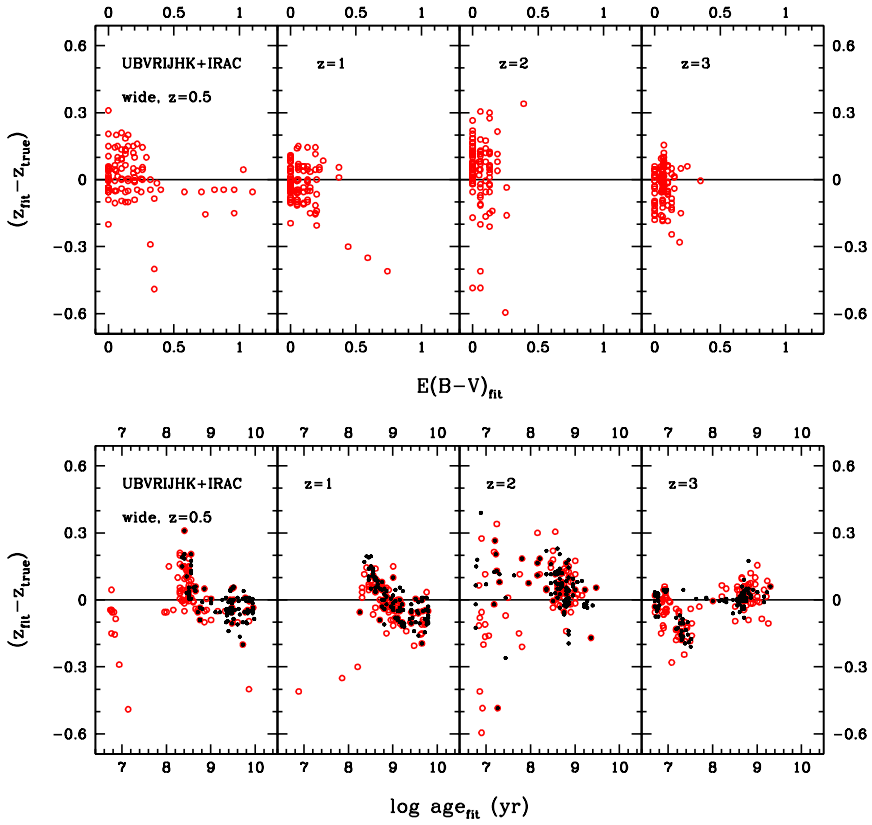

Figure 5.5: Redshift recovery for mock star-forming galaxies as a function of derived reddening (top row) and derived age (bottom row). Redshift increases from left to right. Red symbols refer to the case with reddening, black to the unreddened case.

Table 5.1: Redshift recovery as median($z_{fit} - z_{true}$) and 68% confidence levels for mock star-forming galaxies as a function of template setup, IMF and metallicity at each true redshift.

setup	$z_{true} = 0.5$	$z_{true} = 1$	$z_{true} = 2$	$z_{true} = 3$
no reddening				
wide Salpeter	$-0.0125^{+0.0675}_{-0.0525}$	$-0.0250^{+0.1150}_{-0.0750}$	$0.0600^{+0.0800}_{-0.0850}$	$-0.0050^{+0.0400}_{-0.1300}$
wide Kroupa	$-0.0100^{+0.0700}_{-0.0800}$	$-0.0400^{+0.1250}_{-0.0600}$	$0.0525^{+0.0775}_{-0.0925}$	$-0.0100^{+0.0500}_{-0.1400}$
wide Chabrier	$-0.0100^{+0.0650}_{-0.0750}$	$-0.0400^{+0.1250}_{-0.0650}$	$0.0500^{+0.0850}_{-0.0750}$	$-0.0050^{+0.0450}_{-0.1600}$
wide top-heavy	$-0.0225^{+0.1325}_{-0.0775}$	$-0.0300^{+0.1350}_{-0.0850}$	$0.0450^{+0.1150}_{-0.1650}$	$-0.1000^{+0.1450}_{-0.0700}$
wide best IMF	$-0.0050^{+0.1000}_{-0.0700}$	$-0.0200^{+0.1000}_{-0.0800}$	$0.0550^{+0.0800}_{-0.0750}$	$-0.0050^{+0.0500}_{-0.1200}$
wide Z=0.004	$0.0000^{+0.1000}_{-0.0700}$	$0.0075^{+0.0875}_{-0.0675}$	$0.0525^{+0.0925}_{-0.0875}$	$0.0050^{+0.0400}_{-0.1100}$
wide Z=0.01	$-0.0425^{+0.0475}_{-0.0475}$	$-0.0075^{+0.0975}_{-0.0975}$	$0.0450^{+0.1150}_{-0.1000}$	$0.0050^{+0.0450}_{-0.1750}$
wide Z=0.02	$-0.0400^{+0.0750}_{-0.0550}$	$-0.0100^{+0.0700}_{-0.0900}$	$0.0550^{+0.0750}_{-0.0750}$	$-0.0050^{+0.0400}_{-0.0450}$
wide Z=0.04	$-0.0600^{+0.1750}_{-0.0900}$	$-0.0550^{+0.1100}_{-0.1000}$	$-0.0200^{+0.1350}_{-0.1600}$	$-0.0300^{+0.0500}_{-0.0550}$
only-τ	$-0.0400^{+0.0800}_{-0.0550}$	$-0.0150^{+0.0700}_{-0.0850}$	$0.0525^{+0.0725}_{-0.1075}$	$0.0200^{+0.0300}_{-0.0500}$
with reddening				
wide Salpeter	$0.0500^{+0.1250}_{-0.0600}$	$-0.0200^{+0.0800}_{-0.0800}$	$0.0550^{+0.0950}_{-0.1100}$	$-0.0075^{+0.0675}_{-0.1175}$
wide Kroupa	$0.0050^{+0.1100}_{-0.0600}$	$-0.0125^{+0.0675}_{-0.0875}$	$0.0600^{+0.0850}_{-0.1150}$	$-0.0175^{+0.0625}_{-0.1075}$
wide Chabrier	$0.0025^{+0.1225}_{-0.0875}$	$-0.0075^{+0.0625}_{-0.0975}$	$0.0500^{+0.1000}_{-0.1200}$	$-0.0150^{+0.0650}_{-0.1000}$
wide top-heavy	$0.0050^{+0.1100}_{-0.0550}$	$-0.0500^{+0.1100}_{-0.0900}$	$0.0450^{+0.1050}_{-0.1500}$	$-0.0450^{+0.0750}_{-0.0600}$
wide best IMF	$0.0225^{+0.1075}_{-0.0725}$	$-0.0100^{+0.0750}_{-0.1100}$	$0.0650^{+0.0800}_{-0.1050}$	$-0.0075^{+0.0675}_{-0.0975}$
wide Z=0.004	$0.0025^{+0.1325}_{-0.0575}$	$0.0000^{+0.0750}_{-0.0600}$	$0.0600^{+0.1000}_{-0.0950}$	$-0.0025^{+0.0575}_{-0.1025}$
wide Z=0.01	$-0.0050^{+0.1150}_{-0.0600}$	$-0.0050^{+0.0650}_{-0.0950}$	$0.0450^{+0.0900}_{-0.1100}$	$-0.0125^{+0.0575}_{-0.1375}$
wide Z=0.02	$-0.0050^{+0.1250}_{-0.0850}$	$-0.0050^{+0.0600}_{-0.0600}$	$0.0650^{+0.0850}_{-0.1200}$	$-0.0150^{+0.0650}_{-0.0900}$
wide Z=0.04	$0.0025^{+0.0875}_{-0.1025}$	$-0.0525^{+0.0875}_{-0.0575}$	$0.0250^{+0.1250}_{-0.1700}$	$-0.0300^{+0.0850}_{-0.0850}$
only-τ	$-0.0050^{+0.1200}_{-0.0850}$	$-0.0100^{+0.0700}_{-0.0450}$	$0.0625^{+0.0875}_{-0.1025}$	$-0.0050^{+0.0650}_{-0.0800}$

at higher redshift.

With respect to the findings of Fig. 5.5 we investigated whether redshifts can be better recovered by using only one particular reddening law in the fit or by using a different age grid. Constraining the age grid by rebinning or applying a minimum age of 0.1 Gyr does not improve the median redshift estimate. For single objects at low redshift a minimum age constraint helps. Equivalently, we do not find any reddening law performing better than another or the best fit out of all reddening laws.

In summary, we find that redshifts are recovered quite well overall and the redshift recovery depends only weakly on template setup, IMF and metallicity because of compensating effects. Since the inclusion of reddening seems to help the redshift recovery the most economic template setup to use is an only-τ setup including reddening in the fit.

Redshifts are best recovered with a Salpeter IMF and low metallicity because the mock star-forming galaxies are based on a Salpeter IMF and consist predominantly of sub-solar metallicity populations. Redshifts are best recovered with a broad wavelength coverage which comprises the Lyman-limit and the 4000 Å break. Thus, red optical and near-IR filter bands are crucial in recovering the right redshift of high redshift objects. The redshifts of $z = 2$ objects are recovered worst, those of $z = 3$ objects best for this reason. Median recovered redshifts with their 68% confidence levels are summarised in Table 5.1.

5.3.2 Age

In Chapter 4 we established that mass-weighted ages seem to be best recovered in the fit, but that age is overall poorly recovered, especially for the oldest galaxies with little on-going star formation (see Fig. 4.2). Here, we confirm this result when redshift is a free parameter. In comparison to the fixed redshift case, ages of the oldest galaxies are better recovered (Fig. 5.6) such that very young ages ($< 10^8$ yr)[4] are less common in the fitting when reddening is included. However, ages are still underestimated in most cases because of the age-dust degeneracy (see Renzini, 2006, for a detailed description of this degeneracy and its effects). Additionally, fitted ages tend to anti-correlate with true ages (luminosity or mass-weighted) for the majority of the oldest objects when reddening is used in the fitting. This is clearly an effect of the added degeneracy with redshift.

In the unreddened case ages are better recovered compared to the reddened case and to the fixed redshift case but are still mostly underestimated. The only-τ setup recovers ages slightly better than the wide setup in the unreddened case. Because we find negligible difference to the case of fixed redshift studied in Chapter 4 at high redshift we do not show it here. Generally, ages at high redshift are better determined because of a smaller age range available in the fitting. Hence, the age-dust degeneracy has little effect and only the youngest obtained ages (below 10^8 yr) are underestimated. As already discussed in the previous chapter this is due to two reasons: 1) age-metallicity degeneracy - template metallicities are much higher than mock galaxy metallicities, thus, bluer colours are reproduced by younger ages, and 2) SFH mismatch between templates and mock star-forming galaxies.

Mono-metallicity wide template setups help to separate metallicity effects. Similarly to our findings in the previous chapter, when reddening is switched off and template metallicity is high, sub-solar metallicity galaxies are fitted with a younger age to compensate

[4] As in Section 4.3.1 these are predominantly fit with highly dust-reddened SSPs.

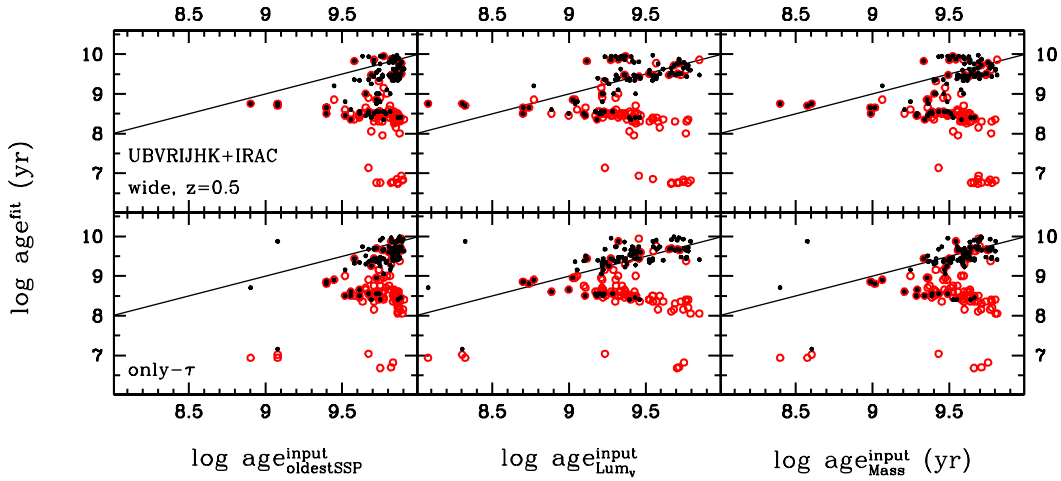

Figure 5.6: Best fit ages compared to input ages of mock star-forming galaxies for the wide and only-τ setups at redshift 0.5. Symbols as in Fig. 5.4. *Left:* Age of oldest present SSP. *Middle:* V-band luminosity-weighted ages. *Right:* mass-weighted ages. Fig. 4.2 shows the case at fixed redshift.

this mismatch. This trend persists even when reddening is introduced. When redshift is known metallicity effects are partly compensated by the age-dust degeneracy.

Although IMF effects on the redshift recovery are small, ages are more affected. Unlike in Chapter 4 where ages derived with templates of different IMF differ significantly, especially in the reddened case and at low redshift, ages are much more similar at low redshift when redshift is left free. Scatter in the reddened case is significantly reduced at low redshift. Because ages are otherwise very similar, we do not show them and only recap the effect. At $z \geq 2$ top-heavy IMF models give much older ages (and higher reddening) then Salpeter IMF models because of the age-dust degeneracy. Kroupa and Chabrier IMF models show systematically younger ages at these redshifts. In the unreddened case the effect of Kroupa and Chabrier IMF models is the same as in the reddened case. Ages derived with a top-heavy IMF are much younger.

Finally, we study the wavelength dependence of the derived ages. We showed in Fig. 5.4 that redshifts are significantly worse recovered for narrower wavelength coverages. However, results are similar to the ones in Chapter 4, thus we only summarise them here. In the unreddened case the oldest galaxies ($z = 0.5$) are affected very little by a lack in wavelength coverage. Excluding IRAC filters and using only optical wavelengths in the fitting focusses the age distribution between 0.1 and 1 Gyr. For higher redshift and intrinsically younger objects derived ages become younger as wavelength coverage decreases.

The more the wavelength coverage is restricted to the rest-frame UV, the younger the derived ages. Neglecting blue filter bands has a very small effect such that a few objects are rejuvenated. The inclusion of reddening has little impact on the general dependence of derived ages on wavelength coverage. Of course, due to the age-dust degeneracy ages are poorly recovered overall.

In summary, we find in agreement with Chapter 4 that ages are poorly recovered and underestimated in most cases. This depends on the redshift estimate at low redshift such that ages are underestimated[5] when redshifts are overestimated and vice versa. At high redshift ages are overestimated when redshift is overestimated and vice versa. However, at low redshift ages are slightly better determined when redshift is a free parameter. The age-metallicity degeneracy has a clearer effect and is not overshadowed by the age-dust degeneracy. Ages derived with different IMFs are more similar to each other than at fixed redshift, scatter is particularly reduced in the reddened case at low redshift. The difficulty of recovering the oldest age remains.

5.3.3 Metallicity

In Chapter 4 we showed that most template metallicities were too high and consequently metallicity was overestimated for most star-forming objects (Fig. 2.2 and 4.5). This is also the case when redshift is free, particularly at high redshift (Fig. 5.7), even when reddening is switched off. In the free redshift case the highest metallicity templates are chosen more frequently. However, when reddening is included derived metallicities are on average lower for the oldest galaxies. Furthermore, the metallicity is better recovered in the reddened case at free redshift compared to the reddened case at fixed redshift shown in the previous chapter (Fig. 4.5). The fact that statistically the fit is sensitive to metallicity is preserved when redshift is a free parameter in the fitting. This means that the number of best fit templates with low metallicities is larger at high redshift and vice versa for high metallicities.

The wavelength dependence of the metallicities in the unreddened case is such that when filter bands are omitted (red or blue alike) more objects are fitted with the lowest metallicity templates at low redshift. At high redshift the number of low metallicity best fit solutions decreases and that of high metallicity best fit solutions increases. This is further enhanced at each redshift when reddening is included in the fit. At known redshift the dependence on wavelength coverage was smaller overall and largest when only optical

[5] in comparison to the mass-weighted age

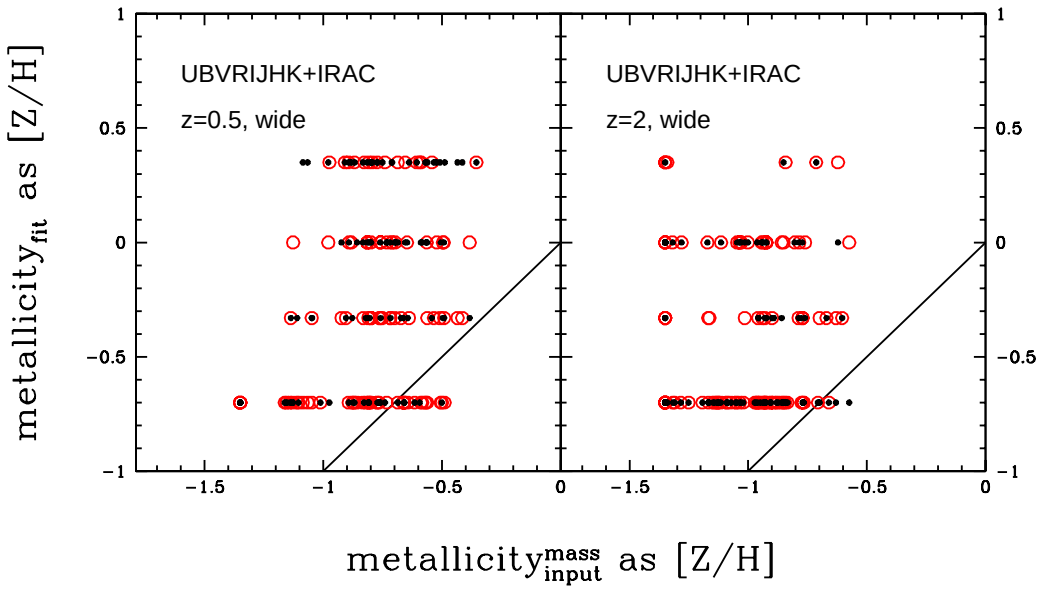

Figure 5.7: Comparison between recovered and mass-weighted metallicity of mock star-forming galaxies at redshift 0.5 and 2 for the wide setup. Black and red symbols refer to the cases without and with dust reddening, respectively. Template metallicities are -0.7, -0.33, 0 and 0.35 (from a fifth solar metallicity to twice solar metallicity). The black solid line is the line of equality. Fig. 4.5 shows the case at fixed redshift.

filter bands were used such that most galaxies were best fitted with the highest metallicity templates.

The conclusion remains that metallicities are poorly recovered because ages are poorly recovered.

5.3.4 E(B-V)

The recovery of dust reddening in the free redshift case studied in this chapter is very similar to the one at fixed redshift of Chapter 4. Therefore, we refer the reader to Fig. 4.6 and restrict ourselves here to a mere description of the reddening recovery and its dependence on template setup and wavelength coverage.

At $z \leq 1$ reddening is overestimated for all setups. However, the recovery is better than at fixed redshift. At $z = 2$ reddening is very well recovered for each template setup. At $z = 3$ reddening derived with the wide setup is slightly underestimated. Fits with the only-τ setup provide slightly larger reddening values (compare also Fig. 20 in M10, and

Section 6.1) and more scatter than those with the wide setup.

Again, as in Chapter 4, we find that fitted ages are younger at low redshift when reddening is included because of the age-dust degeneracy. However, compared to the previous chapter the degeneracy is weaker at redshift 0.5 [6] because redshift compensates.

When redshift is a free parameter the recovered reddening values are much more sensitive to the wavelength coverage, especially at high redshift, because the redshift depends on the wavelength coverage (see Fig. 5.4). Particularly, scatter increases at $z = 3$ when the rest-frame near-IR is not covered in the fit. When the filter setup only comprises optical filter bands reddening is overestimated at $z \geq 2$ (by up to $E(B-V) = 0.5$) because redshift is underestimated. Additionally, we find that omitting blue filter bands results in overestimated reddening at $z = 2$ because higher reddening and higher redshift are degenerate with a younger age.

Reddening depends only little on template metallicity. The largest effect is seen for the highest metallicity wide setup for which the scatter at $z = 3$ increases.
A cap on minimum age is less helpful as at fixed redshift because there are fewer very young objects. Still the overestimation of $E(B-V)$ is reduced from maximal $\Delta E(B-V) = 1.1$ to 0.6 at $z = 0.5$ and the scatter is smaller at high redshift. Rebinning the age grid does not improve the reddening estimate at any redshift.

5.3.5 Stellar Mass

We demonstrated in M10 (Section 6.1) and Chapter 4 that star formation histories are the most important factor for recovering the stellar mass. Hence, the choice of template setup affects the result. At fixed redshift we found that masses are underestimated by a median of 0.6 dex at low redshift and in the reddened case because of the age-dust degeneracy and SFH mismatch. At high redshift masses are perfectly recovered using inverted-τ models with high formation redshift and τ's larger than 0.3 Gyr (M10 and compare Fig. 4.7).

Although masses are still underestimated, the mass recovery is on average better at low redshift for the wide setup when redshift is a free parameter in the fitting (Fig. 5.8 and Fig. 5.9). In the unreddened case the improvement on the median mass is 0.1 dex, in the reddened case 0.3 dex for one σ uncertainties in redshift of ± 0.06 and -0.06 to 0.12,

[6] Fewer objects have $E(B-V) \sim 0.4 - 1.2$ and ages are lower by ~ 3 dex

respectively (median redshifts are within $\pm \sim 0.01$). Overall, differences between the reddened and unreddened case are much smaller than at fixed redshift (Chapter 4) because redshift compensates for SFH and metallicity mismatch, age-dust degeneracy and overshining - the main reasons why masses are underestimated for the oldest galaxies when redshift is fixed. However, when reddening is included, the mass recovery fails completely for objects for which the redshift is underestimated the most. For these objects a very low redshift combined with a high amount of reddening, mostly very young ages and a single burst SFH results in very low stellar masses. In Chapter 4 solutions with the largest mass underestimation because of the age-dust degeneracy could largely

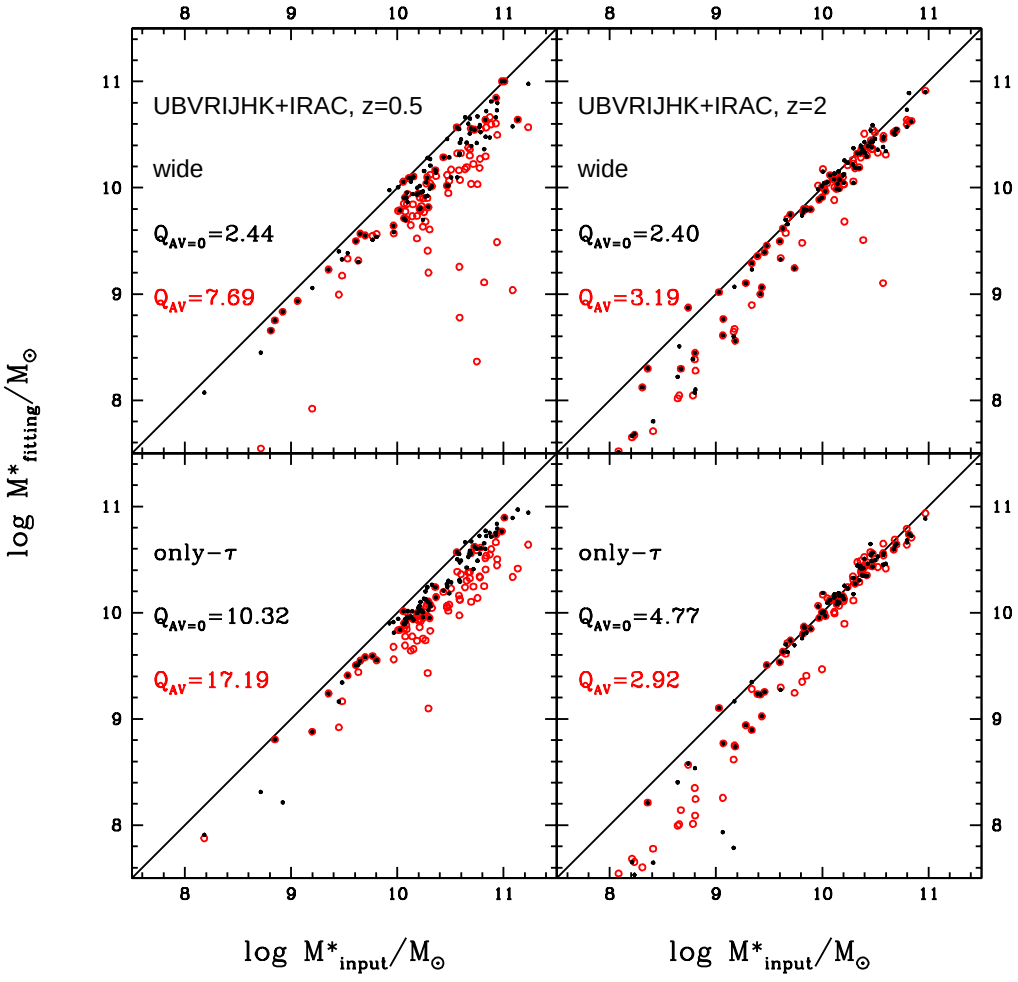

Figure 5.8: Stellar mass recovery at redshift 0.5 (left) and 2 (right) as a function of template setup (from top to bottom in each panel: wide, only-τ). Red circles refer to cases with reddening, black dots to no reddening. Quality factors are given for the entire mass range for reddened and unreddened cases, respectively. Fig. 4.7 shows the case at fixed redshift.

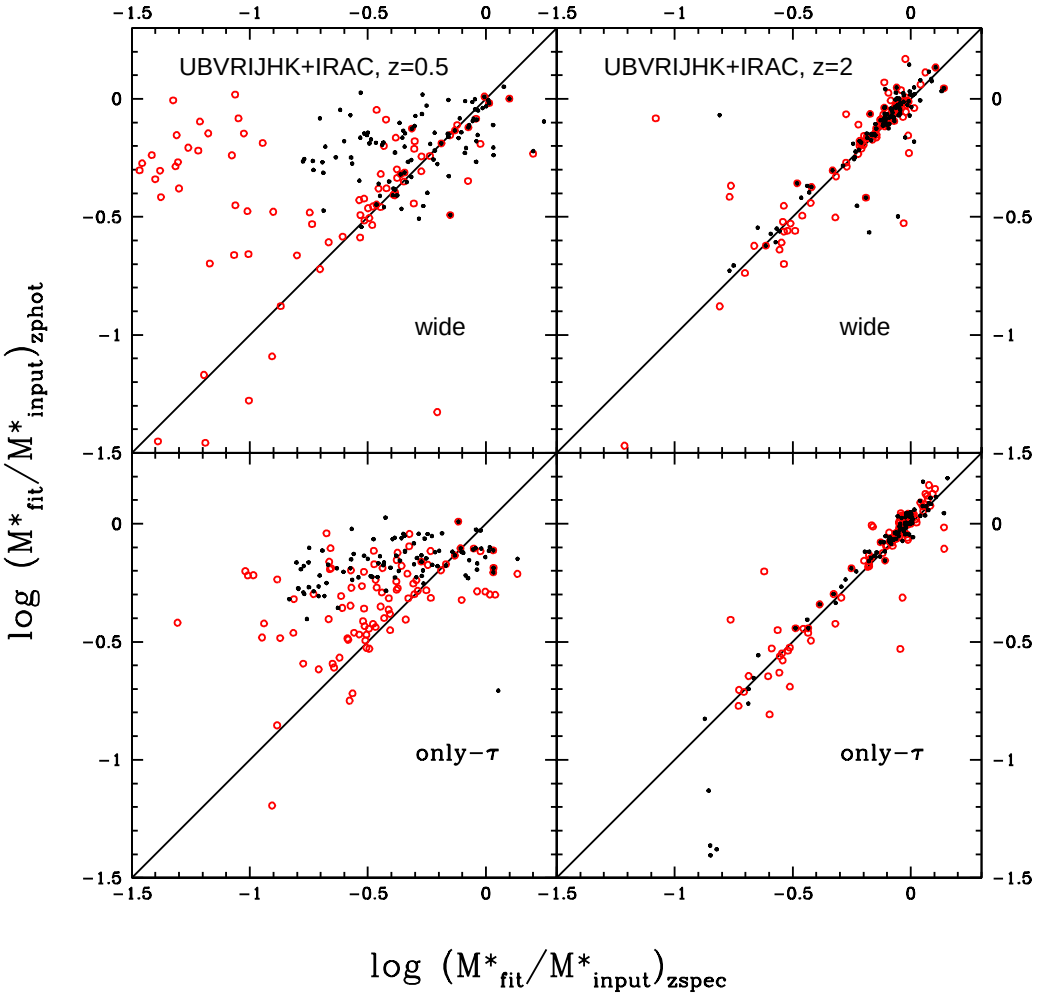

Figure 5.9: Stellar mass recovery at redshift 0.5 (left) and 2 (right) as a function of template setup (from top to bottom in each panel: wide, only-τ) when redshift is fixed or a free parameter in the fit. Red circles refer to cases with reddening, black dots to no reddening. The most extreme outliers for which the mass recovery fails when redshift is a free parameter are not shown in this plot.

be avoided by 1) excluding SSPs or 2) introducing a minimum age. For the mass recovery at unknown redshift the minimum age constraint is most effective at low redshift (see discussion below). Excluding SSPs has no effect at low redshift, but improves the mass estimate slightly at higher redshift.

The only-τ setup seemingly performs better than the wide setup at low redshift because SFHs are a better match. But as the quality factors in Fig. 5.8 indicate, this setup produces a few outliers in redshift and the mass recovery fails (both are 0) in both the reddened and unreddened case. These objects belong to the most metal-poor ones. Apart from

that, masses are generally less underestimated (Fig. 5.9). At high redshift masses are nearly equally as well recovered as in the fixed redshift case for both setups independently of dust reddening, meaning a good recovery for masses between 10^{10} and $10^{11} M_{\odot}$ and underestimation at the low mass end. As discussed in the previous chapter these are small disks and show increasing star formation (compare panel a) of Fig. 2.3 left-hand side). In particular, for redshifts above 2 this means that photometry seems sufficient to accurately determine redshifts and stellar population parameters, such as stellar mass, simultaneously.

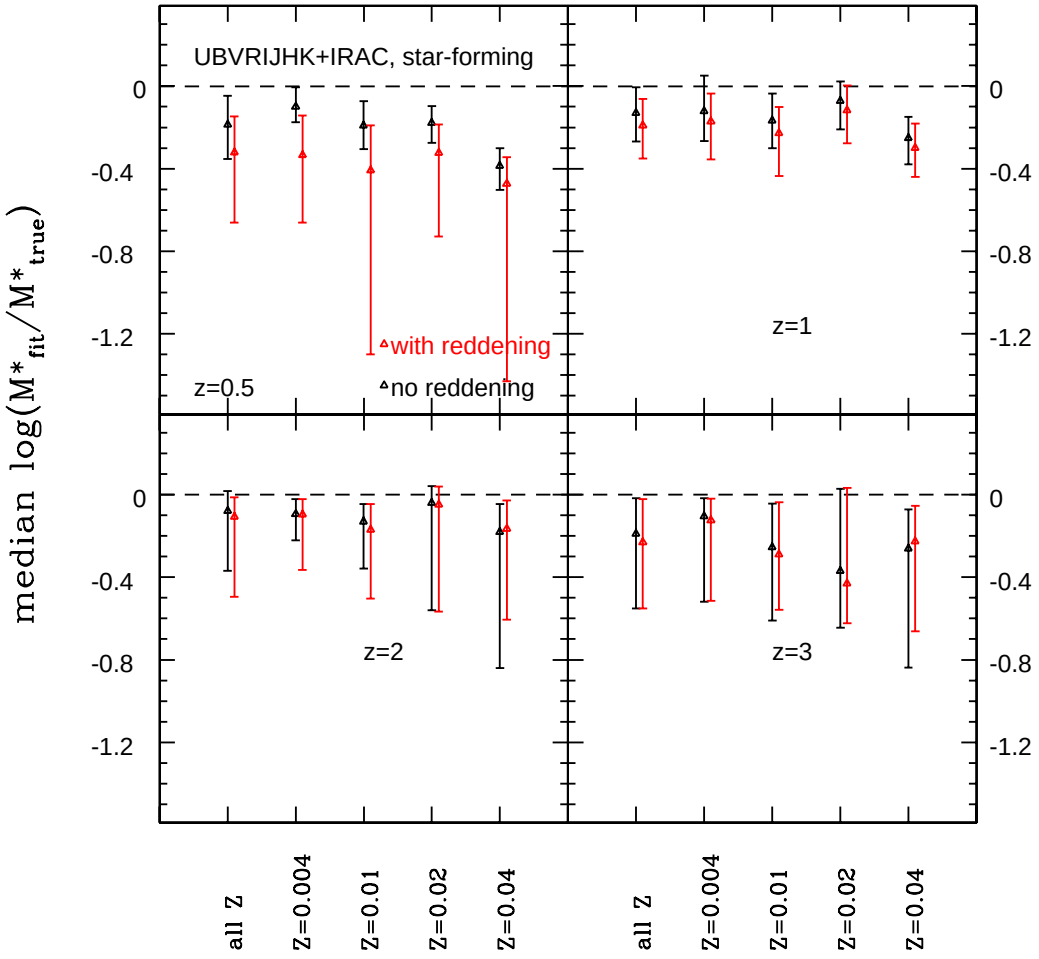

Figure 5.10: Median recovered stellar mass with 68% confidence levels as function of template metallicity. Redshift increases from upper left to lower right. Red and black symbols refer to mock star-forming galaxies with and without reddening, respectively. The number of catastrophic failures ($z = 0$ and mass $= 0$) increases with metallicity. Fig. 4.8 shows the case at fixed redshift.

In Fig. 5.10 we show the metallicity dependence of the mass recovery in more detail. Overall, metallicity effects are of similar size as at fixed redshift. This means that at low redshift, the median difference between true and recovered mass changes by ~ 0.2 dex between the lowest and the highest metallicity setup. At redshift 3 metallicity effects can alter the median mass recovery by ~ 0.3 dex (~ 0.2 dex at fixed redshift). The lowest metallicity setup provides the best mass recovery at most redshifts because the template metallicity is closer to the input metallicity of the mock galaxies (compare Fig. 2.2). Generally, the scatter is largest at high redshift and for the highest metallicity templates. Reddening affects mostly the low redshift case resulting in a larger offset and larger scatter. Overall metallicity effects are small and metallicity cannot be recovered in the fit. Hence, it is sufficient and more economic to fit star-forming galaxies with a mono-metallicity setup as concluded in the previous chapter and Bolzonella et al. (2010).

It is common practice to introduce a cut in minimum age in the fit in order to improve upon the mass estimate (Wuyts et al., 2009; Bolzonella et al., 2010) and we have demonstrated in the previous chapter that $age_{min} = 0.1$ Gyr works sufficiently well, particularly at low redshift. Although the minimum age constraint does not affect the median (or mean) redshift estimate much, the mass estimate still profits from this restriction at low redshift (Fig. 5.11) such that the mean recovered mass improves from -0.49 ± 0.59 to -0.33 ± 0.20 (median improves by ~ 0.01 dex). At high redshift, the underestimation at the low mass end worsens with this age constraint and also the mean recovered redshift is much worse (particularly at $z = 3$). We find that a simple rebinning of the age grid has a negligible effect at low redshift and can even damage the mass estimation at high redshift, similarly to our findings in Chapter 4.

Differences in stellar mass recovery when using different IMFs for the fitting templates (Salpeter, Kroupa and Chabrier IMF) are small and amount to ~ 0.2 dex (Fig. 5.12, also compare Fig. 4.11). However, other parameters in the fitting like age and SFH can compensate for the wrong IMF and consequently, mass offsets between the IMFs show significant scatter, particularly for galaxies with little star formation. However, the scatter is smaller for these galaxies compared to the one reported in Chapter 4. Masses derived with top-heavy IMF templates are very poorly recovered and show large scatter. Although the fit is sensitive to the choice of IMF the correct IMF cannot be identified by means of the smallest χ^2_ν among all IMFs. This was already the case at fixed redshift in Chapter 4 and confirms conclusions of M10 (Section 6.1) and the previous chapter that the minimum χ^2_ν does not necessarily provide the best physical solution.

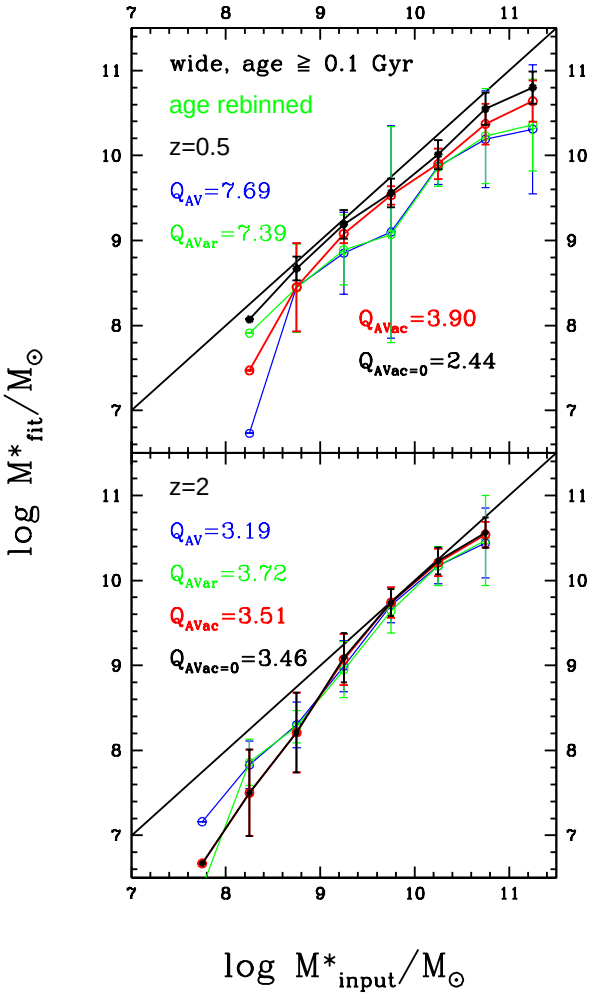

Figure 5.11: Average recovered stellar mass in given input mass bin (binsize 0.5 dex) for the wide setup with a minimum age of 0.1 Gyr and a rebinned age grid. Red points and lines represent the reddened case, black stands for the unreddened case, blue thin lines show recovered masses obtained with the full age grid including reddening, green thin lines refer to a setup with rebinned age grid and reddening. Errorbars are one standard deviation. Quality factors are given for the entire mass range. Fig. 4.9 shows the case at fixed redshift.

Finally, we focus on the effect of different filter setups, i.e. wavelength coverage, on the stellar mass recovery for the wide setup (Fig. 5.13). The mass recovery follows the redshift recovery such that when redshifts are poorly recovered, stellar masses are poorly recovered as seen in the case for the highest metallicities. This means, for older galaxies with little on-going star formation ($z = 0.5 - 1$) the lack of coverage in the IRAC bands results in a median mass recovery that is underestimated more by 0.2 dex (~ 0.1 dex in the reddened case) compared to the full wavelength coverage. Also the scatter increases

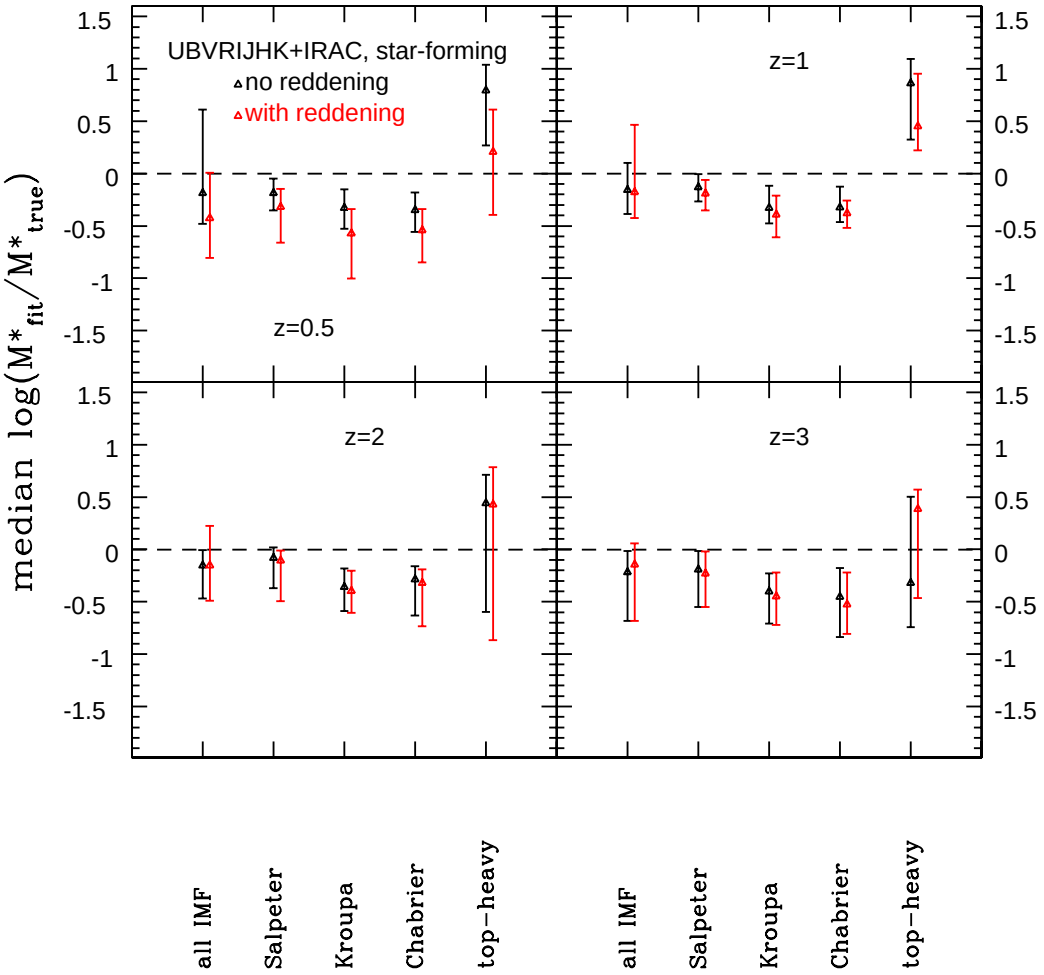

Figure 5.12: Median stellar mass recovery as a function of redshift and IMF (wide template setup and UBVRIJHK+IRAC wavelength coverage for each). Errorbars are 68% confidence levels. Redshift increases from the top left to the bottom right. Red and black mark solutions for mock star-forming galaxies obtained with and without reddening, respectively. The missing median values at $z = 2$ for UBVRI are $-2.39^{+1.43}_{-3.85}$ in the unreddened case and $-2.23^{+1.43}_{-1.48}$ in the reddened case. The case at fixed redshift is shown in Fig. 4.11.

with the lack of IRAC filter bands. When near-IR filter bands are missing, too, the scatter increases even further such that now masses are also overestimated. Generally, the scatter is larger when reddening is included. The lack of blue filter bands has only very little effect on the mass recovery because the effect on the redshift recovery is small, too. For young galaxies with high SFRs at $z = 2$ excluding IRAC and near-IR filter bands in the fit results in a catastrophic failure of the mass recovery. For the narrowest wavelength coverage the median recovered mass is underestimated by more than two orders of magnitude and the scatter spreads across five orders of magnitude (for UBVRI at $z = 2$). This

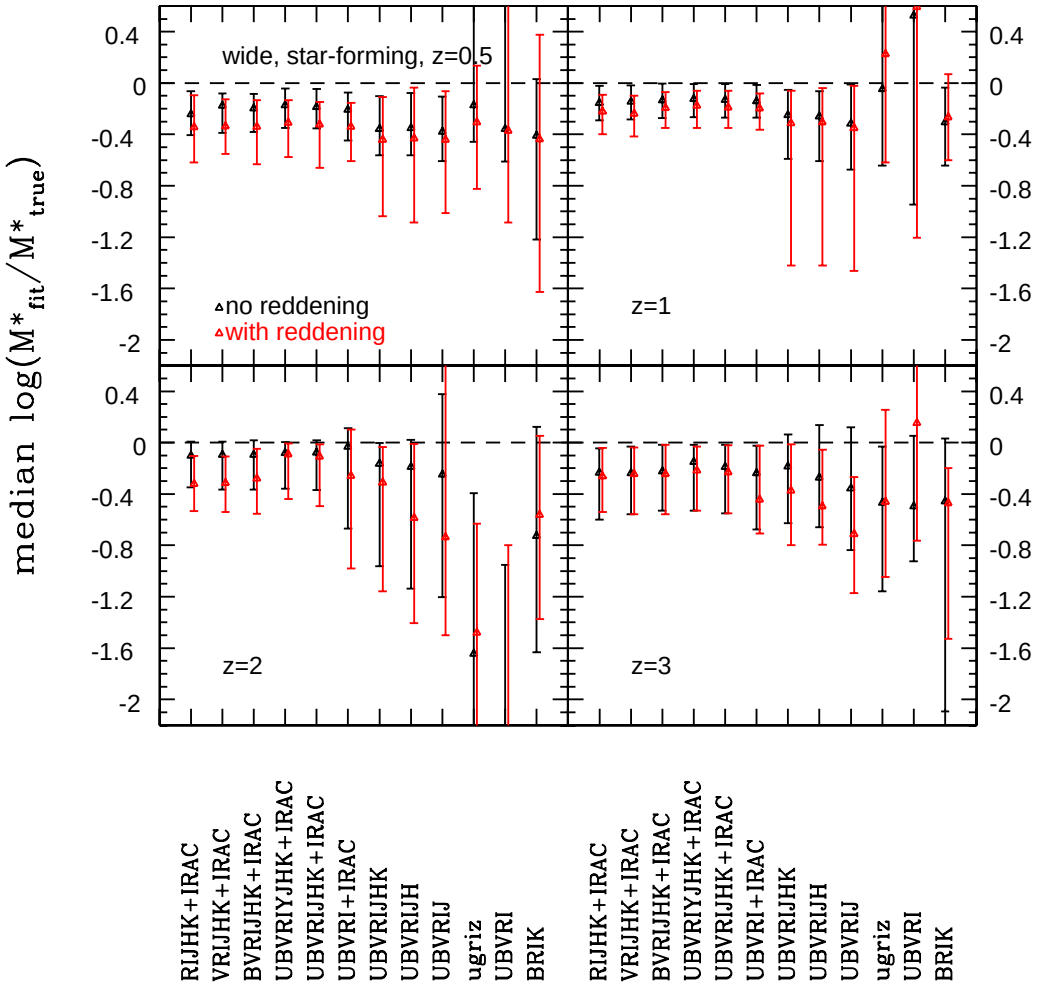

Figure 5.13: Median difference between true and recovered stellar mass with 68% confidence levels as function of wavelength coverage and filter set at redshifts 0.5, 1, 2 and 3. The filter setup is varied from left to right in each panel, redshift increases from the top left to the bottom right. Symbols as in Fig. 5.8. The case of fixed redshift is shown in Fig. 4.12.

is clearly due to the failure in recovering the redshift with these filter setups. Because the redshift recovery is better at $z = 3$, masses are not underestimated as much as those at $z = 2$ for similar wavelength coverages. The median recovered mass is underestimated by ~ 0.3 dex more than for the broadest wavelength coverage. Omitting blue filter bands has little effect in the unreddened case. In the reddened case masses are underestimated by ~ 0.35 dex at $z = 2$.

At each redshift, masses are best recovered when the wavelength coverage is broad independently of the use of reddening. Especially, the coverage of the rest-frame near-IR

is crucial as already concluded by Lee et al. (2009) and Kannappan & Gawiser (2007); Bolzonella et al. (2010) and M06 at known redshift.

When redshift is known and held fixed in the fit, we found that the mass recovery of older galaxies with little star formation (at $z = 0.5$) is worse than when redshift is free but depends only weakly on the wavelength coverage. At fixed, low redshift masses are underestimated by ~ 0.3 dex in the unreddened case and ~ 0.7 dex in the reddened case and the scatter is large. At $z = 1$, the main effect is that scatter increases when wavelength coverage decreases. At $z \geq 2$ the dependence on wavelength coverage is similar to the one shown here but less strong. e.g. the median recovered mass is underestimated by one order of magnitude in the reddened case for UBVRI at $z = 2$. Masses are better determined at fixed, high redshift when the rest-frame UV is excluded in the fit because the fit is carried out on the mass-sensitive part of the SED while ignoring the contribution of recently formed stars. When redshift is free, however, the exclusion of the rest-frame UV is harmful because the redshift recovery crucially depends on this wavelength range. We identified mismatch in SFH and overshining as the main reasons for underestimated ages and thus underestimated masses in Chapter 4. With inverted-τ models we were able to rectify this. Here, a large factor is also the recovery of the correct redshift and we do not expect inverted-τ models to help with that.

Excluding SSPs from the wide template setup, reduces the scatter in the reddened case for fitting setups adopting a narrower wavelength coverage at $z \leq 2$ as long as at least 6 filter bands and either near-IR or IRAC bands are added to the optical. At $z = 3$ the median mass recovery improves for filter setups excluding the UV.

In summary, we find that although the stellar masses of mock star-forming galaxies are still underestimated, they are better determined in most cases when redshift is a free parameter in the fit, independently of template setup. This is valid for a redshift recovery within ~ 0.1 at low redshift. At low redshift, some catastrophic failures occur however, due to catastrophic failures in redshift. Metallicity adds an uncertainty of ~ 0.2 dex to the mass estimate. The same is true for IMF effects. The mass estimate can be improved with an artificial age constraint at low redshift, whereas at high redshift this does not help. As in the fixed redshift case, masses are best determined at each redshift using a broad wavelength coverage in the fit because then also redshifts and ages are best determined. A lack in filter bands generally results in a worse performance and larger scatter. The inclusion of reddening has the largest impact at low redshift because of degeneracies between age, dust and redshift.

5.3.6 Star formation history and star formation rate

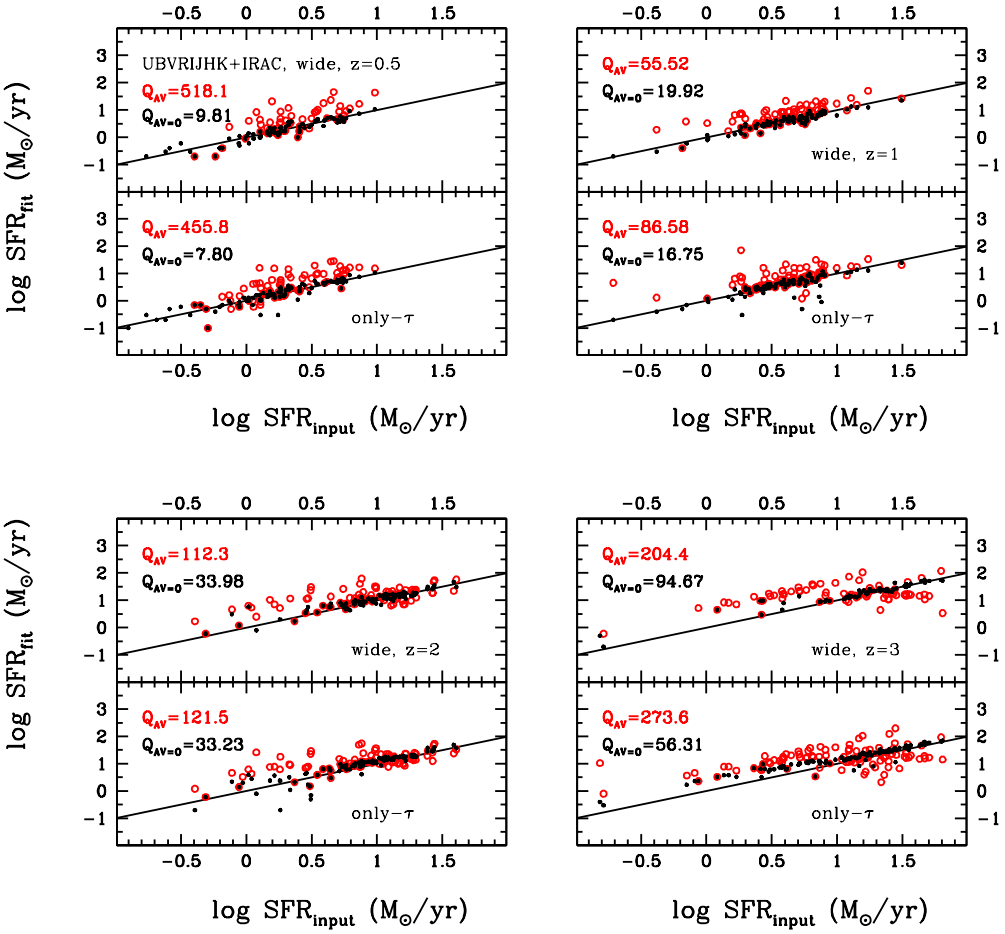

Figure 5.14: Comparison between SFR derived from SED-fitting and input SFR as a function of template setup and redshift. The template setup is varied in each panel (wide, only-τ and inverted-τ from top to bottom), redshift increases from top left to bottom right. Symbols are the same as in previous figures. Objects with SFR=0 are not shown. SFR=0 indicates that the best fit solution is an SSP or a truncated SF model with an age larger than the truncation time. Fig. 4.14 shows the case at fixed redshift.

In Fig. 5.14 we show the SFR recovery as a function of template setup. SFRs agree very well with input SFRs only when the reddening is switched off. However, the recovery gets worse with increasing redshift, and thus increasing SFR. At $z = 3$ the difference between the wide and only-τ setup is largest, such that the only-τ setup overestimates the SFR and many SFRs are zero with the wide setup because the best fit template is a SSP. At each redshift the only-τ setup recovers the SFRs best according to Q. When reddening is included the wide setup takes the lead at $z \geq 1$. However, SFRs are overestimated for

all template setups due to underestimated ages caused by the age-dust degeneracy. At redshift 3 the highest SFRs are underestimated instead.

Qualitatively, the SFR recovery is similar to the one at fixed redshift shown in Fig. 4.14. When redshift is left free, though, SFRs are overestimated less at $z \leq 1$ and underestimated more at $z = 3$. We concluded in the previous chapter that the mismatch between template and mock galaxy SFH is the biggest driver. Clearly, the rising SFRs at high redshift are not very well matched by any SFH in the wide or only-τ setup. Inverted-τ models (with high formation redshift and $\tau > 0.3$) recovered the SFRs for star-forming galaxies with rising SFH best in M10 (Section 6.1) and Chapter 4. Furthermore, we demonstrated in M10 that the SFRs derived from inverted$-\tau$ models are in excellent agreement with those derived from the UV-slope method for high-redshift star-forming galaxies in the GOODS-S sample (see Fig. 19 in M10).

Similarly to the mass estimate, the SFR recovery profits from a minimum age constraint mainly at low redshift where the age-dust degeneracy is controlled the most by this practical trick. The biggest effect is seen for the lowest SFRs which are less overestimated (Fig. 5.15). Rebinning the age grid, however, causes SFRs to be even higher. At higher redshift the high-SFR end is affected the most such that SFRs are less underestimated. Again, the SFR estimate is hampered by rebinning the age grid, the highest SFRs are now even more underestimated. These results are very similar to the ones obtained at fixed redshift in Chapter 4 (compare Fig. 4.15).

Because SFRs obtained with Kroupa, Chabrier or top-heavy IMF templates show the same behaviour independently of redshift as a free or fixed parameter we only summarise the effect here and refer the reader to Fig. 4.16. In the unreddened case, SFRs from Kroupa and Chabrier IMF templates are lower than those from Salpeter IMF templates and thus underestimate the SFRs. Top-heavy IMF templates perform significantly worse such that SFRs are even lower, show a clear offset and are mostly zero at high redshift. When reddening is included SFRs from Kroupa and Chabrier templates are overestimated at low redshift and underestimated at high redshift. SFRs from a top-heavy IMF are underestimated at each redshift when reddening is involved.

The effect of wavelength coverage on the derived SFRs is shown in Fig. 5.16. As in the fixed redshift case SFRs are generally well recovered in the unreddened case partly because of compensating effects. The recovery gets worse when rest-frame near-IR and red optical filter bands are excluded. At low redshift, SFRs are then overestimated. At high redshift more SFRs are zero. The same happens at low redshift when reddening is

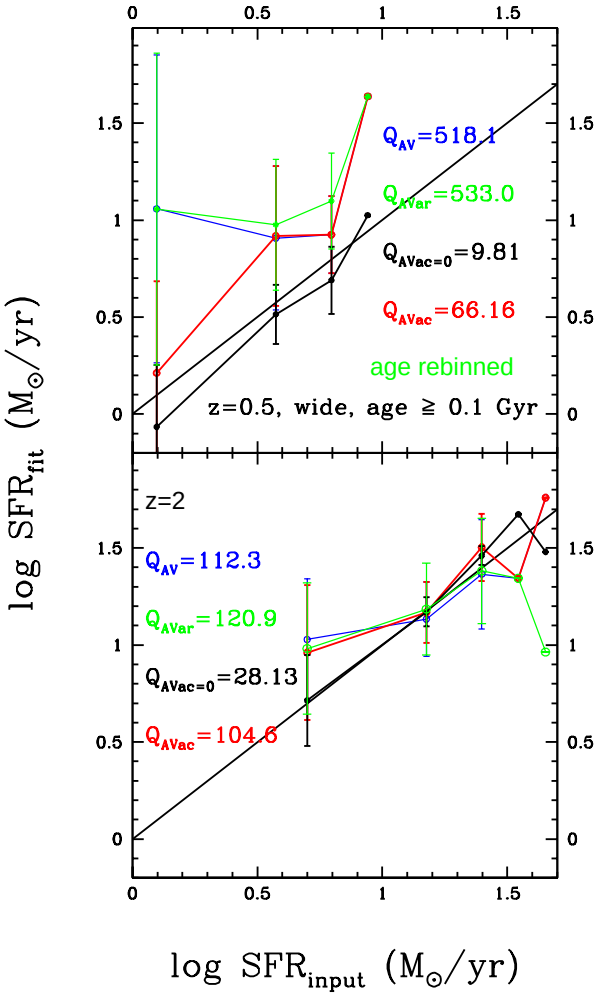

Figure 5.15: Average recovered SFRs (y-axis) compared to known binned SFRs at redshift 0.5 and 2 as a function of age grid. Red dots and lines represent solutions with reddening, black ones those without reddening, for both a wide setup with minimum age of 0.1 Gyr is used in the fit. Blue thin lines show the SFR recovery with a wide setup and reddening for the full age grid. Green lines show the result for the rebinned age grid when reddening is included. Bin sizes vary from $2.5\ M_\odot$/yr to $20\ M_\odot$/yr from $z = 0.5$ to $z = 3$. Errorbars are one standard deviation. Quality factors are given for the entire SFR range. The case at fixed redshift is shown in Fig. 4.15.

included. At high redshift scatter increases for the shortest wavelength coverage. Taking out blue filter bands results in higher SFRs at low redshift and particularly at $z = 2$ because of a larger offset in redshift for these filter sets (compare Fig. 5.4). In Chapter 4 (at fixed redshift) we found the largest effect on the recovered SFRs in the reddened case when blue filter bands are lacking because the most recent star formation is encoded in the rest-frame UV.

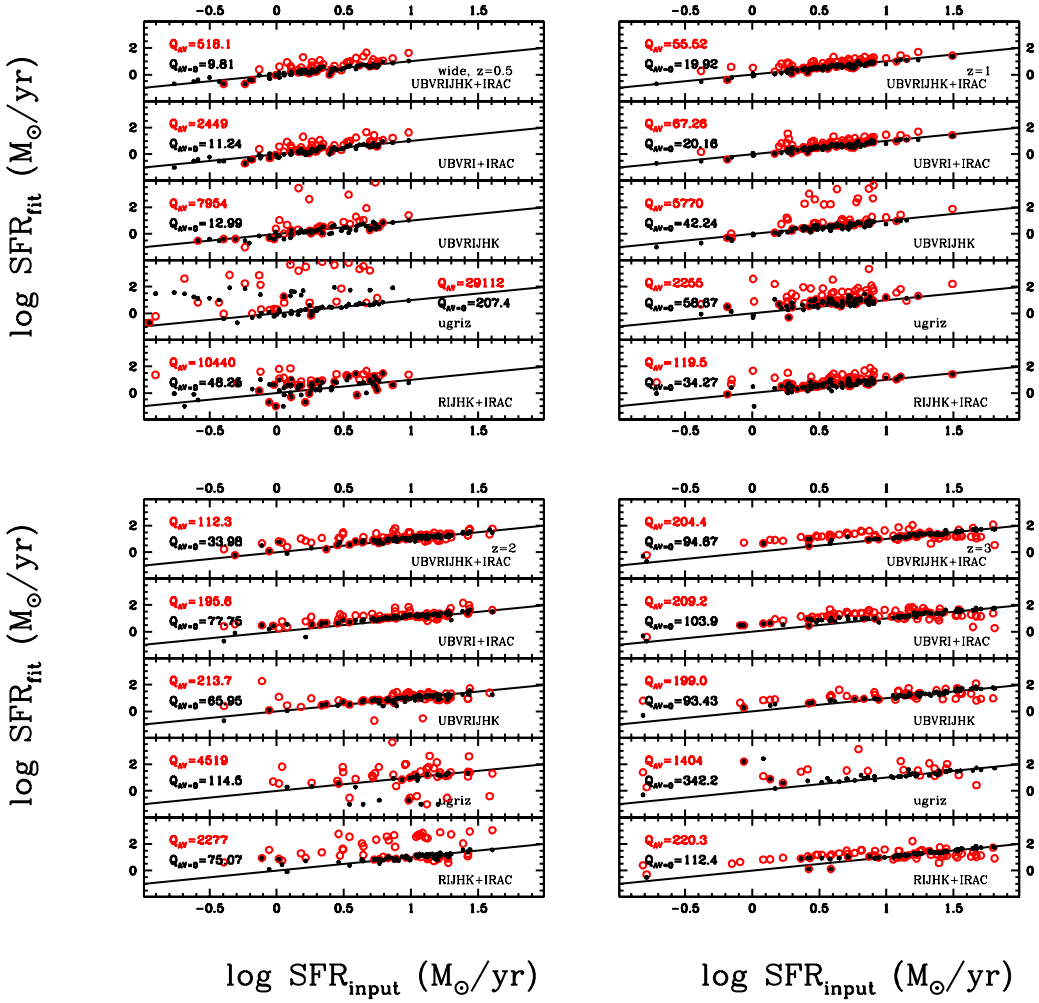

Figure 5.16: SFR recovery at $z = 0.5$, 1, 2 and 3 as a function of wavelength coverage. Objects with SFR=0 are best fit with a SSP or a truncated model with age larger than the truncation time and are not shown in this plot. The filter setup is varied from top to bottom in each panel, redshift increases from top left to bottom right. Red circles refer to the reddened case, black dots to the unreddened case. Fig. 4.17 shows the fixed redshift case.

In summary, when redshift is a free parameter in the fit SFRs are best recovered with the broadest wavelength coverage and a wide template setup although the right SFHs might not be contained in it. SFR estimates can be improved at low redshift using an age constraint. Using templates with Kroupa, Chabrier or top-heavy IMF results in underestimated SFRs. Reddening causes SFRs to be overestimated instead.

5.4 Results for passive galaxies

After describing the results for mock star-forming galaxies for redshift, age, reddening, metallicity, stellar mass and star formation rates, we now focus our attention on the recovery of the listed properties (except star formation rates) for mock passive galaxies.

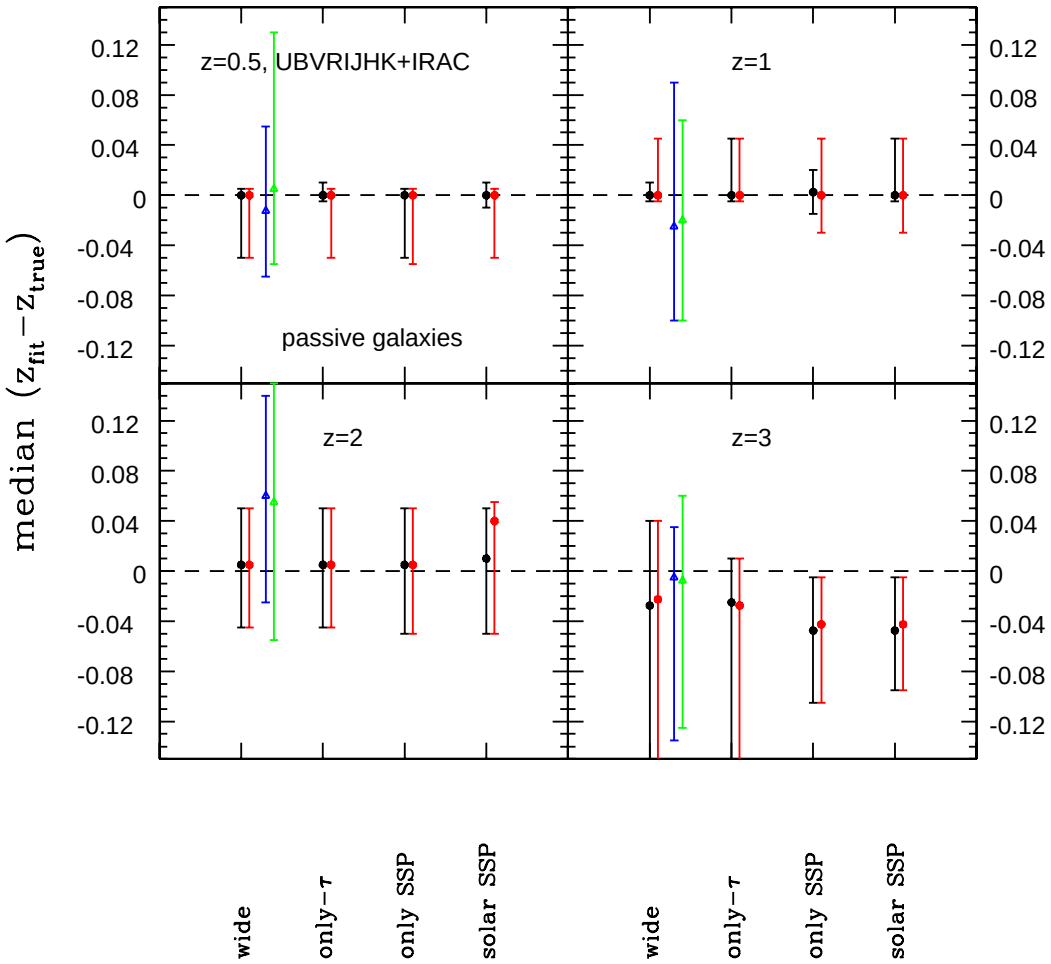

Figure 5.17: Median redshift recovery for mock passive galaxies as a function of template setup, namely wide, only-τ, only SSPs and solar SSP, using a broad wavelength coverage (UBVRIJHK+IRAC). Black symbols refer to the case without reddening, red ones to the reddened case. The blue and green symbols refer to the redshift recovery of mock star-forming galaxies obtained with the wide setup without and with reddening, respectively (compare also points for 'all Z' in Fig. 5.2). Errorbars are 68% confidence levels.

5.4.1 Photometric redshift

In Fig. 5.17 we show the redshift recovery of mock passive galaxies as a function of template setup. Due to their age and passive nature which results in a well established 4000 Å break and absence of overshining we expect the redshift estimation for these passive galaxies to be better than those for mock star-forming galaxies. Overall, redshifts are recovered very well, independently of template setup in the unreddened case. Redshifts of $z = 3$ objects are recovered slightly worse ($\Delta z \lesssim 0.1$) than those of lower redshift ones because of the slight mismatch in age[7] which is overcompensated by a combination of older age, prolonged SFH and lower redshift. In the reddened case we find larger scatter at the lowest redshift in general and for setups with wide ranges in metallicities in particular. Here, the redshift recovery fails for a few objects (5%) because of degeneracies between age, dust, metallicity and redshift. Instead of being old, these objects are misidentified as very young, very dusty, high metallicity, high redshift single bursts.

In order to single out the effect of metallicity we performed the fitting using mono-metallicity wide setups. The resulting median redshift recoveries are shown in Fig. 5.18. Clearly, redshifts are best recovered with templates of the right metallicity even when the SFH is not the right one. When reddening is excluded the SFH can compensate for the wrong metallicity and when the template metallicity is not too low (or high) the redshift recovery is still decent. Redshifts are systematically overestimated for the lowest metallicity templates. When reddening is included, the scatter and outlier fraction increases, particularly for the oldest objects ($z \leq 1$). For the lowest metallicity, the redshift recovery is still the worst and the scatter is very large. Although lots of objects are fit with the right SFH (namely a SSP), albeit with very young ages, large amounts of dust and a high redshift fail in compensating the blue colour required by the metallicity.

Fig. 5.3 in Section 5.3.1 showed that the IMF plays a minor role with respect to the redshift recovery of mock star-forming galaxies. We find the same for the mock passive galaxies and hence abstain from displaying it here. As for the mock star-forming galaxies, the right IMF cannot be identified for mock passive galaxies by pure means of minimum χ^2_ν.

Fig. 5.19 summarises the effect of wavelength coverage on the redshift determination for mock passive galaxies. Overall, like for mock star-forming galaxies, the redshifts of mock passive galaxies are best determined with a broad wavelength coverage. In the

[7] For ages of 1 and 1.5 Gyr the closest matching age of the template age grids are 1.015 Gyr and 1.434 Gyr.

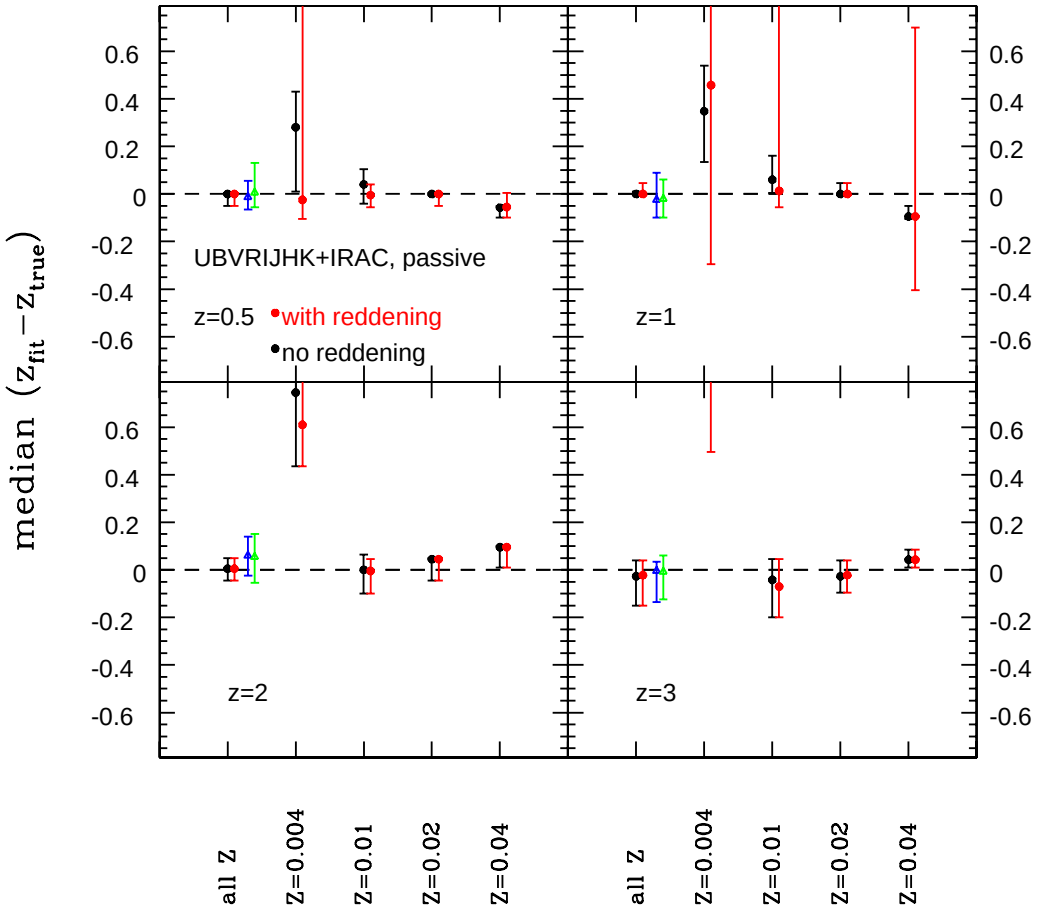

Figure 5.18: Median redshift recovery for mock passive galaxies as a function of metallicity using a broad wavelength coverage (UBVRIJHK+IRAC). Symbols and colours are the same as in Fig. 5.17, but note the different scale.

unreddened case, the wavelength dependence is weak and only for the most restricted wavelength coverages (mainly for a BRIK filter set) and youngest galaxies does scatter increase such that the redshift is overestimated. In the reddened case, the redshift estimate becomes less robust and shows large scatter when near-IR and IRAC bands are omitted for the oldest galaxies. Likewise a lack of blue filter bands results in overestimated redshifts at $z = 0.5$ because the rest-frame blue and thus the 4000 Å break is not covered anymore. At higher redshift, redshifts are overestimated when the wavelength coverage is most restricted. Additionally, a lack of near-IR filters results in a worse redshift recovery because the 4000 Å break is excluded.

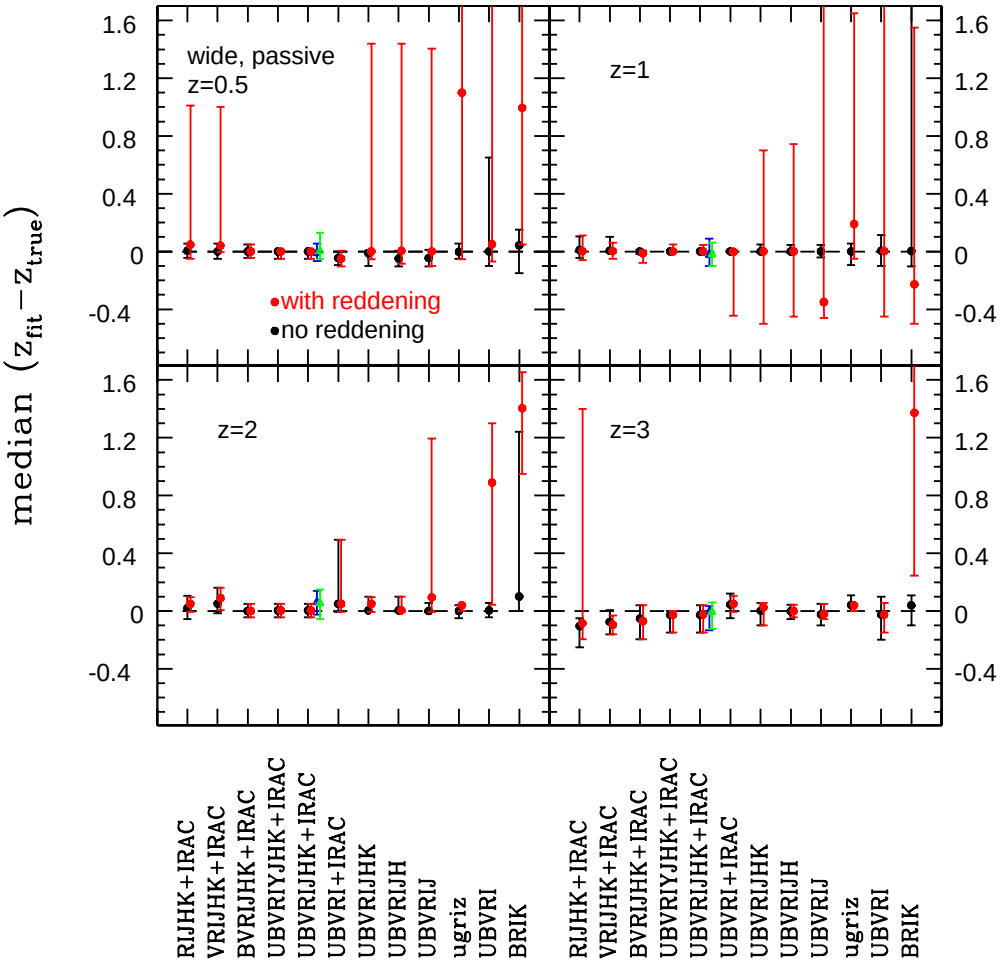

Figure 5.19: Median redshift recovery with 68% confidence levels for mock passive galaxies as a function of wavelength coverage using a wide setup in the fit. Symbols and colours are the same as in Fig. 5.17.

In summary, redshifts of mock passive galaxies can be very well determined, independently of template setup, meaning SFH, and IMF. Metallicity plays an important role in the redshift recovery and because the right metallicity can be identified passive mock galaxies should be fit with a wide range in metallicities. As for mock star-forming galaxies, redshifts of mock passive galaxies are best determined when a broad wavelength coverage is used in the fit. Restricted wavelength coverages result in overestimated redshifts, especially when reddening is included because of degeneracies between age, dust and redshift.

5.4.2 Age

The effect of template setup on the derived ages of mock passive galaxies is similar to the fixed redshift case in Chapter 4. Fig. 5.20 compares the success of the wide, only-τ, only SSPs and only solar SSP template setups in recovering the correct age. Overall, the median recovered ages show very little offset. The wide setup generally tends to overestimate the ages and shows the largest scatter at each redshift. This is due to the wide range in star formation histories and metallicities included in this setup. Ages are still slightly overestimated for the only-τ setup at low redshift although it contains only the correct metallicity (solar in our case). Here, the star formation history mismatch is compensated by older ages. The comparison with the age recovery of the SSP setups at

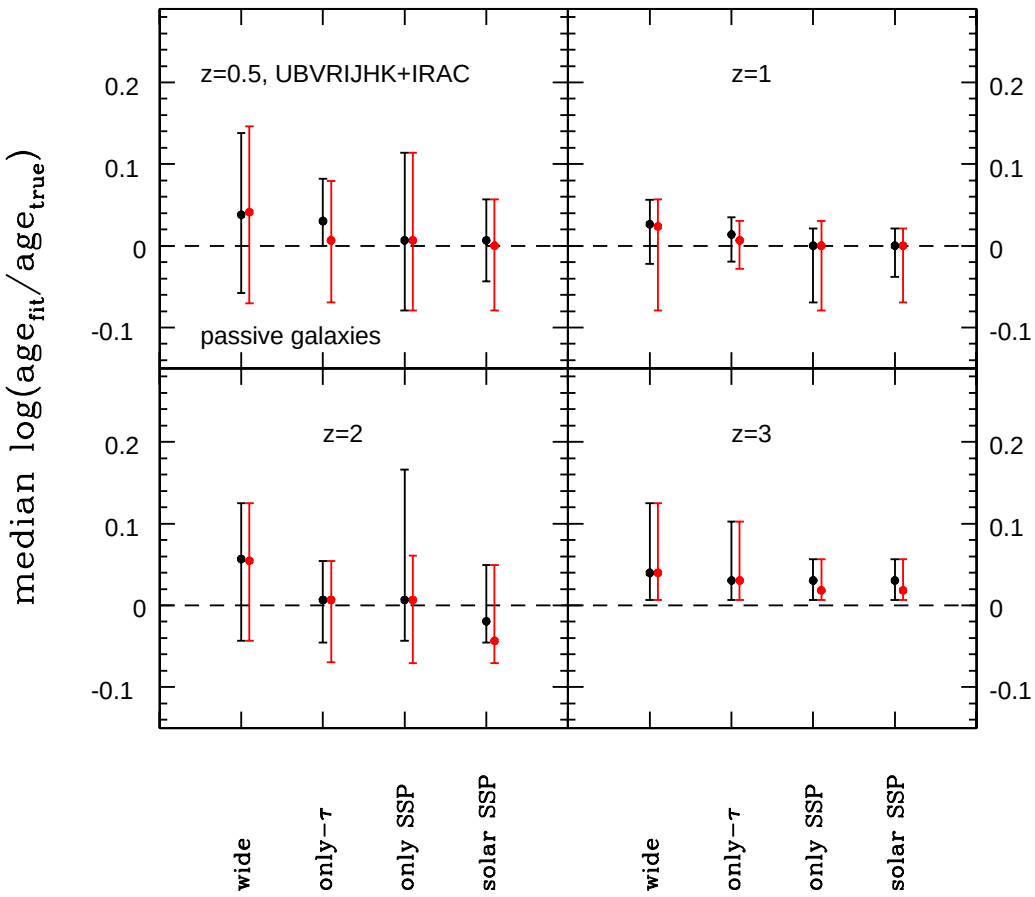

Figure 5.20: Recovery of age (median) for mock passive galaxies as a function of redshift and template setup. Black and red symbols refer to the cases without and with reddening, respectively. Errorbars are 68% confidence levels. Fig. 4.19 shows the case at fixed redshift.

$z \leq 1$ shows that the overestimation in the wide and only-τ setup is mainly driven by the mismatch in SFH although τ-models with short values of τ closely resemble a SSP. At $z = 2$, the correct template underestimates the age because redshift is overestimated by a small amount (~ 0.05) in the majority of cases. When redshift is underestimated, ages are overestimated. At $z = 3$ all template setups overestimate ages equally, merely the scatter is smaller for the only-SSP setups. We have seen in Chapter 4 that this is caused by a small mismatch between galaxy age and template age grid[8] and photometric uncertainties. This in turn causes underestimated redshifts at $z = 3$. The effect of including reddening only increases the scatter by a small amount. Overall, ages are best determined with a template of the right SFH and metallicity but even setups that inhibit a wider range of SFHs and metallicities recover ages within ± 0.06 dex (median). This is only slightly larger than in Chapter 4.

We further investigate metallicity effects on the age recovery in Fig. 5.21 by using mono-metallicity wide setups. Obviously, ages derived with a solar metallicity setup are recovered best. The remaining scatter stems from the SFH mismatch. In the unreddened case, fits with sub-solar metallicity template setups result in overestimated ages because older ages compensate bluer colours due to metallicity. Although most galaxies get assigned the right SFH (a SSP) - meaning the reddest solution is picked by the fit - for the lowest metallicity template setup, ages are still required to be maximally old to compensate for the underestimated metallicity. Yet, this is not effective enough if the true galaxy age is already very old, hence the fit tries to compensate with overestimated redshifts as well (compare Fig. 5.2). Additionally, as in the previous chapter, all χ^2_ν are larger than 2, most are larger than 10, and fits are getting worse towards higher redshift. No other parameter in the fit, i.e. age, SFH and redshift, can compensate such a large discrepancy in metallicity. At the highest redshift, ages are underestimated because a combination of longer star formation, younger age and very high redshift gives the best solution (χ^2_ν are still large). For the highest metallicity template setup, ages are underestimated because of the age-metallicity degeneracy.

Compared to the previous chapter in which we studied the case of known redshift, here underestimated (overestimated) redshifts compensate some of the effect. Consequently, ages are underestimated (overestimated) by ~ 0.1 dex less than in the fixed redshift case. The inclusion of reddening affects the age derivation mostly when sub-solar metallicity template setups are used in the fit. For these dust reddening is an additional way to redden galaxy colours. However, because of the age-dust degeneracy galaxies are now identified

[8] For ages of 1 and 1.5 Gyr the closest matching age of the template age grids are 1.015 Gyr and 1.434 Gyr

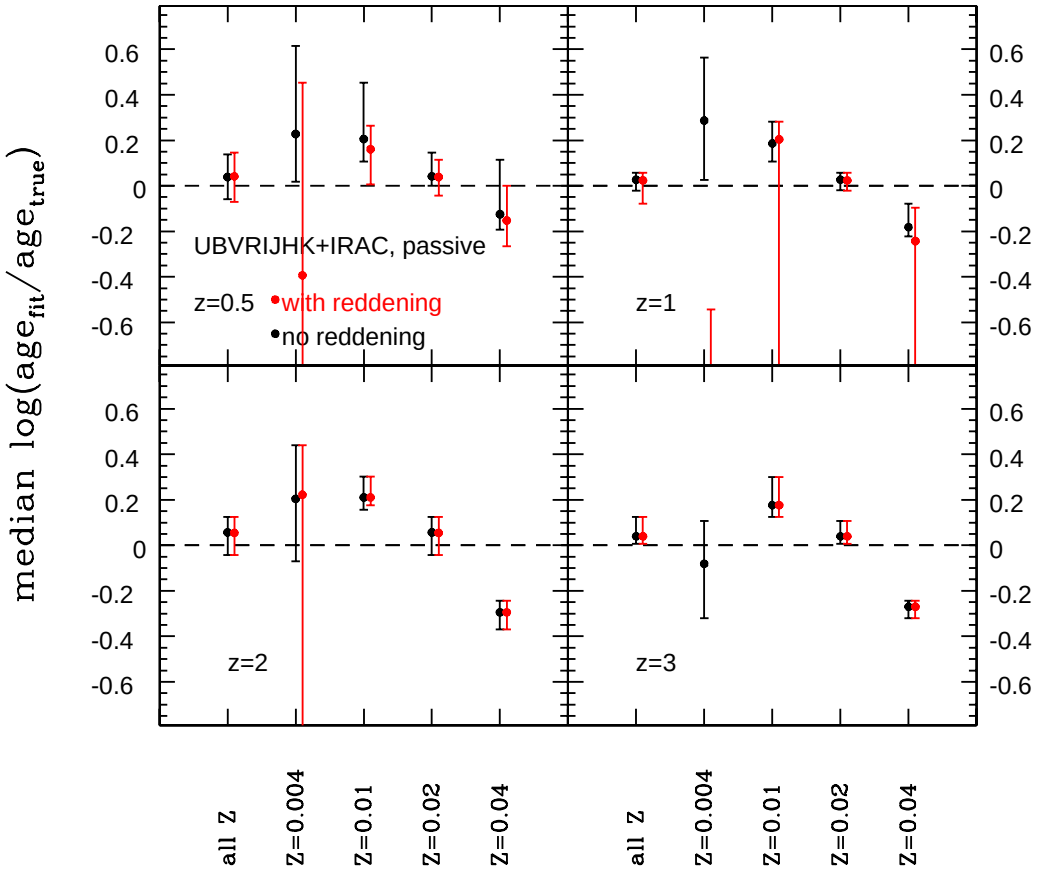

Figure 5.21: Median age recovery of mock passive galaxies as a function of redshift and metallicity. Black symbols refer to the unreddened case, red to the case that includes reddening in the fit. Shown are 68% confidence levels. The missing point at $z = 1$ for Z=0.004 in the reddened case lies at $-2.55^{+2.01}_{-0.60}$, and at $z = 3$ at $-2.28^{+0.03}_{-0.35}$. Fig. 4.20 shows the case at fixed redshift.

to be very young and dusty instead of old and dust-free and the scatter is very large (more than 2 dex). Even though recovered ages are offset when template setups of the wrong metallicity are used in the fit, the age determination works very well when the template setup contains a wide metallicity range because the correct metallicity is identified for most objects (see next section) and thus ages can be very well recovered.

Similar to the fixed redshift case, the age recovery is almost independent of the template IMF (Fig. 5.22). At low redshift only scatter is larger for a Kroupa, Chabrier or top-heavy IMF because the available age range in the fit is larger and age compensates for

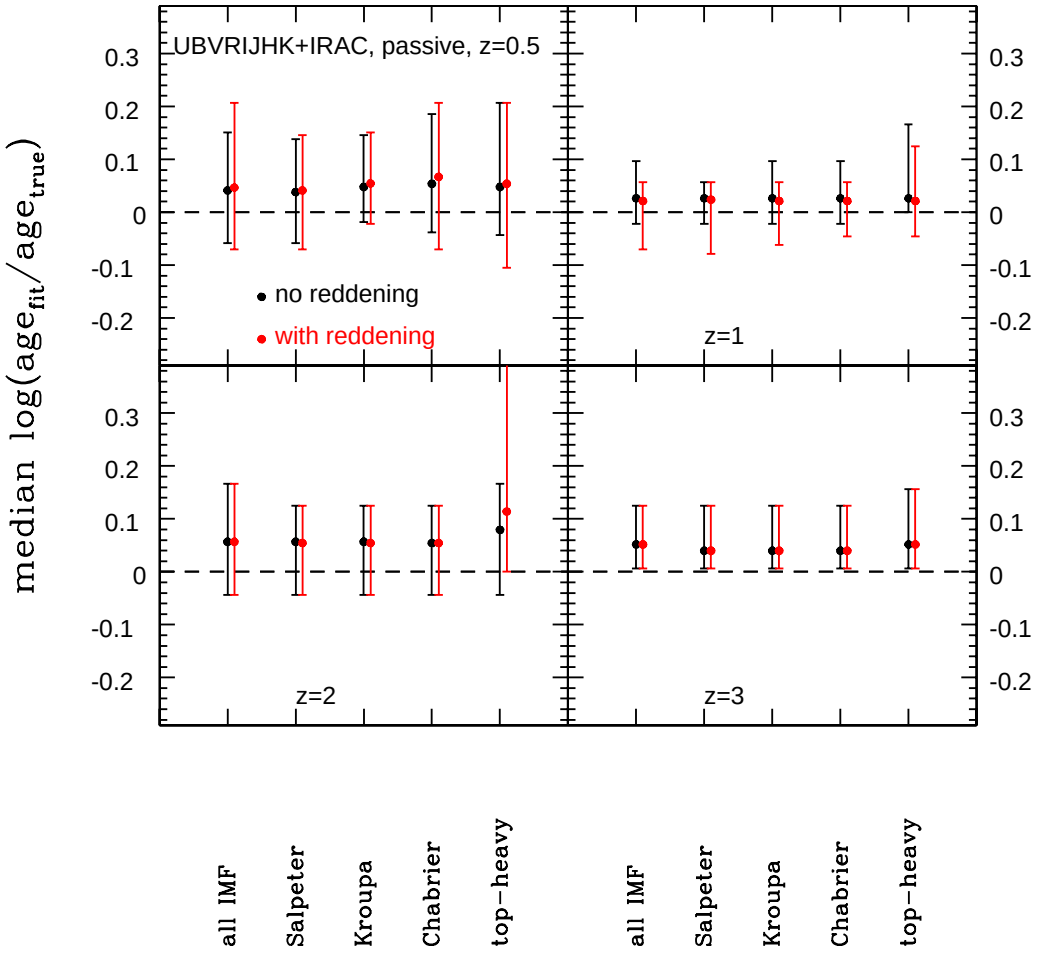

Figure 5.22: Median age recovery of mock passive galaxies as a function of redshift (i.e. wavelength coverage and also intrinsic age) and template IMF. Symbols and colours are the same as in Fig. 5.21. Errorbars refer to 68% confidence levels.

the wrong IMF. At high redshift, only the ages derived with top-heavy IMF templates are overestimated by a small amount more than those derived with the other IMFs. However, the scatter is larger than at known redshift. We discussed above already that the general trend of overestimating the age with the wide setup is mainly driven by SFH mismatches. Including reddening in the fit has a very small effect and merely increases the scatter at low redshift. As for the mock star-forming galaxies, the right IMF cannot be identified by choosing the best fit solution among all IMFs. Ages are best determined using a template setup based on the Salpeter IMF.

The dependence of the age recovery on the wavelength coverage shown in Fig. 5.23 reveals that median ages are recovered within ~ 0.1 dex for most filter setups in the

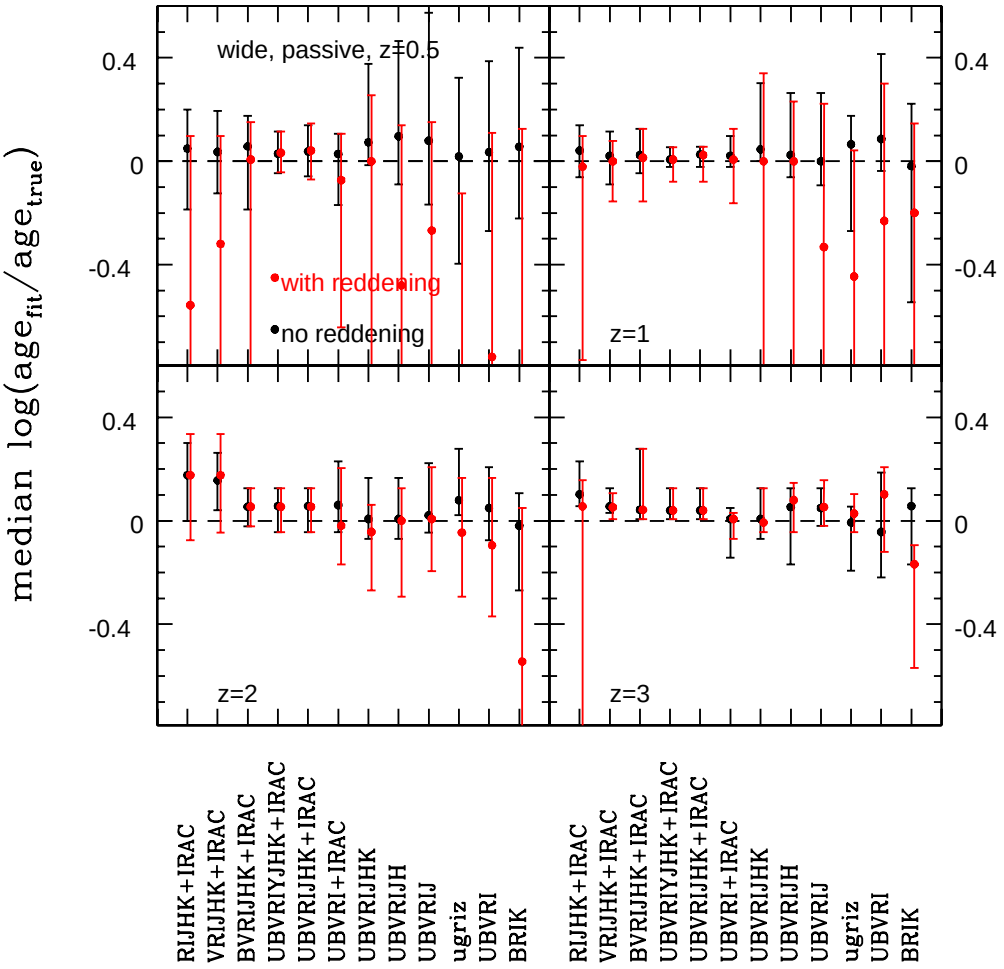

Figure 5.23: Median age recovery of mock passive galaxies as a function of wavelength coverage at redshifts from 0.5 to 3. Black symbols refer to the unreddened case, red to the case that includes reddening in the fit. Errorbars reflect 68% confidence levels. Missing points at $z = 0.5$ lie at $-0.88^{+0.76}_{-1.42}$ for ugriz, at $-2.31^{+2.43}_{-0.72}$ for BRIK and at $z = 2$ at $-0.54^{+0.59}_{-0.65}$ for BRIK. Fig. 4.21 shows the age recovery at fixed redshift.

unreddended case. However, scatter increases with decreasing wavelength coverage. At high redshift ages derived from setups that lack coverage in the bluest filter bands are overestimated more. For these filter setups redshifts are overestimated and star formation histories are mismatched. In comparison to the fixed redshift case, the scatter in the age determination is larger when redshift is an additional free parameter. The age recovery becomes very poor, particularly at low redshift, when reddening is included and the filter coverage lacks rest-frame near-IR and rest-frame red optical filter bands. Fig. 5.19 illustrated that also redshifts show large offsets and scatter in these cases. This is clearly

caused by the degeneracy between age, dust and redshift as the main driver. At low redshift, reddening and redshifts are overestimated, therefore ages have to be underestimated to compensate. The lack of blue filter bands has similar effects. For the youngest galaxies (at high redshift) ages are underestimated when the reddest rest-frame filter bands are missing mainly because redshifts are overestimated and show large scatter. When blue rest-frame filter bands are omitted in the fit ages are similarly overestimated as in the unreddened case. The age-dust degeneracy merely increases the scatter. At $z = 3$, the large scatter in the reddened case for a RIJHK+IRAC filter setup is generated by the degeneracy with redshift which also shows large scatter (see Fig. 5.19). Although a BRIK filter setup recovers ages similarly well as wider wavelength coverages in the case of known redshift, the age recovery fails when redshift is a free parameter because redshifts cannot be constrained reasonably well with these four filter bands alone. Overall, ages are best derived using the full wavelength coverage. Compared to the star-forming galaxies, ages of aged and passive galaxies can be better determined in the fit due to a well-defined 4000 Å break and the absence of overshining from young populations.

In summary, ages are best determined with templates of the right SFH and metallicity but even setups that inhibit a wider range of SFHs and metallicities recover ages within ± 0.06 dex (median). Template setups used to fit passive galaxies should contain a wide range in metallicity, as 1) the correct metallicity can be identified in the fit (see Section 5.4.3) and 2) using the wrong metallicity offsets the recovered ages by $\pm 0.2 - 0.3$ dex in the unreddened case and fails when reddening is included (Fig. 5.21). The choice of IMF has very little influence on the overall age determination of mock passive galaxies. The inclusion of reddening in the fit has overall only very little effect on the derived ages and mostly only increases the scatter. The best age determination is achieved when a broad wavelength coverage is used in the fit. The lack of rest-frame near-IR and red optical filter bands results in underestimated ages. When reddening is involved in the fit, the age is degenerate with dust and redshift and thus poorly recovered.

5.4.3 Metallicity

For nearly passive objects, we confirmed the findings of M06 in Chapter 4 that metallicity plays an important role in robustly determining the stellar population parameters when redshift is known. In Section 5.4.2 we showed further that this still holds when redshift is not known a priori. Because results are very similar to those in Chapter 4 we restrict ourselves to a description here. Despite the wide choice of metallicity provided in the template setup metallicity is closely recovered for most objects. The addition of

reddening has only a small influence on this.

The dependence of derived metallicities on the wavelength coverage in the fitting is similar to the fixed redshift case described in the previous chapter. In the dust-free case at low redshift, a lack in red filter bands decreases the number of objects for which the metallicity is correctly determined such that more metallicities are overestimated. Higher metallicities and higher redshifts compensate for underestimated ages and longer star formation. When blue filter bands are excluded metallicities are underestimated for a few more objects. In the reddened case, more objects get assigned underestimated metallicities for restricted wavelength coverages. Generally, effects are largest at low redshift.

As concluded in M06, Chapter 4 and the previous section, for passive galaxies it is important to fit with a wide choice of metallicities because metallicity can be recovered and estimates of the remaining stellar population properties are more robust. Metallicities are best recovered with a wide template setup and broad wavelength coverage.

5.4.4 E(B-V)

As described in Section 2.1 the mock passive galaxies used in this thesis are designed without reddening. Hence, any dust reddening obtained from the fit overestimates the true amount. Generally, reddening is recovered equally well when redshift is fixed or free in the fit, therefore we do not show it here. Most objects are correctly identified to be dust-free, the remainder contains only little reddening. Due to the age-dust degeneracy, we find the largest effect for the oldest galaxies (low redshift) independently of template setup.

However, reddening is much more sensitive to the wavelength coverage when redshift is a free parameter and best recovered with the broadest wavelength coverage. When the wavelength coverage decreases (in red and blue wavelength) many more objects are wrongly identified to be reddened because ages and redshifts are poorly recovered. Underestimated ages are compensated by overestimated reddening and redshift, particularly at low redshift. This effect is much stronger when redshift is a free parameter compared to the case of fixed redshift.

5.4.5 Stellar Mass

We found in the previous chapter that the stellar masses of mock passive galaxies can be recovered very well in general. In this section we investigate if that is still true when

redshift is not known and therefore cannot be used as a constraint in the fit. Firstly, the median masses of mock passive galaxies are recovered within ~ 0.02 dex for all template setups (Fig. 5.24) as in Chapter 4. For the oldest galaxies in the unreddened case the median mass recovery is nearly perfect but scatter is larger than at fixed redshift, particularly for template setups with a wider choice in metallicity. For these also the redshift is recovered slightly worse. At higher redshift masses tend to be underestimated for all template setups. For the wide and only-τ setups this is generated by a mismatch in SFH and degeneracies between redshift, SFH and age. For the only-SSP setups this stems

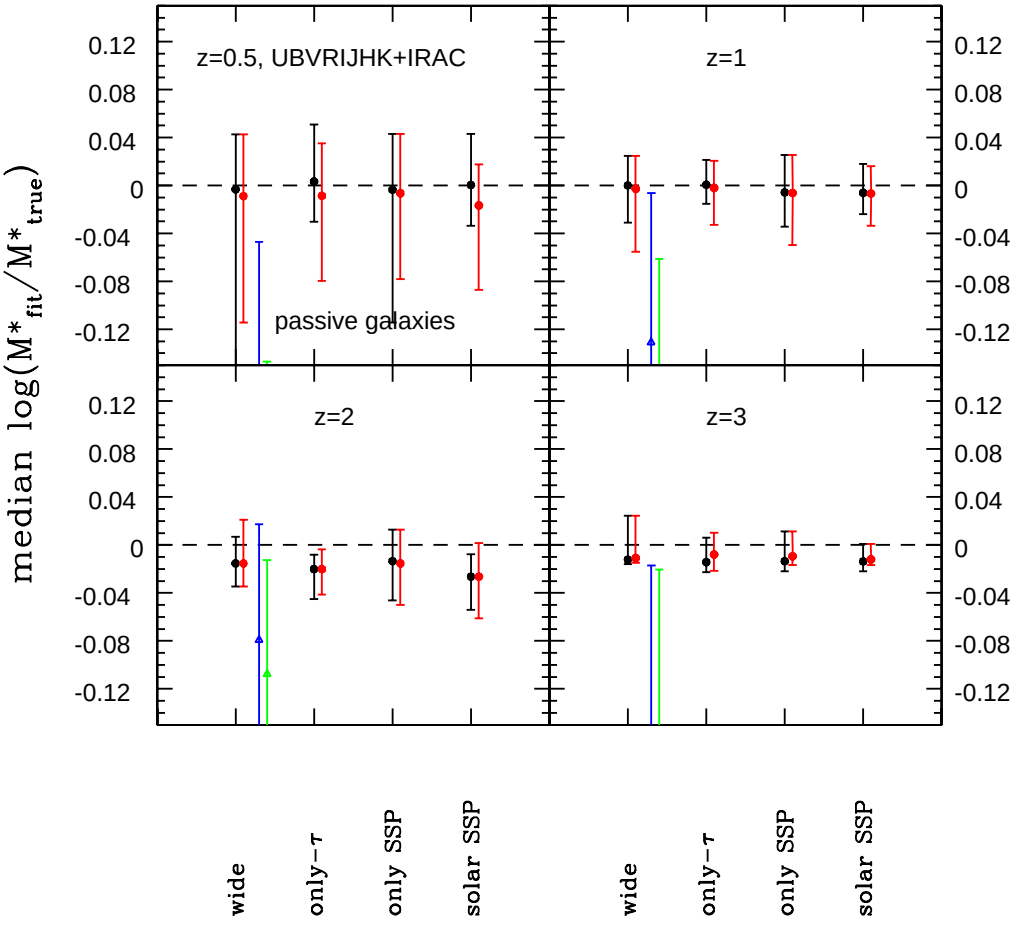

Figure 5.24: Median mass recovery of mock passive galaxies achieved with different template setups as a function of redshift. Red symbols refer to the case with reddening, black to the unreddened case. Errorbars show 68% confidence levels. Fig. 4.24 shows the case at fixed redshift. The blue and green symbols refer to the mass recovery of mock star-forming galaxies obtained with the wide setup without and with reddening, respectively (compare also points for 'all Z' in Fig. 5.10).

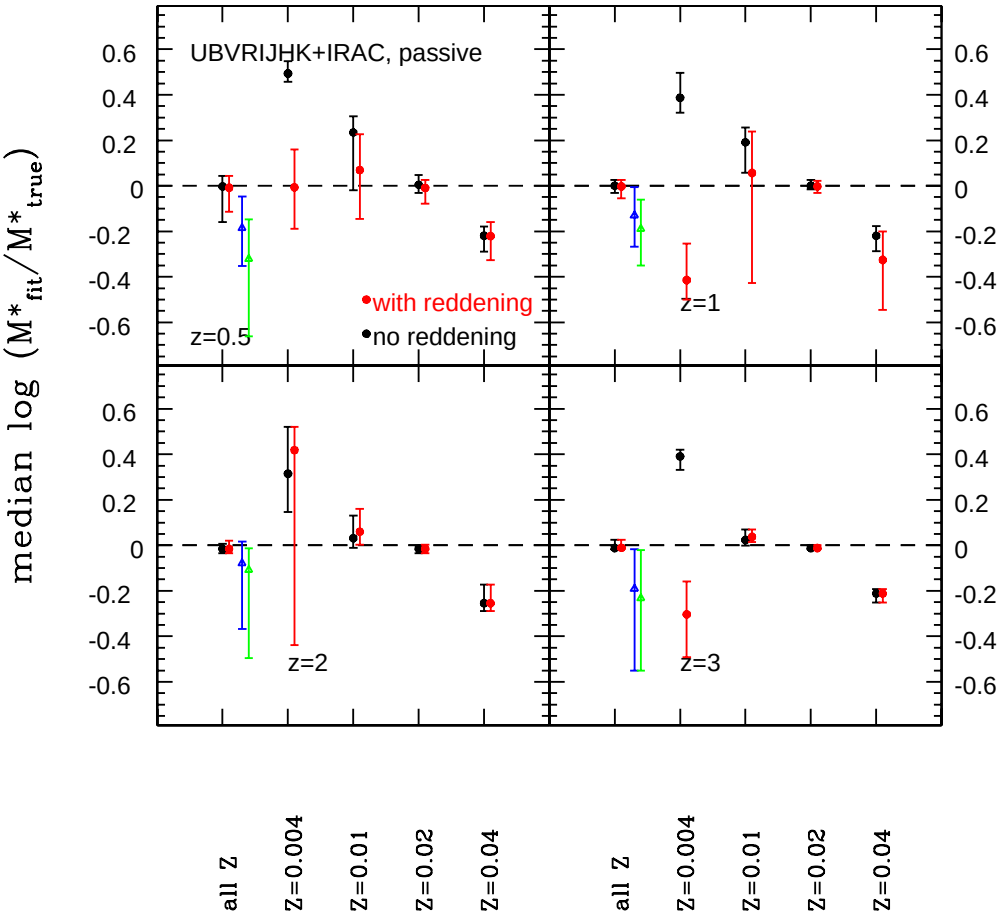

Figure 5.25: Median mass recovery of mock passive galaxies as a function of template metallicity. The input metallicity is solar. Symbols are the same as in Fig. 5.24. The case at fixed redshift is shown in Fig. 4.25.

from the degeneracy between redshift and age because SFHs and metallicities match the input. Note that for all template setups also photometric uncertainties and mismatch in age between template age grid and mock galaxy age contribute (see Sections 5.4.2 and 5.7). Scatter is smaller than at fixed redshift because redshift compensates. Differences between the reddened and unreddened case are small.

In the unreddened case the effect of metallicity on the stellar mass recovery is very clear. When metallicity is underestimated masses are overestimated by ~ 0.4 dex. When metallicity is overestimated masses are underestimated by ~ 0.2 dex. In comparison to the fixed redshift case for which the mass determination with low metallicity template setups fails at most redshifts, here redshift overcompensates. In fact, we showed in Fig. 5.18

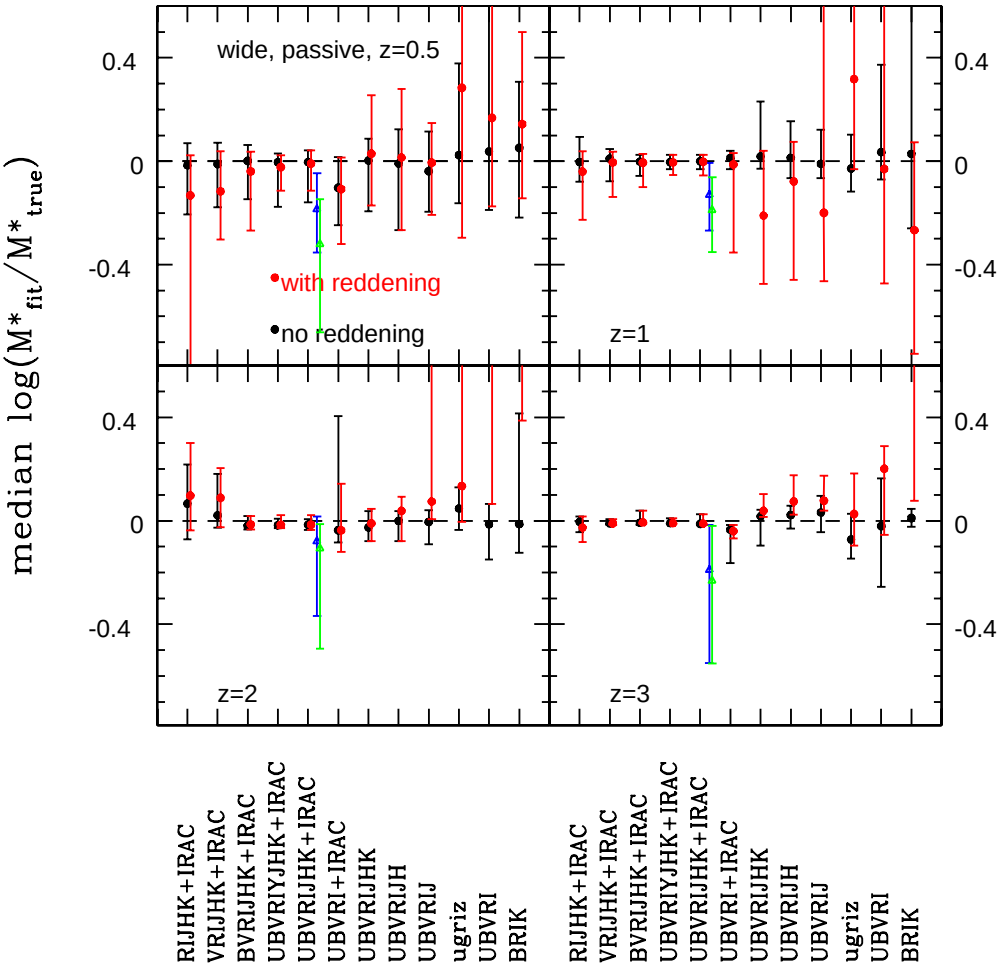

Figure 5.26: Median mass recovery of mock passive galaxies as a function of wavelength coverage. Symbols are the same as in Fig. 5.24. Missing points in the reddened case at $z = 2$ are at $0.64^{+1.56}_{-0.57}$ (UBVRI) and at $0.81^{+0.19}_{-0.42}$ (BRIK) and at $z = 3$ at $0.78^{+0.63}_{-0.71}$ (BRIK).

that redshift is not recovered at all for the lowest metallicity template setup. The inclusion of reddening has the largest effect for the lowest metallicity template setup for which masses tend to be underestimated according to underestimated ages and still poorly recovered redshifts. Overall, masses are best recovered with a solar metallicity template setup because it matches the input metallicity. Since metallicity is recovered in the fit (see also Section 5.4.3) a wide template setup with a broader choice in metallicity recovers masses equally well.

We established in the previous sections that the choice of IMF influences the overall fit only very little. Furthermore, the result for the mass recovery is very similar to the one

shown in Chapter 4 (Fig. 4.26) at fixed redshift, thus we do no repeat it here. Instead, we summarise the effect into three points:

- Masses are best recovered with a Salpeter IMF template setup.
- The masses obtained using a Kroupa or Chabrier IMF template setup are underestimated at each redshift by ~ 0.2 dex. Those obtained with a top-heavy IMF template setup are overestimated by ~ 1 dex.
- Reddening has very little impact on the previous two points.

We discussed in the previous chapter that the difference in stellar mass estimates with various IMFs stems from their different mass-to-light ratios (M^*/L). As already concluded in Chapter 4 and the previous sections, we again confirm here the notion that, although the choice of IMF is felt in the fit, an identification of the correct IMF based on the minimum χ^2_ν is impossible.

We present the dependence of the derived stellar masses on the wavelength coverage in Fig. 5.26. The median recovered stellar mass depends only little on the wavelength coverage in the unreddened case. The biggest effect is an increase in scatter when the wavelength range is restricted because mass is directly correlated with age and redshift, which both have large uncertainties. As for the age and redshift determination the recovery of stellar masses is greatly hampered by the inclusion of reddening due to the many degeneracies. Particularly, a lack in rest-frame near-IR and red optical coverage results in vastly overestimated masses. These filter bands are crucial for the correct redshift and age determination at high redshift because they include the 4000 Å break and the TP-AGB. At low redshift masses are underestimated when blue filter bands are missing because they cover the rest-frame wavelength range which is most crucial for the redshift and age determination (i.e. the 4000 Å break). At each redshift masses are best recovered when the full wavelength range is used in the fit. Compared to the case of known redshift, masses are more affected by a lack of wavelength coverage and the inclusion of reddening when redshift is a free parameter.

In summary, the stellar masses of mock passive galaxies can be recovered within ± 0.02 dex when a wide setup and a broad wavelength coverage is used even when redshift is a free parameter in the fit. Differences between template setups are small. Metallicity effects can bias the recovered mass by at most ~ 0.5 dex. Masses estimated with Chabrier and Kroupa IMF are lower than Salpeter masses by ~ 0.2 dex, those from a top-heavy IMF overestimate the mass by ~ 1 dex. Masses depend much more on wavelength coverage and are overestimated when rest-frame near-IR and red optical filter bands are

missing. The inclusion of reddening affects then the most because of the age-dust-redshift degeneracy.

5.5 Measuring the strength of the latest starburst

The results of M10 and Chapter 4 clearly show that recent star formation influences the fit such that a robust recovery of age, stellar mass, reddening and star formation rate of star-forming galaxies *simultaneously* is very difficult. We further investigated whether the recovered properties then reflect the characteristics of the latest starburst rather than that of the entire galaxy. Here, we carry out the same exercise leaving the redshift free. For this we use the same simulated galaxies (a combination of young and old SSPs) as described in Section 4.5.

Table 5.2: Derived redshifts, ages and stellar masses for a $10^{11} M_{\odot}$ galaxy composed of a 5 Gyr old population and a low percentage - 1 or 10% - of a younger population. Burst characteristics are listed in the first column, while the second, third and fourth columns list the derived redshifts, ages and masses.

Burst no reddening	derived redshift	derived age	derived M^* $[M_{\odot}]$
1% 1Gyr	0.645	3.5 Gyr	10.91
1% 100Myr	0.965	4.5 Gyr	10.83
1% 10Myr	1.295	3.0 Gyr	10.89
1% 1Myr	1.240	47.5 Myr	9.73
10% 1Gyr	1.025	2.75 Gyr	10.87
10% 100Myr	1.125	227 Myr	10.60
10% 10Myr	0.890	8.7 Myr	9.82
10% 1Myr	1.190	6.6 Myr	10.04
Burst + reddening	derived redshift	derived age	derived M^* $[M_{\odot}]$
1% 1Gyr	0.645	3.0 Gyr	10.60
1% 100Myr	1.240	6.3 Myr	9.74
1% 10Myr	0.630	8.7 Myr	8.84
1% 1Myr	1.010	13.8 Myr	9.31
10% 1Gyr	0.605	4.75 Gyr	10.70
10% 100Myr	0.690	7.6 Myr	8.98
10% 10Myr	0.890	8.7 Myr	9.82
10% 1Myr	1.190	6.6 Myr	10.04

The fitting is carried out using the broadest wavelength coverage and a wide setup. For simplicity, we stick to solar metallicity for the simulated galaxies and the fitting setup. Results for redshift, age and stellar mass are listed in Table 5.2.

In any case derived ages and masses are underestimated. Redshifts deviate by up to 0.4 from the true redshift but because of the many degeneracies there is no systematic trend. Compared to the results obtained at known redshift (Table 4.2), ages are similar and much closer to the age of the burst when the burst component accounts for 10% and is younger than a few 100 Myr or very young and makes up only 1%. The mass estimate is improved somewhat when the redshift is overestimated. When reddening is included in the fit ages are very young unless the burst component is close in age to the old component. Due to the age-dust degeneracy ages can even be younger than the age of the burst component. Compared to the fixed redshift case the burst component starts to affect already when the percentage is very low and reddening is included. The combination of underestimated ages with underestimated redshifts results in stellar masses that only reflect the mass of the burst. In some cases the mass is even lower than the burst mass.

Overall, we confirm that also when redshift is a free parameter in the fit, young burst components can hide a large percentage of the total stellar mass, especially when there is a large gap between the age of the burst and the age of the old component. Masses and ages resemble the properties of the entire galaxy best when the burst component is old, carries very little mass, and no reddening is used in the fit. When reddening is included the offset from the true mass is still $0.3 - 0.4$ dex.

5.6 Reddening laws

We devote this section to the dependence of the fitting result on the particular reddening law adopted in the fit. Specifically, our focus lies on the question whether an overall better result can be achieved for mock star-forming galaxies by considering only one reddening law. This option would also be more economic. M06 showed that the highest accuracy for passive galaxies is achieved by choosing the best fit among all available reddening options. For the mock star-forming galaxies one would expect the Calzetti reddening law to outperform all other reddening options due to the particular design of the mock galaxies.

We do not show the redshift recovery as a function of reddening law because results are very similar. Qualitatively, the mass and SFR recovery are the same as in Chapter 4 at

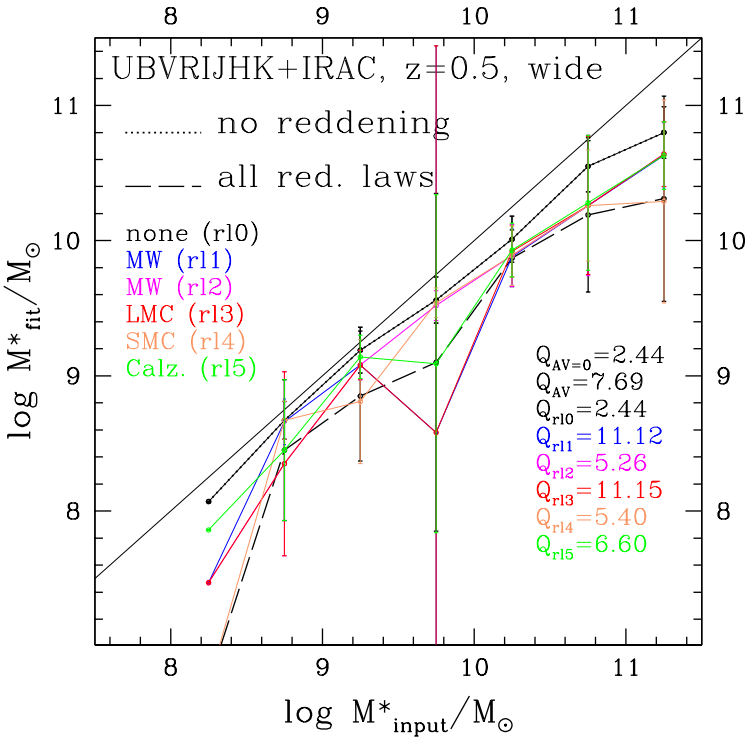

Figure 5.27: Average mass recovery as a function of reddening law at redshift 0.5. The dotted black line shows the mass recovery when no reddening is used in either spectra or fitting. The dashed thick black line shows the result when the best fit out of all reddening laws is chosen for each object. The coloured thin lines represent the results applying only one reddening law on the reddened spectra. Quality factors are for the entire mass range. Fig. 4.28 shows the case at fixed redshift.

fixed redshift. The largest difference in mass recovery between the reddening laws is found at $z = 0.5$ (Fig. 5.27) because of the age-dust (and redshift) degeneracy. These galaxies have only little (or no) reddening and the age range available in the fit is largest. The MW law by Allen and the LMC law give a significantly worse mass recovery. As in the redshift fixed case the exact type of reddening law is on average less important at high redshift, hence we do not show it again here. In any case, the best mass estimate is achieved when no reddening is used in the fitting independently of the actual amount of reddening present in the galaxies.

SFRs on the other hand are much more sensitive to the type of reddening law (Fig. 5.28). At high redshift the results are very similar to the ones in Chapter 4, meaning the fitting code is able to identify the right reddening law for most objects. Fitting without reddening results in underestimated SFRs. At low redshift, SFRs are generally better recovered than in the fixed redshift case. Star formation rates are best recovered when no reddening is

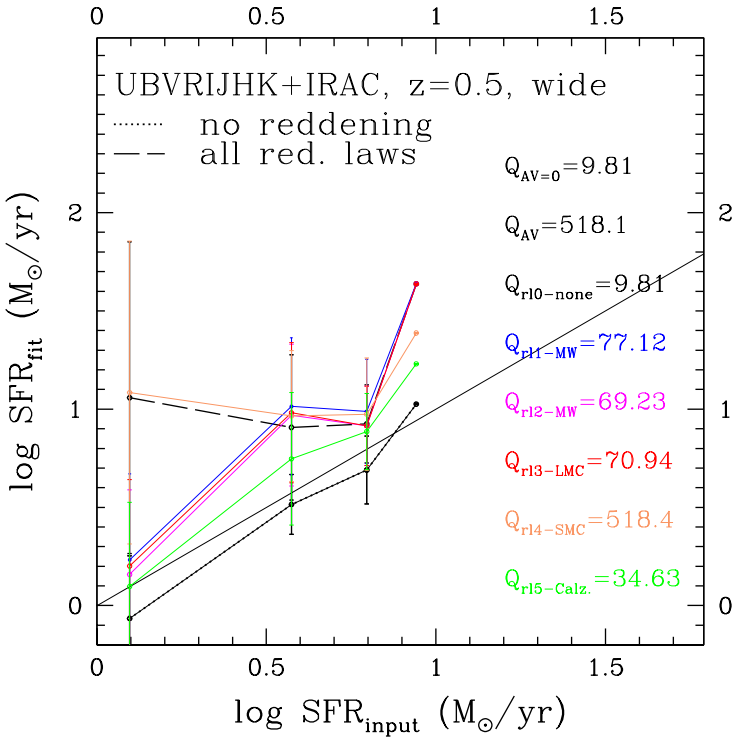

Figure 5.28: Average SFR recovery as a function of reddening law at redshift $z = 0.5$. Solutions are for a wide setup only. Colours and lines are the same as in Fig. 5.27. Note that the data point at the highest SFR consists of only one object and is merely shown for completeness. Fig. 4.29 shows the case at fixed redshift.

used. The Calzetti law performs best when reddening is included. When the best fit among all reddening laws is chosen however, SFRs are overestimated more.

5.7 The effect of photometric uncertainties

Finally, we compare results obtained using original magnitudes and those scattered with Gaussian errors[9] in the fit to study the effect of photometric uncertainties. For simplicity only the unreddened case is considered. As in Section 4.7 at fixed redshift we focus on older galaxies with little or no on-going star formation (mocks at $z = 0.5$). Mock star-forming galaxies are fit with the wide setup. Mock passive galaxies are fit with a solar metallicity SSP only. Note, that templates do not comprise the exact SFH of the mock star-forming galaxies.

Firstly, we compare the derived redshifts of the mock star-forming galaxies (Fig. 5.29, bottom left). The redshift estimate is clearly better when original magnitudes (labelled

[9]Original magnitudes were scattered with their three σ photometric errors.

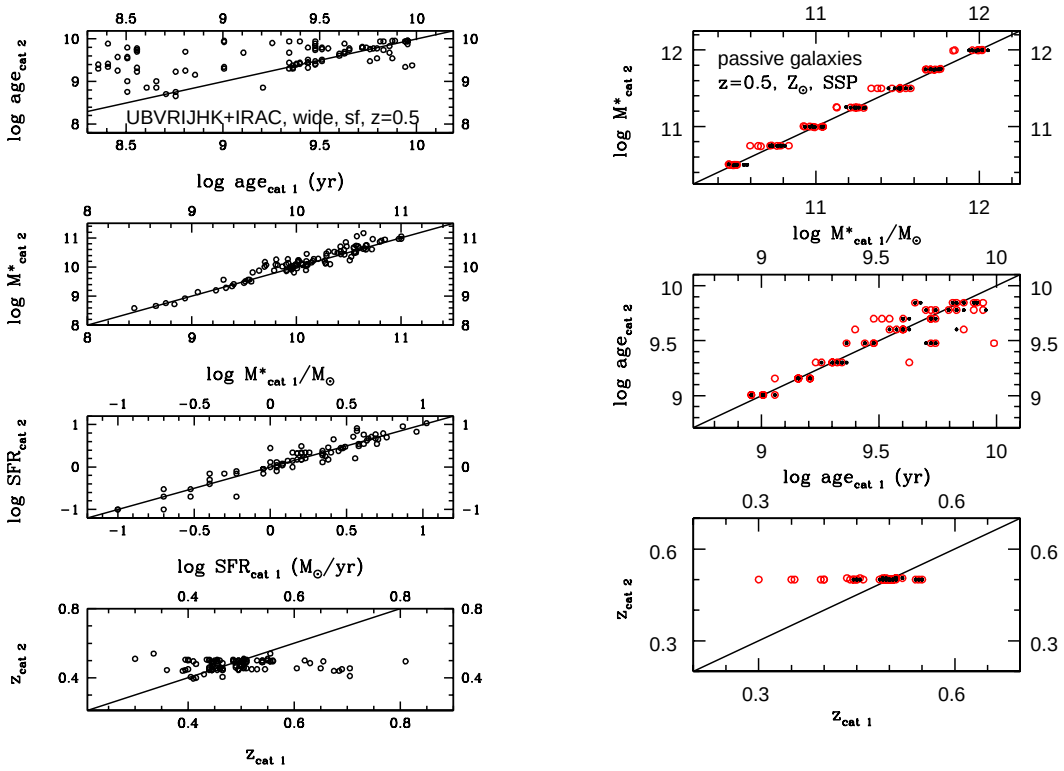

Figure 5.29: *Left:* The effect of photometric uncertainties for mock star-forming galaxies at $z = 0.5$ for a wide template setup and broad wavelength coverage. From top to bottom: derived ages, stellar masses, star formation rates and redshift, respectively. *Right:* Effect for passive galaxies. From top to bottom: derived stellar masses, ages and redshift, respectively.

as $cat\,2$ in Fig. 5.29) are used and there are no photometric uncertainties. Redshifts are then determined within ~ 0.1. For magnitudes that are scattered with Gaussian errors they are only correct within 0.5. This has the biggest effect on the derived ages (Fig. 5.29, top left). When original magnitudes are used ages are systematically older and thus better estimated overall. At fixed redshift this trend is less clear. The maximum deviation is similar to the one in Chapter 4 (~ 1.6 dex). Despite this large change in age for single objects, masses differ only little; on average by 0.08 ± 0.16 dex similar to the fixed redshift case. Consequently, the overall trend of underestimating the masses of older galaxies with little on-going star formation remains also when redshift is a free parameter. The mean difference between the derived SFRs is also small and smaller than at fixed redshift.

Since we fitted the mock passive galaxies with the same model that was used to simulate them, a solar metallicity SSP, differences between redshifts, stellar masses and ages can

- independently of redshift - be mostly ascribed to photometric uncertainties caused by scattering the magnitudes with photometric errors. Fig. 5.29, right-hand side, shows that for the passive galaxies the effect is small in the unreddened case. Redshifts are nearly perfectly recovered for original magnitudes ($cat\ 2$) and within 0.05 for magnitudes scattered with Gaussian errors. Ages on the other hand differ more from each other and also scatter more than at fixed redshift. The largest deviations are found for the oldest galaxies which differ by maximal ~ 0.2 dex. Stellar masses differ by ~ 0.1 dex at most. The inclusion of reddening has a large effect on the redshifts because of the age-dust-redshift degeneracy. They now differ by maximal 0.25. Ages - again mainly at the old end where spectra look very similar - differ by at most 0.5 dex. Masses deviate from each other by ~ 0.2 dex.

5.8 Comparison to results in the literature

Not much work has been devoted to the study of the robustness and accuracy of the derived stellar population parameters from SED-fitting when redshift is a free parameter, although many studies that involve the derivation of photometric redshifts evaluate the quality of their photometric redshift estimates and calibrate them by using control samples for which spectroscopic redshifts are available (e.g. Ilbert et al., 2006; Quadri & Williams, 2010; Dahlen et al., 2010, to name only a few). Firstly, we compare the recovery of our redshifts to the work of Bolzonella et al. (2000) in which they tested their *HyperZ*-code. They also studied the dependence of the derived photometric redshifts on various parameters in the fit, such as template setup, photometric uncertainties, wavelength coverage, reddening and reddening law, metallicity and IMF. Then we focus on the results of Lee et al. (2009) and Wuyts et al. (2009, W09) for other stellar population parameters when redshift is left free.

Bolzonella et al. (2000) use a set of simulated galaxies produced from the template set (based on Bruzual A. & Charlot 1993 stellar population models) under the assumption of a homogeneous redshift distribution. Ages and spectral types are drawn randomly from the template set. Magnitudes in all filter bands are scattered within fixed one σ values. These range from 0.05 and 0.3mag (i.e. 5 to 30% error). They showed when testing their photometric redshift code *HyperZ* that the determination of photometric redshifts is best for a wide wavelength coverage and small photometric errors. For photometric errors as used for our mock galaxies (i.e. $\sim 10\%$) Bolzonella et al. (2000) report a mean photometric accuracy (expressed as mean difference $< \Delta z >= (\sum(z_{true} - z_{fit}))/N$ under

exclusion of catastrophic failures[10]) of -0.02, -0.02, -0.01 and 0.03 for redshift bins of $z = 0 - 0.4$, $0.4 - 1$, $1 - 2$ and $2 - 3$, respectively, when using a UBVRIJHK filter set. Photometric redshift accuracies are similar in other studies (Ilbert et al., 2006; Wuyts et al., 2009, e.g.). Our equivalent values but including catastrophic failures are -0.10, -0.14, 0.27 and 0.04 for redshift $z = 0.5$, 1, 2 and 3 using a wide setup with reddening[11]. Catastrophic failures for $z = 1$ amount to 1% and for $z = 2$ to 8%. At $z = 0.5$ and 3 we do not have catastrophic failures according to the definition of Bolzonella et al. (2000). Our values for the photometric accuracies are larger than those of Bolzonella et al. (2000) very likely due to the age-dust degeneracy (at low redshift) and SFH mismatch between template and mock galaxies. Note that Bolzonella et al. (2000) create the mock galaxies from the template set that is used to fit them. Additionally, they restrict the reddening to $A_V \leq 1$ mag and Calzetti law in their fit while we allow values up to $A_V = 3$ mag and use all reddening laws. It is also worth to note that the metallicity of templates and simulated galaxies of Bolzonella et al. (2000) is fixed to the solar value, while both our simulated galaxies and template setup cover a wide range in metallicities. At redshift 3 however our value for the redshift accuracy is very similar due to the fact that for these objects both the Lyman break and the 4000 Å break are covered by the chosen filter set. This significantly improves the redshift recovery. However, including the rest-frame near-IR improves our redshift recovery to -0.01, 0.02, -0.04 and 0.03 for redshift $z = 0.5$, 1, 2 and 3 , respectively, using a wide setup and reddening.

Overall, Bolzonella et al. (2000) conclude that although the redshift determination is most sensitive to the photometric accuracy and wavelength coverage a sufficiently wide range of ages and reddening is still important for deriving accurate photometric redshifts. They find that for high redshift objects reddening is more essential for the redshift accuracy and that the MW and LMC laws are not suitable. Our median recovered redshifts when using different reddening laws (but a full wavelength coverage) differ only very little. Furthermore they conclude that metallicity effects on the redshift recovery are negligible at high-z and that the IMF seems to play a secondary role. Both findings are in agreement with our work. Bolzonella et al. (2000) also showed that the redshifts of old and passive galaxies are determined better than those of younger ones which we confirmed in the previous sections.

We already compared our results at fixed redshift to the work of Lee et al. (2009) and W09 in Chapter 4. Let's briefly recap the basis of their works. Lee et al. (2009) address

[10] Catastrophic failures are defined by Bolzonella et al. (2000) as $|\Delta_z| = |z_{true} - z_{fit}| \geq 1$

[11] Median values of $(z_{fit} - z_{true})$ are 0.04, -0.003, -0.08 and -0.015 for $z = 0.5$, 1, 2 and 3 using a wide setup with reddening and a UBVRIJHK filter set.

the robustness of stellar population properties derived from SED-fitting of Lyman break galaxies at $3 < z \leq 5$ (U-, B- and V-dropout galaxies). Mock galaxies are created from a semi-analytic galaxy formation model using BC03 stellar population models with a Chabrier IMF and are selected via the Lyman break criterion. SED-fitting is carried out using BC03 templates of three metallicities (0.2 to 1 $Z_{\odot}$), exponentially declining SFRs ($\tau = 0.2 - 15$ Gyr) and Chabrier IMF. Dust extinction is treated with the Calzetti law. Compared to their results at fixed redshift stellar masses are underestimated more when redshift is free. While at fixed redshift the means of the intrinsic and recovered mass distribution differ between 19 and 25%, they differ between 25 and 51% when redshift is free. We found at fixed redshift a difference of only $\sim 15\%$ at the highest redshift (using a wide setup, reddening and a minimum age of 0.1 Gyr). When redshift is free we find the same because the redshift of $z = 3$ objects is very well recovered and the available age range in the fitting is small.

Lee et al. (2009) also report large deviations of mean age and SFR from the true values such that mean SFRs are underestimated and (mass-weighted) ages are overestimated caused by SFH mismatch and overshining. They find that SFRs and ages are better recovered, if only slightly, when redshift is left free. We find that ages and SFRs at $z = 3$ are recovered slightly worse because of the added degeneracy with redshift. Recovered redshifts of Lee et al. (2009) are in general slightly underestimated with $(z_{fit} - z_{true})/(1 + z_{true})$ ranging from -0.137 to 0.043 for U-dropouts. The ranges are smaller for B and V-dropouts, i.e. they get narrower with increasing redshift. At redshift 3 we find a median offset in redshift expressed as $(z_{fit} - z_{true})/(1 + z_{true})$ of -0.002 (and -0.007 for the mean) and a maximum deviation of -0.070 when using a wide setup and reddening which is slightly smaller than the values of Lee et al. (2009). In agreement with our findings Lee et al. (2009) also recommend a wide wavelength coverage from the optical to the rest-frame near-IR for the best recovery of the galaxy physical parameters.

We showed in the previous chapter and in M10 (Section 6.1) that when redshift is known using inverted-τ models with fixed formation redshift ($z_{form} \sim 5$) improves the mass and SFR estimate for mock star-forming galaxies at $z = 2$ and 3 and recovers stellar masses perfectly. For the inverted-τ models the difference between the means of true and recovered stellar mass distributions was less than 1%. As explained in the previous chapter, the use of inverted-τ models solves both problems identified by Lee et al. (2009) (SFH mismatch and overshining) to be responsible for offsets in recovered stellar population properties. Therefore, when redshift is a free parameter, we suggest for high redshift, star-forming objects that redshifts should be determined with the best setup first and then

used in a separate fit with inverted-τ models to obtain masses and SFRs.

This approach is taken by Wuyts et al. (2009). In the case of unknown redshift they derive redshifts first and use these then in a separate fit to derive stellar population properties, such as ages, reddening, stellar masses and SFRs. Mock galaxies for this exercise are extracted from a hydrodynamical merger simulation. The photometry of their mock galaxies placed at intermediate redshifts is based on BC03 models. The SED-fitting is carried out using *HyperZ* with solar metallicity, Salpeter IMF BC03 templates of three star formation histories: SSP, constant SFR, and a τ-model with $\tau = 0.3$ Gyr. Reddening is varied between A_V from 0 to 4 but only the Calzetti law is considered. The mock galaxies in W09 are distinguished into disk, merger and spheroid phase of the simulation. Thus the mock star-forming galaxies used in our work compare mostly to galaxies in the disk and merger phase of W09, the mock passive galaxies to galaxies in their spheroid phase. At fixed redshift W09 find reddening, stellar masses and SFRs to be underestimated on average. The properties of spheroidal galaxies are better recovered than those of the disk and merger phase in general. When redshift needs to be derived in the fitting, they use the template fitting code EAZY (Brammer et al., 2008) which fits a linear combination of templates to the data and the redshift is derived by evaluating the probability distribution function. Their median $\Delta z/(1+z)$ is 0.031 which is comparable to our findings. The main effect found by W09 on the stellar parameters caused by this uncertainty in redshift is the broadening of the 68% confidence levels by 1% in $\Delta\, log\, age$, 7% in $\Delta\, log\, M^*$, 5% in $\Delta E(B-V)$ and 1% in $\Delta\, log\, SFR$. They find offsets in stellar mass and reddening only for the dustiest objects. For these derived stellar masses are larger by 0.05 dex and reddening smaller by ~ 0.02 mag. But they point out that these effects are smaller than those caused by SFH mismatches and reddening and might be template setup specific. Compared to W09 the increase in stellar mass estimates that we find are not confined to the dustiest objects but mainly affect the oldest galaxies with little on-going star formation.

Finally, Pozzetti et al. (2007) note for similar redshift accuracies an additional ~ 0.2 dex (at $z < 0.4, \sim 0.1$ dex at $z = 2$) uncertainty in the stellar mass for their sample of K-selected galaxies from the VIMOS VLT Deep Survey (Le Fèvre et al., 2003).

5.9 Homogenising derived properties via scaling relations

In Chapter 4 we provided scaling relations for stellar mass that allowed us to transform derived masses from one fitting setup to another because differences in the fitting setup,

such as different models, templates, IMFs etc, influence the results. This enabled us to homogenise and combine data sets that were analysed with different fitting parameters. However, we relied on the availability of spectroscopic redshifts. For many up-coming surveys, e.g. DES, these will not be accessible and one has to rely on photometrically obtained redshifts instead. For this reason, we provide here the equivalent scaling relations for stellar mass to those in Chapter 4 but when redshift is a free parameter in the fit in Tables 5.3 and 5.4. We use a least squares fit and gain statistical robustness by using the entire merger tree for mock star-forming galaxies. Note that these relations provide information only about statistical differences, the difference in stellar mass between various fitting setups for a single object can significantly deviate from this.

Table 5.3: Scaling relations for mock star-forming galaxies in the form of $log\, M^*_{wideSalpeter} = a_1 + a_2 * x$ where x stands for $log\, M^*$ of the various fitting setups. The coefficients a_1 and a_2 represent the unreddened case, b_1 and b_2 represent the reddened case. Table 4.3 lists the according values when redshift is known.

redshift	x	a_1	a_2	b_1	b_2
0.50	wide Chabrier	2.4652	0.7689	1.0713	0.9066
1.00	wide Chabrier	0.9667	0.9194	0.6539	0.9514
2.00	wide Chabrier	0.4726	0.9714	0.4078	0.9793
3.00	wide Chabrier	0.5029	0.9713	0.3796	0.9855
0.50	wide Kroupa	0.9823	0.9160	0.8023	0.9415
1.00	wide Kroupa	0.7665	0.9391	0.9961	0.9185
2.00	wide Kroupa	0.2099	1.0010	0.1410	1.0084
3.00	wide Kroupa	0.0043	1.0229	-0.0278	1.0271
0.50	wide $Z_\odot$	3.8500	0.6220	2.7551	0.7217
1.00	wide $Z_\odot$	1.2727	0.8723	1.1847	0.8779
2.00	wide $Z_\odot$	0.9155	0.9069	0.5792	0.9404
3.00	wide $Z_\odot$	0.7625	0.9258	0.5972	0.9421
0.50	only-τ	1.8875	0.8135	-0.0098	0.9878
1.00	only-τ	1.0996	0.8877	0.8531	0.9082
2.00	only-τ	1.6317	0.8354	0.5326	0.9429
3.00	only-τ	0.8059	0.9178	0.6248	0.9383
0.50	wide BC03	4.7388	0.5371	9.5668	0.0257
1.00	wide BC03	1.7411	0.8271	5.5878	0.4454
2.00	wide BC03	0.9954	0.8799	0.7234	0.9045
3.00	wide BC03	1.1207	0.8734	0.9429	0.8886
0.50	BC03 only-τ	6.0939	0.4064	9.3264	0.0524
1.00	BC03 only-τ	2.6001	0.7333	3.3156	0.6591
2.00	BC03 only-τ	2.4519	0.7361	1.3094	0.8447
3.00	BC03 only-τ	1.3444	0.8495	1.1954	0.8627

Table 5.4: Scaling relations for mock passive galaxies in the form of $log\, M^*_{wideSalpeter} = a_1 + a_2 * x$ where x stands for $log\, M^*$ of the various fitting setups. The coefficients a_1 and a_2 represent the unreddened case, b_1 and b_2 represent the reddened case. Table 4.4 lists the according values when redshift is known.

redshift	x	a_1	a_2	b_1	b_2
0.50	wide Chabrier	-0.2011	1.0279	-0.1207	1.0214
1.00	wide Chabrier	-0.0626	1.0169	0.2429	0.9899
2.00	wide Chabrier	0.1971	0.9966	0.2053	0.9959
3.00	wide Chabrier	0.0941	1.0058	0.0792	1.0070
0.50	wide Kroupa	-0.1339	1.0206	-0.1769	1.0244
1.00	wide Kroupa	0.0134	1.0084	0.2191	0.9895
2.00	wide Kroupa	0.1573	0.9970	0.1497	0.9977
3.00	wide Kroupa	0.0686	1.0051	0.0528	1.0063
0.50	wide $Z_\odot$	0.0085	0.9954	-0.2862	1.0251
1.00	wide $Z_\odot$	-0.2216	1.0187	-0.4324	1.0365
2.00	wide $Z_\odot$	-0.0265	1.0026	-0.0251	1.0024
3.00	wide $Z_\odot$	0.1417	0.9881	0.1424	0.9881
0.50	only-τ	0.0237	0.9940	-0.1676	1.0144
1.00	only-τ	-0.2621	1.0224	-0.5312	1.0451
2.00	only-τ	0.1464	0.9884	0.1460	0.9882
3.00	only-τ	0.0489	0.9965	0.0354	0.9975
0.50	SSPs	0.0201	0.9973	-0.0340	1.0028
1.00	SSPs	-0.0973	1.0086	-0.0747	1.0065
2.00	SSPs	0.1210	0.9897	0.1676	0.9858
3.00	SSPs	-0.0371	1.0036	-0.0368	1.0036
0.50	wide BC03	0.5146	0.9411	11.0290	0.0195
1.00	wide BC03	0.3867	0.9504	2.0655	0.8387
2.00	wide BC03	-0.4636	0.9866	2.3464	0.7772
3.00	wide BC03	0.1364	0.9565	3.5024	0.6933

5.10 Summary and conclusions

We analyse the problem of recovering galaxy stellar population properties - such as photometric redshifts, ages, star formation rates, stellar masses - through broad-band spectral energy distribution fitting as a function of the various parameters of the fit, namely: star formation history, metallicity, age grid, IMF, reddening law, wavelength coverage and filter setup used in the fitting. As test particles we use the same mock galaxies (passive and star-forming) as in Chapter 4 for which we know the properties. The investigated redshift range is $0.5 \leq z \leq 3$. The photometry of mock galaxies is based on the stellar population models by Maraston (2005) which we also used for the fitting templates. Results for BC03 stellar population models (for mock galaxies and fitting templates) are fully

discussed in the Appendix. Mock galaxies are treated as real observed galaxies such that their observed-frame magnitudes are obtained and SED-fitting with various templates is carried out on these. The properties derived from the fitting are then compared to the true values of the mock galaxies.

This work complements the previous chapter such that here redshift is a free parameter in the fit which allows us to analyse how this affects the results. In the previous chapter at fixed redshift we found that for mock star-forming galaxies a mismatch in SFH is the main driver for underestimated ages and masses and overestimated reddening and SFRs due to overshining and the age-dust degeneracy. The galaxy physical properties can only be determined *simultaneously* when SFHs between template and galaxy match. For mock passive galaxies the stellar population properties are much better recovered.

When redshift is left free in the fit, we can summarise our results for the mock star-forming galaxies to:

- A broad wavelength coverage is even more crucial in the simultaneous and robust determination of galaxy properties (ages, stellar masses, reddening and SFRs) when redshift is a free parameter in the fit because photometric redshifts are best recovered - within 0.01 to 0.06 (median Δz) - when the rest-frame wavelength range comprises important features such as the Lyman-limit or the 4000 Å break. The redshifts of $z \sim 3$ objects are best recovered because here both features are covered by the broad wavelength range. The redshifts of $z \sim 2$ objects are recovered worst because the Lyman-limit is not covered by the filter setup and a well established 4000 Å break is missing.

- The redshift recovery depends only weakly on the template setup, IMF, metallicity, age grid and reddening law due to compensating effects, thus the most economic option to obtain redshifts is via the use of a mono-metallicity wide setup or an only-τ setup.

- The mismatch between template and galaxy SFH is still the most important driver for underestimated ages and stellar masses and overestimated reddening and SFRs because of the overshining and degeneracies between age, dust and redshift.

- Stellar masses at low redshift are better recovered when redshift is left free in the fit because redshift compensates. At $z = 0.5$ a sacrifice of ~ 0.01 (0.05) in accuracy for the median redshift improves the median recovered stellar mass by 0.1 dex (0.3 dex) in the unreddened (reddened) case. However, the mass recovery fails when the redshift recovery fails completely.

- The effect of the age-dust-redshift degeneracy at low redshift which causes ages and stellar masses to be underestimated can be reduced by fitting without reddening. In this way unrealistically young and dusty solutions are avoided while redshifts are recovered similarly well.

- Similarly, the mass and SFR estimate are improved at low redshift by using a cap on the minimum age. The redshift recovery is not affected by this.

- Ages are generally underestimated similar to the fixed redshift case. However, because of compensating effects with redshift, the age recovery is better at low redshift when redshift is a free parameter compared to the case of fixed redshift.

- Metallicity effects play a secondary role as in the fixed redshift case.

- SFRs are best recovered with a wide setup although the correct SFH is not included. SFRs at low redshift are generally better recovered than at fixed redshift.

- Photometric uncertainties account for 0.4 in redshift uncertainty, masses are affected on average by 0.08 ± 0.16 dex, SFRs are less affected than at fixed redshift.

For the mock passive galaxies our results are:

- Redshifts of mock passive galaxies are very well determined independently of template setup, SFH and IMF. Again a broad wavelength range guarantees the best redshift recovery.

- Stellar masses of passive galaxies can be very well recovered - within 0.02 dex for a wide setup and wavelength coverage (0.05 dex for a wide setup and no reddening but varying wavelength coverage) even when redshift is unknown.

- As in the fixed redshift case, metallicity plays an important role and the best option is to use a wide range of metallicities in the fitting.

- The age recovery for old passive galaxies is less dependent on the wavelength coverage than for star-forming galaxies but the inclusion of the rest-frame near-IR helps to significantly reduce the scatter.

- The effect of photometric uncertainties on redshifts is 0.05, on ages and masses 0.2 dex and 0.1 dex, respectively.

We conclude that photometric redshifts are recovered very well in almost any case as long as the wavelength coverage is wide. The stellar population parameters of star-forming and passive galaxies can then be reasonably well determined provided one uses the right

setup and wavelength coverage. In comparison to the fixed redshift case shown in Chapter 4 masses and SFRs are better determined at low redshift when redshift is left free because of the added degeneracy with redshift. Still the mismatch between observed and assumed SFHs dominates the parameter estimate at low redshift. This and the larger range in stellar ages means that the stellar population properties of low redshift galaxies are recovered worse than those of high redshift galaxies. We conclude that at $z \leq 1$ the best parameter recovery overall is achieved with a wide setup and excluding reddening from the fit. In the case of star-forming galaxies the metallicity range can be reduced for economic reasons without affecting the overall results. As in the fixed redshift case discussed in Chapter 4 this solution is not optimal but acceptable and future work is needed to obtain a better description of the SFHs for these galaxies.

For $z \geq 2$ star-forming galaxies good results for redshift, mass and SFR can be obtained simultaneously with a wide setup and no reddening in the fit, too. This means that photometry appears to be sufficient for the robust determination of the stellar population properties of high redshift galaxies. But as shown in Chapter 4 at fixed redshift, the best recovery for stellar masses and SFRs is given when inverted-τ models are used in the fit. We therefore recommend to obtain redshifts in the most robust way for these galaxies first and to carry out a separate fit at fixed redshift with inverted-τ models to determine stellar masses and SFRs even better.

Conclusions about the wavelength coverage remain unchanged from the fixed redshift case, meaning a coverage of UV to near-IR rest-frame wavelengths in the fitting is crucial. Again these effects are quantified and will be useful for the planning of purely photometric surveys and observational proposals.

As stressed in Chapter 4 a variety of assumptions are made in the literature with regard to fitting methods and parameter setups and thus we confirm what was already concluded by Lee et al. (2009) and in Chapter 4 that one has to be cautious when comparing results from different studies. We also provide scaling relations for the transformation of stellar masses between fitting setups for the free redshift case to ease comparisons between studies that rely on photometric redshifts.

Chapter 6

Recovering stellar population properties of real galaxies

So far we studied the uncertainties involved in SED-fitting, mostly due to user-dependent choices of the fitting parameters, and demonstrated under which circumstances and assumptions robust results can be obtained for stellar masses and other galaxy properties. For this we used mock galaxies with known properties. In this chapter, we focus on the data samples of real galaxies introduced in Chapter 2. We will give a summary of the particular assumptions and parameters used in the fitting for each sample based on the findings of the previous chapters and show the obtained galaxy stellar population properties.

We start with high-redshift star-forming galaxies in the GOODS-S survey (Section 6.1) and work our way via the luminous galaxies in the SDSS-III/BOSS survey (Section 6.2) towards the nearby Universe with the largest galaxy survey undertaken so far - the SDSS-I/II survey (Section 6.3). By doing so, we cover not only different redshift regimes but also different galaxy types. For each of these three surveys spectroscopic redshifts are available and used in the fitting.

6.1 Star-forming galaxies in GOODS-S - $1.4 < z < 2.9$

Fitting synthetic spectral energy distributions to the multi-band photometry of galaxies to derive their star formation rates, stellar masses, ages, etc. requires making a priori assumptions about their star formation histories. A widely adopted parameterisation of the star formation history, the so-called τ-models where SFR $\propto \mathrm{e}^{-t/\tau}$ is shown to lead to unrealistically low ages when applied to a sample of actively star-forming galaxies at $z \sim 2$, a problem shared by other star formation histories when the age is left as a free

parameter in the fitting procedure. This happens because the SED of such galaxies, at all wavelengths, is dominated by their youngest stellar populations, which outshine the older ones. Thus, the SED of such galaxies conveys little information on the beginning of star formation, i.e., on the age of their oldest stellar populations. To cope with this problem, besides τ-models (hereafter called direct-τ models), we explore a variety of SFHs, such as constant SFR and inverted-τ models (with SFR $\propto \mathrm{e}^{+t/\tau}$), along with various priors on age, including assuming that star formation started at high redshift in all the galaxies in the test sample. We find that inverted-τ models with such latter assumption give SFRs and extinctions in excellent agreement with the values derived using only the UV part of the SED, which is the one most sensitive to on-going star formation and reddening. These models are also shown to accurately recover the SFRs and masses of mock galaxies at $z \sim 2$ constructed from semi-analytic models (see Section 2.1), which we use as a further test. All other explored SFH templates do not fulfil these two tests as well as inverted-τ models do. In particular, direct-τ models with unconstrained age in the fitting procedure overestimate SFRs and underestimate stellar mass, and would exacerbate an apparent mismatch between the cosmic evolution of the volume densities of SFR and stellar mass. We conclude that for high redshift star-forming galaxies an exponentially increasing SFR with a high formation redshift is preferable to other forms of the SFH so far adopted in the literature.

This section is organised as follows. Firstly, we give a brief introduction to the specific topic of this section (Section 6.1.1). In Section 6.1.2 we describe the template setups and models used for the GOODS-S data sample (introduced in Section 2.2). Then we present the results obtained for the different star formation history templates and their comparisons (Section 6.1.3). Finally, we give a general discussion and present our conclusions (Section 6.1.4).

In this section only, we adopt a cosmology with Ω_Λ, Ω_M and $h = H_0/(100\,\mathrm{kms}^{-1}\mathrm{Mpc}^{-1})$ equal to 0.7, 0.3 and 0.75, respectively, for consistency with most previous works[1]. The age of the best-fit model is required to be lower than the age of the Universe at the given spectroscopic redshift. The SFR and masses are always in $M_\odot$/yr and $M_\odot$ units, respectively.

[1]Differences in derived stellar population parameters arising from a cosmology using Ω_Λ, Ω_M and $h = H_0/(100\,\mathrm{kms}^{-1}\mathrm{Mpc}^{-1})$ equal to 0.719, 0.258 and 0.742 as used in Chapters 4 and 5, respectively, are small.

The work in this chapter was carried out in collaboration with C. Maraston, A. Renzini, E. Daddi, M. Dickinson, A. Cimatti and C. Tonini and is published in Maraston et al. (2010).

6.1.1 Background

In this section we focus on star-forming galaxies at $1.4 \lesssim z \lesssim 2.5$, hence covering the epoch of major star formation activity, and explore a wide set of SFHs showing advantages and disadvantages of different parameterisations of them. The case of passively evolving galaxies at $z \gtrsim 1.4$ was already addressed in Maraston et al. (2006).

It is well known that at $z \sim 2$ galaxies with SFRs as high as a few $\sim 100 M_{\odot}$/yr are quite common (e.g. Daddi et al., 2005), and by analogy with the rare objects at $z \simeq 0$ with similar SFRs (like Ultra Luminous Infra-Red Galaxies, ULIRGs), it was widely believed that such galaxies were caught in a merging-driven starburst. However, integral-field near-infrared spectroscopy has revealed that at least some of these galaxies have ordered, rotating velocity fields with no kinematic evidence for on-going merging (Genzel et al., 2006). Still, the disk was shown to harbour several star-forming clumps and to have high velocity dispersion and gas fraction. All this makes such disks quite different from local disk galaxies, and it is now well documented that the same properties apply to many similar objects at $z \sim 2$ (Förster Schreiber et al., 2009).

That high SFRs in $z \sim 2$ galaxies do not necessarily imply *starburst* activity became clear from a study of galaxies in the GOODS fields (Daddi et al., 2007). Indeed, for star-forming galaxies at $1.4 \lesssim z \lesssim 2.5$ the SFR tightly correlates with stellar mass (with SFR $\propto\sim M^*$), with small dispersion (~ 0.3 dex), as shown in Fig. 2.6. Only a few galaxies lie far away from the correlation: a relatively small number of passive galaxies (with undetectable SFR, not shown in the figure), and sub-mm galaxies (SMG) with much higher SFRs, which may indeed be the result of gas-rich major mergers. Among star-forming galaxies, the small dispersion of the SFR for given M^* demonstrates that these objects cannot have been caught in a special, starburst moment of their existence. Rather, they must sustain such high SFRs for a major fraction of the time interval between $z = 2.5$ and $z = 1.4$, i.e. for some $1 - 2$ Gyr, instead of the order of one dynamical time ($\sim 10^8$ yr) typical of starbursts. Similar correlations have also been found at lower redshifts, notably at $z \sim 1$ (Elbaz et al., 2007), $0.2 \sim z \sim 1$ (Noeske et al., 2007), and $z \sim 0$ (Brinchmann et al., 2004).

In a recent study, Pannella et al. (2009) have measured the average SFR vs. stellar mass for $1.4 \lesssim z \lesssim 2.5$ galaxies using the 1.4 GHz flux from the VLA coverage of the COSMOS field (Schinnerer et al., 2007). When combined also with data at lower redshifts (see references above), Pannella et al. derive the following relation for the average SFR as a function of galaxy mass and time:

$$< \mathrm{SFR} > \simeq 270 \times (M^*/10^{11} M_\odot) \times (t/3.4 \times 10^9 \mathrm{yr})^{-2.5} \quad (6.1)$$

where the SFR is in $M_\odot$/yr units and t is the cosmic time, i.e., the time since the Big Bang. Beyond $z \sim 2.5$ ($t \lesssim 2.7$ Gyr) the specific SFR (= SFR/M^*) appears to flatten out and remain constant all the way to very high redshifts (Daddi et al., 2009; Stark et al., 2009; González et al., 2010).

In parallel with these observational evidences, theorists are shifting their interests from (major) mergers as the main mechanism to grow galaxies, to continuous *cold stream* accretion of baryons, that are then turned into stars in a quasi-steady fashion (e.g. Dekel et al., 2009). Clearly, a continuous, albeit fluctuating SFR such as in these cold stream models provides a far better match to the observed tight SFR-M^* relation, compared to a scenario in which star formation proceeds through a series of short starbursts interleaved by long periods of reduced activity. This is not to say that major mergers do not play a role. They certainly exist, and can lead to real giant starbursts bringing galaxies to SFRs as high as $\sim 1000 M_\odot/\mathrm{yr}$, currently identified with SMGs (e.g. Tacconi et al., 2008; Menéndez-Delmestre et al., 2009).

Deriving SFRs, ages, stellar masses, etc. from SED-fitting requires making assumptions on the previous SFH of galaxies. A widespread approach is to fit the SED of galaxies at low as well as high redshifts with so called "τ-models", i.e., synthetic SEDs in which the SFH is described by an exponentially declining SFR as defined in Eq. 3.14, starting at cosmic time t_0. For a galaxy at cosmic time t a χ^2 fit then gives the age (i.e., $t - t_0$, the time elapsed since the beginning of star formation), the SFR e-folding time τ, the reddening $E(B-V)$, the metallicity Z and finally the stellar mass M^* via the scale factor A. The SFR then follows from Eq. 3.14, where t is the cosmic time corresponding to the observed redshift of each galaxy. Of course, the reliability of the results depends on the extent to which the actual SFH is well represented by a declining exponential.

It is worth recalling that the first applications of τ-models were to figure out the ages of local elliptical galaxies, and the typical result was that the age is of the order of one Hubble time, and τ of the order of 1 Gyr or less (e.g. Bruzual A., 1983). This approach

confirmed that the bulk of stars in local ellipticals are very old, hence formed within a short time interval compared to the present Hubble time. Later, the usage of τ-models was widely extended also to actively star-forming galaxies at virtually all redshifts, to the extent that it became the default assumption in this kind of studies (e.g. Papovich et al., 2001; Shapley et al., 2005; Lee et al., 2009; Pozzetti et al., 2010; Förster Schreiber et al., 2009; Wuyts et al., 2009). Such an assumed SFH may give reasonable results for local spirals, as their star formation activity has been secularly declining for an order of one Hubble time (e.g. Kennicutt, 1986), but we shall argue that it may be a rather poor representation of the SFH of high-z galaxies, and may lead to quite unphysical results.

Cimatti et al. (2008) noted that the age of elliptical galaxies at $z \sim 1.6$ turns out to be ~ 1 Gyr both when using only the rest-frame UV part of the SED, and when using the whole optical-to-near-IR SED in conjunction with τ-models. However, they also noted that the former "age" is actually the age of the population formed in the last significant episode of star formation, while the latter "age" corresponds to the time elapsed since the beginning of star formation. The near equality of these two ages suggests that the SFR peaked shortly before being quenched, rather than having peaked at an earlier time and having declined ever since. Moreover, using τ-models one implicitly assumes that galaxies are all caught at their minimum SFR, which is possibly justified for local ellipticals and spirals, but not necessarily for star-forming galaxies at high redshifts that may actually be at the peak of their SF activity.

Indeed, an integration of $dM^*/dt =< \mathrm{SFR} >$ where $< \mathrm{SFR} >$ is given by Eq. 6.1 shows that the SFR can *increase* quasi-exponentially with time before the effect of the declining term $t^{-2.5}$ takes over, or star formation is suddenly quenched and the galaxy turns passive (Renzini, 2009). Mass and SFR formally increase exponentially when SFR $\propto\sim M^*$, independent of time, as appears to be the case for $z \gtrsim 2.5$ (González et al., 2010). Thus, the observations of both passive and star-forming galaxies at $1.4 \lesssim z \lesssim 2.5$ suggest that the SFRs of these galaxies may well have increased with time, rather than decreased. For these reasons, in this chapter (Section 6.1) we use both *direct*-τ models, with the SFR given by Eq. 3.14, as well as *inverted*-τ models in which the SFR increases exponentially with time, as defined in Eq. 3.15.
Thus, direct-τ models assume that galaxies are caught at their minimum SFR and had their maximum SFR at the beginning, whereas inverted-τ models assume that galaxies are caught at their maximum SFR and had their minimum SFR at the beginning. These two extreme assumptions may to some extent *bracket* the actual SFHs of real galaxies, or at least of the majority of them which, because of the tight SFR-M^* relation, must have a relatively smooth SFH. Here we explore which of the two assumptions gives the

better fit to the SED of $z \sim 2$ galaxies, and discuss the astrophysical plausibility of the relative results. Besides these exponential SFHs we also consider the case of constant SFRs. In principle, other, differently motivated SFHs could also be explored, but in this chapter (Section 6.1) we restrict the comparison to these three simple options, with SFRs increasing with time, decreasing, or constant.

6.1.2 Setup for SED-fitting

The method we adopt for the SED-fitting is similar to the one used in Maraston et al. (2006, hereafter M06). We construct composite population templates based on the stellar population models of M05 and we use the *HyperZspec* code which performs the SED-fit at fixed spectroscopic redshift[2]. In the current version of *HyperZspec*, kindly provided to us by M. Bolzonella, 221 ages (or τ's) are used for each kind of SFH, instead of the 51 used in earlier versions of *HyperZ*. The use of denser grids tends to give somewhat different results, an effect that is explored in detail in Chapter 4 (see also Pforr et al., *submitted*).

A detailed description of the method and *HyperZspec* is given in Chapter 3. It is important to note that the code does not interpolate on the template grids, hence the template set must be densely populated. The extinction $A_{\rm V}$ is allowed to vary from 0 to 3 in steps of 0.2, which corresponds to $E(B-V)$ from 0 to 0.74 according to the reddening law of Calzetti et al. (2000), that we adopt for all fits. By doing so we implicitly assume that the dust composition is the same in all examined galaxies and that there are no major galaxy to galaxy differences in the relative distribution of dust and young, hot stars. Differences in the extinction curve have been detected among $z \sim 2$ galaxies, with some galaxies exhibiting the 2175 Å UV bump, while others do not show it (Noll et al., 2009), but such differences appear to have only minor effects on the derived SFR. Extinction is unlikely to be uniform across the surface of galaxies, particularly in extremely dusty ones (e.g. Serjeant, Gruppioni & Oliver, 2002). However, the tightness of the SFR-mass relation for $z \sim 2$ galaxies (compare Fig. 2.6), together with the agreement of their UV-derived SFRs with those derived from the radio (Pannella et al., 2009) argues for such *average extinction* approximation to be a fairly good one, at least for the majority of the galaxies at these redshifts.

[2]For the fitting procedure we use photometric errors of 0.05 if the formal error is smaller than that, to account for systematics in photometry and colour matching.

For all models we considered only solar metallicity. This is different from the approach adopted by M06 in fitting the near-passive galaxies at $z \lesssim 2$, for which they considered four metallicities and several possible reddening laws. Indeed, we have noticed that varying the reddening law has only a very mild influence on the derived properties of star-forming galaxies (Chapter 4), hence for economy we decided to stick to the reddening law that gives the best-fit in most cases, which is the Calzetti law. As for the metallicity, it is known that super-solar metallicities tend to give younger ages and higher masses and vice-versa for sub-solar metallicities (e.g. M05). However, metallicity effects do not change the main results of the present investigation. Indeed, our focus is on exploring the effects of adopting different functional forms for the SFHs and we restrict the main analysis at fixed, solar metallicity. On the other hand, metallicity effects over the SED of star-forming galaxies are generally less important than age effects (compare Chapter 4).

The main difference with respect to M06, whose work was focused on nearly-passive galaxies, consists in the composite population templates that are used in the fits. In particular, besides a constant star formation and direct-τ models, we explore inverted-τ models for various setups of ages and τ's. The latter models are quite a novelty in this kind of studies, and we describe them in more detail below.

Direct and inverted-τ models

As mentioned above, besides constant SFR models, in this section we consider two main sets of SFHs, namely direct-τ and inverted-τ models, where the evolution of the SFR is given by Eqs. 3.14 and 3.15, respectively. For both types of SFHs, we calculate three model flavours which mostly differ with respect to how the parameter age is treated, namely:

- a) leaving the age as a free parameter;
- b) fixing the age by fixing the formation redshift and varying only τ;
- c) constraining the age to be larger than τ.

The age of composite models is the time elapsed since the beginning of star formation, i.e. is the age of the oldest stars $(t - t_0)$. In the age free case, we simply compute exponentially increasing/decreasing models for various τ's, and 221 ages for each τ. The SED-fit with these age-free models releases for each galaxy a value of age $= t - t_0$, $E(B-V)$, M^* and of τ.

In the case of fixed age (case b), we assume that all galaxies started to form stars at the same redshift $z_{\rm f}$, and therefore the age of a galaxy follows from the cosmic time difference between its individual spectroscopic redshift and $z_{\rm f}$. Thus, in this case the best fit releases a value of τ, $E(B-V)$ and M^*. In this experiment we take $z_{\rm f} = 5$ for the formation redshift, which implies that all galaxies are older than ~ 1 Gyr (ages range between 1 and 3 Gyr, depending on their redshift). In case c) the age can still vary freely, but only within values that exceed the corresponding τ, so e.g. when τ is 0.5 Gyr, the allowed ages for the fit must be ≥ 0.5 Gyr. In practice, among all the fits attempted for case a) those with age $< \tau$ are not considered.

Age is a default free parameter in *HyperZ*, and therefore the procedure had to be modified to cope with case b), for which age is no longer a free parameter. Thus, for each age we have calculated a grid of models for 221 different τ's ranging from 0.05 to 10.3 Gyr in step of 0.045 Gyr, although the cases with $\tau < 0.3$ Gyr will be discussed separately. The best-fit then finds the preferred τ. If we were to consider all kinds of galaxies, including passive galaxies and low-redshift ones, the exponentially-increasing models should be quenched at some point, which could be done either by SFR truncation, or adding a further exponential decline. We did not quench the models here as the galaxies we focus on are all actively star-forming at the epoch of observation. It is worth emphasising that the set-up with fixed age clearly has one degree of freedom less than those with age free, which will affect their χ^2_ν values.

The quality of the fits is measured, as usual, by their χ^2_ν, but we believe that the plausibility of the fits can be assessed only considering the broadest possible astrophysical context. Before presenting our results it is worth adding some final comments on the derived stellar masses and SFRs. In this work we have used templates adopting a straight Salpeter IMF down to $0.1\ M_\odot$. This is not the optimal choice as it is generally agreed that an IMF with a flatter slope or cut-off at low masses, like those proposed by Kroupa (2001) or Chabrier (2003), is more appropriate for deriving an absolute value of the stellar mass or of the SFR. However, the focus of this work is in comparing the results obtained with different SFHs, hence the slope of the IMF below $\sim 1\ M_\odot$ is irrelevant. Note also that the reported stellar mass M^* is the mass that went into stars by the age of the galaxy. This overestimates the true stellar mass, as stars die leaving remnants whose mass is smaller than the initial one, and the galaxy mass decrement in case of extended star formation histories is $\sim 20-30\%$ (see e.g. Maraston, 1998, M06).

6.1.3 Results

In this section we compare the stellar population properties derived under the three different assumptions for the SFH, namely: direct- and inverted-τ models and constant star formation, both leaving age as a free parameter, and also assuming age (i.e., formation redshift) as a prior, as described above.

Age as a free parameter

A first set of best fits was performed allowing the procedure to select the preferred galaxy age. The results are reported in Figs. 6.1 to 6.6, showing the histograms for the resulting ages, τ's, stellar masses, reddening, SFRs and χ^2_ν, respectively.
Surprisingly, all histograms look quite similar, irrespective of the adopted SFH. In particular, the distributions of the χ^2_ν values are almost identical, indicating that no adopted functional shape of the SFH gives substantially better fits than another. However, it would be premature to conclude that the resulting physical quantities (ages, masses, etc.) have been reliably determined. Most of the derived ages are indeed very short in all three cases, with the majority of them being less than $\sim 2 \times 10^8$ yr, with several galaxies appearing as young as just $\sim 10^7$ yr (see Fig. 6.1). We believe that these ages - intended

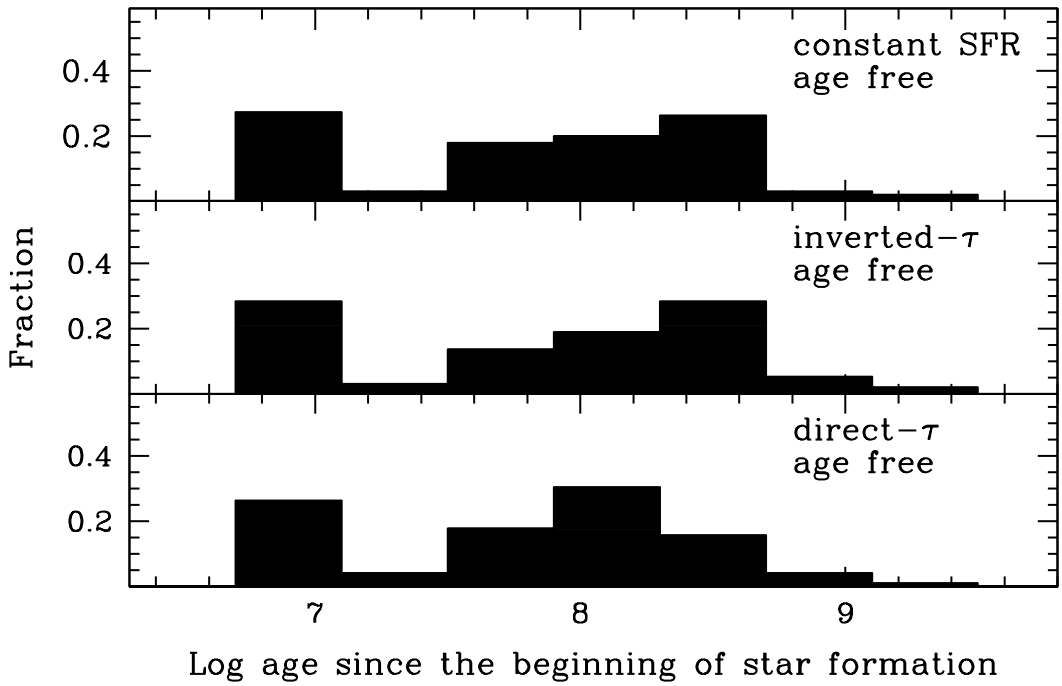

Figure 6.1: The time elapsed since the beginning of star formation, for models with constant star formation (upper panel), and with star formation proceeding as an inverted and direct-τ model (middle and lower panels, respectively). The age is left free in all three models.

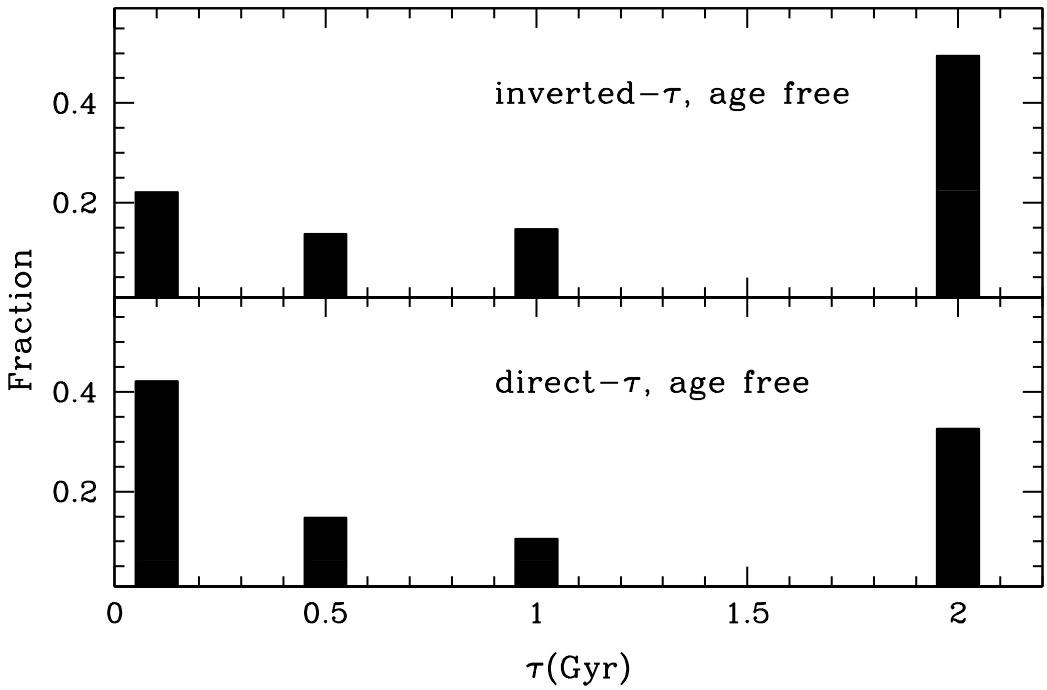

Figure 6.2: Same as Fig. 6.1 for τ (in Gyr).

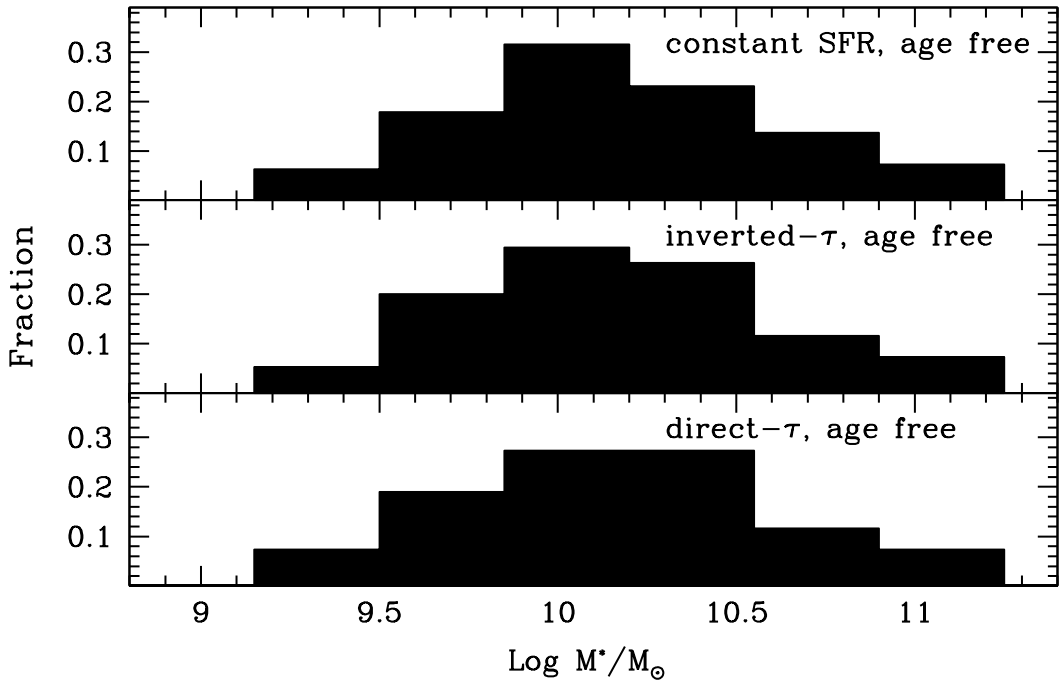

Figure 6.3: Same as Fig. 6.1 for stellar masses.

to indicate the epoch at which the star formation started - cannot be trusted as such, for the following reasons. First, as we shall show later and as also known in the literature, the latest episode of star formation outshines older stars even when composite models are

considered. In addition, cosmological arguments render this interpretation suspicious, as we are going to discuss. Fig. 6.7 shows the redshift of each individual galaxy as a function of its formation redshift, the latter being derived by combing the redshift and age of each galaxy. Note that with the derived ages most galaxies would have started to form stars just shortly before we happen to observe them. If this were true, the implied cosmic SFR should rapidly vanish by $z \sim 3$, while this is far from happening: the cosmic SFR at $z \sim 3$ is nearly as high as it is at $z \sim 2$ (e.g. Hopkins & Beacom, 2006), and the specific SFR at a given mass stays at the same high level all the way to $z \sim 7$ (González et al., 2010).

We consider far more likely that most of the descendants of galaxies responsible for the bulk of cosmic star formation at $z \gtrsim 3$ are to be found among the still most actively star-forming galaxies at $z \sim 2$, rather than a scenario in which the former galaxies would have faded to unobservability by $z \sim 2$, and those we see at $z \sim 2$ would have no counterpart at $z \gtrsim 3$. In other words, massive star-forming galaxies at $z \sim 2$ must have started to form stars at redshifts well beyond ~ 3. Note that some star-forming galaxies at $z \gtrsim 3$ may have turned passive by $z \sim 2$, but the number and mass density of passive galaxies at $z \sim 2$ is much lower than that of $z \gtrsim 3$ star-forming galaxies of similar mass (e.g. Kong et al., 2006; Fontana et al., 2009; Williams et al., 2009; Wuyts et al., 2009).

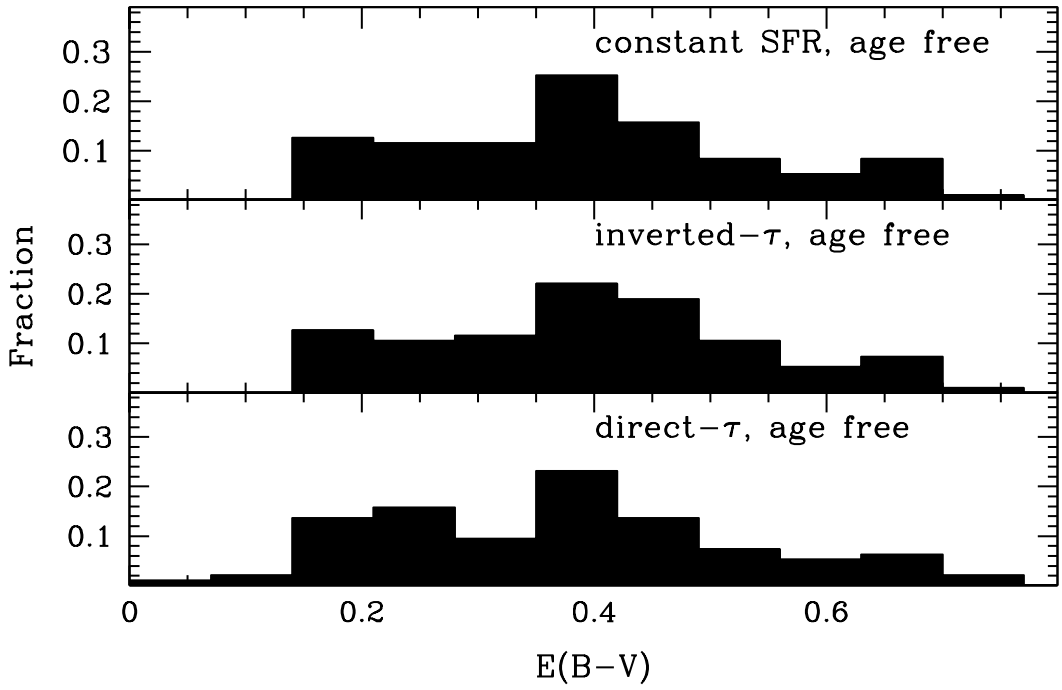

Figure 6.4: Same as Fig. 6.1 for the reddening $E(B-V)$.

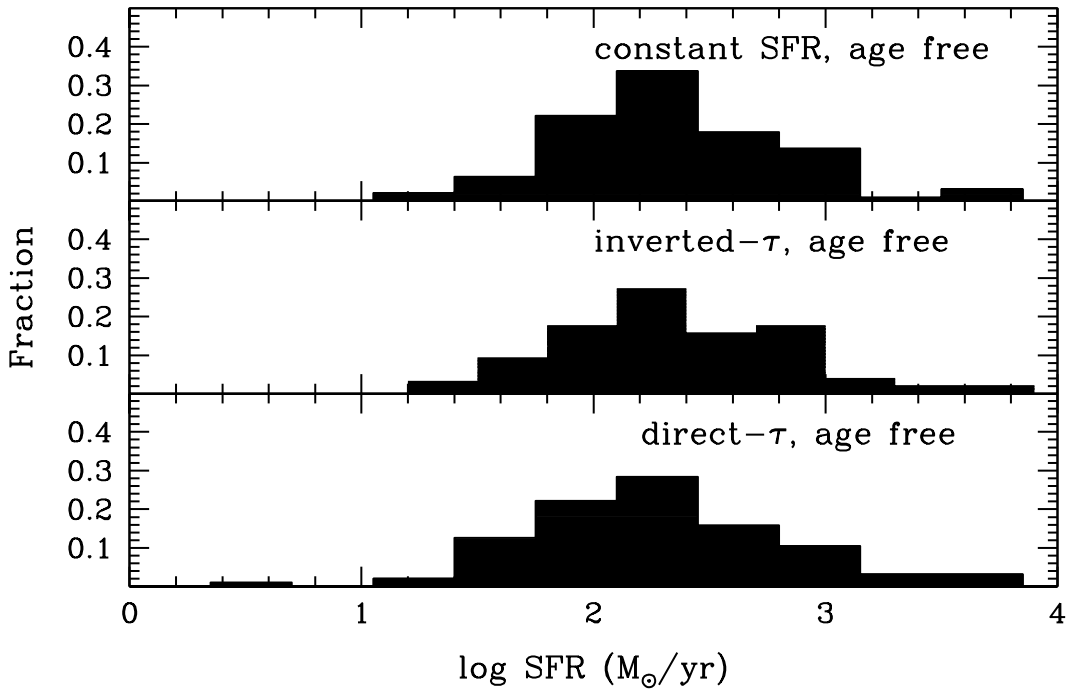

Figure 6.5: Same as Fig. 6.1 for the star formation rates.

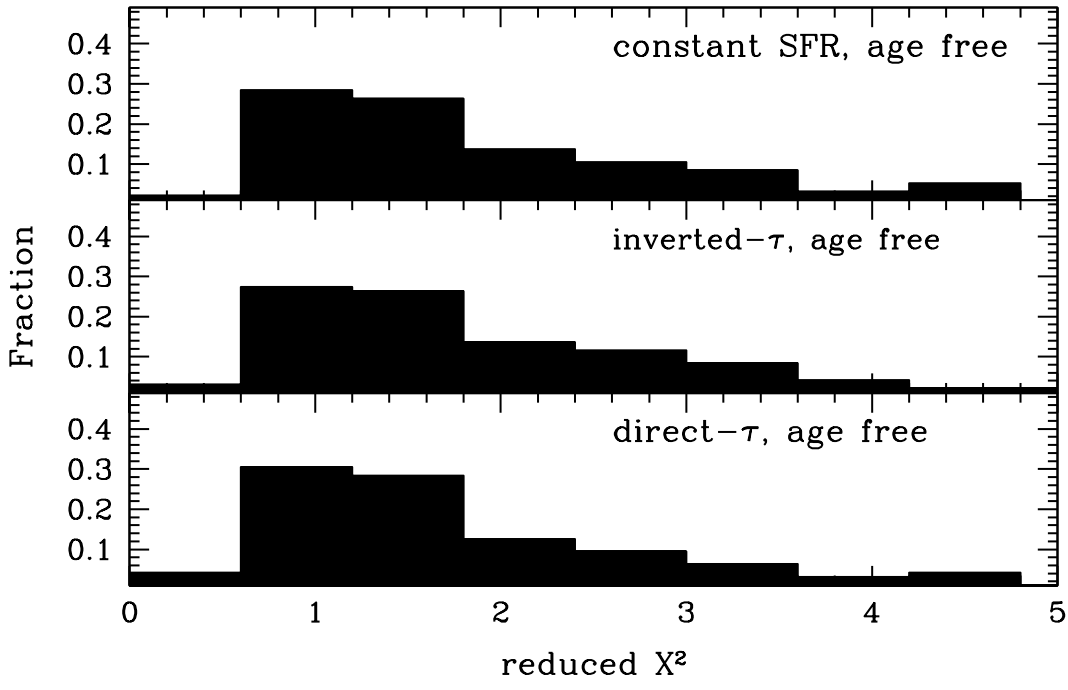

Figure 6.6: Same as Fig. 6.1 for the χ^2_ν.

Thus, the question is why does the best fit procedure choose such short ages? Clearly, the result is not completely unrealistic, as the bulk of the light must indeed come from very young stars. This is illustrated by the example shown in Fig. 6.8, for a typical case

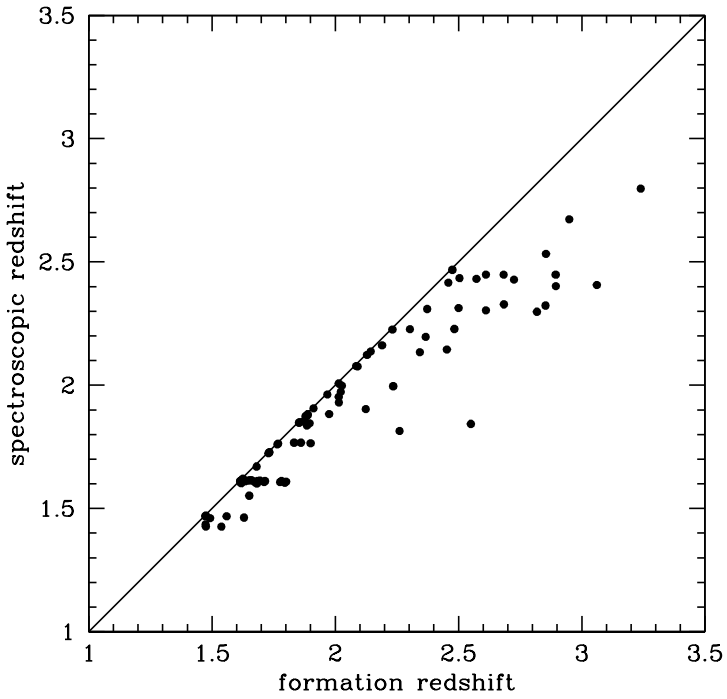

Figure 6.7: The spectroscopic redshift of individual galaxies vs. their *formation redshift* as deduced from their age as derived from inverted-τ models with age as a free parameter. Similar plots could be shown using ages derived from direct-τ models or models with SFR=const.

in which very short ages are returned. The main age-sensitive feature in the spectrum is the Balmer break, which for this galaxy as for most others in the sample, is rather weak or absent. With the whole optical-to-near-IR SED being dominated by the stars having formed in the recent past, the spectrum does not convey much age information at all. Fig. 6.8, lower/left panel, shows that if one forces age to be as large as 1.5 Gyr (and fix the formation redshift accordingly) then the Balmer break deepens and the χ^2_ν worsens. Fig. 6.9 shows the SED and relative best fit spectra for one of the few galaxies for which the procedure indicates a large age (~ 1 Gyr). Clearly, this larger age follows from the much stronger Balmer break present in this galaxy.

Note that for both direct- and inverted-τ models, in most cases $\tau >> (t - t_0)$, i.e., the e-folding time of SFR is (much) longer than the age, i.e., the SFR does not change much within the time interval $t - t_0$. This explains why both kind of models give results so similar to those in which SFR is assumed to be constant.

We shall show in the next subsections that other fits may actually result in more plausible physical solutions, even if they have a *worse* χ^2_ν.

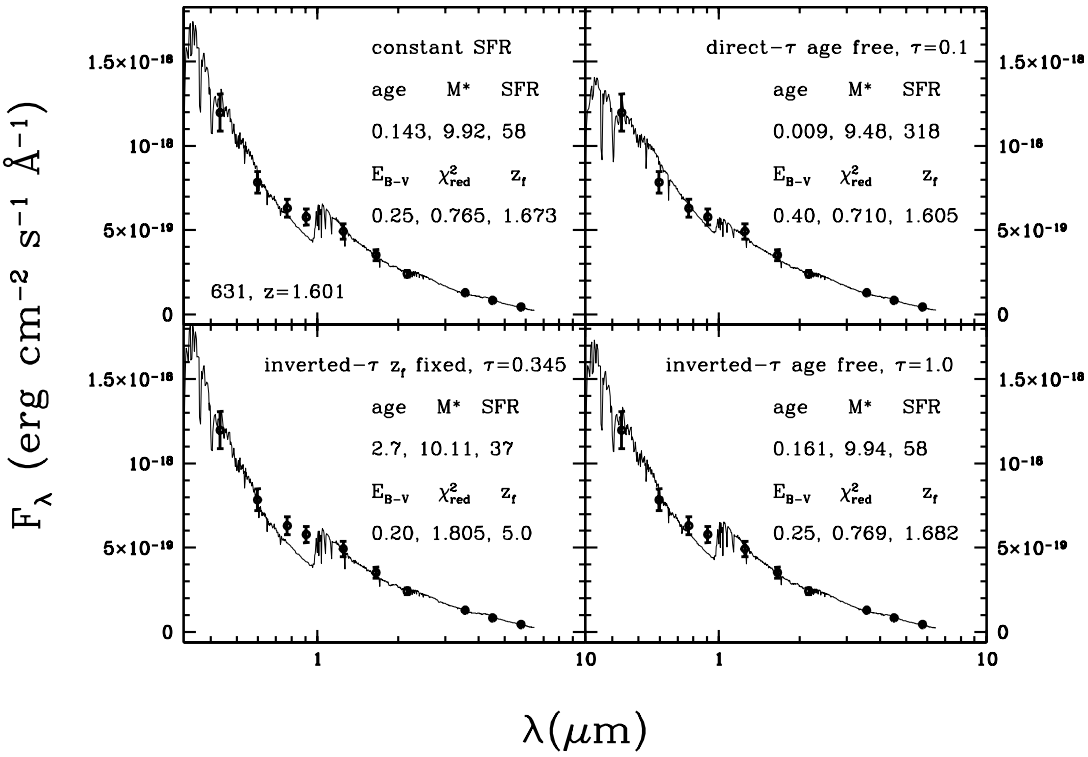

Figure 6.8: The observed spectral energy distributions (filled symbols with error bars) of high-z star-forming galaxies. Object ID and spectroscopic redshift are labelled in the top left-hand panel. In each panel the solid line corresponds to the best fit solution according to the different templates for the star formation history, namely constant star formation, τ with age free, inverted-τ with age fixed and inverted-τ with age free (from top to bottom and left to right). Several parameters of the fits are labelled, namely the age (in Gyr), the τ (in Gyr), the reddening $E(B-V)$, the stellar mass (in log $M_{\odot}$), the star formation rate (SFR) in $M_{\odot}$/yr, the χ^2_{ν}, the 'formation redshift' z_{form} obtained by subtracting the formal age of the object to the look-back time at given spectroscopic redshift.

The extremely young ages and the insensitivity of the fit to different star formation histories when the age is left free should not be so surprising. They are the consequence of the fact that the very young, massive stars just formed during the last $\lesssim$ few 10^8 yr dominate the light at virtually all wavelengths in these actively star-forming galaxies, even if they represent a relatively small fraction of the stellar mass. The capability of a very young population to outshine previous stellar generations is illustrated in Fig. 6.10. Synthetic spectra are shown for a composite stellar population that has formed stars at constant rate for 1 Gyr, and then separately for the contributions of the stars formed during the first half and the second half of this time interval. The contribution of the young component clearly outshines the old component at all wavelengths, making it difficult to assess the presence and contribution of the latter one, even if it represents half of the total stellar mass. This plot demonstrates why it is not appropriate to interpret the "age" resulting from the previous fits as the time elapsed since the beginning of star formation, as it is

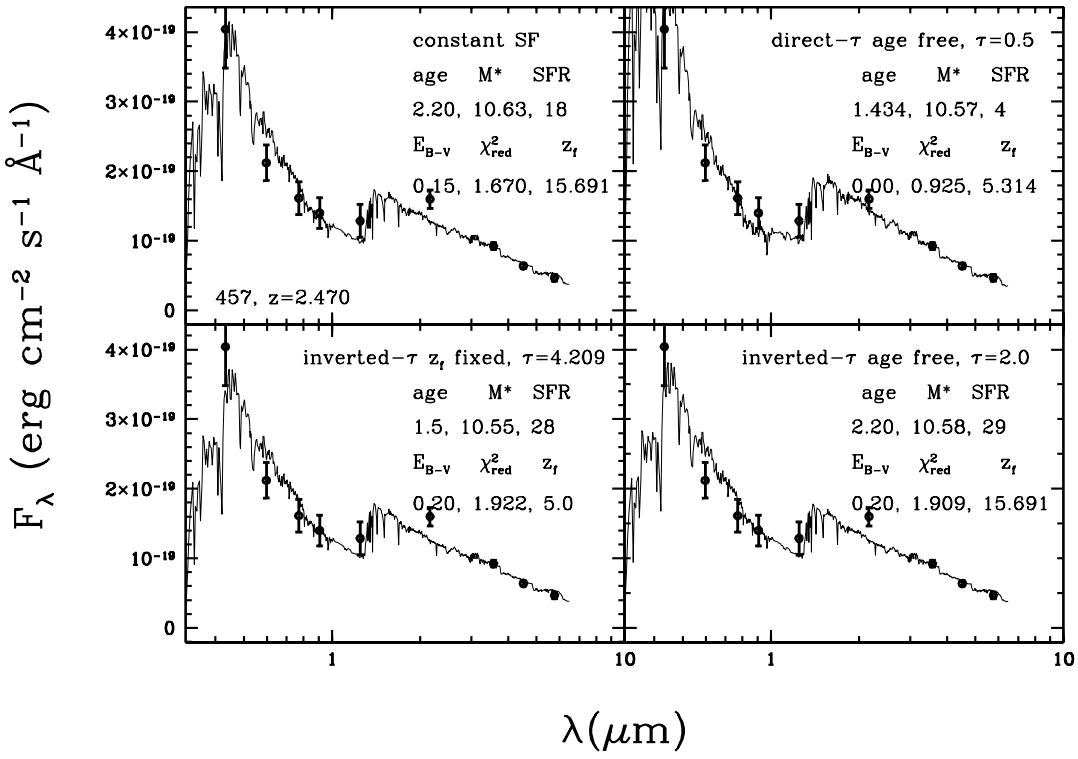

Figure 6.9: The same as in Fig. 6.8, for one of the few galaxies with best fit age $\sim$ 1 Gyr. Note the sizeable Balmer break.

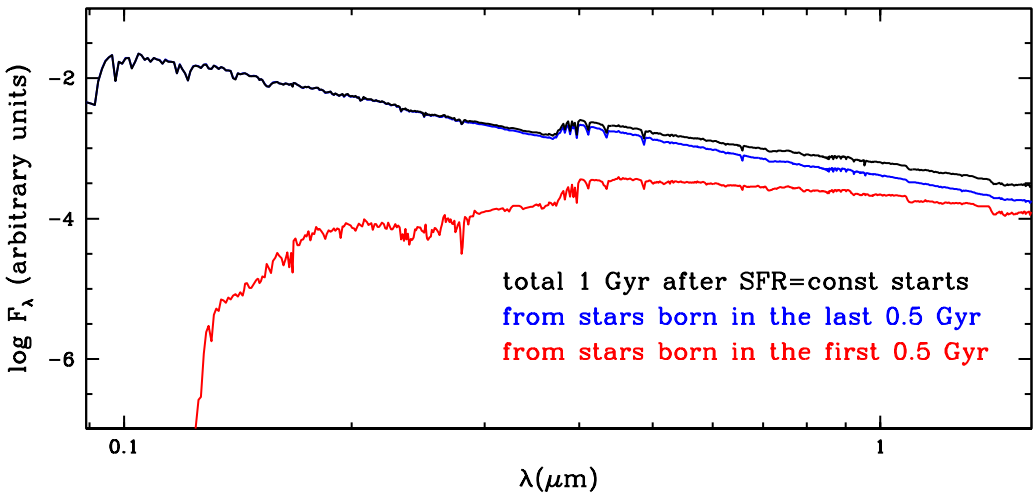

Figure 6.10: The effect of outshining by the youngest fraction of a composite population: the synthetic spectrum is shown of a composite population having formed stars at constant rate for 1 Gyr. The contribution of the stars formed during the first and the second half of this period are shown separately as indicated by the colour code, together with the spectrum of the full population.

formally meant to be in the fitting procedure and as might be suggested by a naive interpretation of the fitting results. It would instead be better interpreted as the age of the stars

producing the bulk of the light. In the next subsection we experiment with a different approach that may circumvent this intrinsic problem and get more robust properties of (high-redshift) star-forming galaxies.

Best fit solutions with fixed formation redshift

Clearly, massive star-forming galaxies at $z \sim 2$ cannot have started to form stars just shortly before we observe them. Instead, they must have started long before, as indeed demonstrated by the fact that star-forming galaxies are found to much higher redshifts. In this section we arbitrarily assume that all our galaxies have started to form stars at the same cosmic epoch, corresponding to $z = 5$, i.e. when the Universe was ~ 1 Gyr old. This implies an age for the galaxy at redshift z which is given by

$$\Delta t = t(z) - t(z_{\rm f}). \tag{6.2}$$

At first sight such an assumption may seem a very strong one. Actually this is not the case. We have already argued that our galaxies must have started to form stars at a redshift much higher than that at which they are observed, i.e., $z_{\rm f} >> 2$. Therefore, the prior

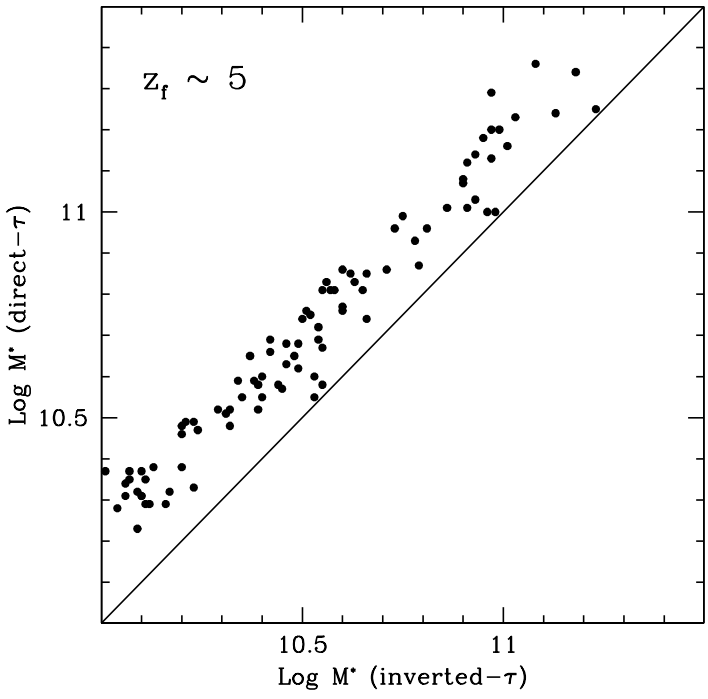

Figure 6.11: A comparison of the stellar masses derived assuming exponentially decreasing star formation rates (direct-τ models) with those obtained assuming exponentially increasing star formation rates (inverted-τ models). The beginning of star formation is set at the cosmic epoch corresponding to $z = 5$ for all models.

age changes only marginally ($\leq 20\%$) if instead of $z_{\rm f} = 5$ we had chosen $z_{\rm f} = 6$, 7, or more, and so does the result of the fit, i.e., such a result is fairly insensitive to the precise value of $z_{\rm f}$, provided it is well in excess of ~ 2. Obviously, the effect is especially strong for exponentially increasing SFRs. Incidentally, we note that exponentially decreasing SFRs have been assumed also for galaxies at very high redshifts (e.g. $z = 4 - 6$, Stark et al., 2009).

For both the exponentially declining and increasing τ models, we identify the best-fitting SFHs, first allowing only values of $\tau \geq 0.3$ Gyr. The results are shown in Figs. 6.11-6.14, in which the parameters of the best-fitting models for these two SFHs are compared. Fig. 6.11 compares the stellar masses obtained with the two SFHs, showing that those obtained with direct-τ models are systematically larger by ~ 0.2 dex with respect to stellar masses derived using the inverted-τ models. Fig. 6.12 shows the comparison of the SFRs, with the SFR from inverted-τ models being systematically higher by ~ 0.5 dex, and therefore the specific SFR turns out to be systematically higher by ~ 0.7 dex. Fig. 6.13 shows how different the τ values derived using the two SFHs are. Direct-τ models prefer very large τ's, up to ~ 10 Gyr, which is to say that they prefer nearly constant SFRs. On the contrary, inverted-τ models prefer short τ's, typically shorter than ~ 0.5 Gyr, hence a SFR that is rapidly increasing with time.

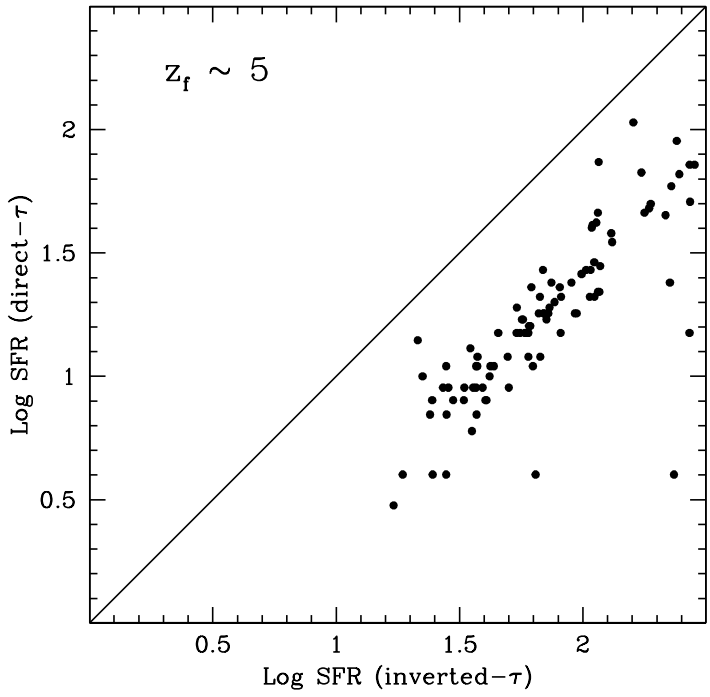

Figure 6.12: The same as in Fig. 6.11, but for a comparison of the derived star formation rates.

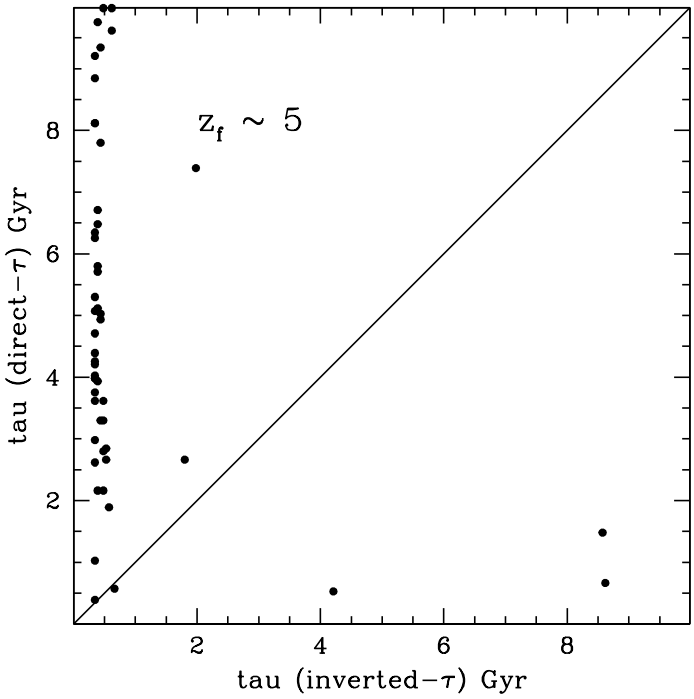

Figure 6.13: The same as in Fig. 6.11, but for a comparison of the derived τ values.

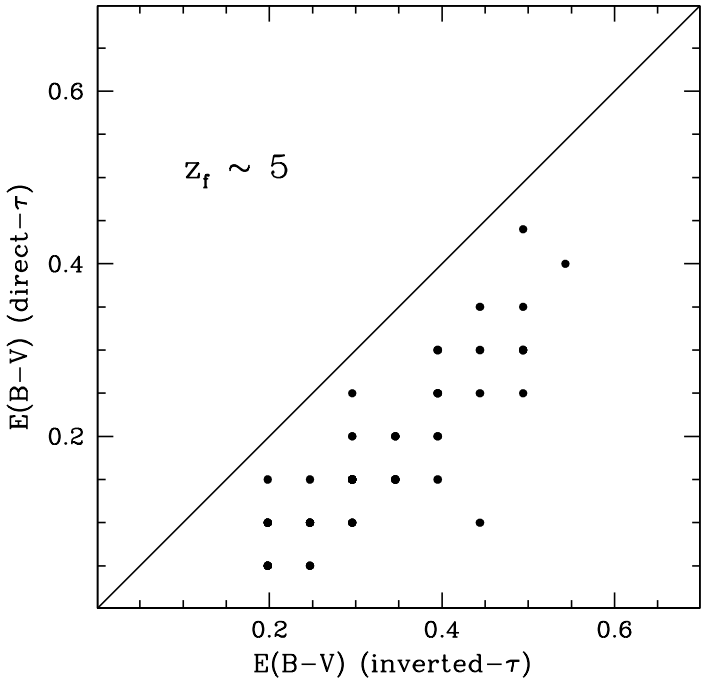

Figure 6.14: The same as in Fig. 6.11, but for a comparison of the derived values of the reddening $E(B-V)$.

Fig. 6.13 gives the key to understand the physical origin of the mass and SFR offsets between the two families of models. Being forced to put more mass at early times, direct-τ

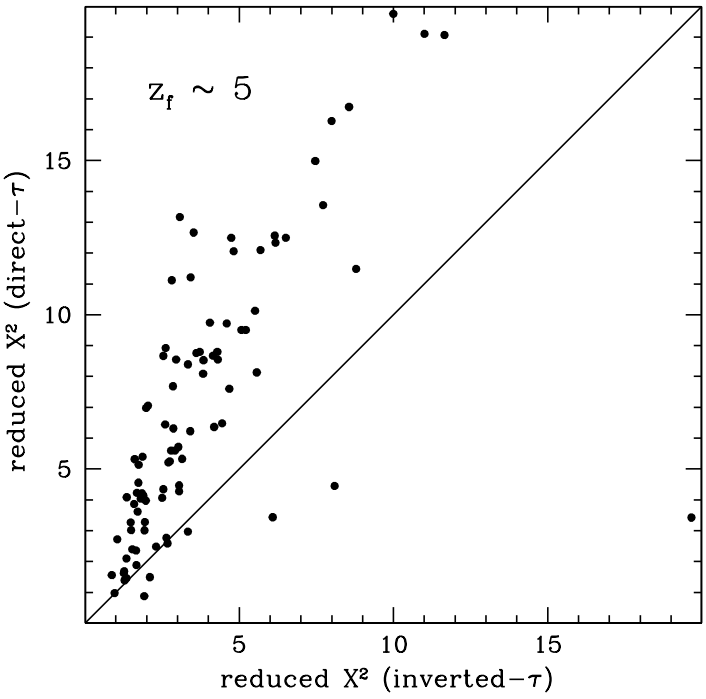

Figure 6.15: The same as in Fig. 6.11, but for a comparison of the χ^2_ν values of the best fit solutions.

models pick very large τ's trying to find the best compromise for mass and SFR, and, compared to inverted-τ models, they overproduce mass at early times and not enough star formation at late times. On the other hand, these latter models by construction put very little mass at early times, and most of it is formed at late times. In order to compromise mass and SFR, they may overestimate the current SFR, and may be forced to hide part of it demanding more extinction.

Indeed, Fig. 6.14 compares the reddening obtained with the two opposite SFH assumptions, showing that to obtain a good fit in the rest-frame UV the higher on-going SFR derived from inverted-τ models needs to be more dust-obscured than in the case of direct-τ models. Finally, Fig. 6.15 compares the reduced χ^2's obtained with the two sets of models. Those relative to inverted-τ models are not very good, but those with direct-τ models are definitely much worse. Still, a robust choice for the SFH cannot rely only on this relatively marginal advantage of inverted-τ models. In the next subsections we try to gather independent evidence that may help favouring one or the other option.

Comparing SFRs and extinctions from SED-fitting and from rest-frame UV only

The rest-frame UV part of the explored spectrum (from observed B band up to Spitzer/IRAC channel 3, i.e. 5.8μm) is the one which most directly depends on the rate of on-going star

formation. On the other hand, when the SFR is estimated with an SED-fitting procedure as in the previous sections, the derived SFR results from the best possible compromise with all the free parameters, given the adopted templates. In other words, the resulting SFR is *compromised* relative to the other free parameters of the fit and the adopted SFHs. SFRs from the UV flux, corrected for extinction using the UV slope (plus a reddening law, such as the Calzetti law) are widely derived in the literature for high redshift galaxies, and shown to be in very good agreement with independent estimates from the radio flux at 1.4 GHz (e.g. Reddy & Steidel 2004,Daddi et al. 2007,Daddi et al. 2007; Pannella et al. 2009), and also from the mid-IR (24μm) and soft X-ray fluxes, for those galaxies with no mid-IR excess (Daddi et al., 2007). Thus, the SFR derived only from the UV flux represents an *uncompromised* template (in the sense that it has no covariance with other parameters of the fit), and therefore with respect to which we may gauge the physical plausibility of a *whole optical-near-IR SED*-fit.

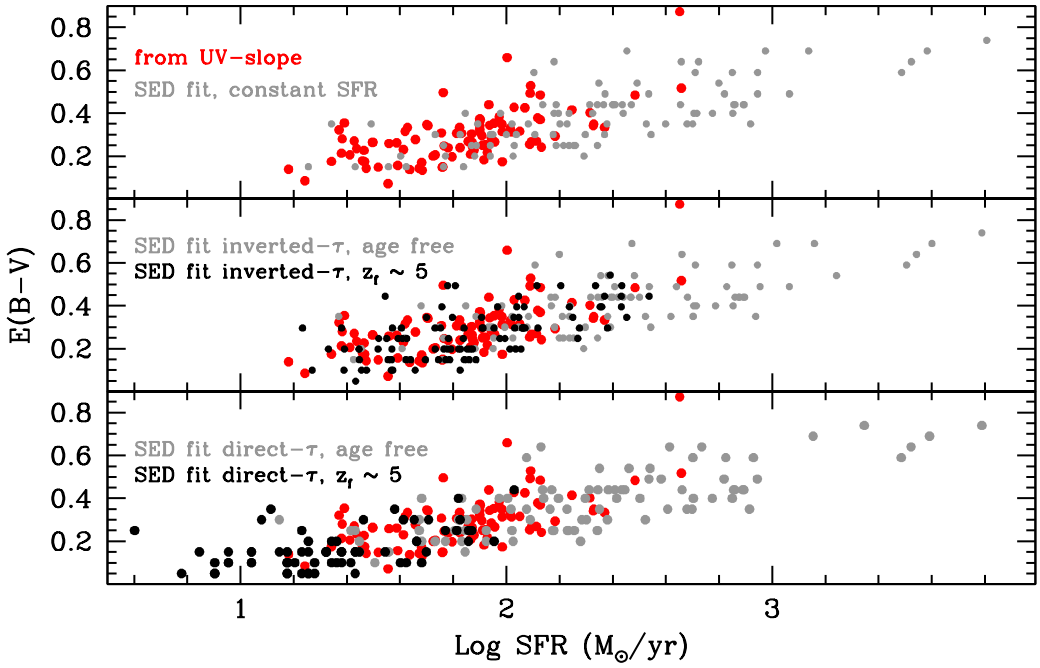

Figure 6.16: The reddening and SFRs derived under different assumptions on the SFH are compared to those derived using only the rest-frame UV part of the spectrum (red points), i.e., the wavelength range that most directly depends on the on-going rate of star formation. The upper panel shows a comparison of such UV-derived SFRs with those derived from SED-fitting assuming SFR=const and leaving age as a free parameter. In the middle panel the comparison is made with inverted-τ models, with both fixed and free age (black and grey points, respectively). Finally, the lower panel shows the comparison with the direct-τ-models.

Fig. 6.16 compares the $E(B-V)$ vs. SFR relations that are obtained from SED-fittings with various SFHs to those obtained using only the UV part of the spectrum. The latter ones were derived by Daddi et al. (2004, 2007) using BC03 models for converting $L_{\rm UV}$ into SFR, following Madau, Pozzetti & Dickinson (1998). $E(B-V)$ is derived by mapping the $(B-z)$ colour into $E(B-V)$ using the Calzetti law. Note that there are no appreciable differences in the UV between the models of BC03 and those of M05 that are used in this section. As clearly shown, the best agreement is between UV-derived SFRs and those obtained from SED-fitting with inverted-τ models and fixed formation redshift. Notice that when leaving age as a free parameter several galaxies are found with exceedingly large SFRs and $E(B-V)$ values (see also previous section), much at variance with the more robust values derived from the UV flux. Direct-τ models with

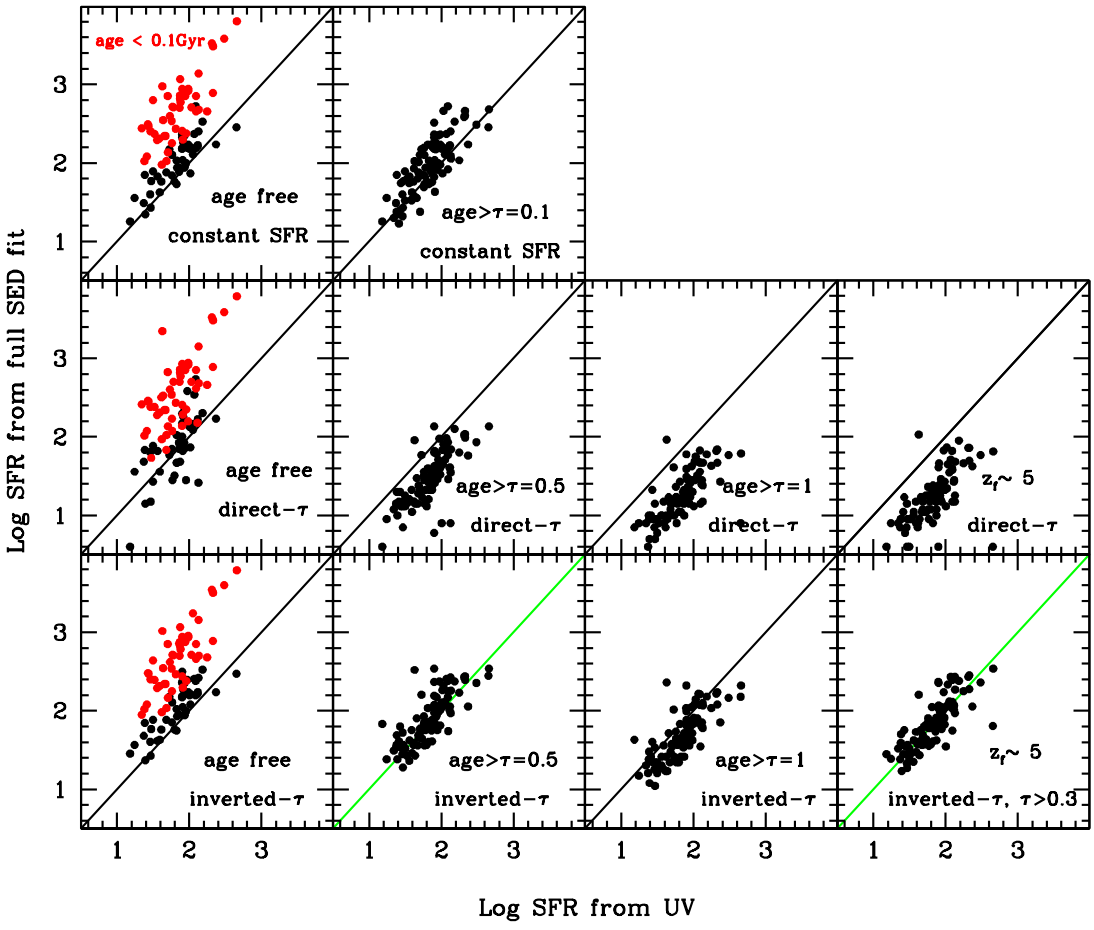

Figure 6.17: The comparison of SFRs derived from SED-fitting with those derived from the rest-frame UV only (plus extinction correction). Inverted-τ models with $z_{\rm form}=5$ (or inverted-τ's with fixed $\tau=0.5$ Gyr and ages constrained to be larger than τ) provide the best result (panels with green lines).

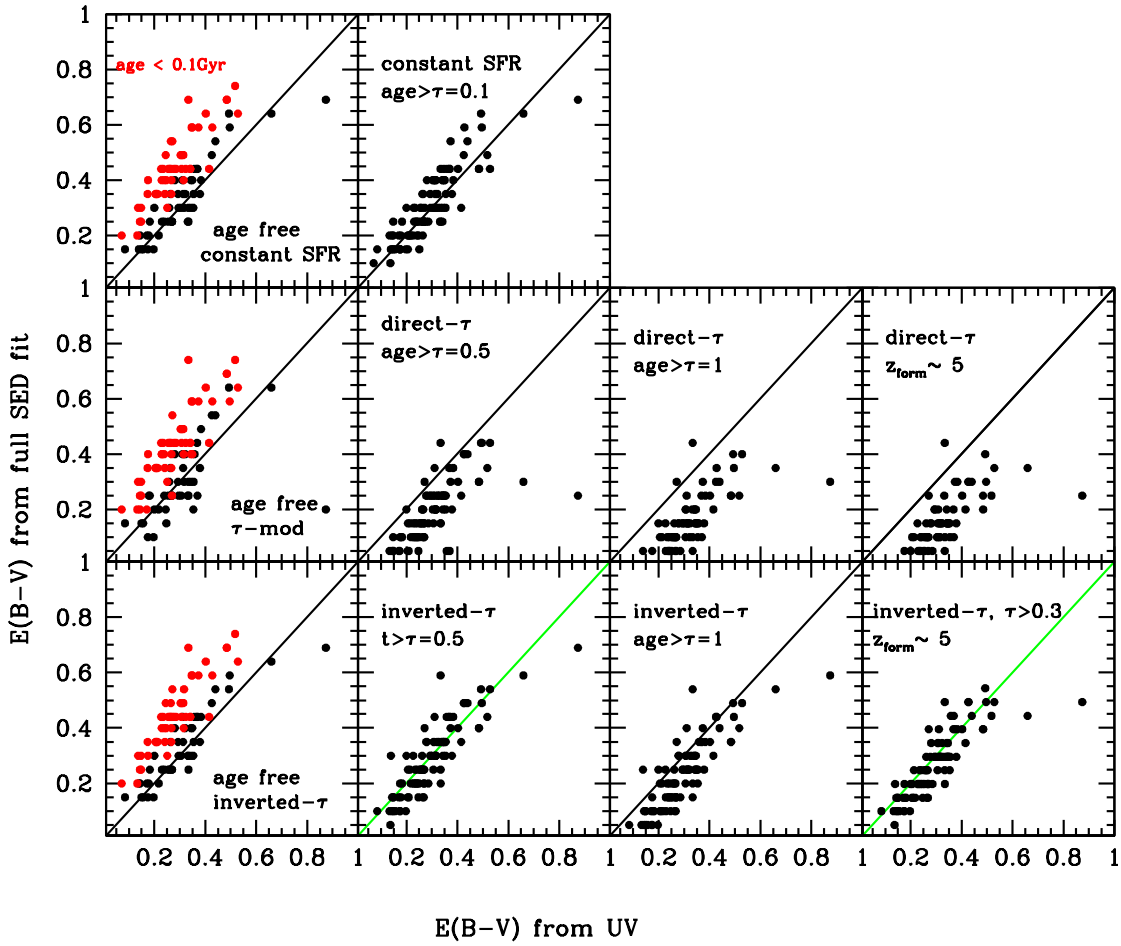

Figure 6.18: The same as Fig. 6.17 for the reddening $E(B-V)$. Conclusions are identical.

fixed formation redshift are in better agreement with the UV-derived SFRs, yet they systematically underestimate the SFR as already noticed above.

This is further illustrated in Fig. 6.17 and Fig. 6.18 which show the SFR and the reddening $E(B-V)$ from the SED-fits directly compared to those from the UV. Among all explored SFHs, the inverted-τ models clearly are in best agreement with the values derived from the UV flux and slope. We interpret this as an indication that the SFHs of inverted-τ models models are closer to those of real galaxies, compared to the SFHs of direct-τ models.

Best fit solutions with fixed τ and age $> \tau$

It is easy to realise that in galaxies that follow a SFR such as that given by Eq. 6.1 the SFR tends to increase exponentially with time (Pannella et al., 2009; Renzini, 2009).

More precisely, if one ignores the t term in this equation the exponential increase proceeds with a $\tau \simeq 0.7$ Gyr. Thus, in this section we present the results of performing a new set of best fits, this time assuming a fixed τ (namely $\tau = 0.5$ and 1 Gyr, that bracket the empirical value), leaving age as a free parameter but constraining it to be larger than τ. We also consider the case of direct-τ models with the same parameters and restrictions. This choice to set limits on age may appear rather artificial, and indeed it is purely meant to avoid the extremely small ages that are found when age is left completely free. In practice, this exercise consists in considering only the cases with age $> \tau$ among those already explored in previous sections.

The comparison of the SFRs derived from direct- and inverted-τ models (Fig. 6.19) is qualitatively similar to the case of fixed formation redshift (compare Fig. 6.12), and the same comments apply also here. The SFR and $E(B-V)$ values that are obtained with these further models are then compared to those obtained from the UV in Figs. 6.17 and 6.18. It is apparent that inverted-τ models with $\tau = 0.5$ Gyr and ages larger than τ give results nearly as good as those derived for the case of fixed formation redshift. Also the case of SFR = constant and age > 0.1 Gyr SFRs results in reasonable agreement with those derived from the UV. All other explored SFHs give results at variance from those obtained from the UV, that we regard as the most robust method to estimate the SFR and reddening.

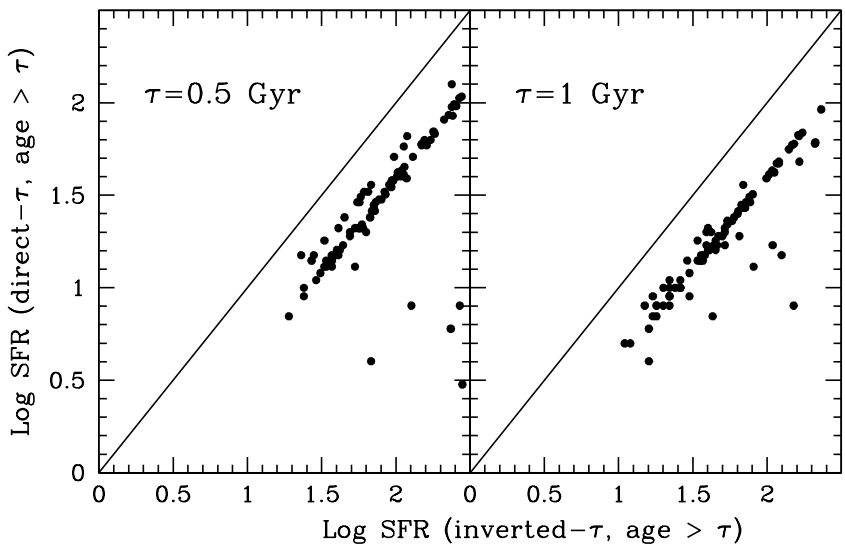

Figure 6.19: Comparison of the star formation rates derived assuming exponentially decreasing star formation rates (direct-τ models) with those obtained assuming exponentially increasing star formation rates (inverted-τ models). In both models, τ has been fixed to two values of 0.5 and 1 Gyr, and the age is constrained to be larger than τ.

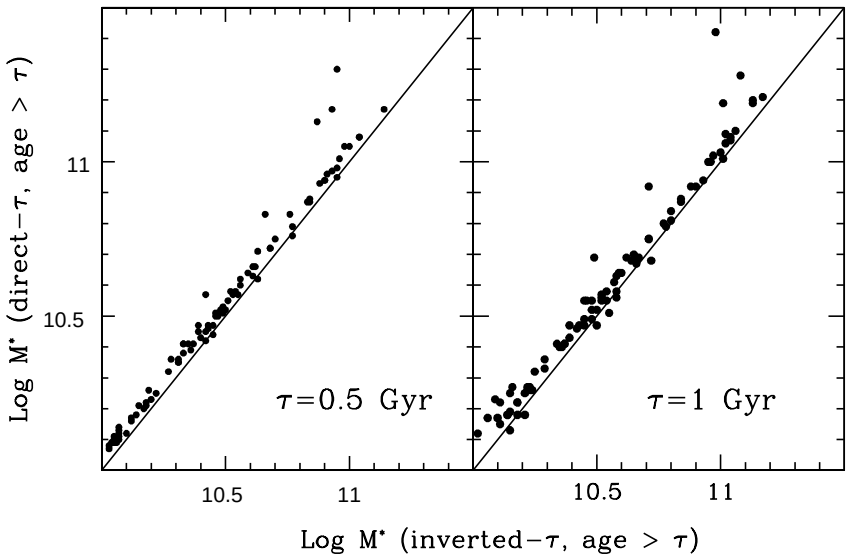

Figure 6.20: The same as in Fig. 6.19, but for a comparison of the derived stellar masses.

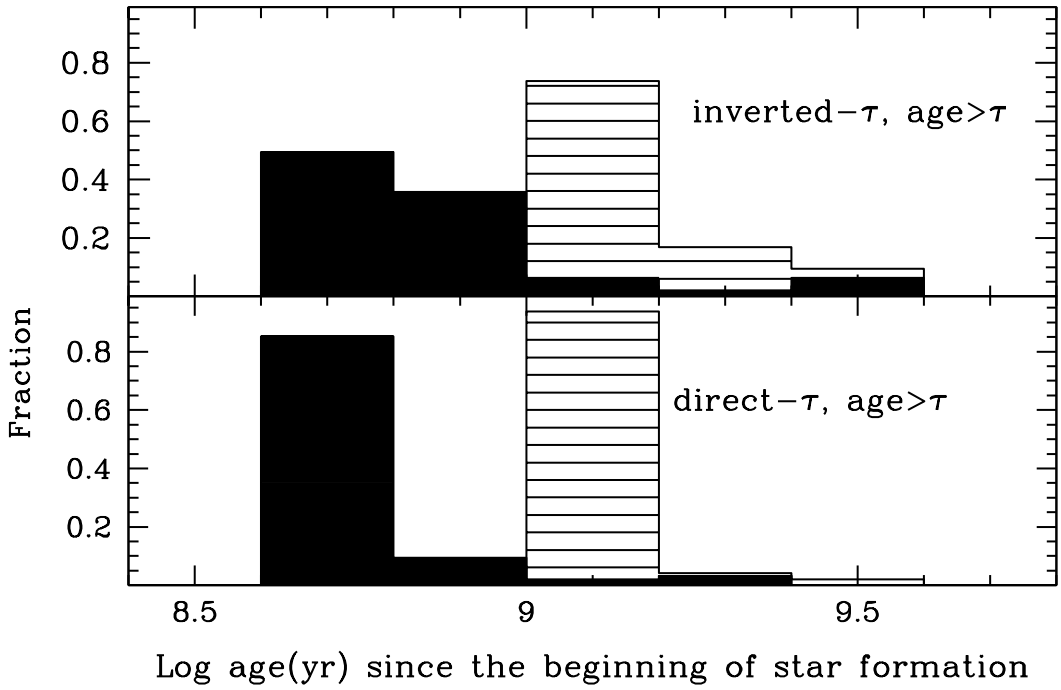

Figure 6.21: Distributions of the ages obtained with models with fixed τ and ages constrained to be larger than τ, for $\tau = 0.5$ Gyr (black histogram) and $\tau = 1$ Gyr (shaded histogram).

Fig. 6.20 shows the derived stellar masses. In this parameterisation there is less difference between the masses that are derived with the age $> \tau$ constraint with respect to the case of fixing the formation redshift. This is due to the fact that direct-τ models indicate lower masses compared to those in the case of fixed formation redshift, because of their lower age, hence shorter duration of the star formation activity. Note, however, that in most

cases the smallest χ^2_ν are obtained for the smallest possible age, i.e. age$\simeq \tau$, or ~ 0.5 Gyr, as shown in Fig. 6.21, again a consequence of the outshining effect.

Blind diagnostics of the star formation history of mock galaxies

The ability of an adopted shape of the SFH to recover the basic properties of a composite stellar population can be tested on mock galaxies with known SFHs. In a parallel project (Pforr et al., *submitted*, Chapter 4) we use synthetic galaxies from semi-analytic models (GalICS, Hatton et al., 2003) in which the input SSPs are the M05 models in the rendition of Tonini et al. (2009, 2010). Their observed-frame magnitudes at the various redshifts are then calculated, fed into *HyperZ* just as if they were relative to real observed galaxies, and best fits are sought using various template composite stellar populations.[3] Here we focus on an experiment involving the templates used in this section, namely inverted- and direct-τ models and constant SF models, applied to mock star-forming galaxies at redshift 2. The model spectra are reddened according to the on-going SFR, using the empirical evidence that the $E(B-V)$ is proportional to the SFR (e.g. Daddi et al., 2007) of each individual galaxy, with $E(B-V)$ as defined in Eq. 6.4. Extinction as a function of wavelength is then applied following the law of Calzetti. Note that we do not take such mock galaxies as representative of real galaxies. The goal of the experiment is to show what happens if the SED of a galaxy with a certain SFH is used to derive its SFR and stellar mass using a different SFH.

Fig. 6.22 and 6.23 show the results. The upper left panel of Fig. 6.22 shows the *input* values, i.e. the distribution of SFRs and masses of the semi-analytic models at redshift 2 (black points). The other panels show the *output* values, i.e. the SFRs and masses that are obtained by fitting the SED of the mock galaxies with the various templates, as indicated, over-plotted to the input values.

The inverted-τ models with fixed formation redshift can recover the input quantities strikingly well (middle panels). Towards the low-mass end ($M \lesssim 10^9 M_\odot$) the SFR is somewhat underestimated, suggesting that the assumed start of star formation is too early. Note also, as shown by the two middle panels in Fig. 6.22, that the result is almost independent of the assumed formation redshift, as already argued earlier.

None of the other SFH templates do as well. With the free age mode a substantial number of outliers with very high SFRs are obtained. The green line in Fig. 6.22 and Fig. 6.23 is

[3] A similar project is described in Wuyts et al. (2009), and a detailed comparison with their results is given in Chapter 4. The systematic offsets introduced by the use of direct-τ models to derive masses and SFRs of mock galaxies at $z > 3$ are also investigated by Lee et al. (2009).

a fit to the outliers found among the real GOODS galaxies from the direct-τ models (the red objects in Fig. 6.17 and Fig. 6.18), and it is quite instructive to note that when the fit produces wrong values, those follow the same relation of fake values in mock galaxies. Finally, Fig. 6.23, analogous to Fig. 6.22, shows the result of the same experiment with mock galaxies, but now using the template SFHs discussed in the previous subsection, i.e., with fixed τ and age $> \tau$. The inverted-τ models with age $\geq \tau$, and $\tau = 0.5$ Gyr give fairly good fits to the actual values in the mock galaxies, but not as good as those with a prior on the formation redshift (see Fig. 6.22, middle panels). Finally, note that some

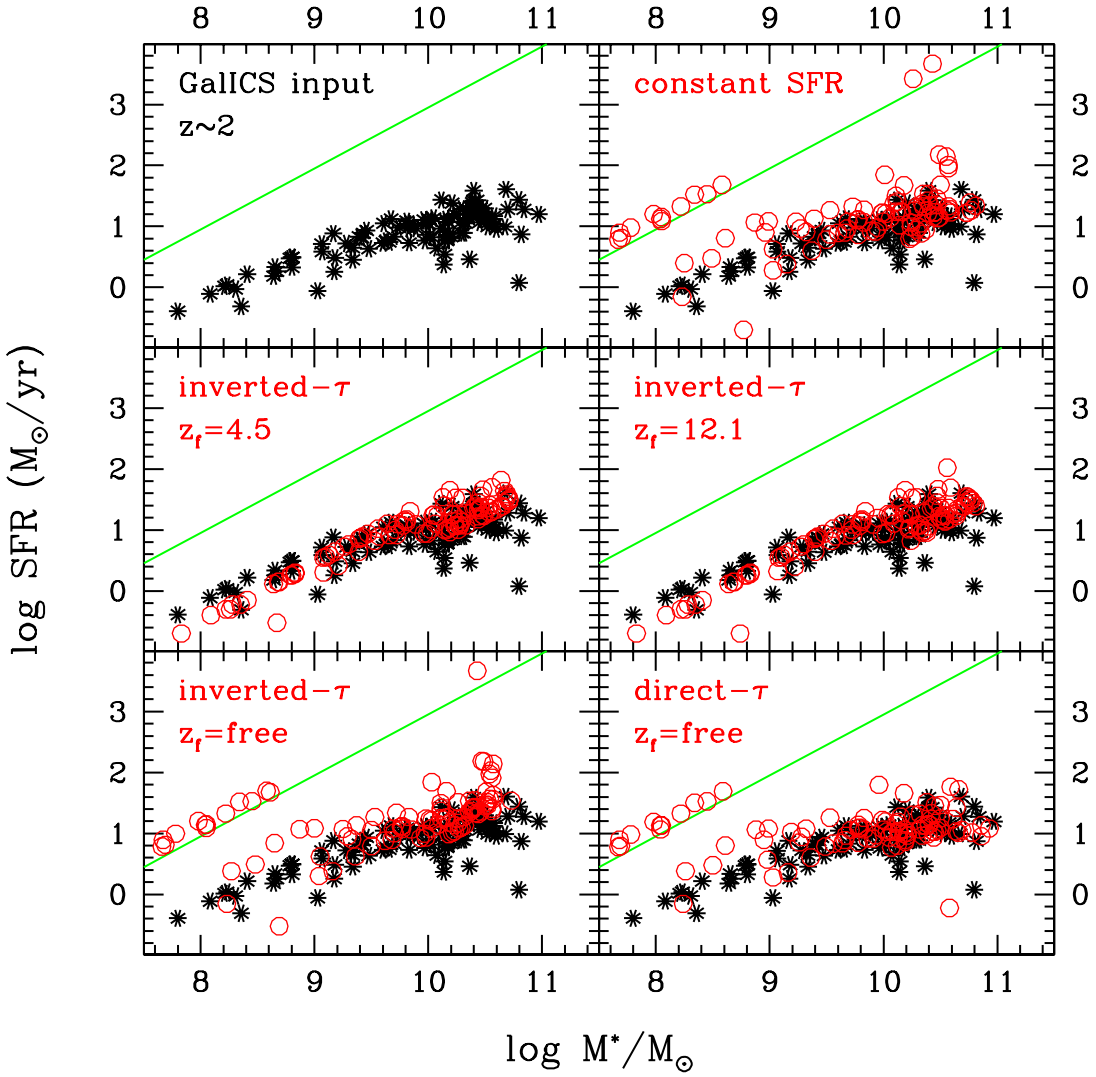

Figure 6.22: Comparison between the input values of SFR and stellar mass of mock galaxies from semi-analytic models (labelled as GalICS, black points) and the same quantities derived from SED-fitting using the various templates (labelled in each panel, red points). The green line highlights the position of the fake outliers.

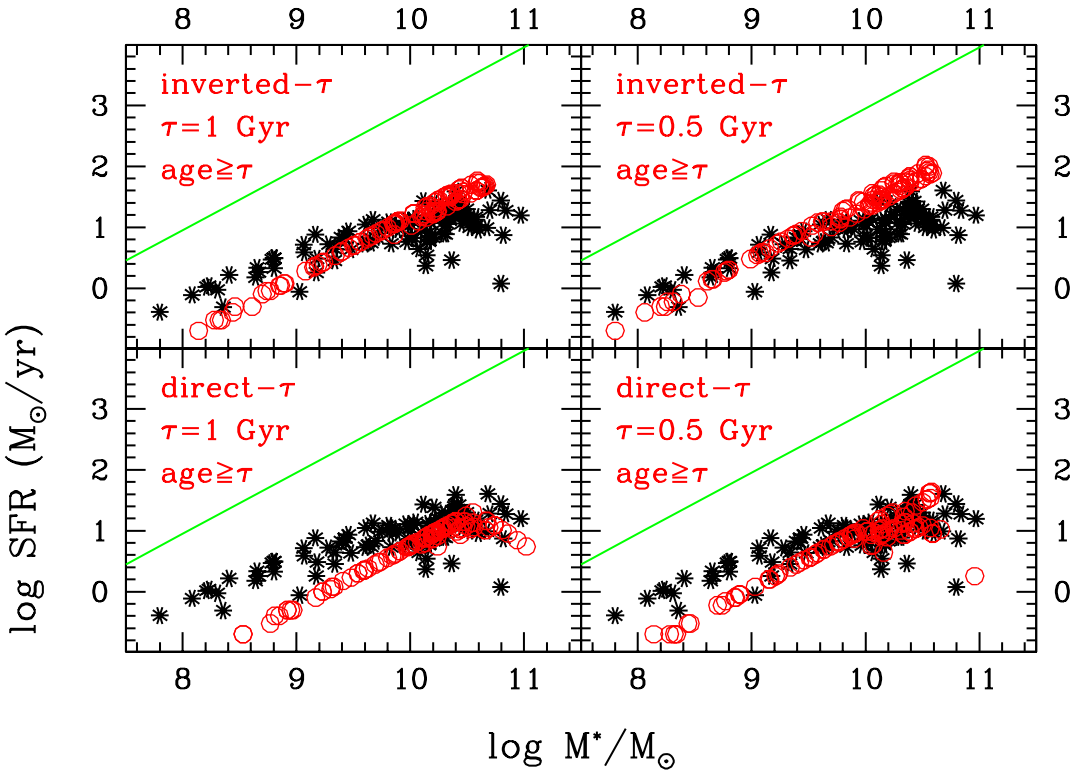

Figure 6.23: The same as Fig. 6.22, for the cases in which τ has been fixed to the indicated values, with the additional restriction imposing the age to exceed τ.

outliers among the mock galaxies, a few with low SFR for their masses (hence almost passive), are poorly reproduced by the explored SFHs, as all assume that star formation is still on-going.

The reason why inverted-τ models fit better is very simple. Most mock galaxies constructed from semi-analytic models exhibit secularly increasing SFRs, as do the cold-stream hydrodynamical models of Dekel et al. (2009) as one expects from the empirical SFR-mass relation (e.g. Renzini, 2009). Therefore, we believe that quite enough arguments militate in favour of preferring exponentially increasing SFRs, as opposed to decreasing or constant.

Allowing very small values of τ

As one can notice from Fig. 6.13, using inverted-τ models the vast majority of the best fits tend to cluster close to the minimum allowed value of τ, i.e. 0.3 Gyr, a limit that was imposed based on the value of τ implied by the empirical SFR$-M^*$ relation, as discussed earlier. But what happens if this limit is removed, and the best fit procedure is allowed to chose any value of τ down to 0.05 Gyr? The results are shown in Fig. 6.24:

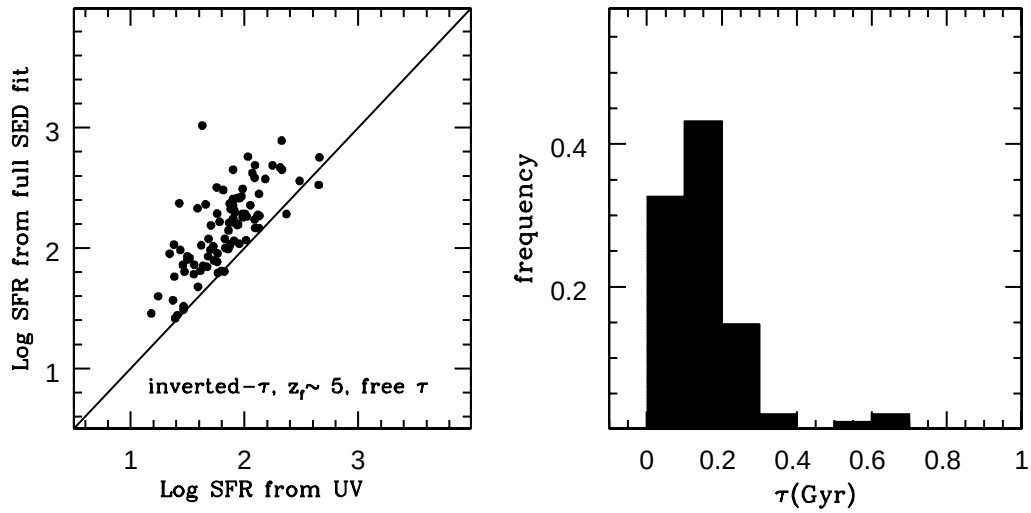

Figure 6.24: *Left panel:* The SFR from the full optical-to-near-IR SED-fit derived from inverted-τ models in which τ is allowed to take very small values, compared to the SFR derived only from the UV part of the SED. *Right panel:* The histogram of the corresponding values of τ.

several galaxies are now "best fitted" with very small τ's, implying SFHs in which most stars formed just shortly before the time at which the galaxy is observed. This is to say that leaving the procedure free to choose very small values of τ results in best fits that closely resemble those obtained with age as a free parameter, that were discussed (and rejected) at the beginning of this section. Fig. 6.24 shows that also in this case SFRs well in excess of those derived from the UV are derived for several galaxies. Therefore, also inverted-τ models with unconstrained τ's suffer from the outshining phenomenon that plagues models with age as a fully unconstrained free parameter.

The lesson we learn from these experiments is that only by setting a prior on age one derives astrophysically more acceptable solutions. Depending on the adopted shape of the SFH, this prior can be a minimum age (for constant SFR models), or setting age$> \tau$ (for direct-τ models), or finally setting a minimum acceptable value for τ (for inverted-τ models). This kind of fix looks quite artificial, and admittedly the resulting procedure is far from being elegant. It is a simple way of avoiding the outshining effect, and obtain SFRs that are in agreement with those derived from other direct methods, such as from UV, radio, or mid-IR (e.g. Daddi et al. 2007; Daddi et al. 2007, b; Pannella et al. 2009).

How robust are stellar mass estimates?

While SFR and reddening can be best evaluated by just using the UV part of a galaxy's spectrum, the determination of the stellar mass, such a crucial quantity for understanding

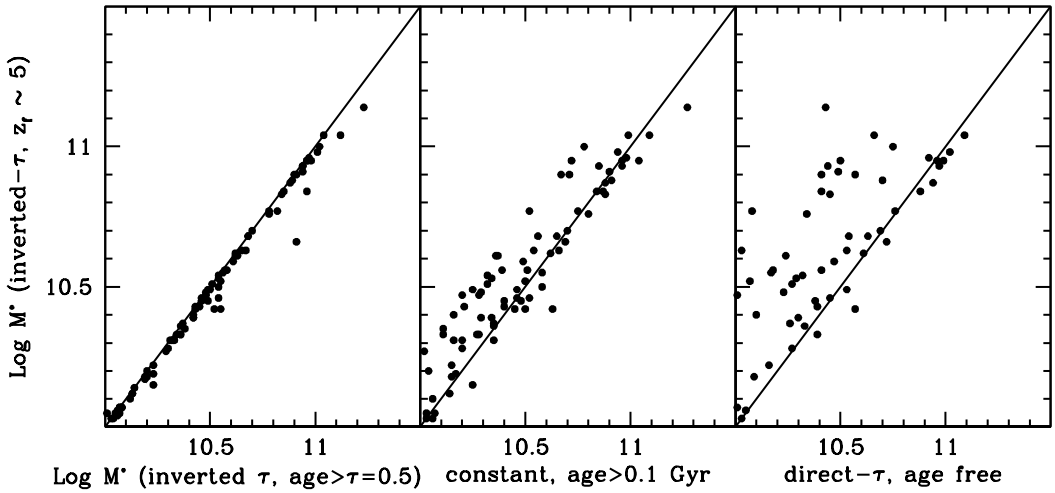

Figure 6.25: A comparison of the stellar masses derived for the GOODS galaxies from inverted-τ models, with $z_{\rm f} = 5$ and $\tau \geq 0.3$ Gyr, with those derived from other adopted SFHs. *Left panel:* vs. inverted-τ models with age $> \tau = 0.5$ Gyr; *Middle panel:* vs. models with SFR=const. and age> 0.1 Gyr; *Right panel:* vs. direct-τ models and unconstrained age.

galaxy evolution, requires the full SED-fitting. Hence, it requires exploring a variety of assumed SFHs. We showed that there are some adopted SFHs that, constrained to avoid the outshining problem, give SFRs and $E(B-V)$ values in excellent agreement with those derived from the UV. Now, how different are the derived stellar masses when using these viable options for the SFH? And, ultimately, how much can we trust such derived masses?

Fig. 6.25 - first and second panel - compares the stellar masses that are derived for the real galaxies studied in this section using these viable SFHs, namely inverted-τ with high formation redshift, inverted-τ with age constrained, and constant SF with age constrained. The corresponding masses agree quite well with each other, systematic differences are quite small ($\lesssim 0.1-0.2$ dex), and also the scatter is quite modest, of the order of 0.1 dex. Can this consistency suffice to conclude that the adopted procedures give a robust estimate of stellar masses? In this respect, the fairly accurate recovery of the masses of mock galaxies should increase our confidence.

Yet, the problem of outshining remains. What we consider viable options are SFHs described by extremely simple functions, i.e. either constant or exponential. Nature certainly realises far more complex SFHs. For example, an early burst of star formation, followed by a continuous SFR, could be easily missed by the best fit procedure, by remaining outshined by the successive and on-going star formation. Thus, we suspect that

derived masses may underestimate the actual stellar mass, at least for those galaxies with early massive starbursts.

We note that Fig. 6.25, third panel compares also the masses derived from direct-τ models with unconstrained age to those derived from the viable SFHs. Clearly, such direct-τ models can substantially underestimate the stellar mass while they overestimate the SFR (compare Fig. 6.17).

To conclude this section, Fig. 6.26 shows the *absolute* values of the stellar mass of star-forming galaxies at redshift $z \sim 2$ that are obtained using our preferred star formation history.

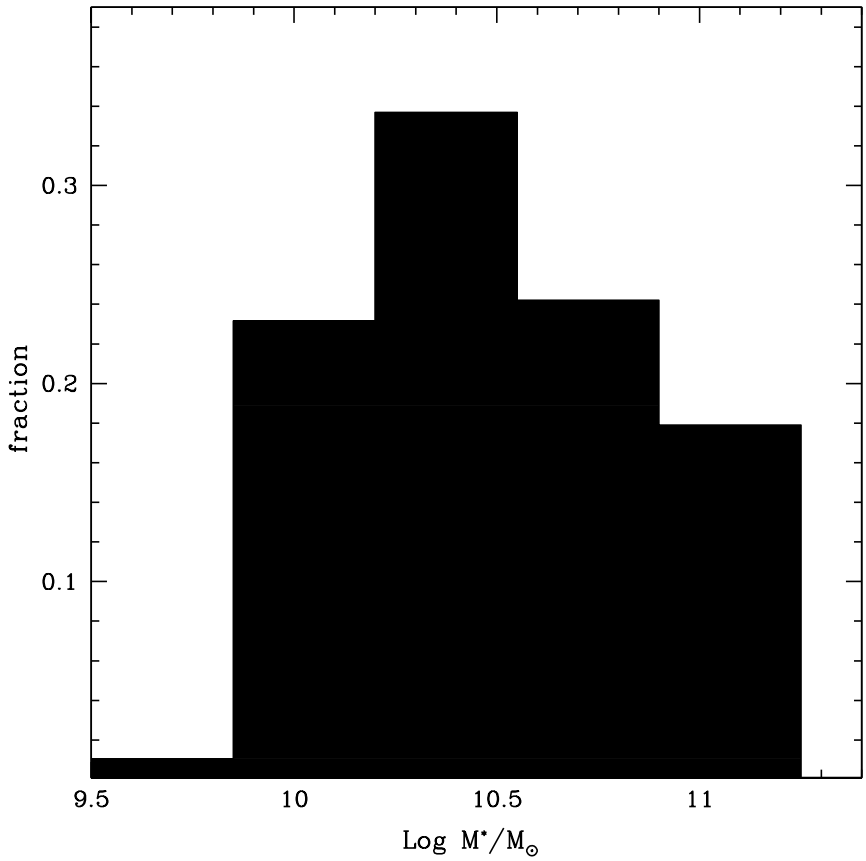

Figure 6.26: Stellar masses for the $z \sim 2$ GOODS star-forming galaxies as derived from inverted-τ models, with $z_{\rm f} \gtrsim 5$ and $\tau \geq 0.3$ Gyr.

6.1.4 Discussion and Conclusions

We tried different priors for the SFH of $z \sim 2$ galaxies and used a χ^2 best fit approach to derive the basic properties of such galaxies: SFR, stellar mass, reddening, age, etc. We do not expect that any of the simple mathematical forms adopted for the SFH (constant SFR, exponentially decreasing, exponentially increasing) is strictly followed by real galaxies. We expect, however, that the two opposite choices for the exponential case are sufficiently extreme to encompass the real behaviour of galaxies, or at least those having experienced a quasi-steady SFR over most of their lifetime. We try various tests to distinguish which of the various options is the most acceptable one (or the least unacceptable) for giving the astrophysically most plausible values for the basic properties of star-forming galaxies in the redshift range between ~ 1.4 and ~ 2.5.

We find that by leaving age as a free parameter the best fit procedure delivers implausibly short ages, no matter which SFH template is adopted. This is so because the SED is dominated by the stars that have formed most recently, and they outshine the older stellar populations that may inhabit these galaxies. Thus, introducing a prior on the beginning of star formation appears to be necessary.

Assuming that star formation started at high redshift (i.e. $z >>\sim 2$, the precise value being almost irrelevant) provides a more credible framework, with models with exponentially increasing SFR (that we call inverted-τ models) giving systematically higher SFRs for the $z \sim 2$ galaxies in the test sample, and lower stellar masses, compared to models with exponentially decreasing SFR. These two systematic differences together imply a specific SFR that is a factor of ~ 5 higher in inverted-τ models, compared to direct-τ models, when star formation is assumed to start at high redshift (e.g. $z = 5$) in both cases.

On the other hand, inverted-τ models offer various notable advantages:

- they indicate SFRs and extinctions in excellent agreement with those derived from the rest-frame UV part of the SED, which most directly relates to the on-going star formation and reddening,
- they fairly accurately recover the SFRs and masses of mock galaxies constructed from semi-analytic models, in which SFRs are indeed secularly increasing in most cases, and
- have systematically better χ^2_ν values compared to models with exponentially decreasing SFRs, though one cannot consider them fully satisfactory.

These advantages are somewhat reduced if the best fit procedure is allowed to pick very small values of τ, down to 0.05 Gyr, as in such case derived SFRs tend to be somewhat overestimated compared to those derived from the UV.

We also explored star formation histories (such as constant SFR, or exponentially decreasing) in which age is a priori constrained to avoid very small values (e.g., age > 0.1 Gyr, or age $> \tau$, or fixed τ). Adopting such priors, though it may seem quite artificial, gives more plausible solutions with respect to cases in which age is left fully free. This is due to the mentioned outshining effect of very young stellar populations over the older ones. Still, models with exponentially increasing SFRs tend to give systematically better results, as judged from the consistency with the UV derived SFRs.

Besides the above arguments, there are other reasons to prefer stellar population models constructed with exponentially increasing SFRs, including:

- The almost linear relation between SFR and stellar mass (SFR $\propto\sim M^*$), and the small scatter about it, that are empirically established for redshift ~ 2 galaxies implies that they can indeed experience a quasi-exponential growth at these cosmic epochs. Later, some process may quench their star formation entirely and turn them into passively evolving *ellipticals*, or keep growing until the secular decrease of the specific star formation rate (the $t^{-2.5}$ term in Eq. 6.1) takes over, and galaxies (such as spirals) continue forming stars at a slowly decreasing rate all the way to the present epoch (Renzini & Daddi, 2009).

- The direct observation of the evolution of the luminosity function in rest-frame UV (which is directly related to SFR) shows that the characteristic luminosity at 1600 Å (M^*_{1600}) brightens by over one magnitude between $z = 6$ and $z = 3$ (Bouwens et al., 2007). Since extinction is likely to increase with time following metal enrichment, the increase of the rest-frame UV luminosity can only be due to an increased SFR in individual galaxies.

The aim of this section is to explore which assumptions and procedures are likely to give the most robust estimates of the basic stellar population parameters, when using data that extend from the rest-frame UV to the near-IR. We argue that on-going SFRs are best derived at wavelengths below about one micron by using the UV part of the SED of galaxies, and inverted-τ models give SFRs in excellent agreement with them. However, the fit to the full optical to near-infrared SED is required to derive the mass in stars. We show that the SFHs, with a prior on age or τ to reduce the outshining effect, give results that agree quite well with each other, giving some confidence on the reliability of the derived masses. However, it is still possible that the mass may be somewhat underestimated

for those galaxies in which a substantial fraction of the stellar mass was produced in a strong burst, early in their evolution.

At first sight the higher SFRs and lower stellar masses indicated by inverted-τ models (compared to direct-τ models, both with fixed formation redshift) may exacerbate an apparent mismatch between the *cosmic* (volume averaged) SFR history ($\dot{\rho^*}(z)$) and the empirical stellar mass density ($\rho^*(z)$), such that the integration of SFR(z) tends to overproduce the stellar mass density at most/all redshifts (e.g. Wilkins, Trentham & Hopkins, 2008). However, SFRs are more often derived from direct SFR indicators, such as the rest-frame UV, radio flux, Hα flux, or mid/far-infrared, rather than from SED-fits. Therefore the 0.5 dex effect on the SFRs relative to the direct-τ models should not affect this discrepancy. There may remain the 0.2 dex effect on the masses, but inverted-τ models, by construction minimising star formation at early times, may systematically underestimate the stellar mass of galaxies, in particular if part of it was formed in early bursts. Thus, with this caveat in mind, the use of inverted-τ models with fixed formation redshift should not appreciably exacerbate the mismatch problem mentioned above. Instead, direct-τ models with unconstrained age most certainly worsen this problem as they underestimate the stellar mass (see Fig. 6.25, right panel), and overestimate the SFR (see Fig. 6.17).

We conclude that the use of synthetic stellar populations with an exponentially declining SFR should be avoided in the case of star-forming galaxies at redshift beyond ~ 1. Exponentially increasing SFRs, with e-folding times of $\sim 0.3 - 1$ Gyr, and a high starting redshift appear to provide astrophysically more plausible results, and while nature may not closely follow such a simple functional behaviour, they should be preferred in deriving SFRs and stellar masses of high redshift galaxies. In any event, we believe that maximum likelihood parameters are not necessarily unbiased estimators of star formation rates and masses of high-redshift galaxies, but the broadest possible astrophysical context should be considered.

6.2 Luminous galaxies in BOSS - $0 < z < 0.7$

After studying a sample of high-redshift star-forming galaxies we now turn our focus to one of the largest surveys of massive (and mostly passive) galaxies at low redshift - the SDSS-III/BOSS survey (hereafter BOSS). In Section 2.3 we described the survey and the galaxy target selection in detail. In this section we first introduce the template setups and parameters employed in the SED-fitting (Section 6.2.1). Then we show the derived ages and stellar masses of BOSS galaxies in Section 6.2.2. We demonstrate that BOSS galaxies are indeed very massive and that the target selection aimed at galaxies of constant and high mass at various redshifts works very well (Section 6.2.3). We draw our conclusions in Section 6.2.4.

The work carried out in this section was carried out in collaboration with C. Maraston, D. Thomas, B. Henriques and D. Wake and will be published in Maraston et al. (2012, in prep.). Since the publication was still in preparation and has not undergone the referee process at the time of submission of this thesis the contents of Maraston et al. (2012, in prep.) might be different from the contents of this section.

6.2.1 SED-fitting setup

We use two different template setups within *HyperZspec* for BOSS galaxies and thus obtain two stellar mass estimates. Firstly, we adopt the template setup of M06 (wide setup, full age grid, Section 4.2.1) which we extensively tested in Chapter 4 but drop the SSP component according to our findings in the same chapter. We use this setup to accommodate for the fraction of massive blue (and star-forming) galaxies in BOSS (Fig. 2.9 and Masters et al., 2011).

Secondly, we use the LRG best-fit template (solar metallicity SSP with 3% metal-poor stars) from Maraston et al. (2009) which was described in detail in Section 3.4.4 because of its ability to reproduce the median gri colours of SDSS LRGs over a wide redshift range. We use age > 3 Gyr following the assumption of a high formation redshift for the galaxies. Since BOSS targets mainly LRGs and the majority of galaxies is expected to be passive, we use this template setup as a means not to underestimate the stellar mass for these galaxies.

Besides a Salpeter IMF, we also assume a Kroupa IMF. We exclude reddening from the fit of BOSS galaxies because they are selected to be mostly passive and following our findings of Chapter 4 for passive galaxies at low redshifts. In the next section we show

the results for stellar ages and stellar masses for the BOSS main galaxy sample (up till 22 July 2011) as a function of template setup and IMF.

6.2.2 The ages and stellar masses of BOSS galaxies

At first, we show the χ^2_ν-distributions for each template setup and IMF in Fig. 6.27. As expected, a wide setup gives fits with better χ^2_ν for more objects due to the wider choice of age, metallicity and SFH. The restriction of the LRG setup in age and SFH results in slightly worse χ^2_ν for some objects. However, overall both template setups provide reasonably good fits for the majority of objects. For the wide setup with Salpeter (Kroupa) IMF 3.3 (3.3) % have $\chi^2_\nu \geq 10$. For the LRG setup we find 11.4 (9.8)%. The difference between Salpeter and Kroupa IMF is negligible, again pointing out what we concluded in Chapters 4 and 5 that SED-fitting cannot identify the correct IMF.

As expected, BOSS galaxies are generally old (Fig. 6.28). Even with a wide setup most galaxies are older than 1 Gyr indicating that these galaxies are not dominated by (recent) star formation. Obviously, this is also an effect of excluding reddening in the fit and therefore disabling the age-dust degeneracy. However, as we have seen in Fig. 4.2 in Chapter 4 the ages of aged galaxies with little on-going star formation are generally

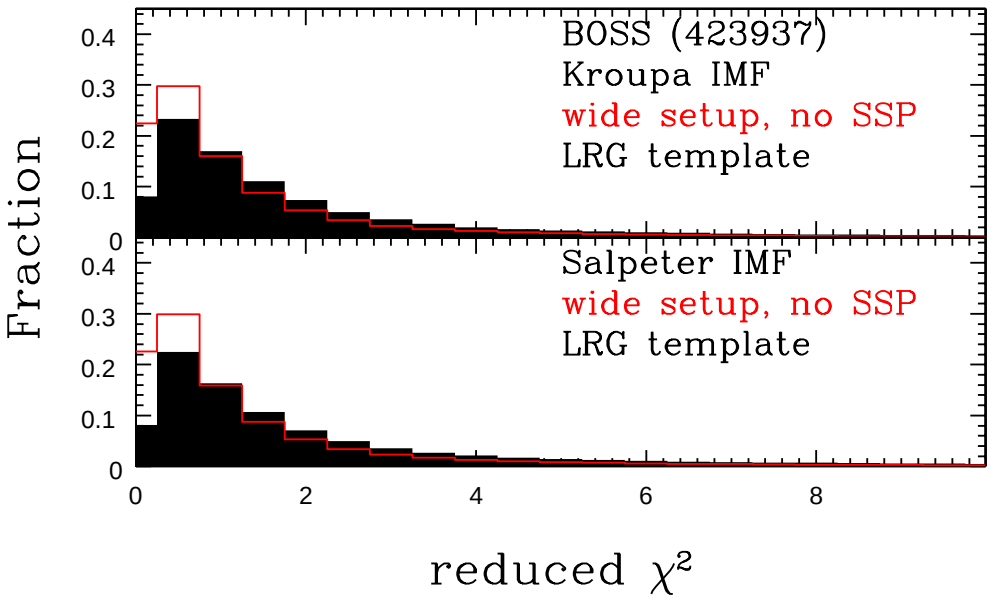

Figure 6.27: χ^2_ν distributions of the SED-fits for the BOSS main galaxy sample as a function of template setup and IMF in the SED-fitting. Black shaded histograms refer to solutions derived with the LRG template, red histograms to the use of a wide template setup without SSPs.

underestimated, especially when reddening is included in the fit. Ages derived with the LRG template are somewhat older than those derived with the wide setup because of the assumed minimum age of 3 Gyr.

The difference in age between Salpeter and Kroupa IMF is such that ages from a Salpeter-based LRG template are somewhat older because age is the only parameter available to compensate for the different IMF (Fig. 6.29). However, note that the range in age difference is very small. In the case of the wide setup ages differ a lot more because age, SFH and metallicity compensate for the IMF, but the effect on the overall age distribution is small.

Fig. 6.30 shows the stellar mass distributions of BOSS galaxies for the two template setups and IMFs. The distributions are very narrow, only spanning about one and a half orders of magnitude. For a Kroupa IMF the distribution peaks at $10^{11.25}\,M_{\odot}$ independently of template setup. Stellar masses derived with the wide setup without SSPs clearly extend to lower masses, the distribution is overall broader compared to the distribution of stellar masses derived with the LRG template. This is clearly an age effect. The LRG template is restricted to old ages and because of the absence of star formation this

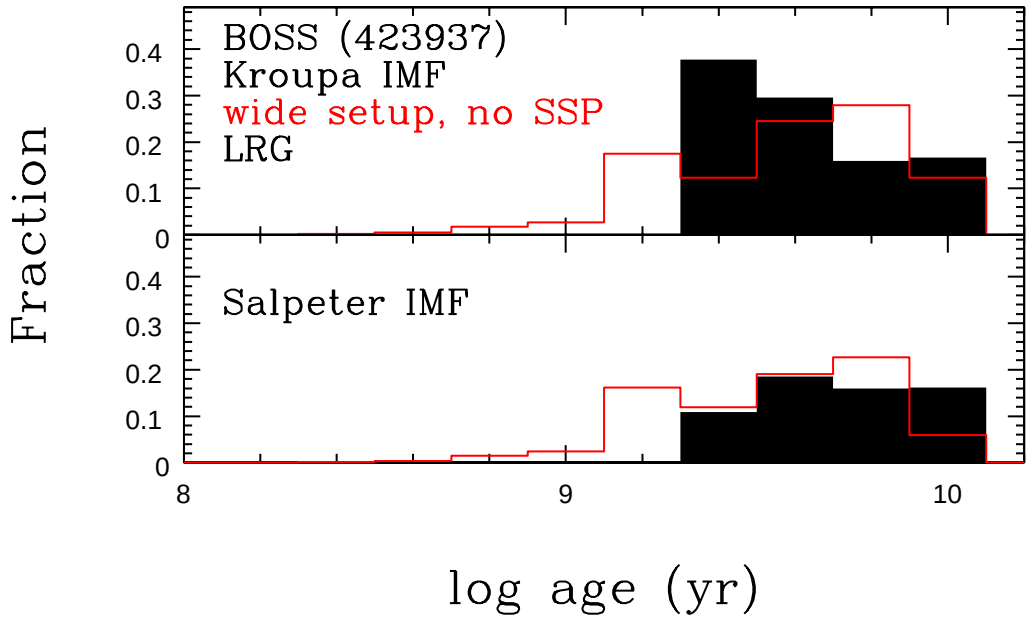

Figure 6.28: Age distributions for the BOSS main galaxy sample as a function of template setup and IMF. Black shaded histograms refer to solutions derived with the LRG template, red histograms to the use of a wide template setup without SSPs.

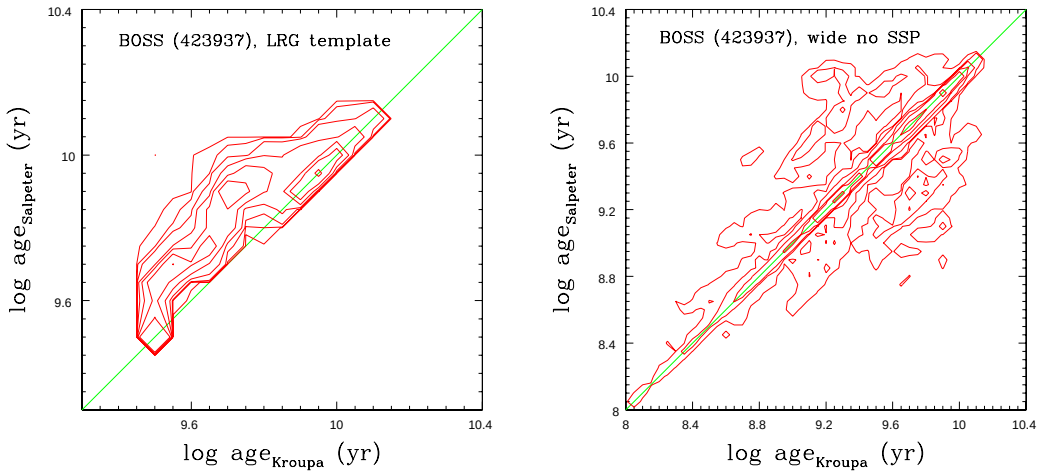

Figure 6.29: Differences in derived ages between Salpeter and Kroupa IMF when the LRG template (left) and the wide setup without SSPs (right) is used. Contours for the LRG template are at 10, 100, 500, 2000, 5000, 10000 and 20000. Contours for the wide setup without SSPs are at 10, 100, 500, 2000, 5000 and 20000. Ages are binned into bins of size 0.05 dex in each case. The green line is the line of equality.

means a restriction to old stellar populations overall. Stellar masses obtained with the wider setup are generally prone to overshining, even if the percentage of recently formed stars is small, because derived ages are dominated by the latest burst. However, the distribution of ages showed that BOSS galaxies are still relatively old. From the exercise carried out in Section 4.5 we can estimate that either the latest burst occurred probably on average more than 100 Myr ago and carried less than 10% of the total mass or occurred more recently but with less than 1 % in mass, otherwise we would find ages significantly younger than 1 Gyr. Obviously, when ages are driven by the latest burst, so is stellar mass which is then underestimated. We showed in Section 4.5 that in this way up to 99% of a galaxy's total mass can be hidden.

Masses derived with Salpeter IMF templates are higher by ~ 0.25 dex and therefore the distribution peaks at $10^{11.5}\,M_{\odot}$. Again, this is independent of template setup. Fig. 6.31 compares results obtained with Salpeter and Kroupa IMF. The offset is similar for the two template setups, but the scatter is significantly smaller for the LRG template because of the discussed restrictions in age and SFH. Alongside, a constant offset of 0.2 dex, we also show the relation in mass between Salpeter and Kroupa IMF determined via a least squares fit which is very similar in slope to the one derived in Section 4.9 for mock passive galaxies at $z = 0.5$. The ordinate is somewhat larger for masses derived with the LRG template due to its specific design and no other available SFHs to compensate.

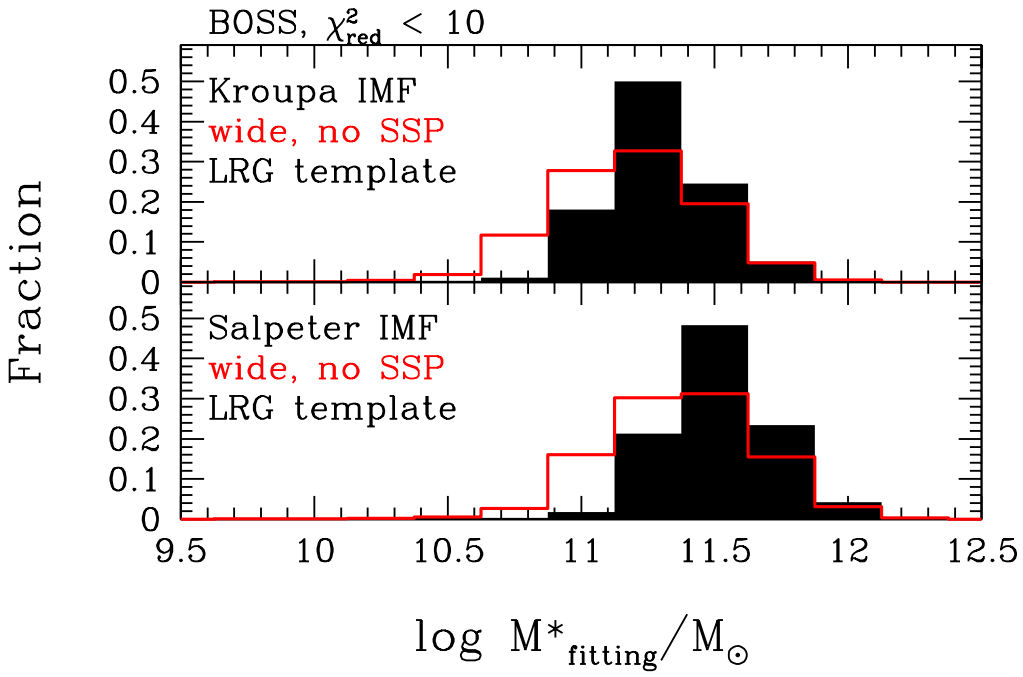

Figure 6.30: Stellar mass distributions derived for BOSS galaxies as a function of template setup. Black shaded histograms refer to the LRG template, red histograms to the wide template setup without SSPs. Included are only objects whose best fit solution has $\chi^2_\nu < 10$ (for the wide, no SSP setup these are for both IMFs 96.7% of the sample, for the LRG template 90.2 % for Kroupa and 88.6 % for Salpeter IMF; fractions are derived using these percentages as the total). *Top*: Kroupa IMF, *bottom*: Salpeter IMF.

We illustrated the mass distribution of the entire BOSS galaxy sample (selected by the LOZ and $CMASS$ cuts) in Fig. 6.30. In Fig. 6.32 we show the mass distribution of only $CMASS$ galaxies (76.4% of the total BOSS sample) when solutions of the two template setups are combined such that for galaxies with $g - i \leq 2.35$ the wide template setup and for the remaining ones the LRG template is chosen (green dashed histogram). In this way, we ensured according to Fig. 2.9 that the majority of elliptical galaxies of the $CMASS$ sample is treated with a template that does not contain star formation and that for the majority of spiral galaxies star formation is allowed in the fit. The majority of BOSS $CMASS$ galaxies (79.8 %) has $g - i > 2.35$ and should therefore be of elliptical and passive nature (black histogram in Fig. 6.32). Depending on the adopted IMF the mass distribution of these peaks between $10^{11.25}$ and $10^{11.5}\,M_\odot$. The remaining 20.2% should be spirals (red histogram in Fig. 6.32). Their mass distribution peaks 0.25 dex lower. This is in good agreement with the picture that elliptical galaxies are more massive than spiral galaxies.

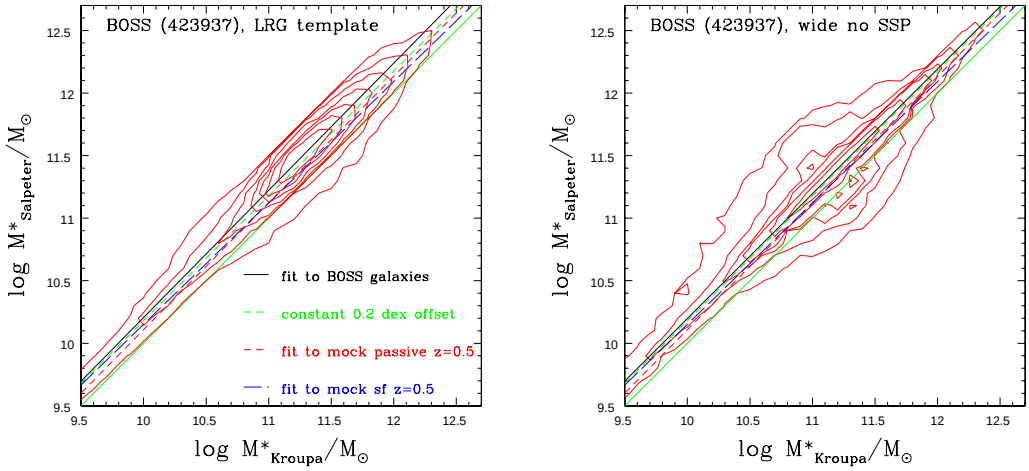

Figure 6.31: Differences in derived stellar masses between Salpeter and Kroupa IMF when the LRG template (left) and the wide setup without SSPs (right) is used. Contours for the LRG template are at 10, 100, 500, 2000, 5000, 10000 and 20000. Contours for the wide setup without SSPs are at 10, 100, 500, 1000, 5000 and 20000. Masses are binned into bins of size 0.1 dex in each case. The green solid line is the line of equality. The green dashed line represents a constant offset of 0.2 dex between Salpeter and Kroupa, such that Salpeter gives higher masses. The black solid line refers to the best fit for all objects as $\log\ M^*_{\rm Salpeter} = a + b \times \log\ M^*_{\rm Kroupa}$.

6.2.3 A successful colour selection

So far we have seen that galaxies targeted, observed and detected by BOSS are indeed very massive. Let's now take a closer look at the effectiveness of the colour selection specific to BOSS. In the following, we focus on results for a Kroupa IMF as the offset to Salpeter is almost constantly 0.25 dex.

As described in Section 2.3 BOSS galaxies are selected as targets via two selection algorithms. The $CMASS$ selection aims at selecting galaxies of constant mass in the redshift range between $z = 0.45$ and 0.7. Fig. 6.33 shows that the chosen colour criteria successfully selects galaxies around $10^{11.25}\,M_\odot$ ($10^{11.5}\,M_\odot$ for Salpeter IMF) for redshifts between 0.1 and 0.6. For higher redshifts the colour selection starts to break down. Here only the highest masses are picked up. At low redshift the selected galaxies have lower masses. This is a volume effect. At low redshift the BOSS area covers less volume than at high redshift because of the expansion of the Universe.

In Section 2.3 we tested the colour selection for BOSS using a sample of AGES galaxies for which we derived stellar masses. We repeat this with BOSS galaxies and show the result in Fig. 6.34 when Kroupa IMF templates are used. The mass grading is clearly

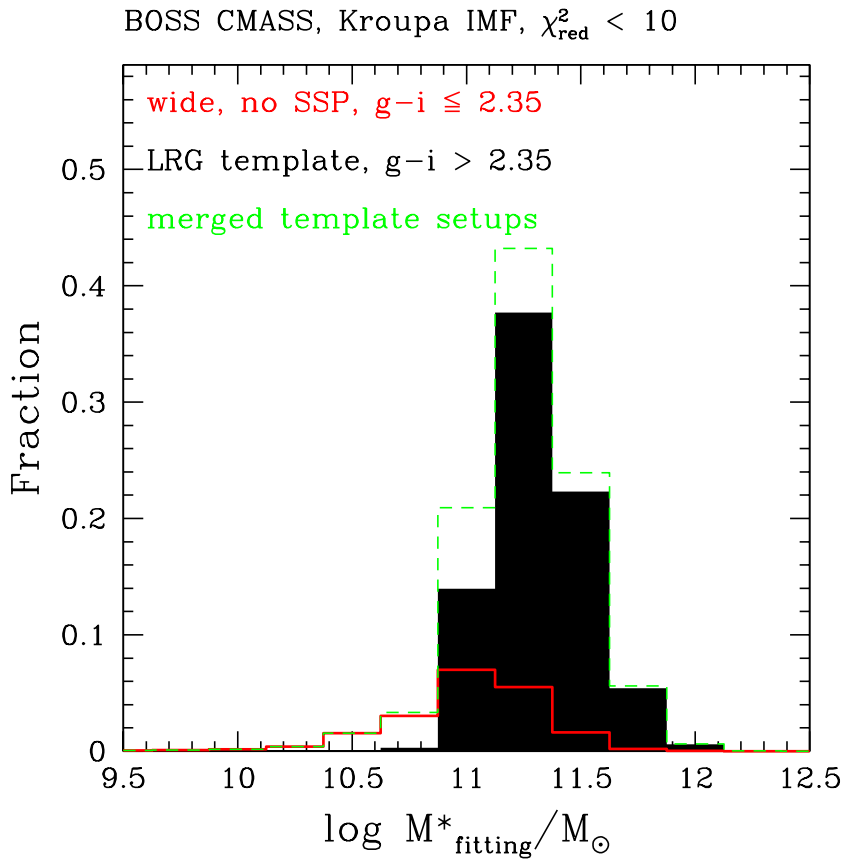

Figure 6.32: Stellar mass distributions of BOSS $CMASS$ galaxies as a function of $g-i$ colour and template setup. The black shaded histogram refers to stellar masses derived with the LRG template, the red histogram to the use of the wide template setup without SSPs, dashed green to the combined setups. All template setups are based on a Kroupa IMF. Included are only objects whose best fit solution has $\chi^2_\nu < 10$ (these are 97.3% of the $CMASS$ sample).

visible. Alongside the derived masses we overlaid the tracks for passively evolving SSPs for various masses, IMFs and stellar population models starting at $z = 0.7$ such that an age of ~ 13 Gyr is reached at $z = 0$. The tracks are essentially shifted towards brighter i-band magnitude when mass increases (from dark blue to orange, right to left, respectively). At the same mass the track for a Kroupa IMF (yellow) is brighter by ~ 0.3 mag than for Salpeter IMF (green). The LRG model is brighter than a M05 SSP by 0.1 mag at given mass and at $z = 0.7$ bluer by 0.06 mag due to the 3% of metal-poor stars.

We also show the location of BOSS galaxies in $r-i$ vs $g-r$ colour-colour space equivalent to the one shown in Fig. 2.9. Clearly, the majority of galaxies has colours redder than $g-i = 2.35$ and galaxies with redder $g-r$ and $r-i$ are on average more massive.

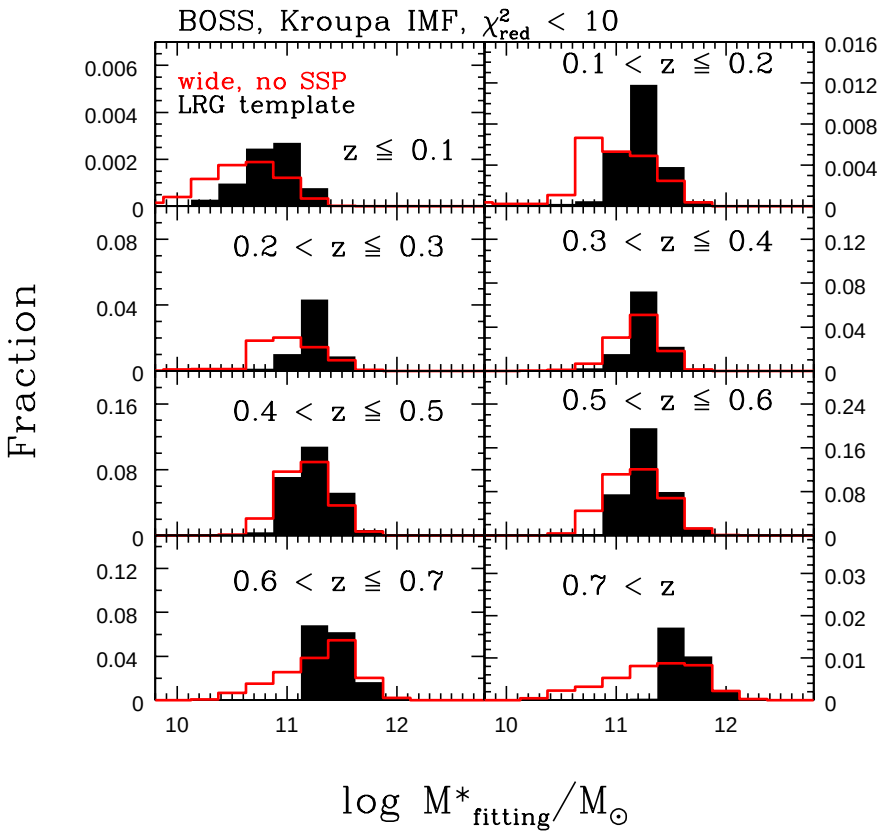

Figure 6.33: Stellar mass distributions for BOSS galaxies in redshift bins. Black shaded histograms refer to stellar masses derived with the LRG template, red histograms to the use of the wide template setup without SSPs. Included are only objects whose best fit solution has $\chi^2_\nu < 10$ (for the wide, no SSP setup these are 96.7% of the sample, for the LRG template 90.2 %; fractions are derived using these percentages as the total). Note the different scales in each panel.

6.2.4 Conclusions

From the previous sections we can conclude the following for the BOSS galaxies. Firstly, with the chosen colour cuts, and the $CMASS$ cut in particular, it is possible to select galaxies of constant stellar mass at various redshifts. The sliding cut tuned with a passively evolving stellar population model is crucial for this. Secondly, BOSS galaxies are massive and old at each redshift. This is true even when templates that allow star formation are used in the fitting[4]. This is in agreement with studies of e.g. Cimatti et al. (2006) that massive and passive galaxies have already assembled a large portion of their total mass at $z \sim 0.5$.

[4]However, it is crucial that reddening is excluded in the fit.

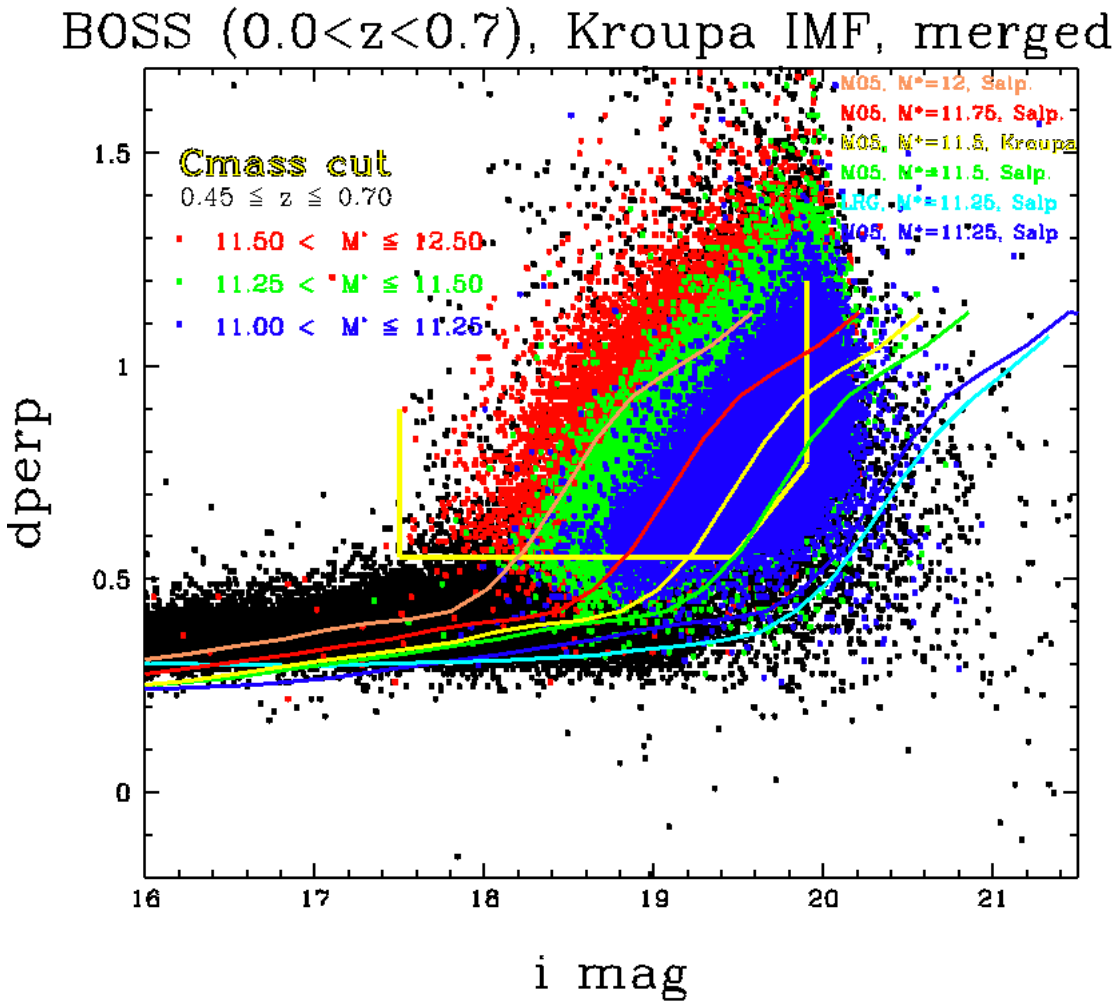

Figure 6.34: $d_\perp = (r-i) - (g-r)/8$ vs i-band c-model magnitude for BOSS galaxies. Black symbols refer to all galaxies. Blue, green and red symbols refer to specific mass ranges for $0.45 \leq z \leq 0.7$ as given in the legend. Masses are derived with Kroupa IMF templates and the mass distribution is determined combining the two template setups according to the $g-i$ colour. The yellow selection box indicates the $CMASS$ cut. Coloured solid lines refer to passively evolving SSPs for various masses and IMFs and stellar population models starting at $z = 0.7$ such that an age of ~ 13 Gyr is reached at $z = 0$.

When applying the $g-i$ colour cut as proposed in Masters et al. (2011) which is tuned towards separating early from late-type galaxies based on the visual morphological classification of a subsample of BOSS galaxies, we find that $\sim 80\%$ of galaxies in BOSS should be early-types. 20% are found to be late-type and whose masses are on average 0.25 dex lower than those of the early-types.

This work will continue in comparing galaxy properties with predictions from semi-analytic models.

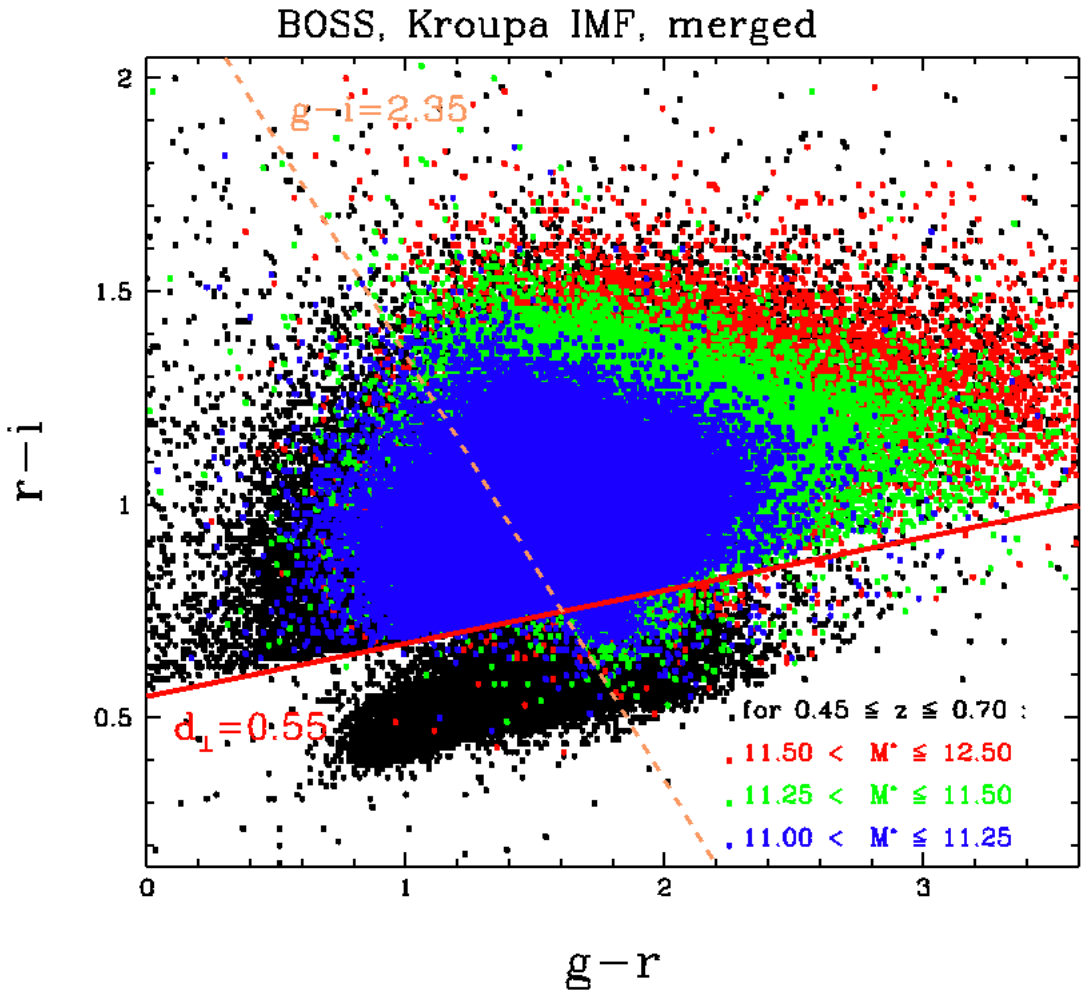

Figure 6.35: $r-i$ vs $g-r$ for BOSS galaxies. Black symbols refer to all galaxies. Blue, green and red symbols refer to specific mass ranges for $0.45 \leq z \leq 0.7$ as given in the legend. Masses are derived with Kroupa IMF templates and the mass distribution is determined combining the two template setups according to $g-i$ colour. The $g-i = 2.35$ line is shown in dashed orange, with galaxies to the right being mostly elliptical and the ones to the left being mostly spirals. The $d_{\perp} = 0.55$ line is shown in solid red. Everything above that line is selected via the $CMASS$ cut.

6.3 SDSS DR7 galaxies - $0.02 < z < 0.2$

In order to connect the results derived for the BOSS galaxies to the already existing data of the SDSS-I/II Legacy survey and to obtain a large set of galaxies for which properties are derived in the same manner we carry out the SED-fit for the SDSS-I/II DR7 galaxies. The data set is described in Chapter 2. In this section, we start with briefly describing the fitting setup (Section 6.3.1). Then we show our results for ages and stellar masses in Section 6.3.2. SDSS DR7 galaxies are less massive than BOSS galaxies. Stellar masses for the DR7 galaxies exist from previous SED-fits with BC03 stellar population models

carried out by the MPA/JHU group[5] (in the same spirit as in Kauffmann et al., 2003; Salim et al., 2007). We describe their method and the differences to ours before comparing results (Section 6.3.3). We find that the largest differences in the mass estimate stem from the use of different stellar population models and SFHs. We draw conclusions in Section 6.3.4.

The work carried out in this section was carried out in collaboration with C. Maraston and D. Thomas.

6.3.1 SED-fitting setup

The fitting setup that we initially employ for the SDSS-I/II DR7 (hereafter DR7) galaxies is the same wide setup without SSPs as used in the previous section (6.2.1) for BOSS galaxies and based on a Kroupa IMF. Effects of various IMFs have been shown numerous times in previous sections and chapters. We do not use the LRG template for the DR7 galaxies because these galaxies are neither selected as LRGs nor assumed to be predominantly passive. In order to better compare to the MPA/JHU masses and single out the difference in the method, we will also use the wide setup with a Chabrier IMF and BC03 stellar population models[6]. The only age constraint applied in the fitting of DR7 galaxies is that ages are required to be younger than the age of the Universe at the given redshift. The fitting is carried out without reddening in agreement with our findings in Chapter 4. For the comparison with the MPA/JHU masses we also carry out the fitting using a Calzetti law.

6.3.2 Ages and stellar masses of DR7 galaxies

In this section we show the basic results for ages and stellar masses of the DR7 galaxies. The comparison to results of the MPA/JHU group is carried out in the next section. In the following we restrict the sample in redshift to $0.02 < z < 0.2$ (80.4% of the sample) and to objects for which we obtain solutions with $\chi^2_\nu < 10$ (∼80% of the sample).

Firstly, we show derived ages using a Kroupa and Chabrier IMF in Fig. 6.36. Both distributions peak around 1.5 Gyr and differences between them are small. The age distribution is much wider than for the BOSS galaxies and extends to lower ages but the majority of objects is old as expected at low redshifts. Also note the striking similarity of the age distribution of the DR7 galaxies and the age distribution of mock star-forming

[5] http://www.mpa-garching.mpg.de/SDSS/DR7/

[6] We have experimented with a large number of template setups and IMFs in the process and only show the most important results here.

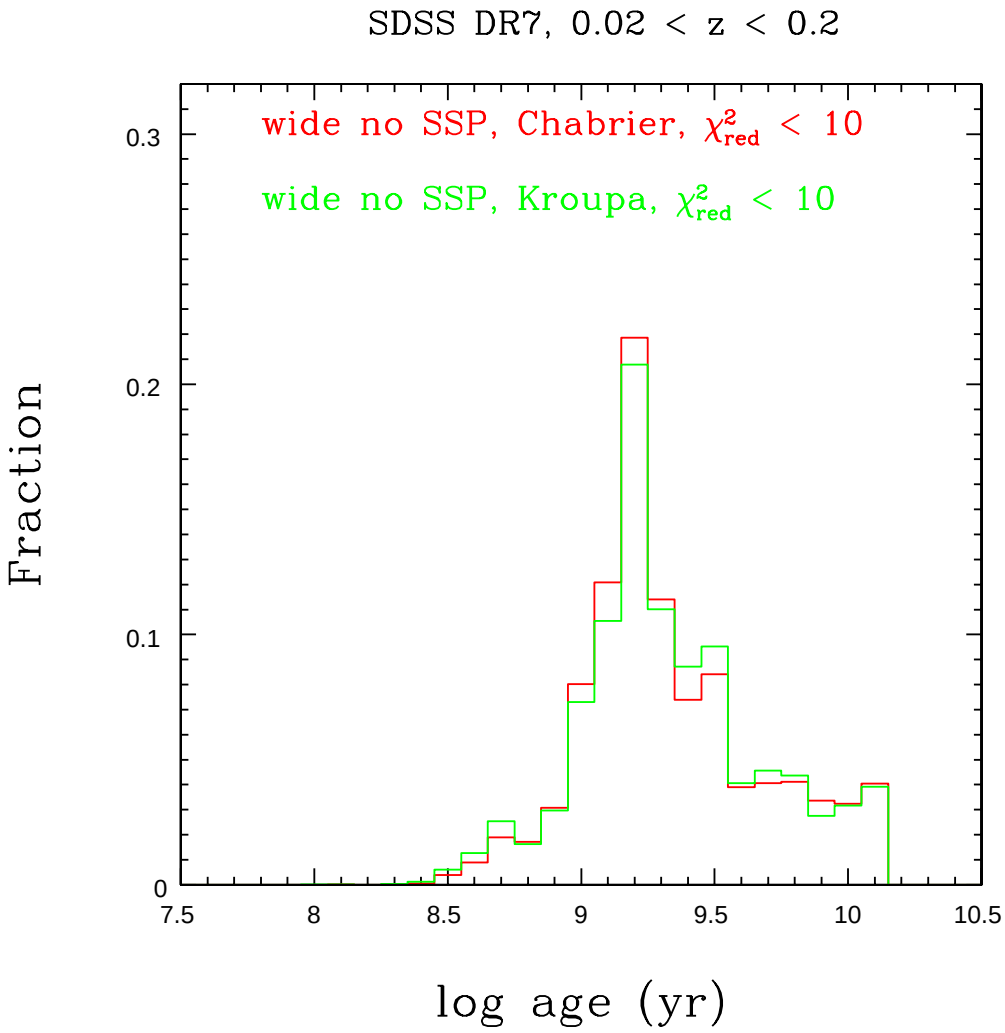

Figure 6.36: Derived ages for SDSS-I/II DR7 galaxies. The green histogram refers to a wide setup without SSPs and a Kroupa IMF, the red to a wide setup without SSPs and a Chabrier IMF. We restrict the sample to solutions with $\chi^2_\nu < 10$ and $0.02 < z < 0.2$ ($\sim$80% of the sample; fractions are calculated using this percentage as the total).

galaxies for a similar wavelength coverage (UBVRI) and no reddening shown in Fig. 4.4.

Stellar mass distributions extend to masses as low as 10^8 $M_\odot$ (Fig. 6.37) because of young ages. The peak of the distribution lies at around log $M^* = 10.25$ log $M_\odot$ for Kroupa and Chabrier IMF template setups (and at log $M^* = 10.75$ log $M_\odot$ for the MPA/JHU masses). This is more than one order of magnitude lower than for the BOSS galaxies again pointing out the different nature and selection criteria of the two surveys. In the next section we compare our results to those of the MPA/JHU group.

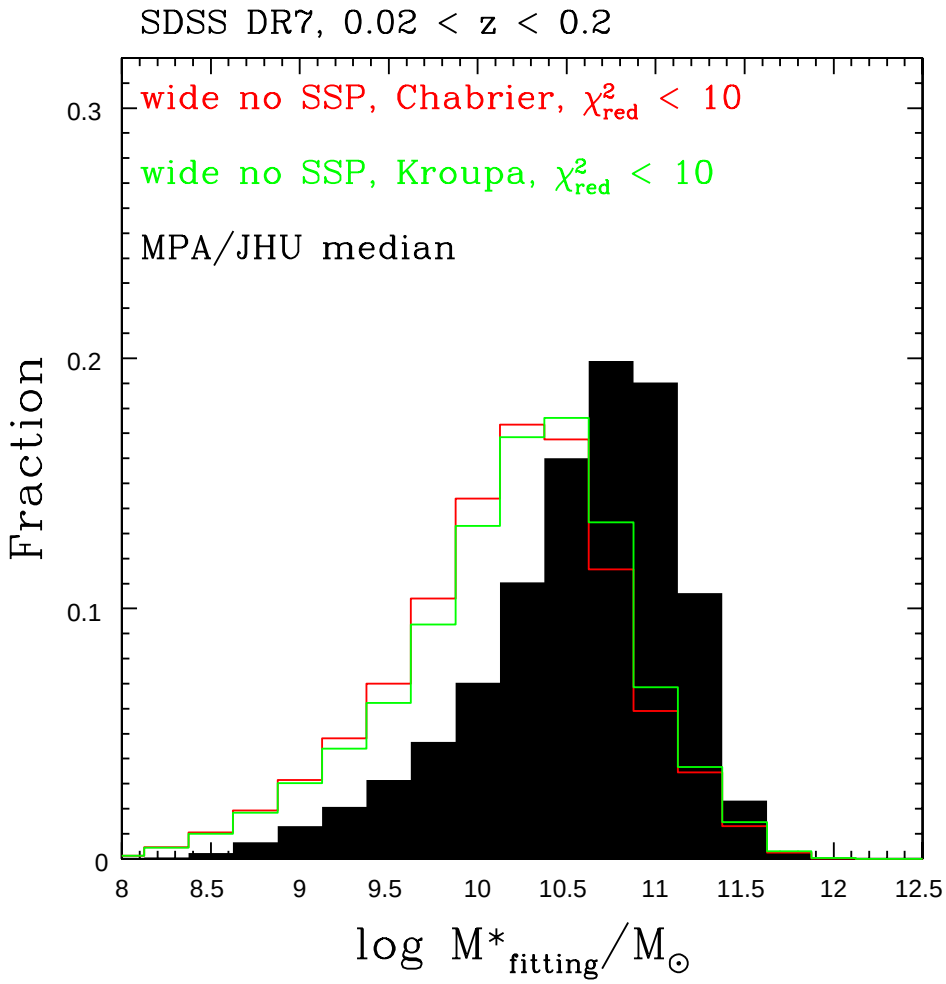

Figure 6.37: Stellar masses of SDSS-I/II DR7 galaxies. The green histogram refers to a wide setup without SSPs and a Kroupa IMF, the red to a wide setup without SSPs and a Chabrier IMF, the black shaded histogram shows the stellar masses as derived by the MPA/JHU group as the median of the probability distribution function. MPA/JHU masses are derived adopting BC03 models with a Chabrier IMF. We restrict the sample to solutions with $\chi^2_\nu < 10$ and $0.02 < z < 0.2$ (∼80% of the sample; fractions are calculated using this percentage as the total). The MPA/JHU sample is only restricted by redshift, resulting in 80.4% of the sample.

6.3.3 Comparison to MPA/JHU masses and method

Before we carry out the comparison let's first have a look at the method that has been used by the MPA/JHU group for the calculation of stellar masses. MPA/JHU stellar masses are also derived via the SED-fitting of model spectra to broad-band photometric data. The main difference to our method is the model library that is used which is described in detail in Salim et al. (2007). Their model library comprises 100,000 model SEDs based

on a Chabrier IMF and BC03 stellar population models. Ages of model galaxies range from 0.1 Gyr to the age of the Universe at any given redshift. Star formation histories are exponentially declining with values of τ randomly drawn between 0 and 1 Gyr. Additionally, random starbursts (lasting $30 - 300$ Myr) are superimposed such that with 50% probability a galaxy has at least one starburst within 2 Gyr. Starbursts carry between 0.03 and 4 times the mass of the galaxy at the time of the burst. On top of these, reddening is added using a Charlot & Fall (2000) reddening law with V-band optical depth ranging from 0 to 6 as motivated empirically from measurements on SDSS spectra (Salim et al., 2007). Metallicities cover the range between 0.1 and 2 times the solar value uniformly and are randomly drawn. This method for creating the model library is also adopted by Walcher et al. (2008) and Gallazzi et al. (2005). Pozzetti et al. (2007) compare the results derived with this method to results obtained using simpler star formation histories in the fitting.

χ^2 is calculated for each model and transferred into a probability (dependent on the model parameters) under the assumption of Gaussian errors. Marginalising over all model parameters but the stellar mass yields the probability distribution function (PDF) for the stellar mass from which the median value is used as the mass derived from the fit. This method is described in detail by Kauffmann et al. (2003) and Brinchmann et al. (2004). In the following we use the median value for the stellar mass when referring to the MPA/JHU masses.

In summary, the main differences between the method used for the derivation of stellar masses by the MPA/JHU group and our work in this section are:

- stellar population model - BC03 for MPA/JHU and M05 in this work
- additional random starbursts added in MPA/JHU, no secondary bursts in our SFHs
- method for obtaining the mass estimate - median of the PDF for MPA/JHU, minimum χ^2_ν in this work

We showed the mass distribution of the MPA/JHU masses alongside the mass distributions derived in this work in Fig. 6.37. Although being similar in shape, the MPA/JHU mass distribution peaks at a higher mass ($10^{10.75}$ $M_\odot$). Here, we investigate which of the three main differences in the method (as summarised above) is the main driver for this difference. In all comparisons we stick to a Chabrier IMF. In order to compare the cleanest sample we restrict the analysis to galaxies for which a fit with $\chi^2_\nu < 2$ is achieved.

Firstly, we compute the difference between our and the MPA/JHU mass estimate. The result is shown in Fig. 6.38 for two reddening options in the fit - no reddening and Calzetti reddening. When no reddening is used we find that our masses are lower by up to 0.8 dex. Since the MPA/JHU method includes reddening our first test involves allowing dust reddening in the fit. For this we use only the Calzetti reddening law and a sub-set of only $\sim 24,000$ ($\sim 19,400$ between $0.02 < z < 0.2$) galaxies because the inclusion of reddening is very computationally intensive. However, as already seen in previous

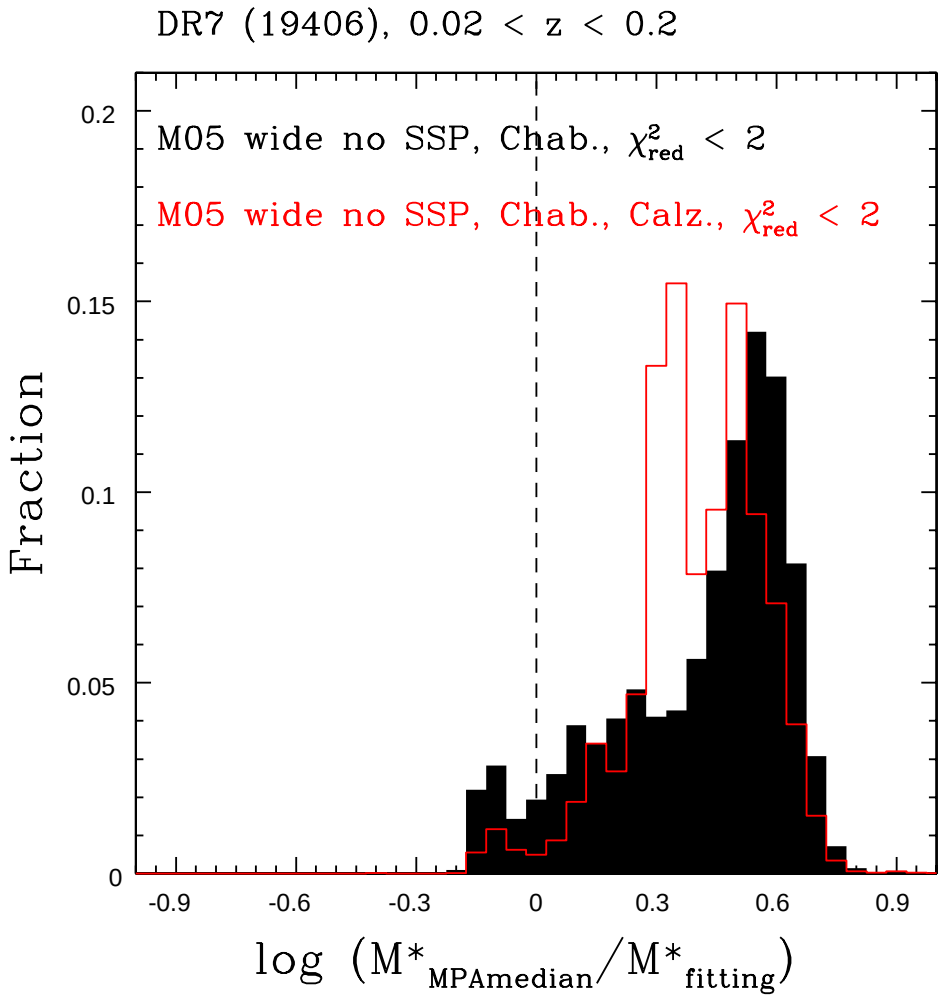

Figure 6.38: Differences in stellar mass between the masses derived in this work and MPA/JHU masses for DR7 galaxies. Our results are based on Chabrier IMF and M05-based templates. The dashed line marks 'no offset'. The black histogram refers to the unreddened case, the red one to the use of a Calzetti reddening law in the fit. We restrict the sample to solutions with $\chi^2_\nu < 2$ and $0.02 < z < 0.2$ (77% of the sample in the unreddened case, 79.5% in the reddened case; fractions are calculated using these percentages as the total). Restricting only by redshift results in 81.1% of the sample (19406 out of 23928).

chapters, the addition of reddening at low redshift results in drastically underestimated masses due to the age-dust degeneracy. Here, we find that including reddening increases our masses slightly. At first glance this seems at odds with our previous results. However, there are important differences between the fitting parameters used here and those used as default in Chapter 4. These are:

- wavelength coverage
- only Calzetti law instead of best fit among all reddening laws
- exclusion of SSPs from the template setup

We verified their effect by using the same fitting setup as adopted for the SDSS DR7 galaxies ($ugriz$ wavelength coverage, wide template setup without SSPs and only Calzetti reddening) for the mock star-forming galaxies at $z = 0.5$. Compared to the full wavelength coverage, a wide setup and all reddening laws the restricted setup used in this section gives larger stellar masses which are similar to the ones derived without reddening (median recovered masses between Calzetti reddening and no reddening are similar). Largely underestimated masses caused by underestimated ages due to the age-dust degeneracy are avoided by excluding SSPs as concluded in Chapter 4. Additionally, the sole use of a Calzetti reddening law instead of all reddening laws increases the estimated masses slightly (compare also the green thin line with the long dashed black line in Fig. 4.28). The true stellar masses are still underestimated by ~ 0.25 dex on average. Lastly, adopted IMFs are also different. This illustrates again that care has to be taken when comparing results from studies that adopt different fitting parameters.

Obviously, one of the biggest differences between the MPA/JHU method and ours is the adopted stellar population model. Therefore, we repeat the procedure using the same template setup (SFHs and IMF) but this time based on BC03-models. Differences between this mass estimate and the MPA/JHU masses are shown in Fig. 6.39, again with and without reddening in the fit. Overall, masses are larger than with the M05-based template setup (peak of distribution at ~ 0.1 dex), but still lower than the MPA/JHU masses. This is not helped by including reddening.

The best fit solution can be driven by degeneracies and sometimes be very isolated. In Chapter 4 we showed that the mass estimate can be improved for some objects by averaging over a range of solutions. Because the MPA/JHU masses are derived by taking the median of the PDF this might have the same effect. *HyperZspec* provides all solutions

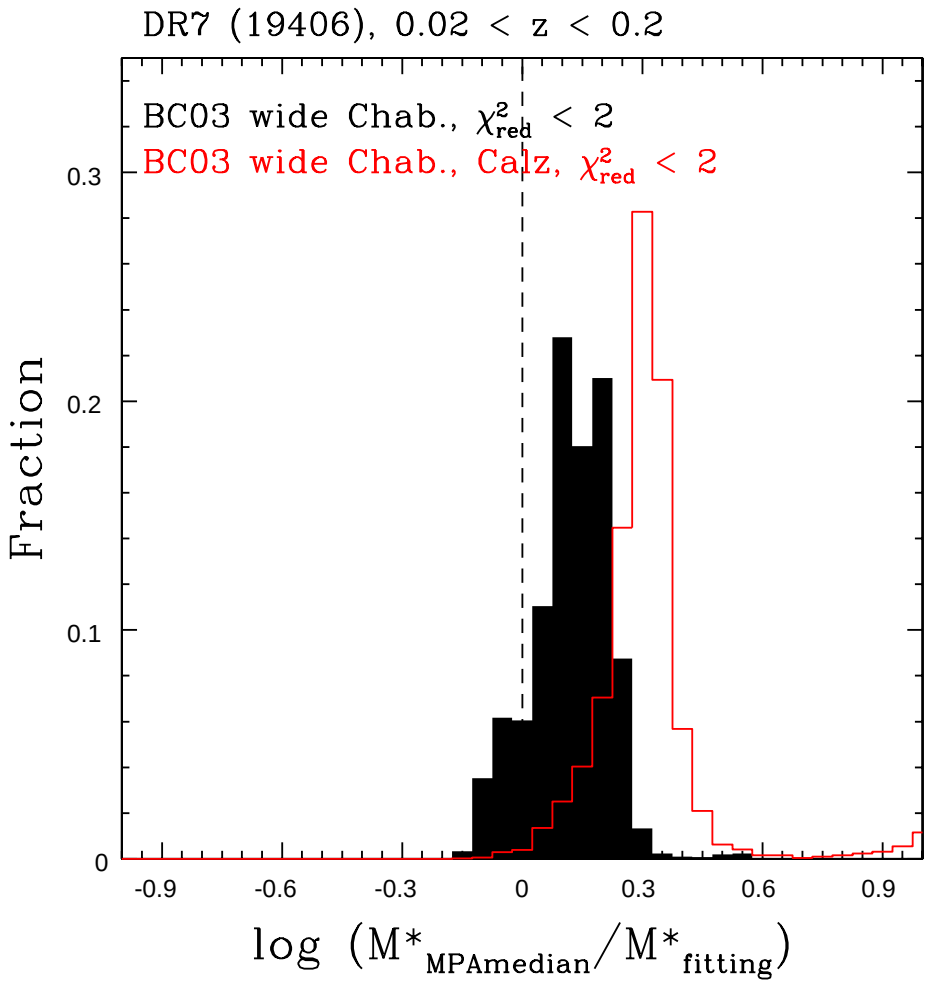

Figure 6.39: Difference in stellar mass between the masses derived in this work and MPA/JHU masses for DR7 galaxies. Our results are based on Chabrier IMF and BC03-based templates. The dashed line marks 'no offset'. The black histogram refers to the unreddened case, the red one to the use of a Calzetti reddening law in the fit. Large outliers for the red histogram are due to the use of SSP templates in this setup. We restrict the sample to solutions with $\chi^2_\nu < 2$ and $0.02 < z < 0.2$ (77.9% of the sample in the unreddened case, 80% in the reddened case; fractions are calculated using these percentages as the total). Restricting only by redshift results in 81.1% of the sample (19406 out of 23928).

(in the *.zm files if one chooses to obtain them[7]) which allow us to calculate a PDF, then take the median and therefore obtain masses in the same manner as the MPA/JHU group. As a first test we derive the masses of the mock star-forming galaxies from Chapter 4 by taking the median of the PDF to check if this does indeed improve the mass estimate in

[7]This is not usually done because these files can get very large and significantly slow down the fitting procedure.

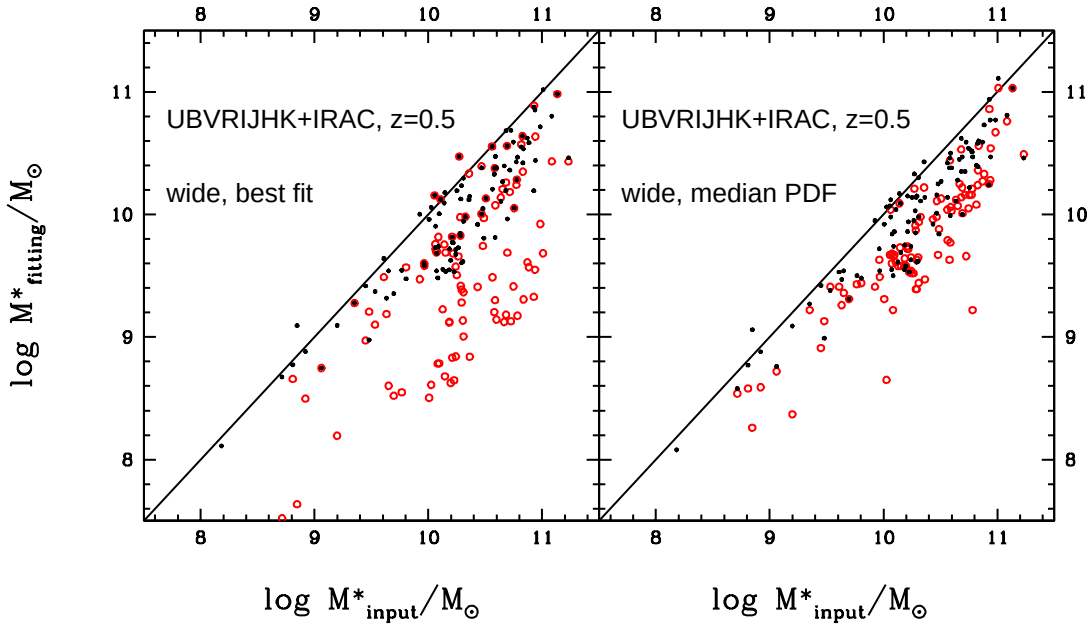

Figure 6.40: Stellar mass recovery when the mass is derived from the SED-fit using the median of the PDF (right) or the best fit (left) for mock star-forming galaxies at $z = 0.5$ used in Chapters 4 and 5 and which are described in Section 2.1. Black dots represent the unreddened case, red circles the case including reddening.

absolute terms (Fig. 6.40). Masses are higher and compare better to the true masses, in particular when reddening is used in the fitting and the age-dust degeneracy affects the result. However, masses are still underestimated overall.

Confident, that the mass estimate is improved by taking the median of the PDF, we now apply this to the DR7 galaxies and show results for BC03-based templates in Fig. 6.41 for the two reddening options investigated previously. When no reddening is used differences between the two masses are reduced such that the distribution peaks at zero difference. However, we still find a tail of objects with underestimated masses. When Calzetti reddening is used the distribution of $\Delta \log M^*$ is very narrow but offset by ~ 0.2 dex such that our masses are lower than the MPA/JHU masses. Only a few differences in the method remain to explain this. These are:

- secondary bursts,
- a fine grid of τ for the underlying exponentially declining SFH,
- a finer spaced range in metallicity and

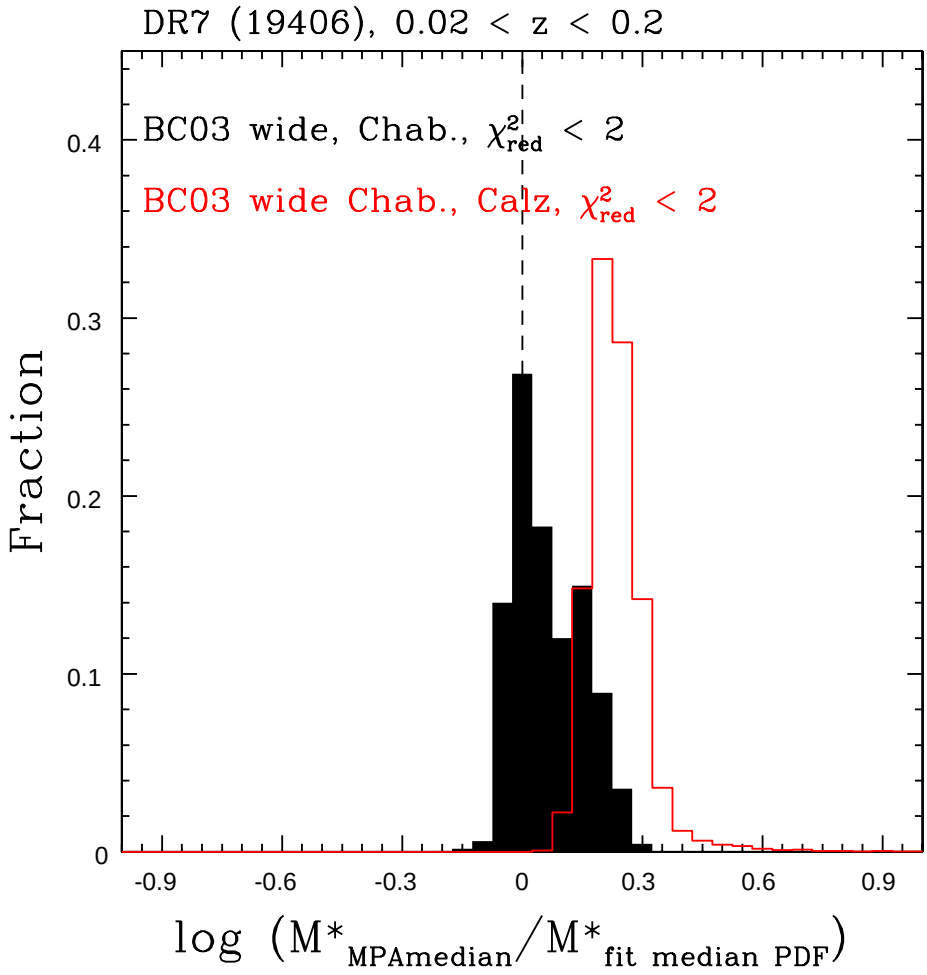

Figure 6.41: Differences in stellar mass between the masses derived in this work and MPA/JHU masses for DR7 galaxies. Our results are based on Chabrier IMF and BC03-based templates. Different to previous figures we obtain the mass by taking the median of the PDF. Colours, symbols and fractions are the same as in Fig. 6.39.

- a minimum age of 0.1 Gyr.

In previous chapters we demonstrated that metallicity effects for star-forming galaxies are of the order of 0.2 dex (see Fig. 4.8) but since we cover a very similar range in metallicity as the MPA/JHU group, just less refined, we believe metallicity to be a small contributor to this offset. Furthermore, differences between template setups are of the same order as the difference between best fit solution and median PDF solution when reddening is included (see Fig. 4.7). A constraint in minimum age has the same effect, when reddening is included (see Fig. 4.9). Fig. 6.42 shows the result when we limit the SFHs of the template setup to τ-models and the minimum age to 0.1 Gyr but keep the wide range of metallicities and use the mass from the median PDF. The distribution of

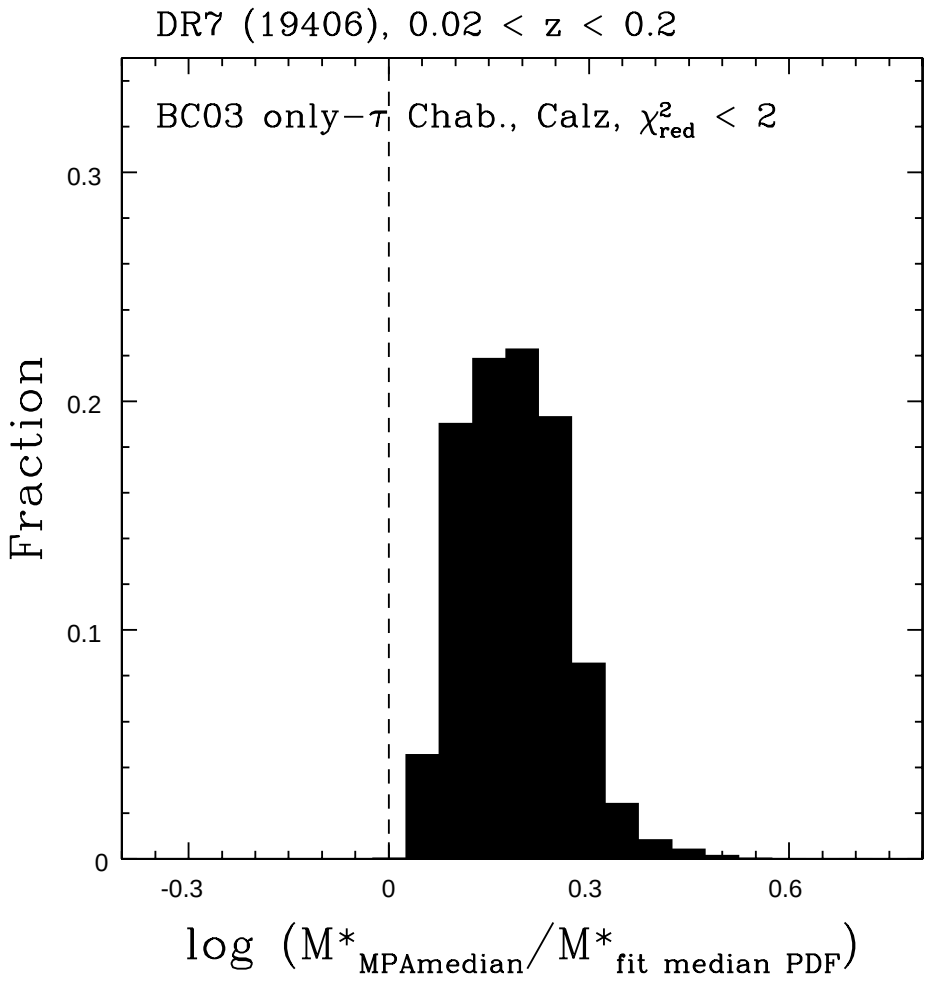

Figure 6.42: Differences in stellar mass between the masses derived in this work and MPA/JHU masses for DR7 galaxies. Our results are based on Chabrier IMF, BC03-based templates, Calzetti reddening and only exponentially declining SFHs. The mass is obtained by taking the median of the PDF. The dashed line marks 'no offset'. We restrict the sample to solutions with $\chi^2_\nu < 2$ and $0.02 < z < 0.2$ (79.9% of the sample; fractions are calculated using this percentage as the total). Restricting only by redshift results in 81.1% of the sample (19406 out of 23928).

$\Delta \log M^*$ broadens but the offset remains. Consequently, the addition of secondary bursts must be the main driver of this offset. Pozzetti et al. (2007) use the MPA/JHU method and model library and find that masses derived from a fit with simple SFHs are by up to 40% lower than those derived with model templates that include secondary bursts. Hence, we believe that the inclusion of secondary bursts in the SFHs explains most of the offset of 0.2 dex (which is equivalent to a factor of 1.6).

Finally, we show stellar masses obtained by taking the median of the PDF when M05-based templates are used in the fit in Fig. 6.43. The offset clearly reduces in the no reddening case, but we gain a double-peak structure which is driven by the difference in stellar population model between MPA/JHU and our masses and clearly a TP-AGB effect. Fits with stellar population models including the TP-AGB provide younger ages due to more flux in the near-IR around ages of 1 Gyr and therefore lower masses (M05, M06, Appendix B). When reddening is included the double-peak structure remains although the rank of the peaks is swapped.

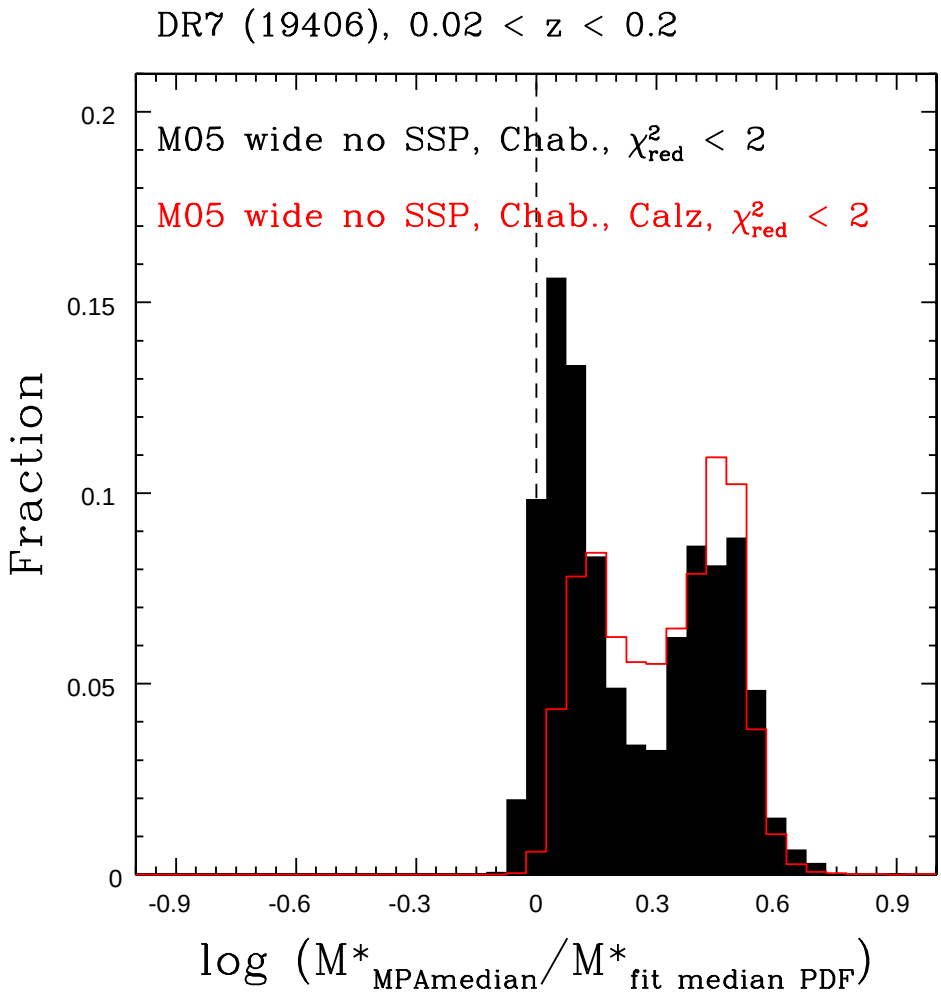

Figure 6.43: Differences in stellar mass between the masses derived in this work and MPA/JHU masses for DR7 galaxies. Our results are based on Chabrier IMF and M05-based templates. The mass is obtained by taking the median of the PDF. Colours, symbols and fractions are the same as in Fig. 6.38.

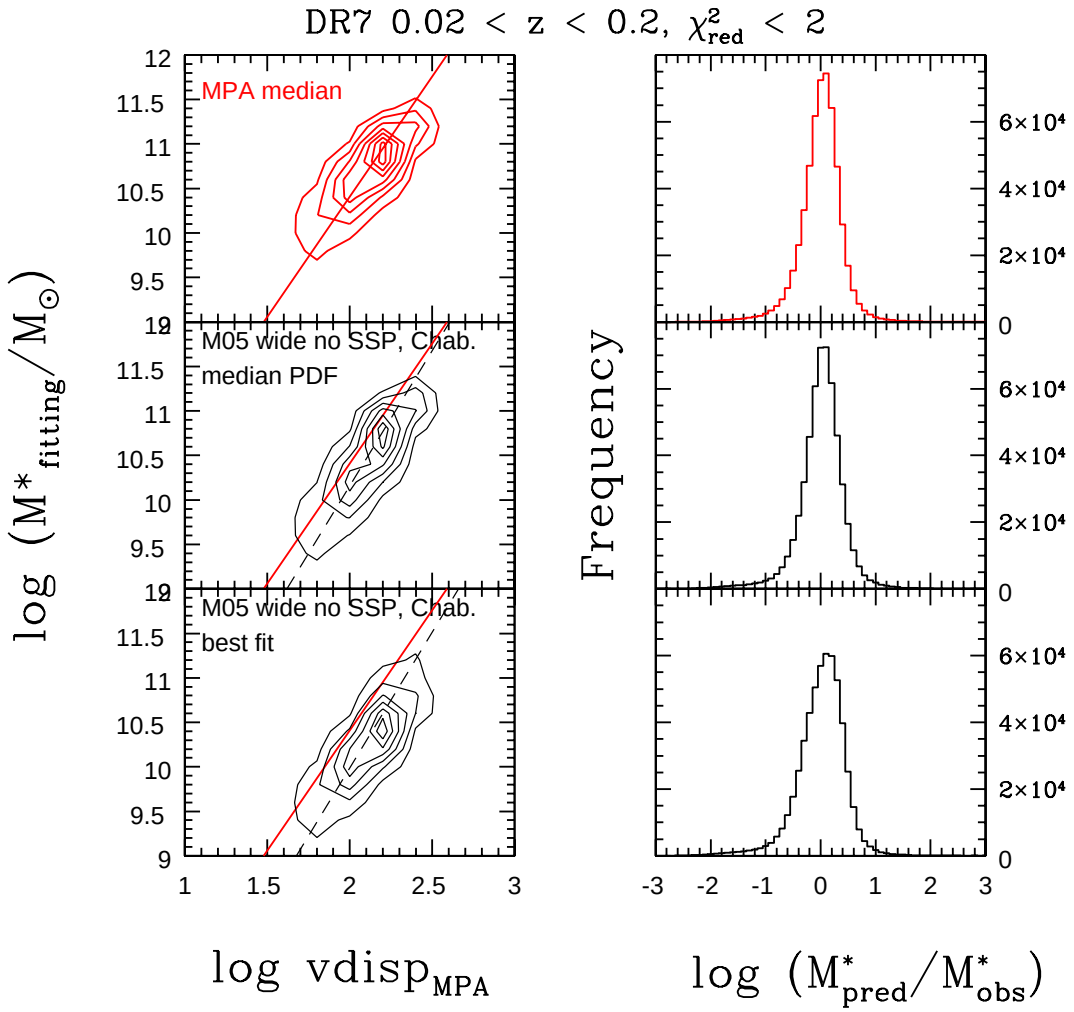

Figure 6.44: Masses compared to velocity dispersions for DR7 galaxies. On the left-hand side we show the contours for the mass-velocity dispersion. Lines represent the result of a linear least square fit using the MPA/JHU masses (red) and our masses (dashed black). On the right-hand side the distributions for the offsets between predicted mass from the line fit and the observed mass are shown. We restrict the sample to solutions with $\chi^2_\nu < 2$ and $0.02 < z < 0.2$ (76.4% of the sample). *Top:* MPA/JHU masses and velocity dispersions. *Middle:* Our masses derived from the median PDF using a wide setup without SSPs and a Chabrier IMF. *Bottom:* Our masses derived from the best fit using a wide setup without SSPs and a Chabrier IMF.

Because we do not know the true masses of the DR7 galaxies we can only compare our estimates to those derived with other techniques. Another way to estimate stellar masses is via stellar dynamics. For this, effective radii and stellar velocity dispersions are needed. For the DR7 galaxies we can compare to stellar velocity dispersions (Fig. 6.44). The comparison shows that both our and the MPA/JHU mass estimate align well although with different slope with the stellar velocity dispersions of the DR7 galaxies.

The slope of the relation is clearly steeper for our masses because they are somewhat lower, especially at the lower mass end.

6.3.4 Conclusions

In the last section we calculated stellar masses for the DR7 galaxies using a similar fitting setup as for the BOSS galaxies. We also compared our results to the stellar masses obtained by the MPA/JHU group based on a somewhat different method and BC03 stellar population models. In the process we confirmed that stellar masses obtained with M05 and BC03 stellar population models are very different because of their treatment of the TP-AGB. We also found that stellar masses are higher when secondary bursts are considered in the SFHs because they compensate for on-going star formation while still allowing older underlying populations. In agreement with our findings in the previous chapters this confirms that the star formation history is the most important driver for correct stellar masses. Additionally, we find that because of degeneracies it may be more robust to not take the mass of the best fit but a measure of all solutions by choosing the mass of the median PDF. However, this is very time consuming and not an ideal solution.

This work will continue in two ways. Firstly, we will focus our efforts on new star formation histories which reflect better the bimodal nature of the mock star-forming galaxies shown in Fig. 2.3 at low redshift. Secondly, in conjunction with the results for the BOSS galaxies we will compare these results to predictions from semi-analytic models.

Chapter 7

Conclusions and Summary

In this thesis we studied the uncertainties involved with the determination of stellar population properties of galaxies via spectral energy distribution fitting of stellar population models. For this purpose we utilised samples of mock galaxies (passive and star-forming) for which the input properties are known a priori. We tested the effect of changing template and fitting parameters on the overall result when redshift is known and used in the fit (Chapter 4) as well as when the redshift is a free parameter (Chapter 5). Finally, we applied our findings to samples of real galaxies of different type and at various distances (Chapter 6). In total we determined the stellar masses of ~ 1.5 million galaxies.

Our conclusions from Chapter 4 are:

- The stellar population parameters of star-forming and passive galaxies can be reasonably well determined when the right setup and a broad wavelength coverage is used in the fit.
- A *simultaneous* derivation of stellar population properties of star-forming galaxies is only possible when the SFHs of the templates match the observed ones. This is achieved at high redshift with inverted-τ models with high formation redshift and not too short values of τ.
- Mismatches in SFH for star-forming galaxies result in underestimated ages and stellar masses and overestimated reddening and SFRs. For older galaxies with residual star formation (at low redshift) the age-dust degeneracy drives the fitting result.
- The stellar masses of passive galaxies are generally well recovered.
- Metallicity effects are only important for old and passive galaxies.

When redshift is left free in the fit (Chapter 5) we can add the following conclusions:

- Redshifts are well determined (median recovered redshift within ~ 0.05) only when a broad wavelength coverage covering the Lyman and 4000 Å break is used in the fit. The exact template setup (SFH, metallicity, IMF etc.) is less important.

- Stellar masses of star-forming galaxies with little star formation (at low redshift) are better recovered than at fixed redshift by up to 0.3 dex (reddened case at $z = 0.5$) because redshift compensates.

- The mismatch between template and galaxy SFH is still the most important driver for underestimated ages and stellar masses and overestimated reddening and SFRs because of the overshining and degeneracies between age, dust and redshift.

- For $z \geq 2$ star-forming galaxies redshifts, stellar masses and SFRs can be obtained *simultaneously* with a wide setup and no reddening in the fit. This means that photometry seems to be sufficient for the robust determination of the stellar population properties of high redshift galaxies.

- The properties of mock passive galaxies are generally recovered very well even when the redshift is unknown. Masses are recovered within 0.2 dex.

The sensitivity of the SED-fit to the stellar population model was studied in Appendices B and C and results can be summarised to:

- When fitting BC03 models to M05 mock star-forming galaxies (Appendix B) ages are older due to the differences in the stellar population model. Consequently, stellar masses are higher and match the input masses better. This better agreement is contrived as it originates from the compensation of the wrong stellar population model.

- Equivalent results are provided in the reverse case (fitting of BC03 and M05 templates to BC03-type mock star-forming galaxies, Appendix C), i.e. masses and ages are underestimated in general. Stellar masses obtained from fits with M05 models are lower than masses derived with BC03 templates and show a clear offset caused by the various differences in the stellar population model (stellar tracks, TP-AGB, etc.) in agreement with findings of e.g. M06.

- The redshift recovery is significantly worse with BC03 templates for M05 mock star-forming galaxies such that redshift recovery fails in up to $\sim 30\%$ of the cases. In these cases recovering the stellar mass fails as well (underestimation of more than 2 dex) and most SFRs are zero.

- When BC03-type galaxies are fit with M05 templates then the redshift recovery is comparable to that with BC03 templates.

- The redshifts of BC03-type galaxies are recovered (with templates of either stellar population model) worse than those of M05-type galaxies with M05 templates and show larger scatter, e.g. at $z = 0.5$ the mean $\Delta z = -0.007 \pm 0.082$ in the unreddened case ($\Delta z = 0.011 \pm 0.115$ in the reddened case) for M05-type galaxies fit with M05 templates and $\Delta z = 0.015 \pm 0.133$ ($\Delta z = 0.128 \pm 0.316$) for BC03-type galaxies fit with M05 templates. BC03 templates recover the redshift of BC03-type galaxies at $z = 0.5$ similarly well and those of M05-type galaxies significantly worse. Thus, it seems to be best to derive redshifts with M05 templates independently of the underlying stellar population model of the mock galaxies.

Overall, we find that stellar masses can be best recovered when no reddening and a wide wavelength coverage is used in the fit. At high redshift we were able to identify the SFH that best matches observed SFH of star-forming galaxies and allows us to recover masses perfectly. In Chapter 6 we applied templates of this particular SFH (inverted-τ with high formation redshift and not too small values of τ) to a sample of star-forming galaxies in the GOODS-S survey for which we also find that SFRs and reddening determined via the SED-fit agree with independent measurements from the UV-slope, thus confirming our results.

For BOSS galaxies we conclude that the chosen colour cuts work very well and stellar masses can be maximised using a specific type of template tuned towards the specific galaxy type observed within BOSS. Again this points out that the correct SFH is crucial for obtaining meaningful galaxy properties from SED-fitting.

For the SDSS-DR7 galaxies we find that the difference in the stellar mass estimate derived with M05 and BC03 models is substantial and driven by different assumptions concerning the TP-AGB evolution in the models. The comparison with the MPA/JHU masses showed that masses are on average higher when the mass at the median of the PDF is used instead of the mass of the best fit. We have also seen that including secondary bursts increases the mass estimate by up to 0.2 dex. Again, an exact prescription of the SFH is important to accurately determine stellar masses (and other stellar population properties).

On-going and future work

Much effort is still needed in order to unify data sets of various existing surveys which have been analysed in different ways before they can be used together to build a uniform picture of galaxy formation and evolution. We have seen that the SFH assumed in the templates is an important driver for the robust estimation of galaxy properties at any redshift. For high-redshift star-forming galaxies we already identified the best SFH that should be used in the fit. For low-redshift, aged galaxies with little on-going star formation a better prescription is needed. Some authors make use of secondary bursts in order to maximise the stellar mass and in order to more realistically model the bursty nature of galaxies where starbursts are triggered by merging and galaxy encounters. However, these contain a large number of free parameters, such as burst duration, time of occurrence and burst strength, on top of the already wide parameter choices. It remains to be determined whether this choice has a physical meaning or is just an effective way of maximising the stellar mass. Covering a large parameter space also always comes with the need for more computation time. Although many high performance supercomputers for astrophysical purposes (e.g. COSMOS and SCIAMA) exist, one still desires to carry out calculations as efficiently as possible. Thus the simplest and most efficient setup for SED-fitting which still allows robust parameter estimation should be used. A way to better match the SFHs of low redshift, aged galaxies with little star formation could be to adopt SFHs that show increasing SFR at young ages, therefore incorporating what we determined to be best at high redshift, and decreasing SFRs after some time. They would thus represent a natural low-redshift extension of the inverted-τ models at high-redshift. These new models can then be tested with simulated galaxies for their ability to recover the galaxy physical parameters.

SERVS - The Spitzer Extragalactic Representative Volume Survey SERVS (Lacy et al., 2008) aims at taking a complete census of massive galaxies between redshift 1 and 6 at 3.6 and 4.5 μm by exploiting the warm phase of the Spitzer Space Telescope. Its specific aims include the study of stellar mass assembly using photometric redshifts and mass estimates from SED-fitting, the study of obscured star formation, the investigation of the role of AGN and the role of environment with respect to galaxy formation and evolution and the study of the highest redshift quasars. Imaging is carried out in 5 well-known extragalactic fields (Lockman Hole, Elias North 1, Elias South 2, Chandra Deep Field South and XMM) covering a total area of $\sim 18\,deg^2$ and providing a vast amount of ancillary data in the optical and near-IR. The method of SED-fitting naturally exploits the broad wavelength coverage available for SERVS and allows the estimation

of robust photometric redshifts and stellar masses. This is crucial for the study of stellar mass assembly, one of the key science goals of SERVS. During the last year we have been working on the derivation of photometric redshifts for SERVS galaxies using SED-fitting. We carried out a comparison between photometric and spectroscopic redshifts (where available) in order to optimise the template and fitting setup with respect to accuracy and economics. Currently, SERVS data and the crossmatch with ancillary data is being finalised but preliminary results for the achieved redshift accuracy are very promising. The agreement between photometric and spectroscopic redshifts is very good ($z_{phot} - z_{spec} < 0.05$). We further verified this by applying the same method to the larger statistical sample of the VVDS -Simple survey. For SERVS, especially the findings of Chapter 5 help in estimating the reliability of the photometric redshift estimation and its dependence on the wavelength coverage as ancillary data in the SERVS fields is not uniformly. Results from the latter have been successfully used in observational proposals for ancillary data in the SERVS fields. This work will continue in estimating the stellar masses of SERVS galaxies adopting composite stellar population models used throughout this thesis.

In the light of the wealth of existing data from past galaxy surveys and new data from upcoming and on-going surveys aimed at galaxy formation and evolution it will be exciting to apply the findings of this thesis to help unify data sets and piece together the puzzle of galaxy formation and evolution.

Appendix A

Parameter files for *HyperZ* and *HyperZspec*

A.1 Input parameter file for *HyperZspec*

```
###########################################################################
################           hyperzspec              ##################
################    version 0.2 - August 27, 2004    ##################
################         by Micol Bolzonella         ##################
###########################################################################
A0VSED       ../../../filtersCM/A0V_KUR_BB.SED # Vega SED
FILTERS_RES  ../../../filtVeganew.res  # filters' transmission
FILTERS_FILE       ../../../filters_Veganew.param  #  filter's file
TEMPLATES_FILE     ../../../spectrasalpwoSSP.param  # templates
CATALOG_FILE       ../../FINALmockcatallVd05JPlyf.cat  # catalogue file
MAG_TYPE               0   # 0: standard Vega magnitudes
                           # 1: AB magnitudes (Oke 1974)
                           # 2: flux in microJansky
ERR_MAG_MIN          0.05  # minimum photometric error
                           # (used in make_catalog if NOISE_TYPE=1)
ERR_MIN_LAW            0   # 0. ERR_MAG_MIN is the minimum phot error
                           # 1. ERR_MAG_MIN is added in quadrature
REDDENING_LAW          0   # reddening law
                           # 0: no reddening
                           # 1: Allen (1976) MW
                           # 2: Seaton (1979) MW
                           # 3: Fitzpatrick (1983) LMC
                           # 4: Prevot (1984) Bouchet (1985) SMC
                           # 5: Calzetti (2000)
AV_MIN                 0.0  # minimum A_v
AV_MAX                 3.0  # maximum A_v
AV_STEP               0.20  # Av_err
```

```
AGE_TYPE                1  # 0. free
                           # 1. free with age <  age universe
                           #  - age(T_FORM) (supersedes AGE_CHECK)
                           # 2. fixed age: age=age of universe-T(Z_FORM)
AGE_MIN              -1.00  # Minimum age to be considered in Gyr
AGE_MAX               20.0  # Maximum age to be considered in Gyr
                           # if AGE_TYPE = 0 both AGE_MIN and AGE_MAX
                           # will be considered
                           # if AGE_TYPE = 1 max age will be the minimum
                           # between age and AGE_MAX, min age = AGE_MIN
                           # if AGE_TYPE = 2 this parameter is ignored
Z_FORM                 20  # formation redshift
                           # (used only if AGE_TYPE=1)
AGE_REBIN               0  # age rebinning (only for BC templates)
                           # 0. no (221 ages), 1. yes (51 ages)
NCOL_ZSPEC              1  # number of the column with zspec after
                           # the photometric catalogue columns
OUTPUT_FILE         FINALmocktreeall2Vd05JPlyfwoSSPnoMCsalpred0
                           # N.B. without extension.
                           # The default file will have .zspec extension
OUTPUT_TYPE             0  # 0: 2.E-17 erg/cm^2/s/A,
                           # 1: microJy, 2: mag_AB
SED_OBS_FILE            y  # file .zobs_sed
SED_TEMP_FILE           y  # file .ztemp_sed
MATRIX                  y  # file .zm for each object
SPECTRUM                y  # file .zspe for each object
FILT_M_ABS              8  # filter for absolute magnitude
WL_MAX              25000. # maximum lambda_eff [A] to be used
IR_FILTERS              1  # 0: use all available filters
                           # 1: use filters with lambda_eff > WL_MAX
                           #    only when lambda_eff/(1+z) < WL_MAX
                           # 2: don't use filters with lambda_eff>WL_MAX
SN_LIMIT                1  # S/N limit for detection (applied in
                           # each filter); if S/N<SN_LIMIT the object
                           # is considered as non detected in that
                           # filter (like mag=99.) '
#M_ABS_MIN             -25.  # minimum absolute magnitude (bright)
#M_ABS_MAX             -12.  # maximum absolute magnitude (faint)
M_ABS_ALG               1 # Algorithm to compute absolute magnitudes
                           # 0. nearest filter
                           # 1. best fit normalization
H0                   71.9  # Hubble constant in Km/s/Mpc
OMEGA_M              0.258 # density parameter (matter)
OMEGA_V              0.742 # density parameter (Lambda)
```

A.2 Input parameter file for *HyperZ*

```
########################################################################
################   hyperz & make_catalog parameters  ###################
################   version 1.2 - January 24, 2003    ###################
################   by Bolzonella, Pello' & Miralles  ###################
########################################################################
#### Reference: Bolzonella, Miralles & Pello', 2000, A&A 363, 476  ####
#### Web:       http://webast.ast.obs-mip.fr/hyperz/               ####
########################################################################
A0VSED       ../../../filtersCM/A0V_KUR_BB.SED  # Vega SED
FILTERS_RES  ../../../filtVeganew.res     # filters' transmission
FILTERS_FILE          ../../../filters_Veganew.param # filter's file
TEMPLATES_FILE     ../../../spectrasalpwoSSP.param # templates
MAG_TYPE               0   # 0: standard Vega magnitudes
                           # 1: AB magnitudes (Oke 1974)
                           # 2: flux in microJansky
ERR_MAG_MIN          0.05  # minimum photometric error
                           # (used in make_catalog if NOISE_TYPE=1)
Z_MIN                 0.   # minimum redshift
Z_MAX                 6.   # maximum redshift
REDDENING_LAW          0   # reddening law
                           # 0: no reddening
                           # 1: Allen (1976) MW
                           # 2: Seaton (1979) MW
                           # 3: Fitzpatrick (1983) LMC
                           # 4: Prevot (1984) Bouchet (1985) SMC
                           # 5: Calzetti (2000)
AV_MIN                0.0  # minimum A_v
AV_MAX                3.0  # maximum A_v
LY_FOREST             1.0  # Lyman Forest
                           # 1. : fixed Madau value
                           # other values: 3 optical depth considered
                           # <tau_eff>/LY_FOREST, <tau_eff> and
                           # <tau_eff>*LY_FOREST
OUTPUT_FILE          FINALmocktreeall2Vd05JPlyfhznewwoSSPnoMCsalpred0
                           # N.B. no extension !!
                           # hyperz: root name for output files
                           #         (see other parameters)
                           # make_catalog: .model  random catalogue
                           #               .cat  catalogue with noise
H0                   71.9  # Hubble constant in Km/s/Mpc
OMEGA_M              0.258  # density parameter (matter)
OMEGA_V              0.742  # density parameter (Lambda)
############################ hyperz only ################################
FILT_M_ABS             8   # filter for absolute magnitude
```

```
                          # 1: use filters with lambda_eff > WL_MAX
                          #    only when lambda_eff/(1+z) < WL_MAX
                          # 2: don't use filters with lambda_eff>WL_MAX
#SN_LIMIT                1  # S/N limit for detection (applied in
                          # each filter); if S/N<SN_LIMIT the object
                          # is considered as non detected in that
                          # filter (like mag=99.) '
M_ABS_ALG                1 # Algorithm to compute absolute magnitudes
                          # 0. nearest filter 1. best fit normalization
CATALOG_FILE     ../../FINALmockcatallVd05JPlyf.cat
                          # catalogue file
CATALOG_TYPE           0   # catalogue type
                          # 0: z/cat
                          # 1: z/obj
Z_STEP                0.05  # step in redshift
ZSTEP_TYPE              0   # 0 step = Z_STEP
                          # 1 step = Z_STEP*(1+z)
AV_STEP               0.20  # Av_err
AGE_TYPE                 1  # 0. free
                          # 1. free with age <  age universe
                          # - age(T_FORM) (will supersede AGE_CHECK)
                          # 2. fixed age: age=age of universe-T(Z_FORM)
AGE_MIN              -1.00  # Minimum age to be considered in Gyr
AGE_MAX               20.0  # Maximum age to be considered in Gyr
Z_FORM                  20  # formation redshift
                          # (used only if AGE_TYPE=1)
AGE_REBIN                0  # age rebinning (only for BC templates)
                          # 0. no (221 ages), 1. yes (51 ages)
PROB_THRESH          10.00  # prob. thresh. for second. max. (0,100)
OUTPUT_TYPE              0   # 0: 2.E-17 erg/cm^2/s/A,
                          # 1: microJy, 2: mag_AB
SED_OBS_FILE              y  # file .obs_sed
SED_TEMP_FILE             y  # file .temp_sed
LOGPHOT_FILE              y  # file .log_phot
CATPHOT_FILE              y  # file .cat_phot
ZPHOT_FILE                y  # file .z_phot
########################   optional parameters    ########################
#Z_CLUSTER                 1.  # redshift of cluster
#M_ABS_MIN               -25.  # minimum Vega absolute magnitude (bright)
#M_ABS_MAX               -12.  # maximum Vega absolute magnitude (faint)
MATRIX                    y  # file .m for each object
SPECTRUM                  y  # file .spe for each object
#EBV_MW                   0.  # E(B-V) for galactic dereddening
```

Appendix B

Fitting BC03 templates to M05 galaxies

B.1 At fixed redshift

It is interesting to see the effect of fitting galaxies adopting a certain stellar evolution with templates adopting another prescription. To this aim we fitted the semi-analytic star-forming galaxies whose spectra adopt the M05 stellar population models with templates based on the BC03 stellar population models. Results are shown in Figs. B.1 - B.5.

Ages derived from BC03 templates are on average older than those from the M05-based templates (Fig. B.1). This is clearly a TP-AGB effect for ages between ~ 0.2 and 2 Gyr (M05, M06). M05 templates contain more flux in the rest-frame near-IR caused by the TP-AGB. BC03 templates have a lower contribution from this phase, hence an older age of these templates is required to match the near-IR flux. At ages ≥ 2 Gyr (and metallicities $\geq Z_{\odot}$) M05 models are bluer than BC03 models because of the warmer Red Giant Branch[1] (RGB) in the Frascati stellar tracks used in M05. The optical/near-IR ratio is most affected by these differences in the stellar tracks, for example the $V-K$ colour is 0.08 mag bluer in the Frascati tracks (see M05 for more details). This is compensated by younger ages obtained with BC03 templates.

For the youngest ages (at low redshift) differences between M05 and BC03-based models stem from the different input stellar tracks for young populations, namely Geneva for M05 and Padova for BC03. Geneva tracks in particular are redder than Padova tracks around 10 Myr, an effect due to the assumed mass-loss and post-MS evolution (Maraston, 2011a). This implies a redder M05 model at very young ages which may drive BC03

[1] most likely caused by a different treatment of the mixing length in these tracks in comparison to the Padova tracks used in BC03, see M05 Fig. 9

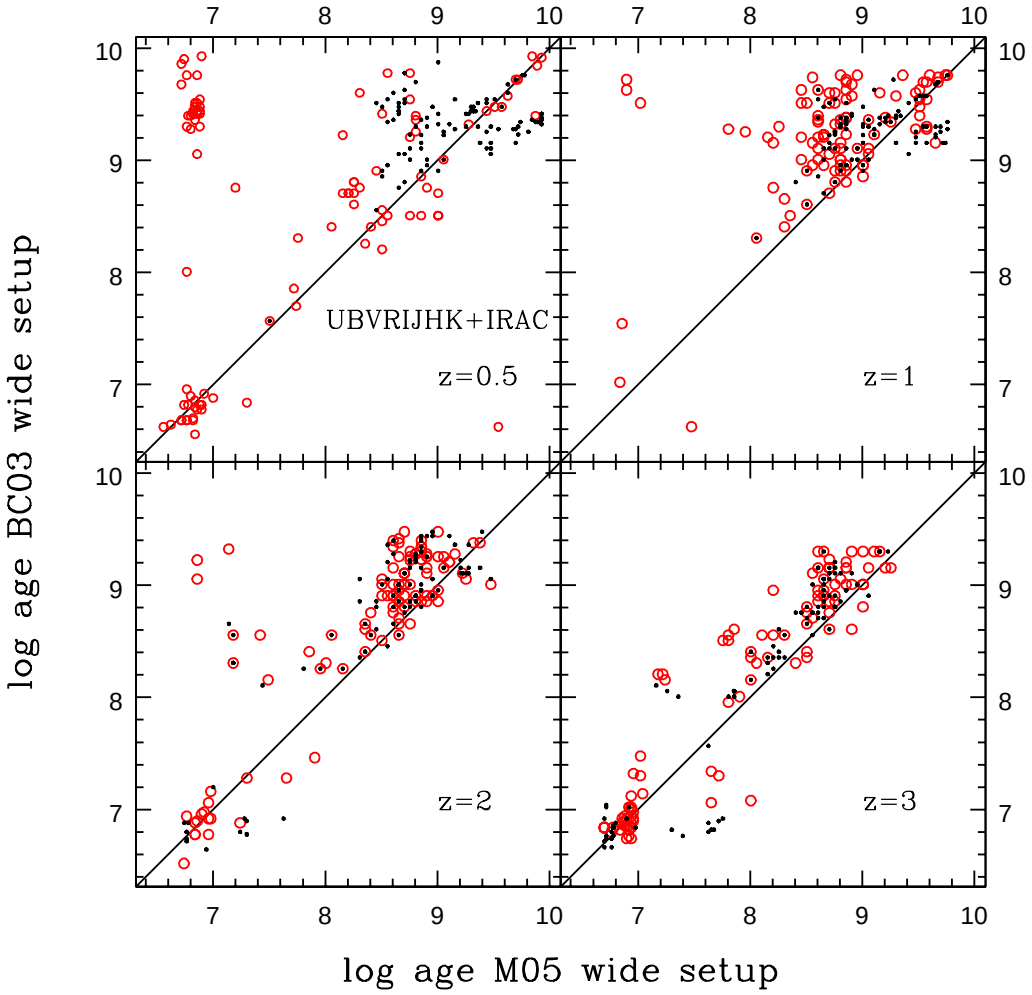

Figure B.1: Ages derived from SED-fitting with different stellar population synthesis models (M05 and BC03) for mock star-forming galaxies based on M05 photometry. A wide setup and wavelength coverage was used. Black refers to the unreddened case, red to the case including reddening.

templates to fit with older ages.

Fig. B.2 shows that the best fit solution obtained from BC03-based templates is on average more metal-rich than that from M05-based templates. This in combination (and degeneracy) with age compensates the lower fuel in TP-AGB and red supergiant stars in the model. At low redshift the reddening is better determined with BC03-based templates which on average provide less reddening (Fig. B.3). Obviously, this is because ages are older and metallicities are higher. However, as the model galaxies evolve à la M05, this better agreement is contrived as it originates from the compensation of the wrong determination of parameters. At high redshift, the reddening values from both models agree

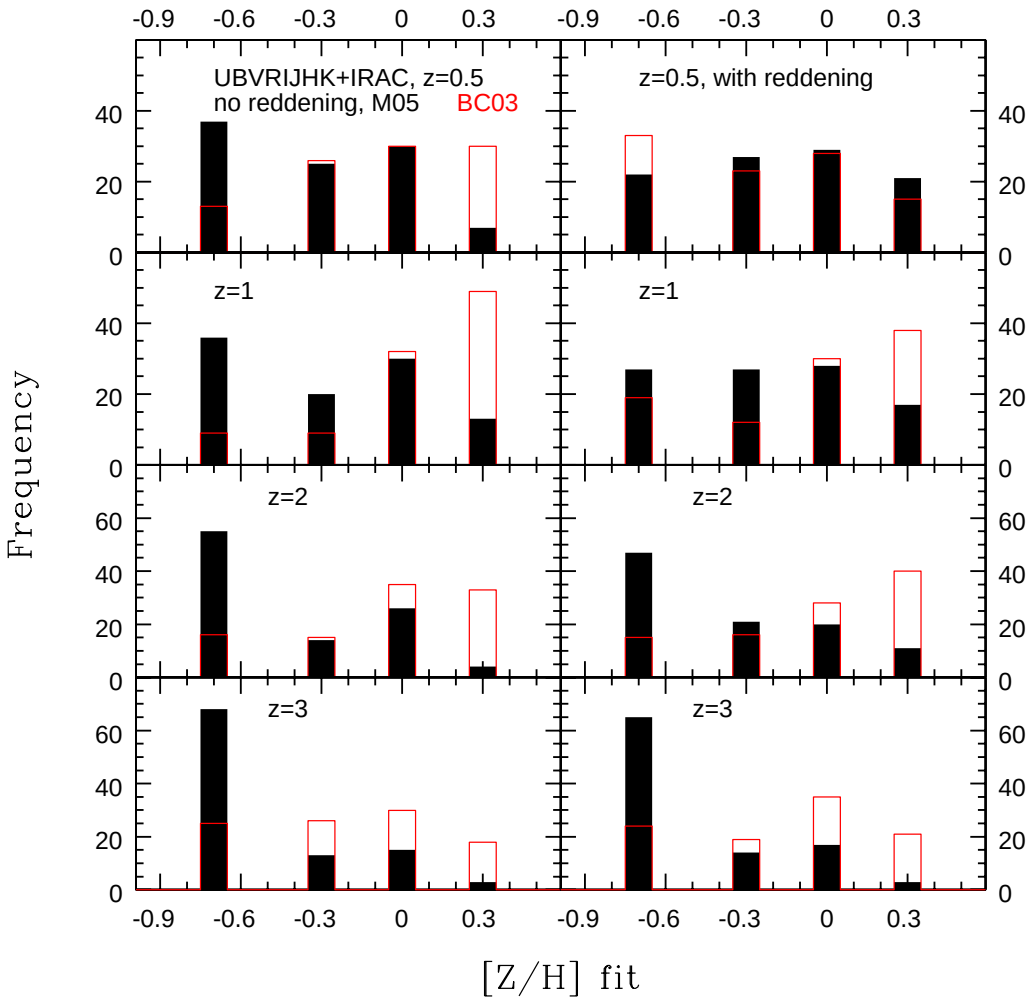

Figure B.2: Same as Fig. B.1 for the derived metallicities. Red histograms stand for BC03-based results, black shaded histograms for M05-based results.

very well.

Masses derived with templates based on BC03 stellar population models are on average higher than M05-based masses by 0.34 to 0.12 dex (at $z = 0.5$ and 3, respectively). The mass for $M^* > 10^{9.5}\,M_\odot$ at $z \geq 1$ is higher by up to 0.6 dex (Fig. B.4). This is in agreement with previous findings of M06 and Pozzetti et al. (2007). In the unreddened case this clearly points out the different TP-AGB, particularly at high redshift where a significant amount of stars is found in this evolutionary phase. In the reddened case the age-dust degeneracy dominates. At $z \leq 1$ the lower TP-AGB in the BC03 models causes just the right amount of overestimation in age to correctly predict stellar masses. Given that the physical effect is to underestimate the mass, the larger masses derived with BC03

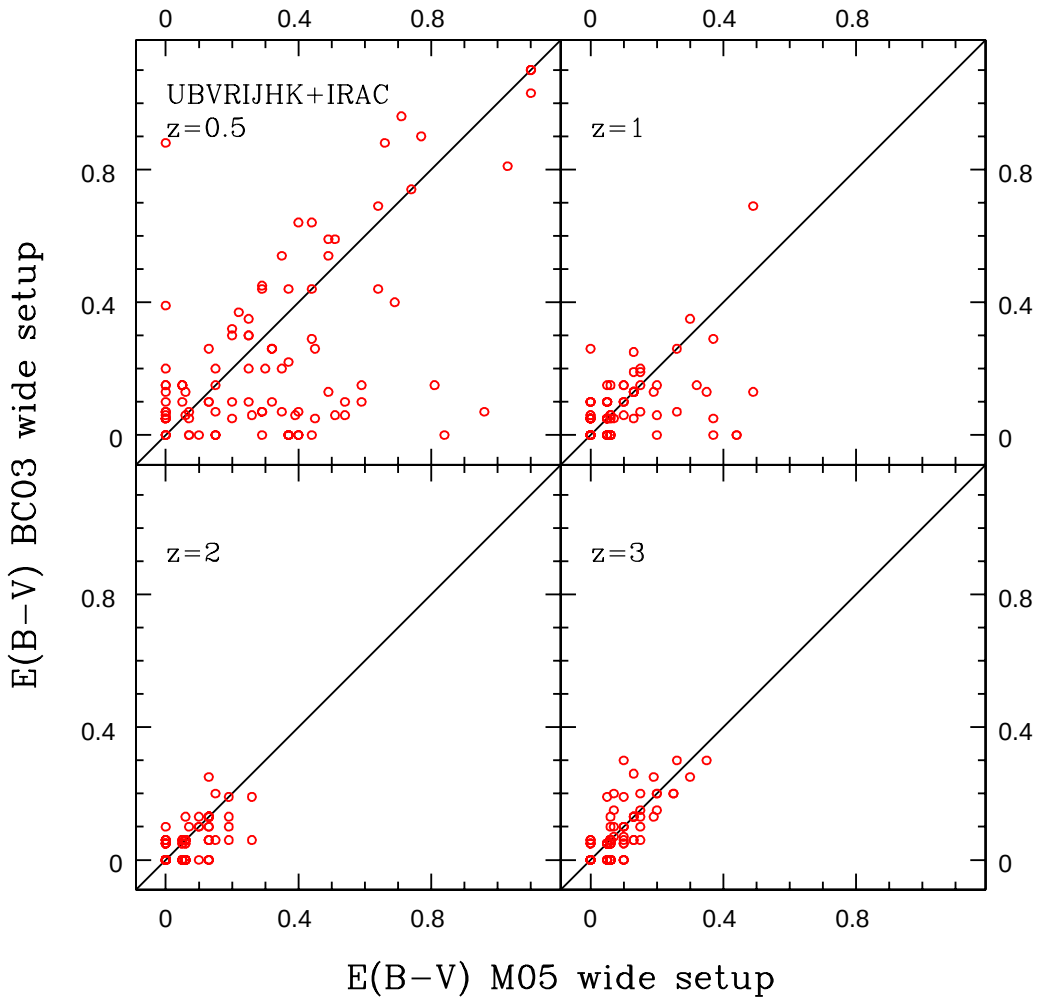

Figure B.3: Same as Fig. B.1 for the comparison of derived dust attenuation.

templates are closer to the correct mass but for the wrong reason. At $z \geq 2$ BC03 templates overestimate the masses at the high-mass end for this reason.

The SFRs derived with both models agree very well at low redshift (Fig. B.5), at high redshift BC03-based template setups give lower SFRs on average in the reddened case.

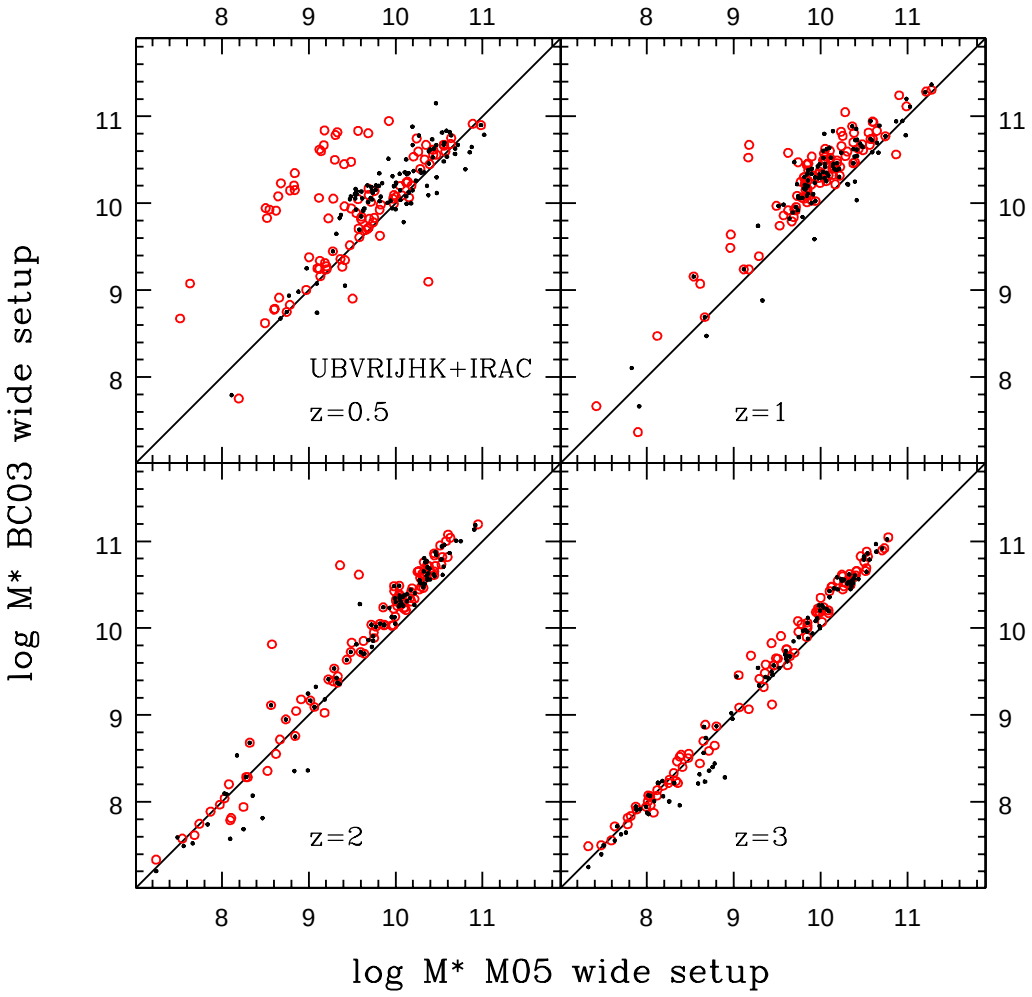

Figure B.4: Same as Fig. B.1 for the comparison of derived stellar masses. Black refers to the unreddened case, red to the case including reddening.

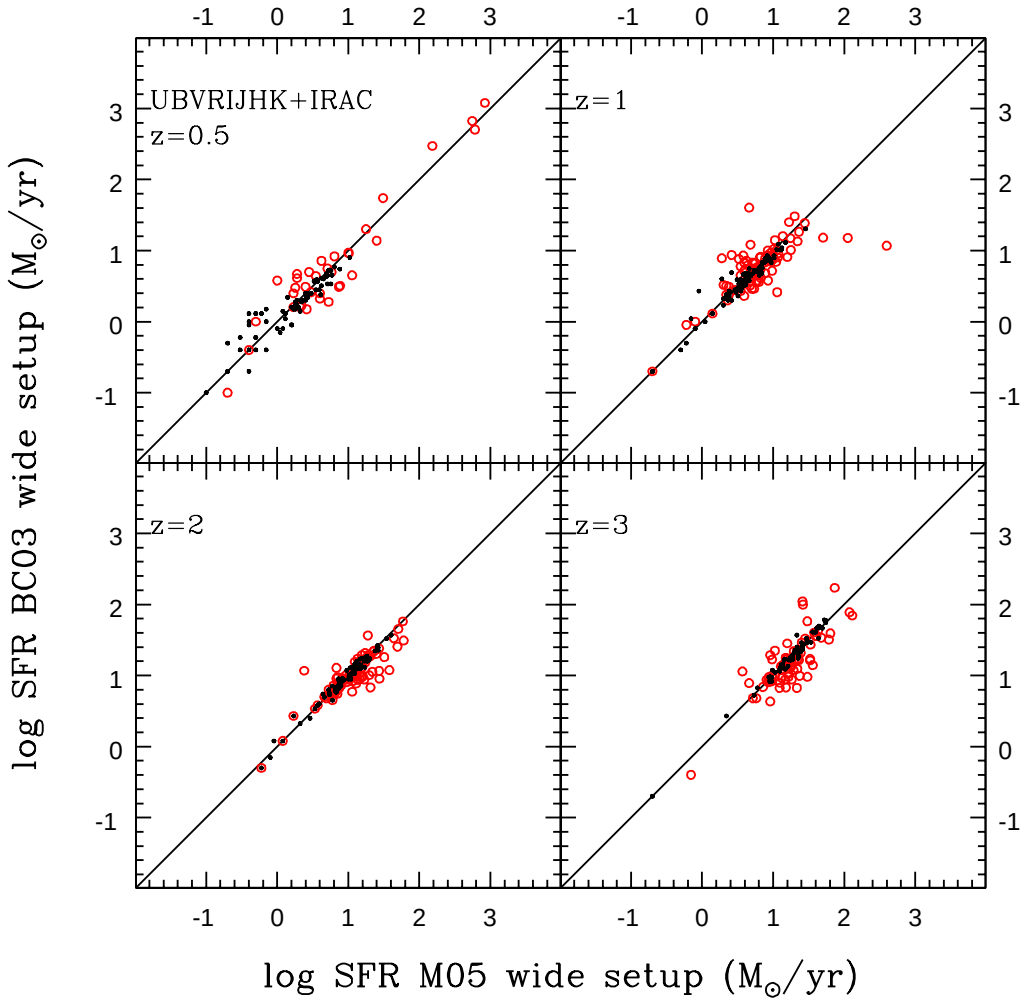

Figure B.5: Same as Fig. B.1 for the comparison of derived star formation rates. Black refers to the unreddened case, red to the case including reddening.

B.2 With redshift as a free parameter

Figs. B.6-B.11 show the results for the recovery of redshift, age, metallicity, reddening, stellar mass and SFR of M05 mock galaxies with BC03 templates when redshift is a free parameter.

Firstly, we show the redshift recovery with BC03 models for M05 galaxies in Fig. B.6. Redshifts for redshift 2 and 3 objects are similarly well recovered as with M05-based models. Redshifts for $z = 1$ objects are better recovered in the unreddened case, those of $z = 0.5$ are systematically overestimated. When reddening is included however, the

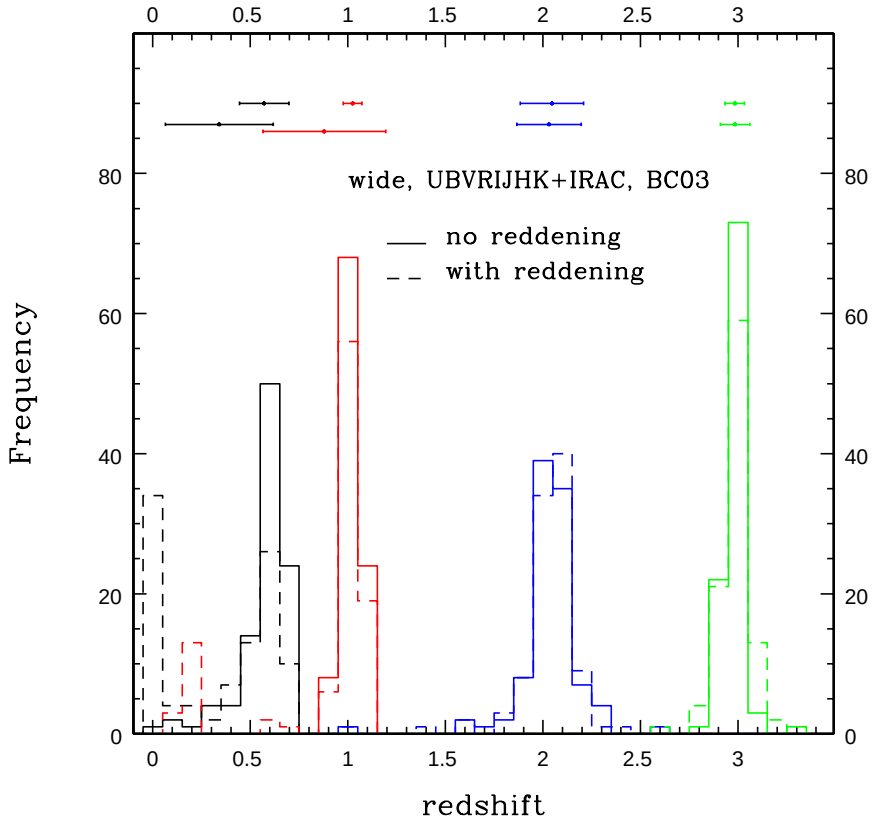

Figure B.6: Redshifts derived from SED-fitting with BC03-based templates for mock star-forming galaxies based on M05 photometry. A wide setup and wavelength coverage was used. Solid lines refer to the unreddened case, dashed lines to the case including reddening. Input redshifts are colour-coded as black for $z = 0.5$, red for $z = 1$, blue for $z = 2$ and green for $z = 3$, respectively. For each redshift we show in each panel the mean redshift and errorbars reflecting one standard deviation for the unreddened case (upper row) and for the dust reddened case (lower row).

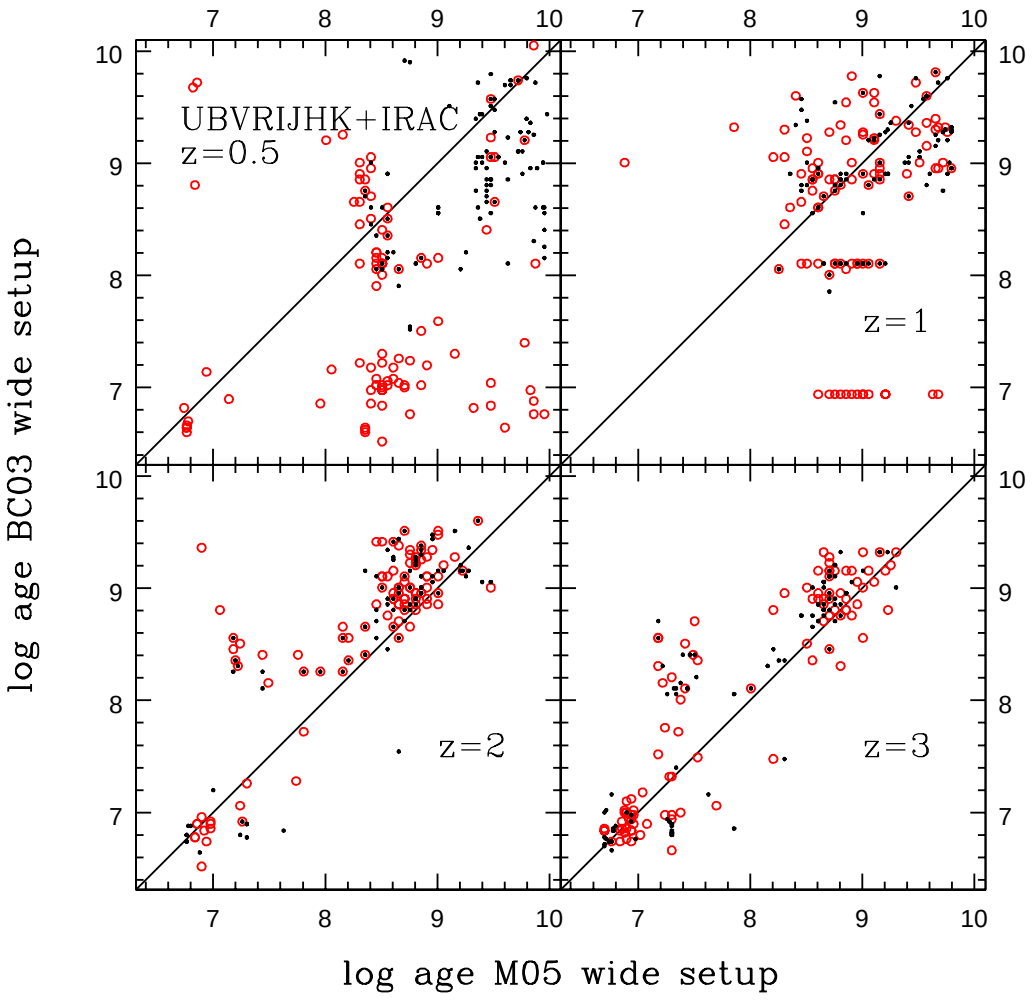

Figure B.7: Ages derived from SED-fitting when redshift is a free parameter with different stellar population synthesis models (M05 and BC03) for mock star-forming galaxies based on M05 photometry. A wide setup and wavelength coverage was used. Black refers to the unreddened case, red to the case including reddening. Fig. B.1 shows the case at fixed redshift.

number of extreme outliers increases for low redshift objects. This is due to the degeneracy between age, dust and redshift.

Fig. B.7 shows that for the lowest redshift, ages derived with BC03 templates are on average younger than those derived with M05 templates. Particularly, when reddening is included in the fit, ages from BC03 templates are very young. At $z = 1$ this is still the case for a few objects for which also the redshift recovery fails. At fixed redshift ages from BC03 templates were much older. In the unreddened case clearly the degeneracy between age and redshift has a stronger effect when the wrong stellar population model is

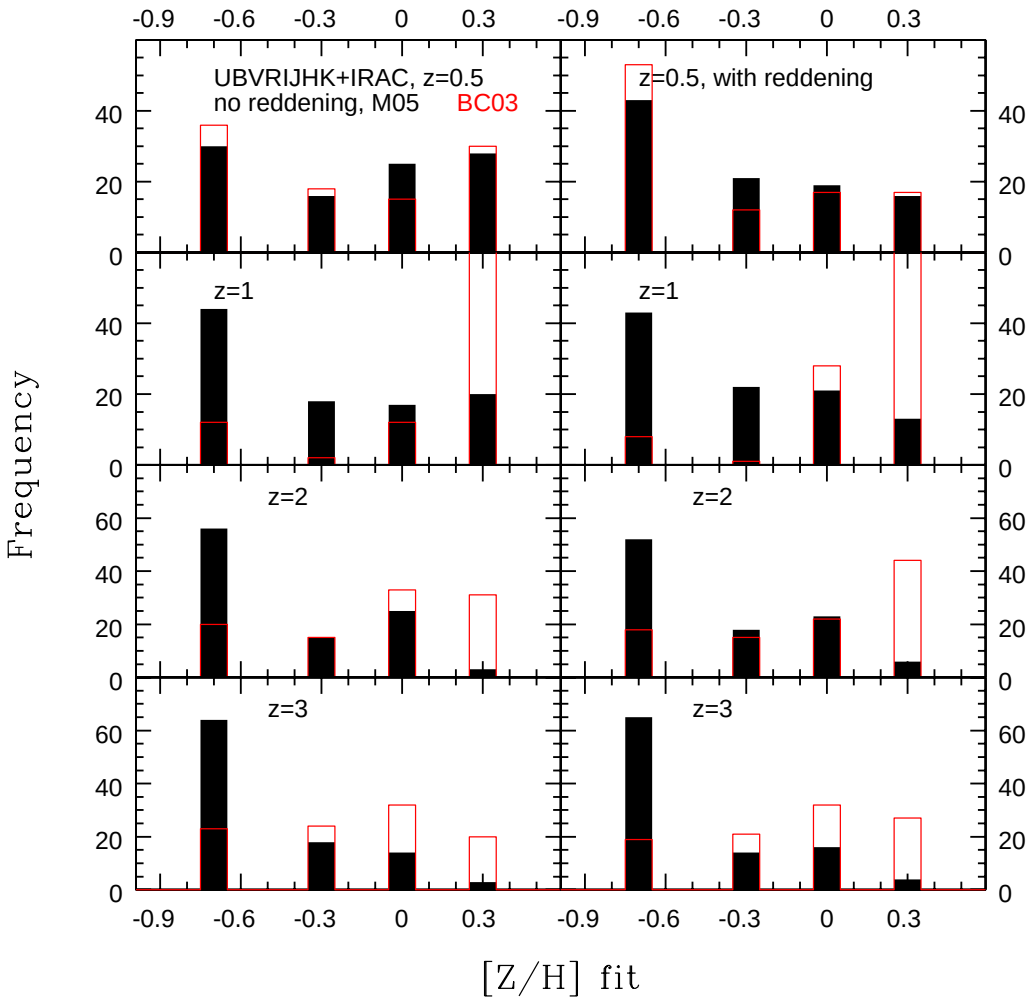

Figure B.8: Same as Fig. B.7 for the derived metallicities. Red histograms stand for BC03-based results, black shaded histograms for M05-based results. Fig. B.2 shows the case at fixed redshift.

used. As explained in the previous section BC03 models are redder than M05 models for older ages due to the different stellar tracks. This in combination with a larger redshift (especially at $z = 0.5$) requires younger ages from the fit. When reddening is included the degeneracy with dust then drives ages to even younger values and the redshift recovery fails. At higher redshift the differences between ages from BC03 and M05-based templates are similar to the case at fixed redshift, meaning ages from BC03 templates are on average older. We already explained in the previous section that this is a TP-AGB effect and for the youngest ages an effect of the different stellar tracks.

In Fig. B.8 we show the distributions of the best fit metallicities inferred from BC03 and M05 templates. Similar to the fixed redshift case fits with BC03 templates provide on

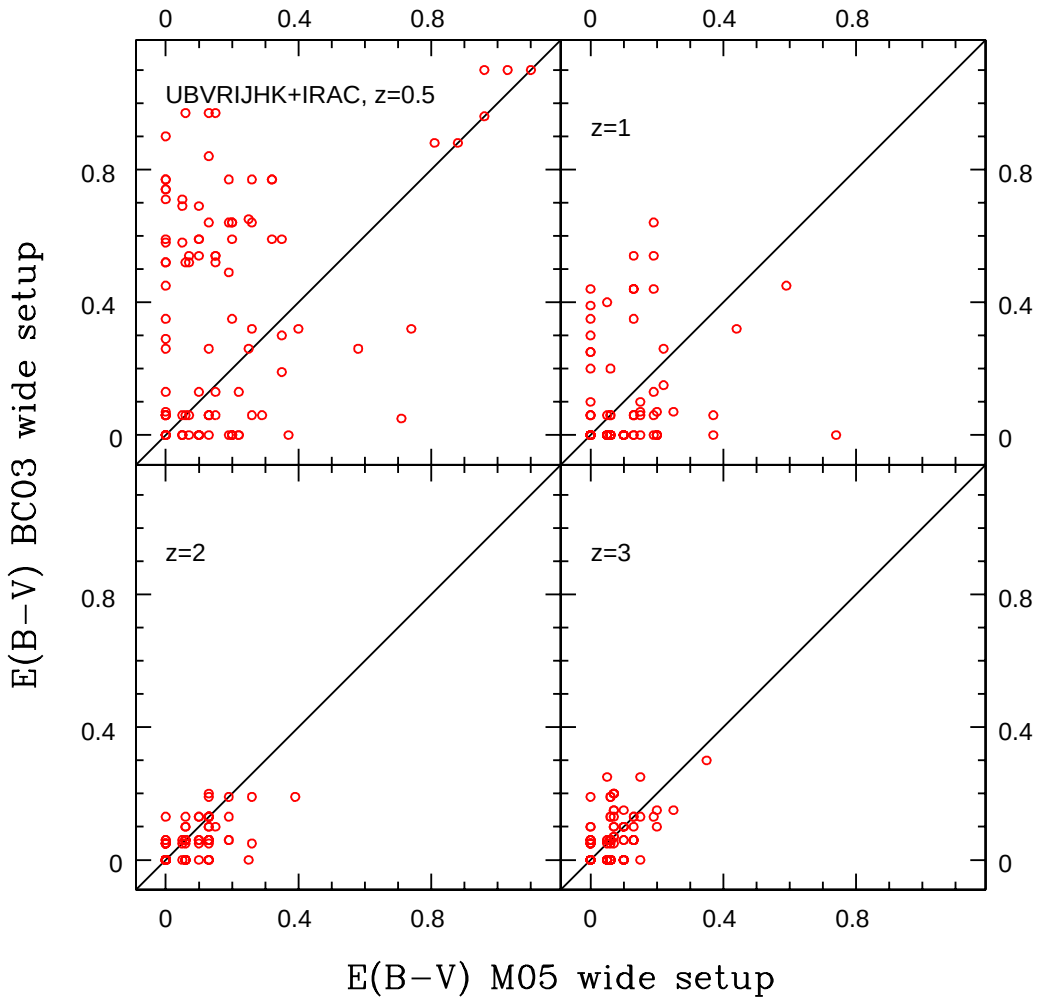

Figure B.9: Same as Fig. B.7 for the comparison of derived dust attenuation. Fig. B.3 shows the case at fixed redshift.

average metal-richer solutions. Again we find the largest differences to the fixed redshift case for the lowest redshifts. Metallicities are also higher on average compared to the fixed redshift case.

While at fixed redshift the reddening of low redshift galaxies was better estimated with BC03 templates, reddening is even more overestimated when redshift is left free (Fig. B.9) because ages and redshifts are underestimated. This again demonstrates the many degeneracies one faces at low redshift where the age range in the fitting is wide and galaxies are mainly old with only little on-going star formation. At high redshift reddening values from M05 and BC03 templates agree better and are comparable to those derived at fixed redshift.

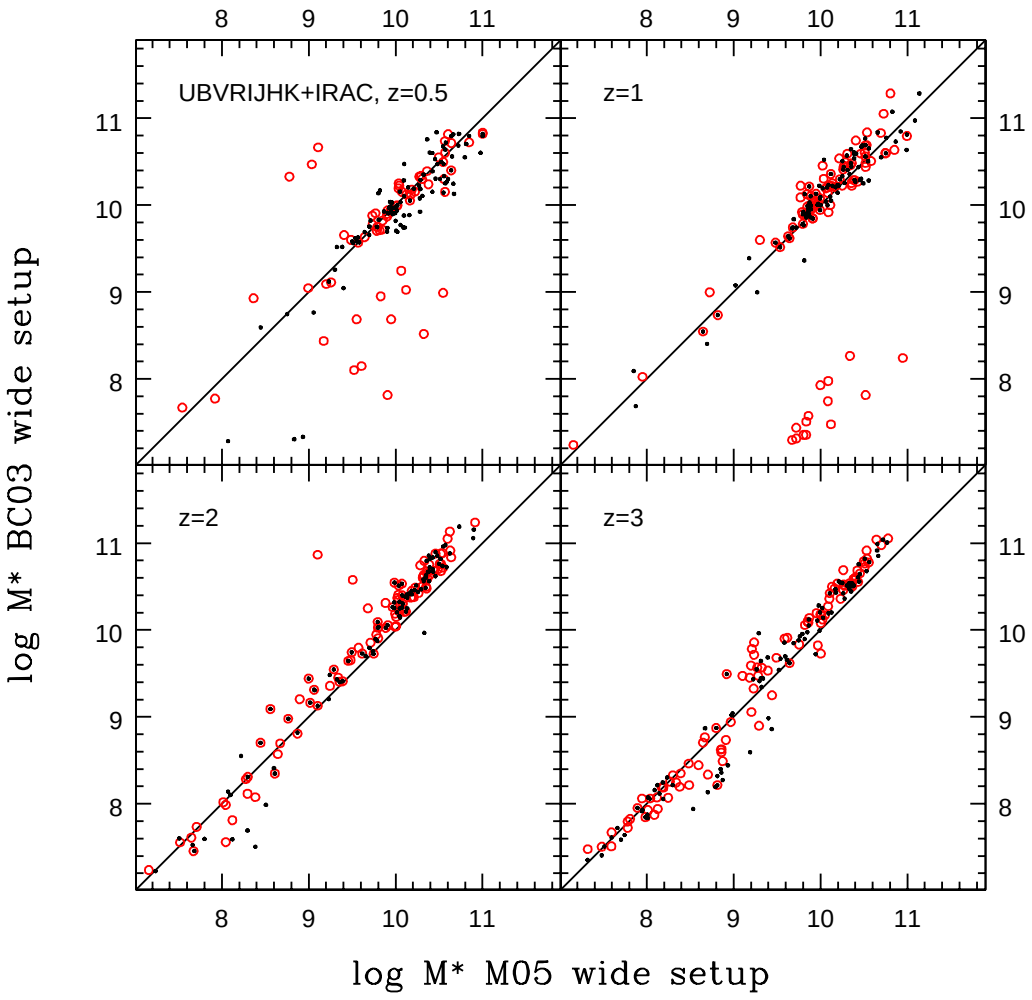

Figure B.10: Same as Fig. B.7 for the comparison of derived stellar masses. Black refers to the unreddened case, red to the case including reddening. Fig. B.4 shows the case at fixed redshift.

Masses derived with templates based on BC03 stellar population models are on average higher than M05-based masses at $z \geq 2$ which is the same as at fixed redshift albeit with slightly increased scatter. Again this is clearest for $M^* > 10^{9.5}\,M_\odot$ where the offset is on average ~ 0.2 dex. This is a TP-AGB effect. At low redshift on the other hand, masses agree much better in the unreddened case because redshift compensates differences in the stellar population model. Note that compared to the true values masses are still underestimated. However, when reddening is included we find a large offset in stellar mass for the objects for which the redshift recovery fails with BC03 templates. This again is an effect of the age-dust-redshift degeneracy which we pointed out earlier. For 34% of objects the redshift is falsely identified as being zero (compare also Fig. B.6), for these objects the mass recovery fails completely. For the remaining outliers (redshift difference ~ 0.4)

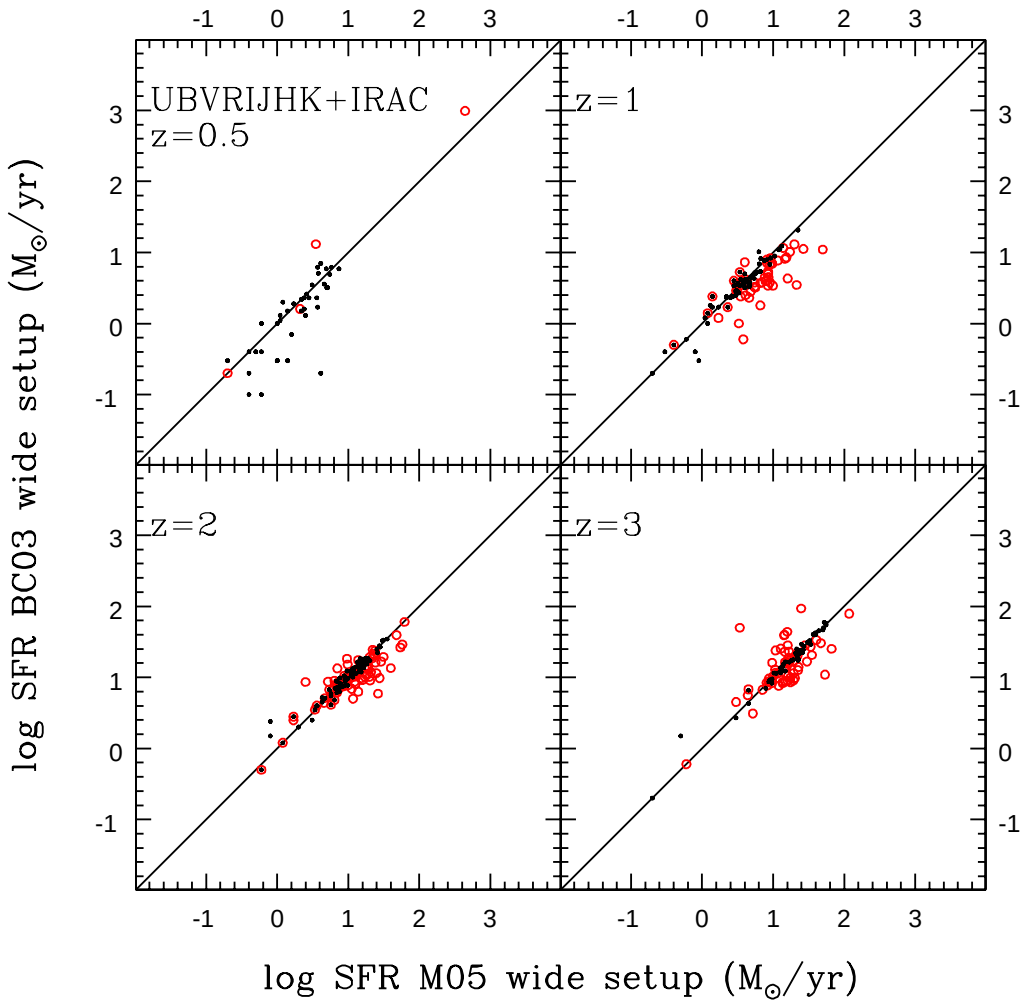

Figure B.11: Same as Fig. B.7 for the comparison of derived star formation rates. Black refers to the unreddened case, red to the case including reddening. Fig. B.5 shows the case at fixed redshift.

masses are smaller by at least 0.7 dex. At redshift 1 they are smaller by at least ~ 2.1 dex.

Finally, we show the comparison for the SFRs in Fig. B.11. At high redshift SFRs compare similarly well as in the fixed redshift case. When reddening is included, SFRs derived with BC03 models are on average lower. This is also the case at low redshift. At $z = 0.5$ most SFRs obtained with BC03 models are zero in the reddened case because of the failure in redshift and mass recovery. When redshift is fixed, SFRs agreed much better.

Appendix C

Fitting M05 and BC03 templates to Pegase-based semi-analytic galaxies

C.1 At fixed redshift

Here we investigate the reverse exercise as in Appendix B, i.e. we fit M05 or BC03 templates to semi-analytic galaxies based on the PEGASE templates (Fioc & Rocca-Volmerange, 1997). The stellar population models from PEGASE use the same stellar tracks and TP-AGB treatment as the BC03 stellar population models. Therefore, this case is similar to fitting BC03-type mock galaxies. Results are shown in Figs. C.1 - C.4.

Overall, we find the same trends as in Section 4.3, ages and stellar masses are underestimated, reddening and SFRs are overestimated.

At each redshift, M05-based templates underestimate the age more than BC03-based templates which is evident in a clear offset at $z = 2$ in Fig. C.1. BC03 templates recover the (mass and oldest SSP) age of the PEGASE galaxies similarly as M05 templates recovered the (mass-weighted and oldest SSP) age of M05 galaxies in Fig. 4.2. Note, that overall ages are not very well recovered. For M05 galaxies BC03 templates overestimate the age.

This effect is carried through to the derived stellar masses. While fitting with M05 templates leads to underestimated masses (with a clear offset), BC03 templates recover masses at high redshift very well (Fig. C.2). At low redshift masses are underestimated. Most important is that BC03 templates show the same behaviour for BC03-type galaxies as M05 templates for M05-type galaxies (compare to Fig. 4.7), meaning the mass is on average underestimated. This shows again that when fitting M05-type galaxies with

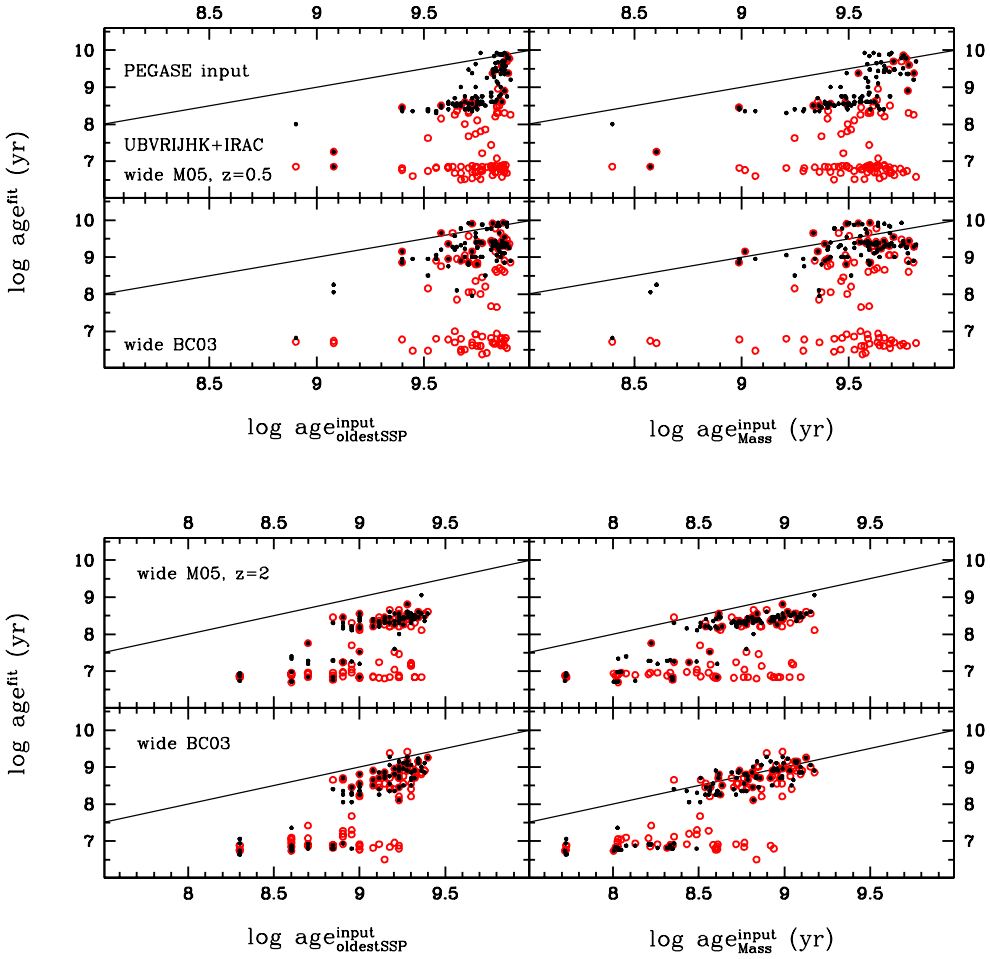

Figure C.1: Ages derived from SED-fitting with different stellar population synthesis models (M05 and BC03) for mock star-forming galaxies based on PEGASE stellar evolution as a function of the age of the oldest SSP in the galaxy (left panels) and mass-weighted ages (right panels). Shown are the cases for $z = 0.5$ (upper part) and $z = 2$ (lower part). A wide setup and wavelength coverage was used for both, M05 and BC03. Black refers to the unreddened case, red to the case including reddening.

BC03 templates the correct determination of the mass is just due to a good concatenation of compensating effects, namely the determination of an older age due to TP-AGB effects, which is by good chance similar to the age of the underlying older population.

Reddening and SFRs are comparable for M05 and BC03 templates, independently of the flavour of the input galaxies.

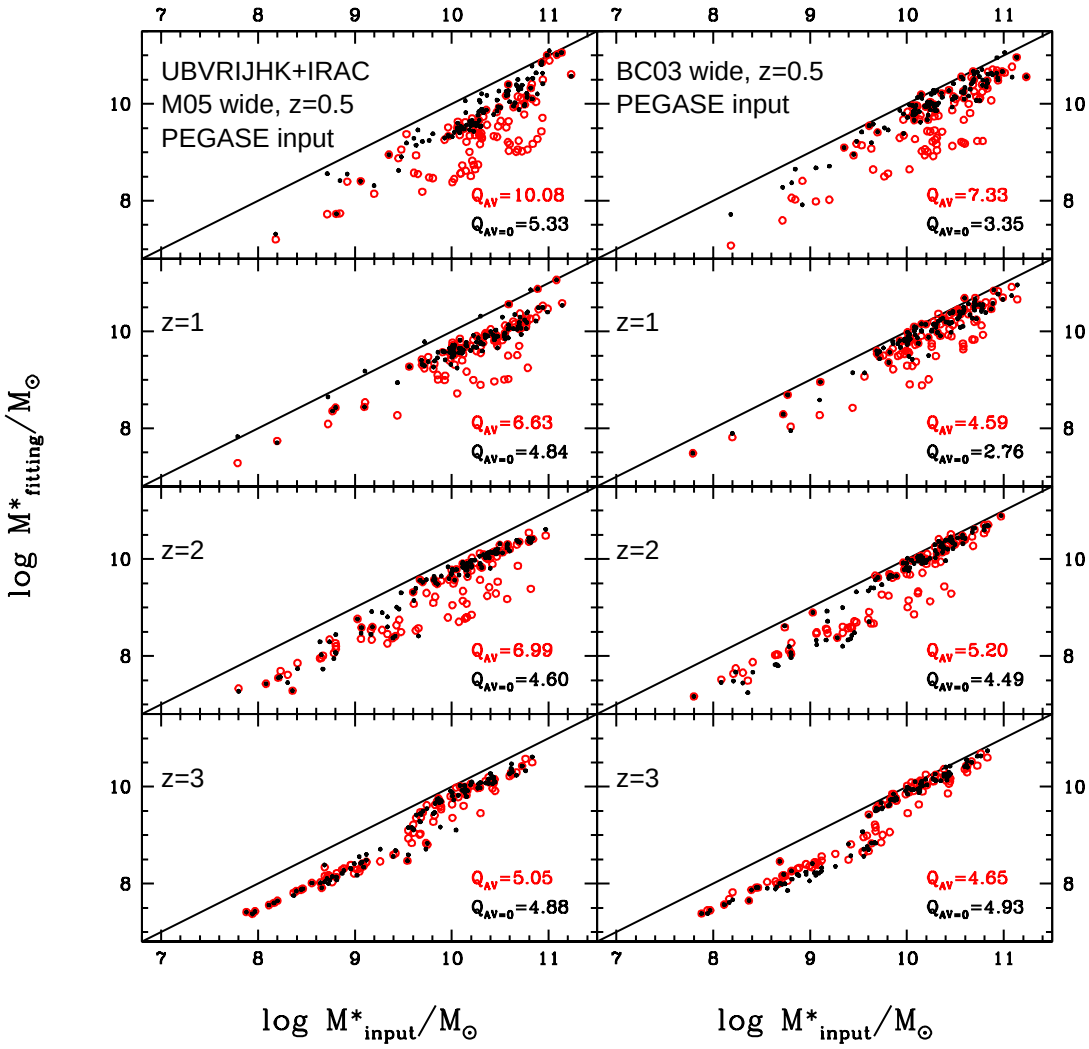

Figure C.2: Same as in Fig. C.1 for stellar masses. Quality factors are given for the entire mass range.

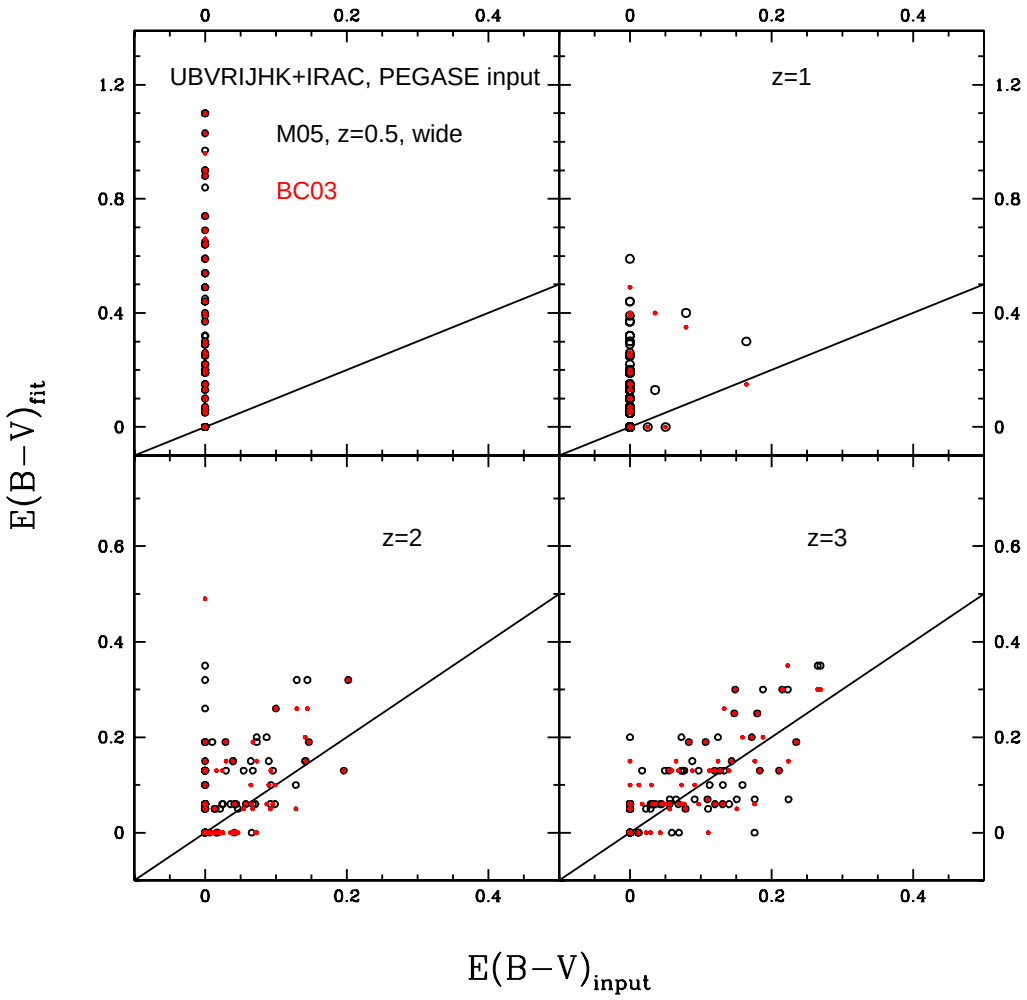

Figure C.3: Same as Fig. C.1 for the comparison of derived dust attenuation when mock star-forming galaxies are based on PEGASE models. Red dots show results derived with BC03-based templates in the fitting, black those with M05-based templates.

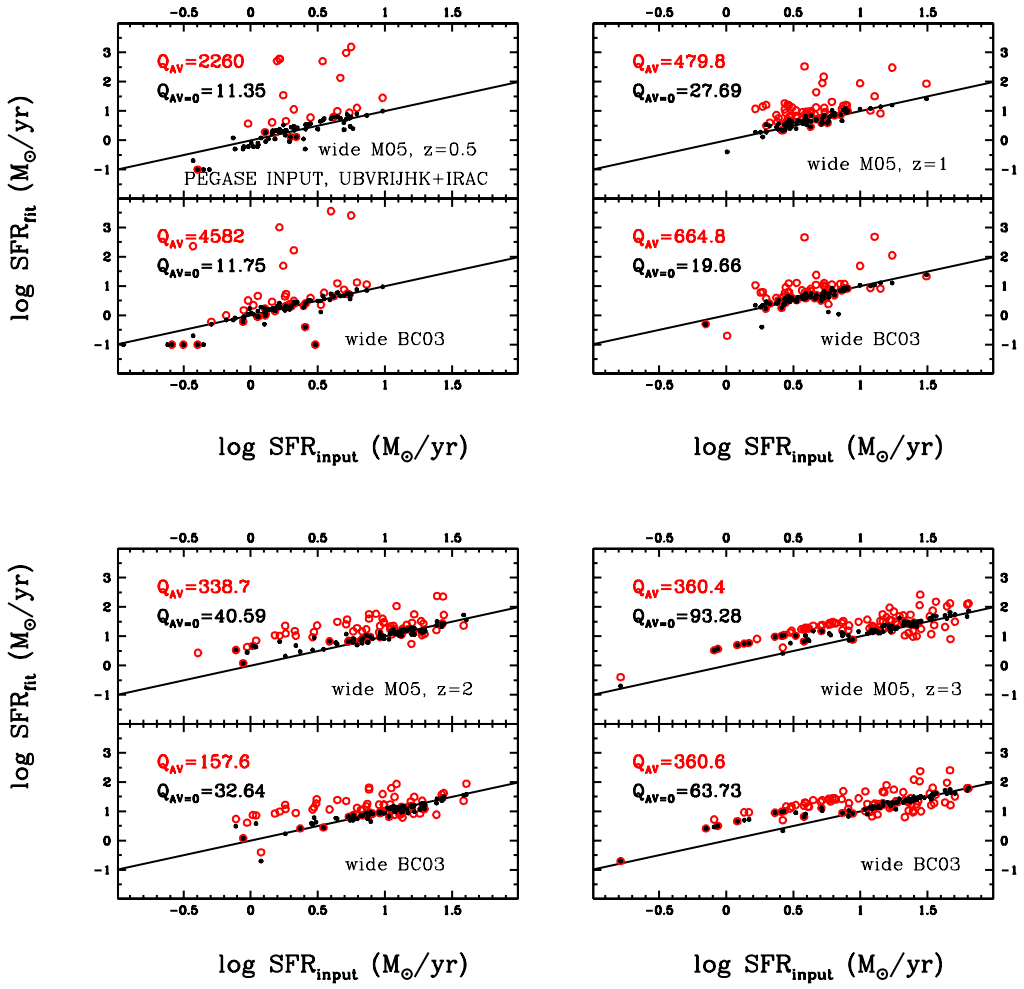

Figure C.4: Same as Fig. C.2 for the comparison of derived star formation rates.

C.2 With redshift as a free parameter

As in Appendix B we also studied the case in which redshift is left free in the fit when we fit M05 or BC03 templates to semi-analytic galaxies based on PEGASE templates (Fioc & Rocca-Volmerange, 1997). Figs. C.5 - C.9 show the results. Overall, we find the same trends as in Section C.1, ages and stellar masses are underestimated, reddening and SFRs are overestimated.

First, we study the redshift recovery in Fig. C.5. Apart from the highest redshift galaxies, the redshift is recovered worse on average than when mock star-forming galaxies are based on M05 models, independently of the stellar population model of the templates that are used in the fit. Particularly, for $z \leq 2$ redshift recoveries show a much wider distribution because the chosen filter set comprises the 4000 Å break but not the Lyman break. Interestingly, it seems that using the M05 templates in the fitting provides overall

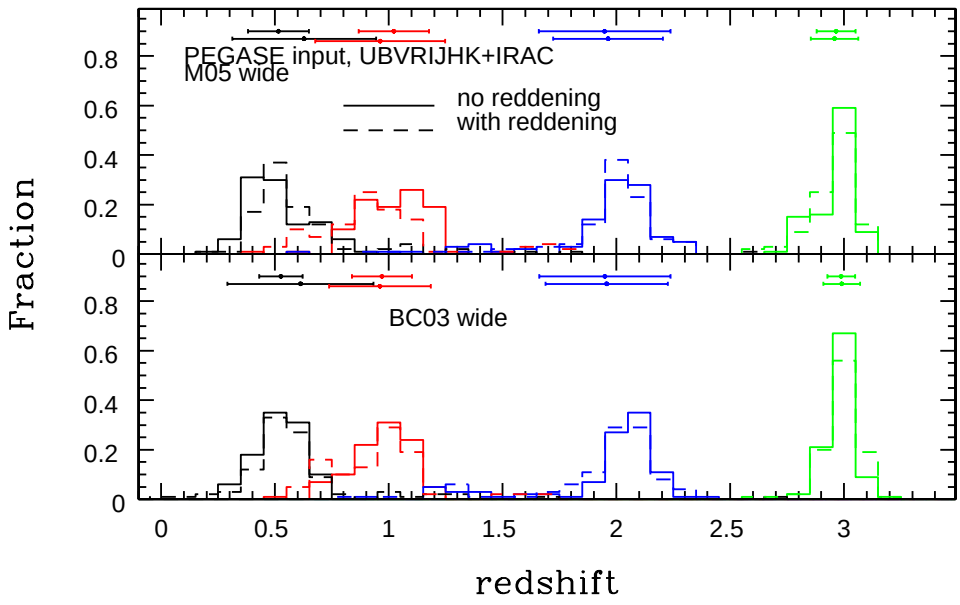

Figure C.5: Redshifts derived from SED-fitting with different stellar population models - M05 (top) and BC03 (bottom) - for mock star-forming galaxies based on PEGASE photometry. A wide setup and wavelength coverage was used. Solid lines refer to the unreddened case, dashed lines to the case including reddening. Input redshifts are colour-coded as black for $z = 0.5$, red for $z = 1$, blue for $z = 2$ and green for $z = 3$, respectively. For each redshift we show in the mean redshift and errorbars reflecting one standard deviation for the unreddened case (upper row) and for the dust reddened case (lower row).

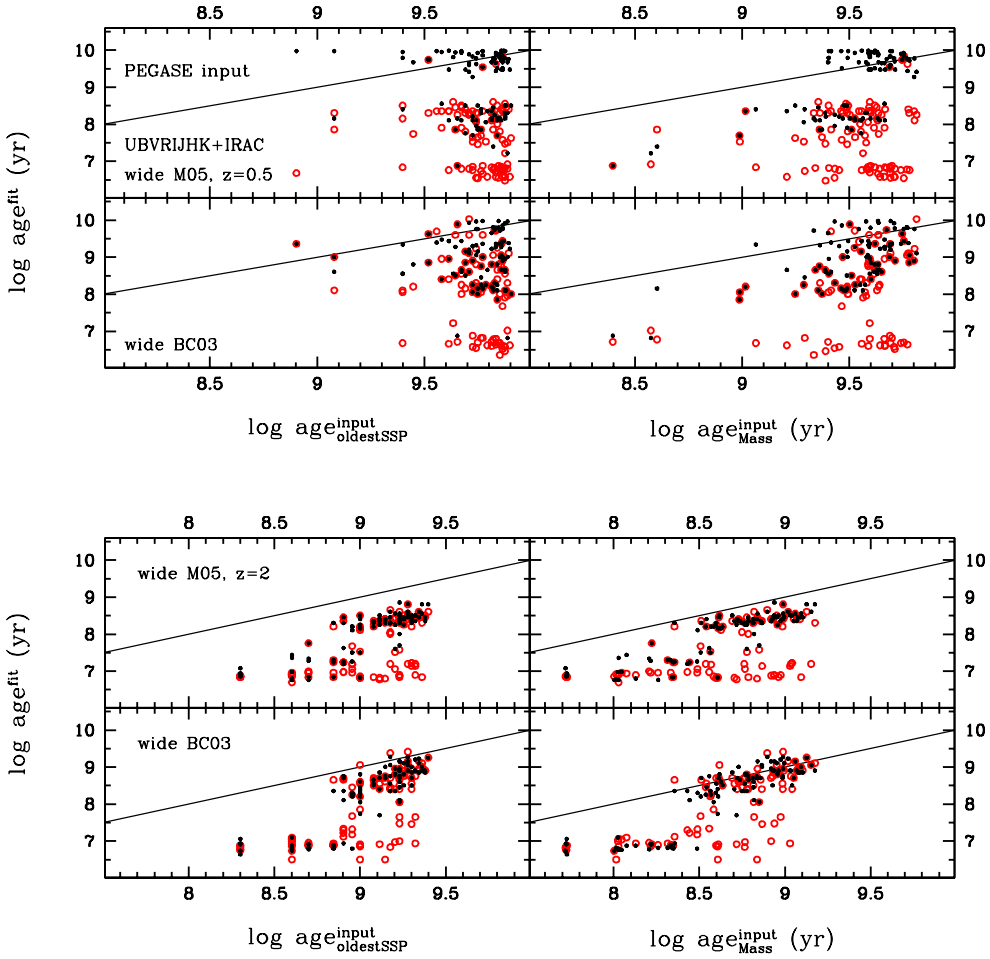

Figure C.6: Age recovery with M05- and BC03-based templates (top and bottom in each panel) for mock star-forming galaxies based on PEGASE photometry when redshift is a free parameter in the fit. A wide setup and wavelength coverage was used. Black refers to the unreddened case, red to the case including reddening. *Left:* Comparison to the age of the oldest SSP present. *Right:* mass-weighted ages. Fig. C.1 shows the case at fixed redshift.

a better photometric redshift determination independently of the real stellar evolution. We had seen in Appendix B that the redshift recovery is significantly worse with BC03 templates on M05 galaxies, especially at low redshift.

Clearly, age is the compensating factor. Fig. C.6 shows that ages derived with M05 models in the unreddenend case at low redshift are either very old (> 3 Gyr) or young (< 300 Myr), i.e. the age range for the TP-AGB is avoided. This distinction is clearer than at fixed redshift where ages from M05 templates were mostly younger than those derived with BC03 templates. When redshift is free older ages are paired with lower redshifts

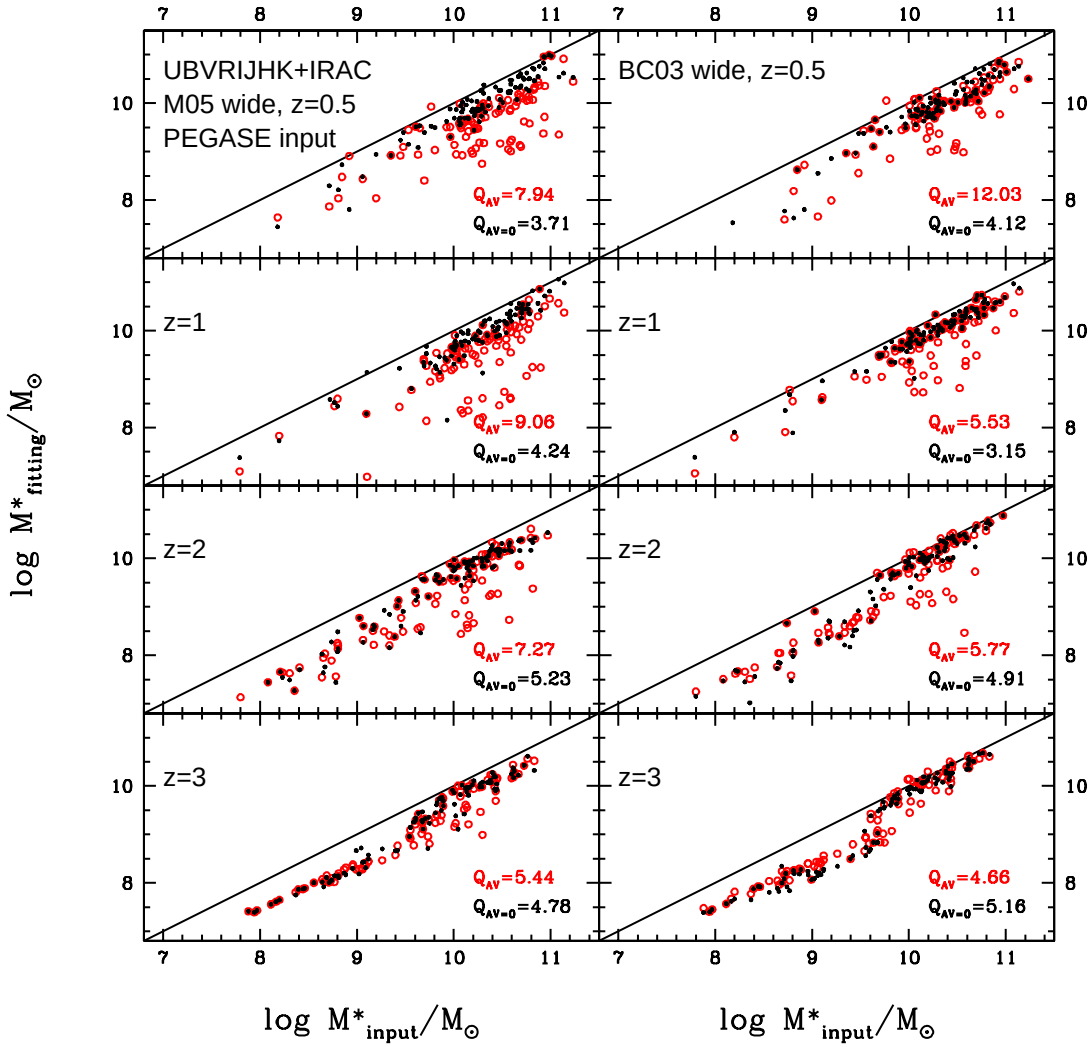

Figure C.7: Stellar mass recovery as a function of stellar population model (M05 and BC03 from left to right) or mock star-forming galaxies based on PEGASE photometry when redshift is left free. Red symbols refer to the reddened case, black to the unreddened case. A wide setup and a UBVRIJHK+IRAC wavelength coverage was used. Redshift increases from top to bottom. Quality factors refer to the entire mass range. Fig. C.2 shows the mass recovery at fixed redshift.

and vice versa to compensate. Ages inferred from BC03 templates are generally younger than at fixed redshift. When reddening is included, the age-dust degeneracy dominates, driving the fit towards very young ages for both template setups. For M05 nearly all ages are below 300 Myr in this case. At high redshift derived ages are very similar to the fixed redshift case. Ages derived with M05 templates are clearly younger than those derived with BC03 templates and therefore show a clear offset to the oldest and mass-weighted ages. This is the same effect which causes overestimated ages from BC03 templates for

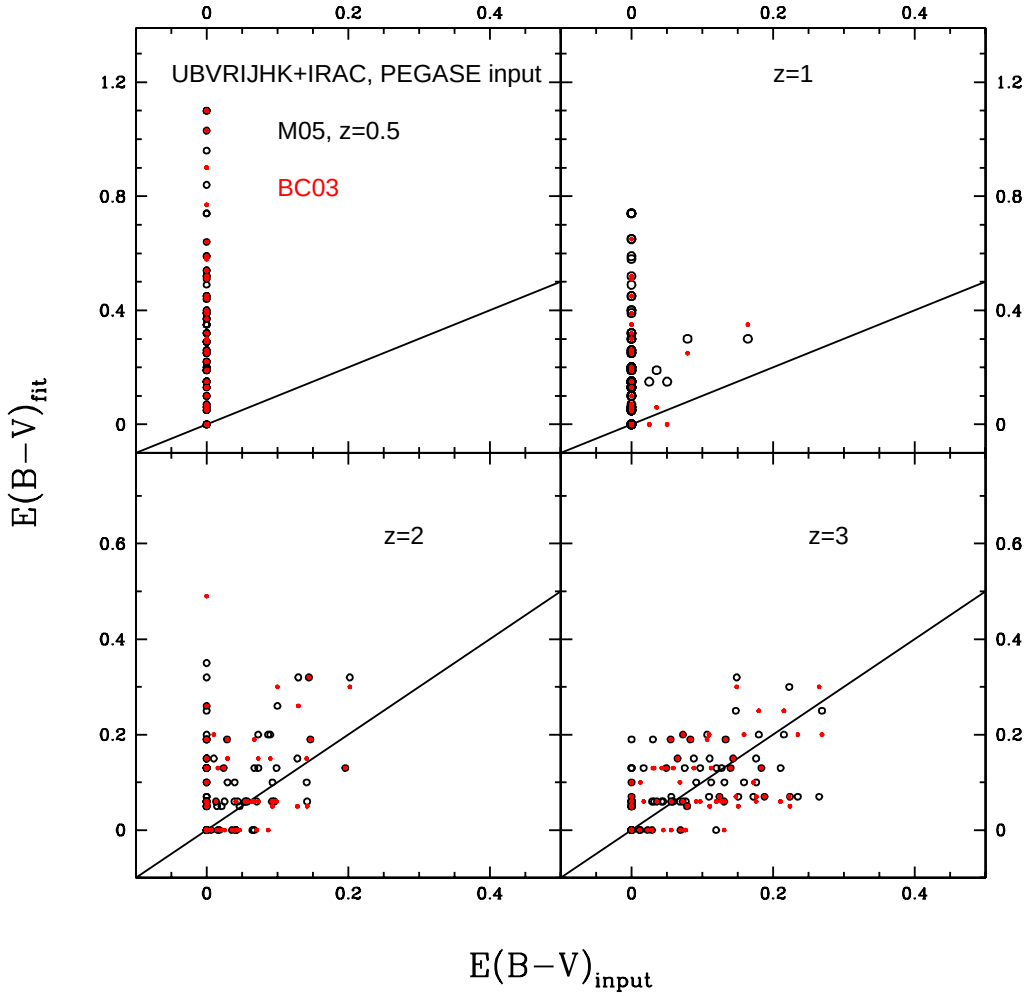

Figure C.8: Recovered $E(B-V)$ when M05 (black) and BC03 (red) templates are used to fit mock star-forming galaxies based on PEGASE photometry and redshift is a free parameter in the fit. Fig. C.3 shows the fixed redshift case.

M05 galaxies.

As shown in Section 5.3 the stellar mass recovery profits from the additional degree of freedom in the fit introduced by leaving the redshift free. This is also the case when BC03-type mock star-forming galaxies are fit with M05 and BC03 templates (Fig. C.7), particularly at low redshift. While at fixed redshift masses derived with M05 templates were underestimated on average by ~ 0.5 dex in the unreddened case (compare Fig. C.2) they are underestimated on average only by ~ 0.25 dex when redshift is left free. For masses derived with BC03 templates the effect is very small instead. Including reddening in the fit worsens the result because of the age-dust degeneracy. This is similar to the case at fixed redshift and true for both stellar population models. It is worth to note that when

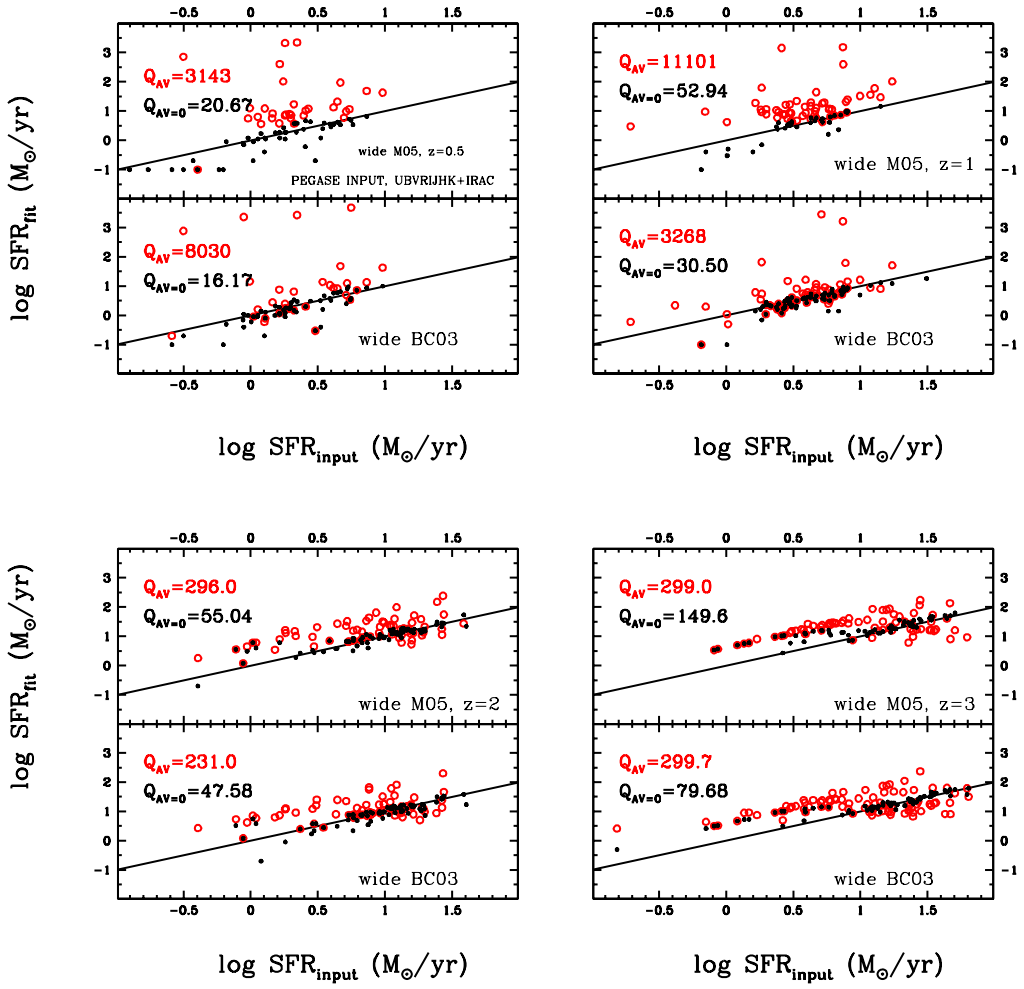

Figure C.9: Star formation rate recovery as a function of stellar population model for mock star-forming galaxies based on PEGASE photometry (M05 and BC03, top and bottom in each panel) when redshift is a free parameter in the fit. Red symbols refer to the reddened case, black to the unreddened case. A wide setup and a UBVRIJHK+IRAC wavelength coverage was used. Redshift increases from top left to bottom right. Quality factors refer to the entire SFR range. Fig. C.4 shows the case at fixed redshift.

reddening is included masses derived with M05 still show the same systematic offset as in the fixed redshift case.

The reddening determination is comparable for M05 and BC03 templates, independently of the flavour of the input galaxies (Fig. C.8). This is similar to the fixed redshift case. However, at low redshift both stellar population models require somewhat less reddening

when redshift is free because redshift compensates.

Finally, we show the SFR recovery of BC03-type galaxies with M05 and BC03 templates when redshift is free in Fig. C.9. When reddening is excluded from the fit SFRs are generally well recovered, although at low redshift many of them are underestimated. With reddening in the fit SFRs are even more overestimated at low redshift than at fixed low redshift (compare Fig. C.4). At high redshift SFRs are overestimated for SFR$<$ $10\,M_{\odot}$/yr and recovered well for SFRs larger than $10\,M_{\odot}$. This is equivalent to our results at fixed redshift.

Appendix D

Comparison to Wuyts et al 2009

D.1 At fixed redshift

In Chapter 4 we studied the dependence of the derivation of stellar population properties from SED-fitting on the fitting parameters using mock galaxies. We compared our results with those of Wuyts et al. (2009) who carried out a similar exercise but using mock galaxies based on a different stellar population model. For a direct comparison with Wuyts et al. (2009) we show here our version of their Fig. 8 in which we swapped the A_V row with a row showing the metallicity (Fig. D.1). We also list median values with 68% confidence levels of the difference between derived and true age, mass, SFR and $E(B-V)$, together with those of Wuyts et al. (2009) in Table D.1.

Table D.1: Comparison of our SED-fitting performance for age, reddening, stellar mass and SFR with Wuyts et al. (2009). We list the median (Δ_m) values of Δ with their 68% intervals, respectively, for mock star-forming galaxies for 3 setups: 1) a wide setup with UBVRIJHK+IRAC filter bands in the reddening case, 2) same as 1) with a minimum age of 0.1 Gyr, 3) inverted-τ at $z = 2$ (age fixed to 2 Gyr) and $z = 3$ (age fixed to 1.1 Gyr). For mock passive galaxies we list only the cases for the wide setup. Values of Wuyts et al. are medians with 68% intervals. Δ is defined as the difference between recovered and true value. For stellar mass, age and SFR the logarithmic values are used. The true age for the mock star-forming galaxies is represented by the mass-weighted age. For inverted-τ models we compare to the oldest age. Ages from Wuyts et. al. refer to mass-weighted ages. Negative values of Δ mean underestimation of the according property, positive values stand for overestimation. In cases in which either true or best-fit SFR equal zero, we adopt a dummy value of $0.001\ M_{\odot}$/yr to be able to express them in logarithm.

Setup/literature	$\Delta_m log\, age$	$\Delta_m E(B-V)$	$\Delta_m log\, M^*$	$\Delta_m log\, SFR$
Wuyts+ disk	$0.03^{+0.19}_{-0.42}$	$-0.02^{+0.13}_{-0.07}$	$-0.06^{+0.06}_{-0.14}$	$-0.22^{+0.23}_{-0.28}$
Wuyts+ merger	$-0.12^{+0.40}_{-0.26}$	$-0.02^{+0.08}_{-0.08}$	$-0.13^{+0.10}_{-0.14}$	$-0.44^{+0.32}_{-0.31}$
Wuyts+ spheroid	$-0.03^{+0.12}_{-0.14}$	$-0.03^{+0.11}_{-0.07}$	$-0.02^{+0.06}_{-0.11}$	$-0.23^{+0.62}_{-0.47}$
mock star-forming with reddening				
wide setup				
$z = 1$	$-0.35^{+0.45}_{-0.64}$	$0.05^{+0.14}_{-0.05}$	$-0.22^{+0.21}_{-0.22}$	$0.11^{+0.29}_{-0.43}$
$z = 2$	$-0.15^{+0.29}_{-0.73}$	$0.00^{+0.06}_{-0.01}$	$-0.12^{+0.09}_{-0.39}$	$0.06^{+0.39}_{-0.41}$
$z = 3$	$-0.12^{+0.34}_{-0.83}$	$0.02^{+0.04}_{-0.05}$	$-0.15^{+0.12}_{-0.43}$	$0.11^{+0.53}_{-0.78}$
wide, age ≥ 0.1 Gyr				
$z = 1$	$-0.33^{+0.43}_{-0.49}$	$0.05^{+0.10}_{-0.05}$	$-0.22^{+0.21}_{-0.20}$	$0.15^{+0.27}_{-0.32}$
$z = 2$	$-0.03^{+0.22}_{-0.28}$	$0.00^{+0.05}_{-0.01}$	$-0.11^{+0.08}_{-0.10}$	$0.06^{+0.14}_{-0.16}$
$z = 3$	$0.09^{+0.27}_{-0.21}$	$0.00^{+0.04}_{-0.04}$	$-0.11^{+0.08}_{-0.11}$	$-0.02^{+0.16}_{-0.25}$
inverted-τ				
$z = 2$	$0.19^{+0.41}_{-0.19}$	$0.01^{+0.09}_{-0.01}$	$0.01^{+0.05}_{-0.06}$	$0.17^{+0.23}_{-0.20}$
$z = 3$	$0.26^{+0.30}_{-0.26}$	$0.00^{+0.05}_{-0.04}$	$0.02^{+0.05}_{-0.06}$	$-0.04^{+0.33}_{-0.29}$
mock passive no reddening				
wide				
$z = 0.5$	$0.03^{+0.12}_{-0.05}$	-	$0.01^{+0.04}_{-0.05}$	$0.00^{+0.00}_{-0.00}$
$z = 1$	$0.02^{+0.04}_{-0.02}$	-	$0.00^{+0.02}_{-0.01}$	$0.00^{+0.00}_{-0.00}$
with reddening				
wide				
$z = 0.5$	$0.02^{+0.10}_{-0.11}$	$0.00^{+0.07}_{-0.00}$	$0.01^{+0.07}_{-0.08}$	$0.00^{+0.00}_{-0.00}$
$z = 1$	$0.02^{+0.03}_{-0.02}$	$0.00^{+0.00}_{-0.00}$	$0.01^{+0.02}_{-0.02}$	$0.00^{+0.00}_{-0.00}$

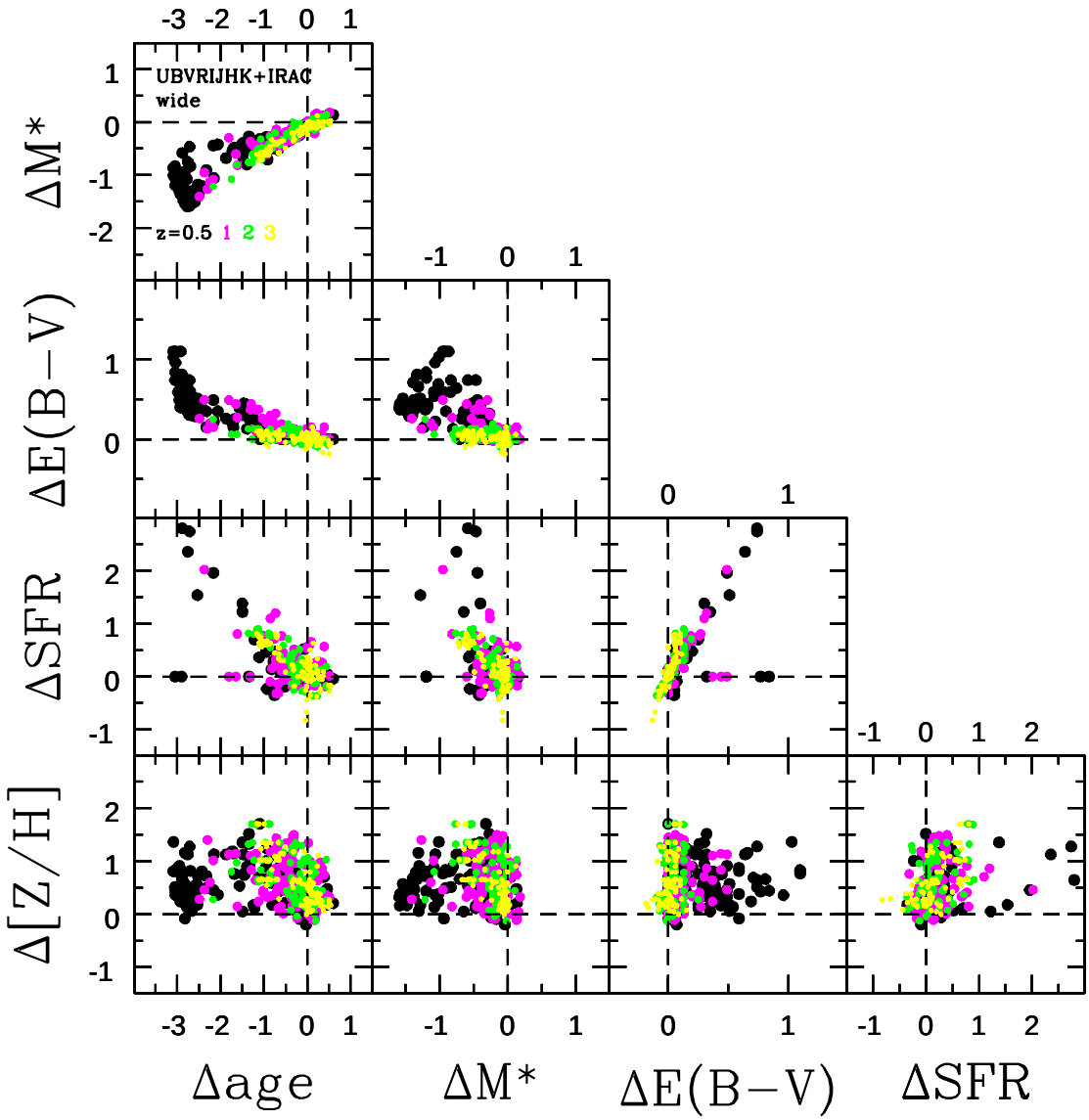

Figure D.1: Basic correlations between age, dust reddening, stellar mass and SFR derived from SED-fitting using a wide setup and a wavelength coverage of UBVRIJHK+IRAC bands in the reddened case. Δ is the difference between estimated and true quantity. For stellar mass, age and SFR we used the logarithmic values. The true age for the mock galaxies is represented by the mass-weighted age. Negative values of Δ mean underestimation, positive values stand for overestimation. We show objects at $z = 0.5$ in black, at $z = 1$ in magenta, $z = 2$ in green and at $z = 3$ in yellow. – Reproduced from Wuyts et al. (2009) with added metallicity row and omitted A_V row.

D.2 Free redshift case

We reproduced Fig. D.1 also for the case in which redshift is left free in the fit. Accordingly we added a column showing the correlation of offsets in metallicity, SFR, $E(B-V)$, stellar mass and mass-weighted age with offsets in redshift. The results are shown in Fig. D.2. We list median values with 68% confidence levels of the difference between derived and true redshift, age, mass, SFR and E(B-V) in Table D.2.

Overall, we find a weak correlation between redshift and stellar mass such that when redshift is underestimated, stellar mass is underestimated, too. For all other properties correlations with redshift are even weaker because of the many degeneracies, e.g. redshifts and ages are underestimated when reddening is overestimated because they are degenerate. Median offsets for the stellar mass, age, reddening and SFR of mock galaxies are similar to the fixed redshift case.

Table D.2: SED-fitting performance for age, reddening, stellar mass and SFR when redshift is a free parameter. As in Table D.1 we list the median (Δ_m) values of Δ with their 68% intervals, respectively, for mock star-forming galaxies. Setups and definitions are the same as in Table D.1. For mock passive galaxies we list only the cases for the wide setup and no reddening in the fitting.

Setup	$\Delta_m z$	$\Delta_m log\, age$	$\Delta_m E(B-V)$	$\Delta_m log\, M^*$	$\Delta_m log\, SFR$
star-forming					
wide setup					
$z=1$	$-0.02^{+0.08}_{-0.08}$	$-0.16^{+0.32}_{-0.67}$	$0.05^{+0.14}_{-0.05}$	$-0.19^{+0.13}_{-0.16}$	$0.10^{+0.28}_{-0.31}$
$z=2$	$-0.06^{+0.10}_{-0.11}$	$-0.17^{+0.25}_{-0.72}$	$0.00^{+0.13}_{-0.02}$	$-0.11^{+0.09}_{-0.39}$	$0.11^{+0.40}_{-0.46}$
$z=3$	$-0.01^{+0.07}_{-0.12}$	$-0.55^{+0.80}_{-0.40}$	$0.00^{+0.06}_{-0.07}$	$-0.23^{+0.21}_{-0.32}$	$-0.04^{+0.69}_{-3.83}$
wide setup					
age ≥ 0.1 Gyr					
$z=1$	$-0.02^{+0.08}_{-0.08}$	$-0.16^{+0.32}_{-0.67}$	$0.05^{+0.14}_{-0.05}$	$-0.19^{+0.13}_{-0.16}$	$0.10^{+0.28}_{-0.31}$
$z=2$	$-0.06^{+0.09}_{-0.11}$	$-0.06^{+0.19}_{-0.25}$	$0.00^{+0.06}_{-0.02}$	$-0.09^{+0.08}_{-0.19}$	$0.08^{+0.16}_{-0.36}$
$z=3$	$-0.01^{+0.07}_{-0.15}$	$0.12^{+0.28}_{-0.18}$	$0.00^{+0.06}_{-0.03}$	$-0.12^{+0.10}_{-0.18}$	$-0.06^{+0.17}_{-2.13}$
passive					
wide setup					
$z=0.5$	$0.00^{+0.01}_{-0.05}$	$0.04^{+0.10}_{-0.11}$		$0.05^{+0.30}_{-0.04}$	
$z=1$	$0.00^{+0.05}_{-0.01}$	$0.02^{+0.03}_{-0.10}$		$0.00^{+0.03}_{-0.05}$	

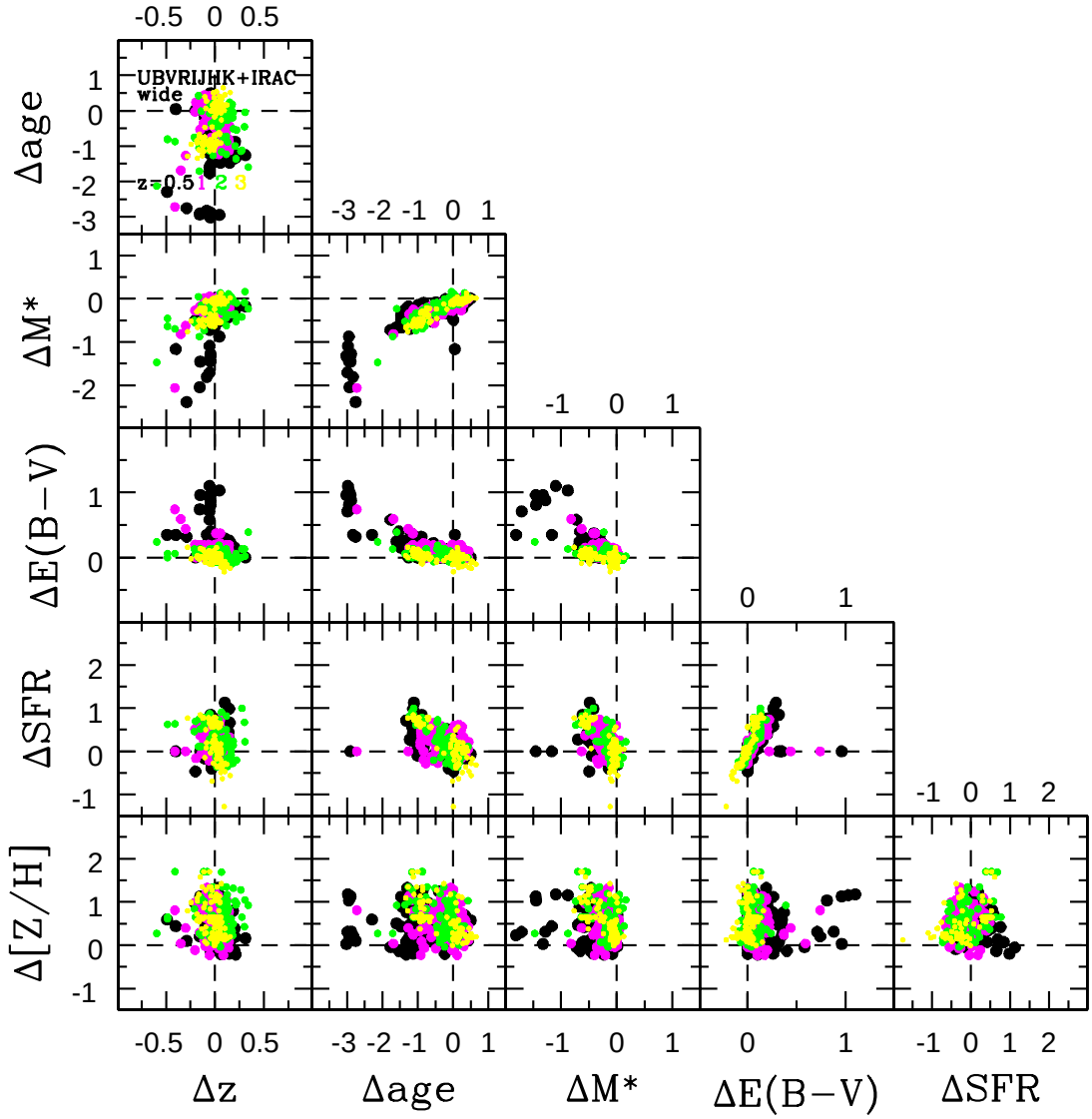

Figure D.2: Basic correlations between redshift, age, dust reddening, stellar mass and SFR derived from SED-fitting using a wide setup and a wavelength coverage of UBVRI-JHK+IRAC bands in the reddened case. Definitions and symbols are the same as in Fig. D.1.

Appendix E

Importance of the SFH code

In order to test the dependence of our results on the SFH code we compare the stellar population properties obtained by using composite stellar population models created with different codes. Composite models are based on the M05 stellar population models. The BC03-routine *csp_galaxev* is only used to add the SFH. Likewise we use composite models calculated with the M05-code. Fig. E.1 shows the differences in flux at various ages between the two versions of a composite stellar population model with an exponentially declining SFH of $\tau = 1$ Gyr, solar metallicity and Salpeter IMF. Clearly, the two SFH codes produce different results, particularly in the rest-frame UV and optical wavelength ranges. These must be due to the different interpolation routines and checks for numerical stability. Although the absolute differences might seem relatively small, M09 and Maraston & Strömbäck (2011b, *in. press*) showed that even such small differences can play an important role for the determination of galaxy colours. In Figs. E.2-E.4 the effect on the stellar population properties become apparent. Fig. E.2 compares the best fit ages as a function of redshift. Differences are larger at lower redshift, independently of dust reddening. The reason for this lies in the larger age range that is available in the fitting and a stronger influence of the age-dust-degeneracy when dust reddening is included. Accordingly, in Fig. E.3 we illustrate the dependence of the obtained dust reddening on the SFH code. Again, the largest differences are found at low redshift. Overall, the reddening agrees reasonably well for models created with the two codes. The same picture is evident in the stellar masses (Fig. E.4). At redshift 0.5 masses can differ up to 0.5 dex independently of dust reddening. At high redshift the effect on the stellar masses is very small and negligible in comparison to effects from metallicity, star formation histories and wavelength coverage.

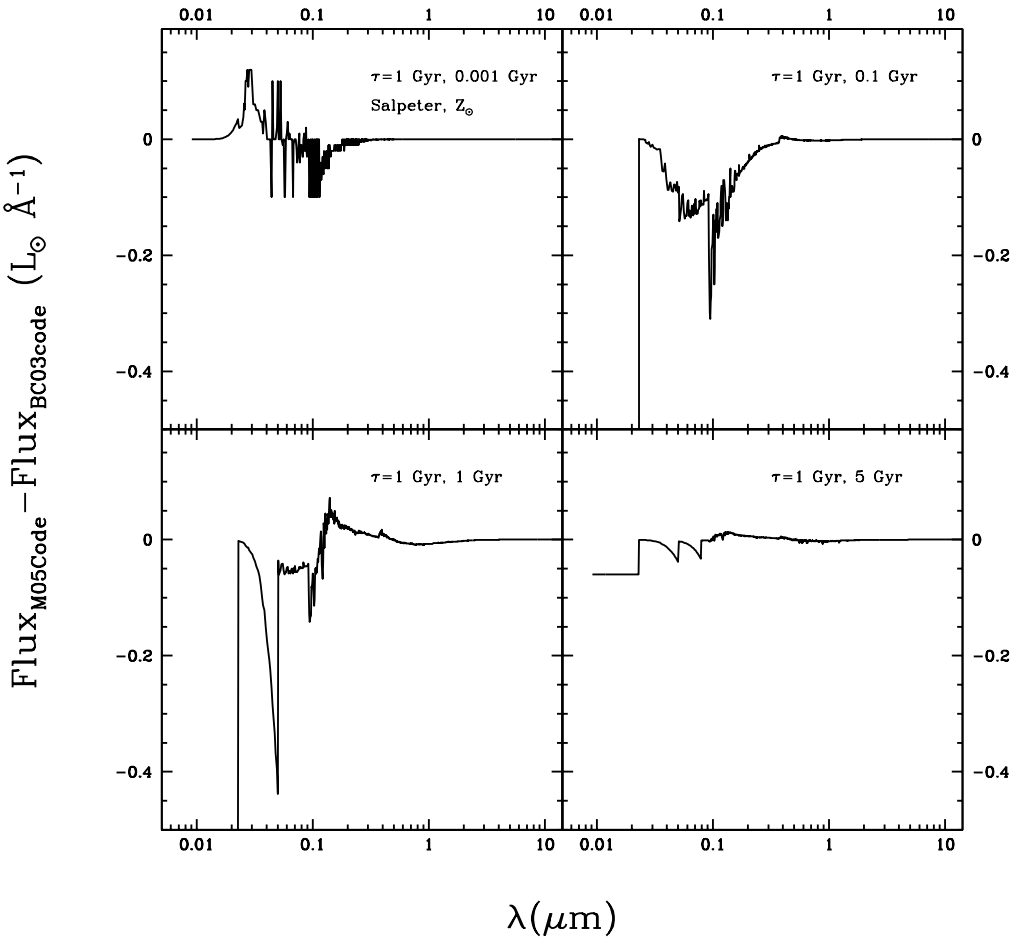

Figure E.1: Difference in the rest-frame SEDs of composite stellar populations created with the code of M05 and BC03. We show ages of 0.001, 0.1, 1 and 5 Gyr of a solar metallicity, Salpeter IMF τ-model with a $\tau = 1$ Gyr. The two codes show clear differences in the UV and optical wavelength ranges. Note that both CSPs are based on the M05 stellar population model and the BC03 code is only used to add the star formation history. The flux of each model is normalised to 1 at 5000 Å.

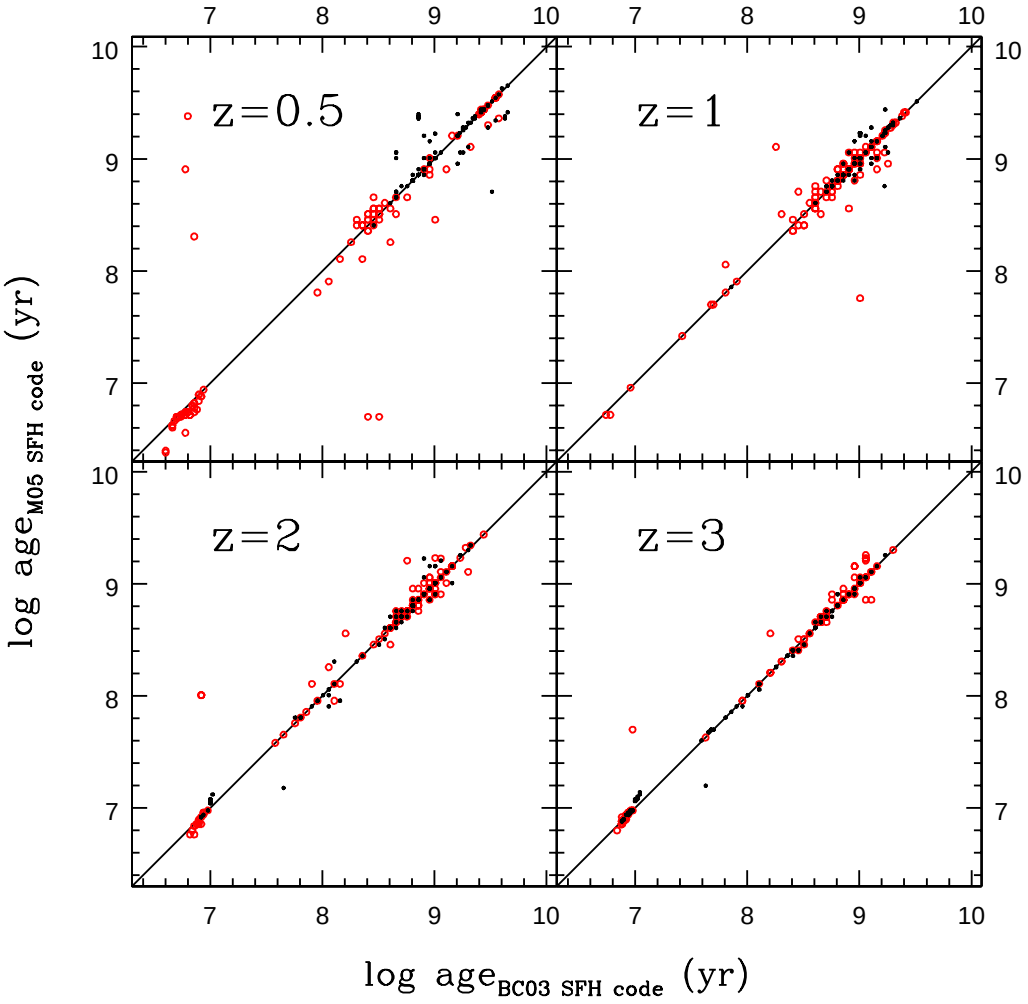

Figure E.2: Comparison between best fit ages for mock star-forming galaxies using only solar metallicity τ-models created with different SFH codes. Black dots refer to the unreddened case, red to the case that includes reddening in the fit.

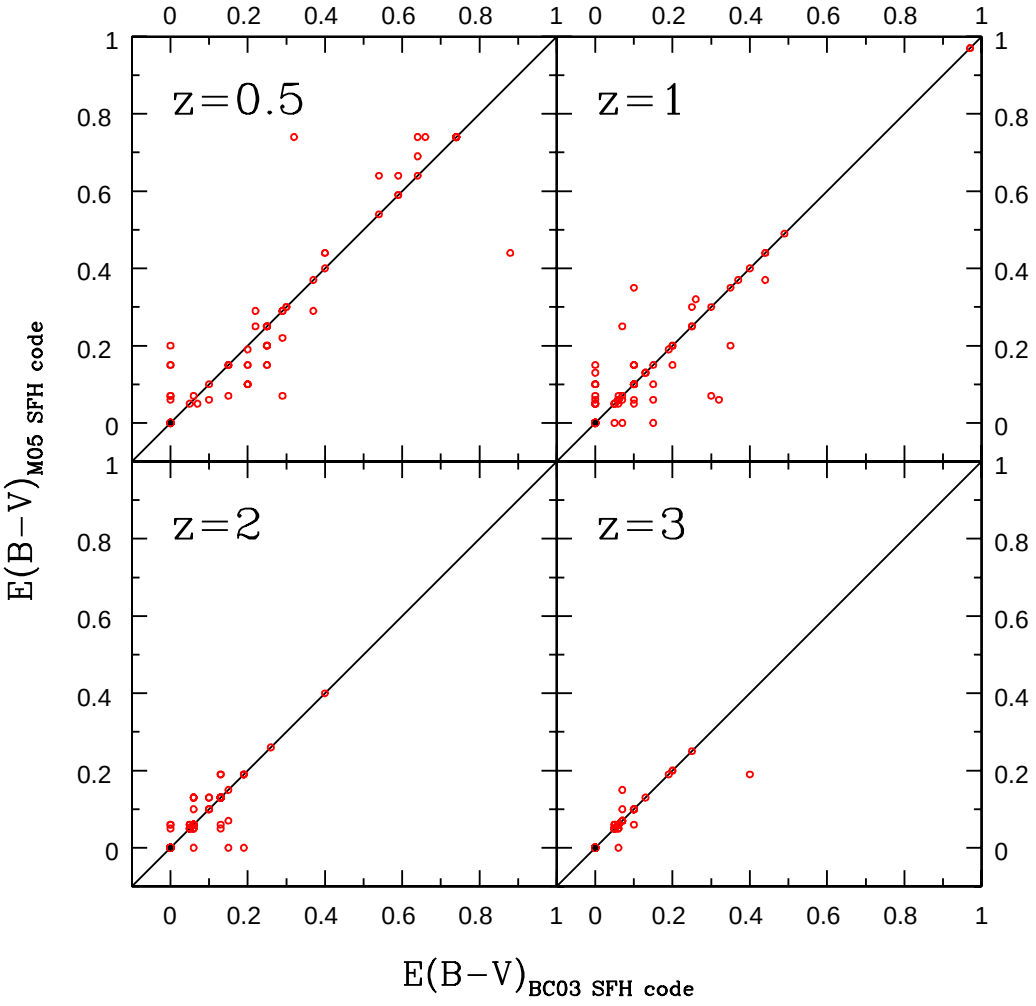

Figure E.3: Comparison between best fit $E(B-V)$ for mock star-forming galaxies using only solar metallicity τ-models created with different SFH codes. Black dots refer to the unreddened case, red to the case that includes reddening in the fit.

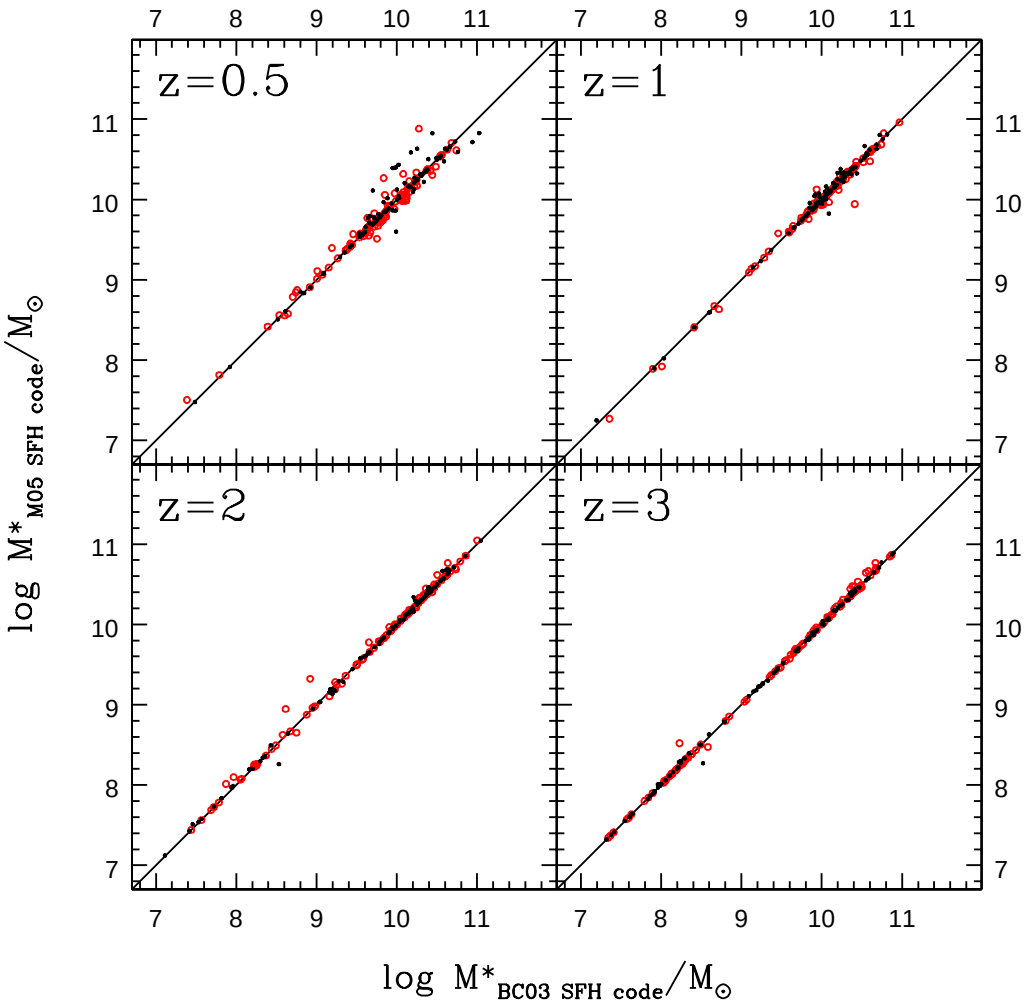

Figure E.4: Comparison between best fit stellar masses for mock star-forming galaxies using only solar metallicity τ-models created with different SFH codes. Black dots refer to the unreddened case, red to the case that includes reddening in the fit.

References

Abazajian K. N., Adelman-McCarthy J. K., Agüeros M. A., et al. 2009, ApJS, 182, 543

Acquaviva V., Gawiser E., Guaita L., 2011, ApJ, 737, 47

Afonso J., Bizzocchi L., Ibar E., et al. 2011, ApJ, 743, 122

Aihara H., Allende Prieto C., An D., et al. 2011, ApJS, 193, 29

Allen C. W., 1976, Astrophysical Quantities. Astrophysical Quantities, London: Athlone (3rd edition), 1976

Aragon-Salamanca A., Ellis R. S., Couch W. J., Carter D., 1993, MNRAS, 262, 764

Arnouts S., Walcher C. J., Le Fèvre O., et al. 2007, A&A, 476, 137

Babbedge T. S. R., Rowan-Robinson M., Gonzalez-Solares E., et al. 2004, MNRAS, 353, 654

Baldry I. K., Balogh M. L., Bower R. G., Glazebrook K., Nichol R. C., Bamford S. P., Budavari T., 2006, MNRAS, 373, 469

Baldry I. K., Glazebrook K., Brinkmann J., Ivezić Ž., Lupton R. H., Nichol R. C., Szalay A. S., 2004, ApJ, 600, 681

Balogh M. L., Baldry I. K., Nichol R., Miller C., Bower R., Glazebrook K., 2004, ApJL, 615, L101

Baugh C. M., 2006, Reports on Progress in Physics, 69, 3101

Baum W. A., 1962, in G. C. McVittie ed., Problems of Extra-Galactic Research Vol. 15 of IAU Symposium, Photoelectric Magnitudes and Red-Shifts. pp 390–+

Beckwith S. V. W., Stiavelli M., Koekemoer A. M., Caldwell J. A. R., Ferguson H. C., Hook R., Lucas R. A., Bergeron L. E., Corbin M., Jogee S., Panagia N., Robberto M., Royle P., Somerville R. S., Sosey M., 2006, AJ, 132, 1729

Bell E. F., McIntosh D. H., Katz N., Weinberg M. D., 2003, ApJS, 149, 289

Bell E. F., Wolf C., Meisenheimer K., Rix H.-W., Borch A., Dye S., Kleinheinrich M., Wisotzki L., McIntosh D. H., 2004, ApJ, 608, 752

Bell E. F., Zheng X. Z., Papovich C., Borch A., Wolf C., Meisenheimer K., 2007, ApJ, 663, 834

Benítez N., 2000, ApJ, 536, 571

Bennett C. L., Halpern M., Hinshaw G., et al. 2003, ApJS, 148, 1

Bernardi M., Nichol R. C., Sheth R. K., Miller C. J., Brinkmann J., 2006, AJ, 131, 1288

Blake C., Brough S., Couch W., et al. 2008, Astronomy and Geophysics, 49, 050000

Blanton M. R., Eisenstein D., Hogg D. W., Schlegel D. J., Brinkmann J., 2005, ApJ, 629, 143

Blanton M. R., Hogg D. W., Bahcall N. A., et al. 2003, ApJ, 594, 186

Blumenthal G. R., Faber S. M., Primack J. R., Rees M. J., 1984, Nature, 311, 517

Bolton A. S., Burles S., Koopmans L. V. E., Treu T., Gavazzi R., Moustakas L. A., Wayth R., Schlegel D. J., 2008, ApJ, 682, 964

Bolzonella M., Kovač K., Pozzetti L., et al. 2010, A&A, 524, A76

Bolzonella M., Miralles J.-M., Pelló R., 2000, A&A, 363, 476

Borch A., Meisenheimer K., Bell E. F., et al. 2006, A&A, 453, 869

Bouwens R. J., Illingworth G. D., Franx M., Ford H., 2007, ApJ, 670, 928

Bower R. G., Benson A. J., Malbon R., Helly J. C., Frenk C. S., Baugh C. M., Cole S., Lacey C. G., 2006, MNRAS, 370, 645

Brammer G. B., van Dokkum P. G., Coppi P., 2008, ApJ, 686, 1503

Brammer G. B., Whitaker K. E., van Dokkum P. G., et al. 2009, ApJL, 706, L173

Brinchmann J., Charlot S., White S. D. M., Tremonti C., Kauffmann G., Heckman T., Brinkmann J., 2004, MNRAS, 351, 1151

Brown M. J. I., Zheng Z., White M., Dey A., Jannuzi B. T., Benson A. J., Brand K., Brodwin M., Croton D. J., 2008, ApJ, 682, 937

Brunner R. J., Connolly A. J., Szalay A. S., Bershady M. A., 1997, ApJL, 482, L21+

Bruzual G., Charlot S., 2003, MNRAS, 344, 1000

Bruzual A. G., 1983, ApJ, 273, 105

Bruzual A. G., Charlot S., 1993, ApJ, 405, 538

Bunker A. J., 1999, in A. J. Bunker & W. J. M. van Breugel ed., The Hy-Redshift Universe: Galaxy Formation and Evolution at High Redshift Vol. 193 of Astronomical Society of the Pacific Conference Series, Near-Infrared Emission Line Searches for High-Redshift Galaxies. p. 448

Calzetti D., Armus L., Bohlin R. C., Kinney A. L., Koornneef J., Storchi-Bergmann T., 2000, ApJ, 533, 682

Cannon R., Drinkwater M., Edge A., et al. 2006, MNRAS, 372, 425

Capak P., Aussel H., Ajiki M., et al. 2007, ApJS, 172, 99

Cassisi S., Castellani M., Castellani V., 1997, A&A, 317, 108

Cassisi S., Castellani V., Ciarcelluti P., Piotto G., Zoccali M., 2000, MNRAS, 315, 679

Cassisi S., degl'Innocenti S., Salaris M., 1997, MNRAS, 290, 515

Chabrier G., 2003, PASP, 115, 763

Charlot S., Bruzual A. G., 1991, ApJ, 367, 126

Charlot S., Fall S. M., 2000, ApJ, 539, 718

Cid Fernandes R., Gu Q., Melnick J., Terlevich E., Terlevich R., Kunth D., Rodrigues Lacerda R., Joguet B., 2004, MNRAS, 355, 273

Cimatti A., Cassata P., Pozzetti L., Kurk J., Mignoli M., Renzini A., Daddi E., Bolzonella M., Brusa M., Rodighiero G., Dickinson M., Franceschini A., Zamorani G., Berta S., Rosati P., Halliday C., 2008, A&A, 482, 21

Cimatti A., Daddi E., Mignoli M., Pozzetti L., Renzini A., Zamorani G., Broadhurst T., Fontana A., Saracco P., Poli F., Cristiani S., D'Odorico S., Giallongo E., Gilmozzi R., Menci N., 2002, A&A, 381, L68

Cimatti A., Daddi E., Renzini A., 2006, A&A, 453, L29

Cole S., Aragon-Salamanca A., Frenk C. S., Navarro J. F., Zepf S. E., 1994, MNRAS, 271, 781

Cole S., Percival W. J., Peacock J. A., et al. 2005, MNRAS, 362, 505

Coleman G. D., Wu C.-C., Weedman D. W., 1980, ApJS, 43, 393

Connolly A. J., Csabai I., Szalay A. S., Koo D. C., Kron R. G., Munn J. A., 1995, AJ, 110, 2655

Conroy C., Gunn J. E., White M., 2009, ApJ, 699, 486

Conselice C. J., 2006, MNRAS, 373, 1389

Cool R. J., Eisenstein D. J., Fan X., et al. 2008, ApJ, 682, 919

Croton D. J., Springel V., White S. D. M., De Lucia G., Frenk C. S., Gao L., Jenkins A., Kauffmann G., Navarro J. F., Yoshida N., 2006, MNRAS, 365, 11

Daddi E., Alexander D. M., Dickinson M., et al. 2007, ApJ, 670, 173

Daddi E., Cimatti A., Renzini A., Fontana A., Mignoli M., Pozzetti L., Tozzi P., Zamorani G., 2004, ApJ, 617, 746

Daddi E., Dannerbauer H., Stern D., et al. 2009, ApJ, 694, 1517

Daddi E., Dickinson M., Morrison G., et al. 2007, ApJ, 670, 156

Daddi E., Renzini A., Pirzkal N., Cimatti A., Malhotra S., Stiavelli M., Xu C., Pasquali A., Rhoads J. E., Brusa M., di Serego Alighieri S., Ferguson H. C., Koekemoer A. M., Moustakas L. A., Panagia N., Windhorst R. A., 2005, ApJ, 626, 680

Dahlen T., Mobasher B., Dickinson M., Ferguson H. C., Giavalisco M., Grogin N. A., Guo Y., Koekemoer A., Lee K.-S., Lee S.-K., Nonino M., Riess A. G., Salimbeni S., 2010, ApJ, 724, 425

Davis M., Faber S. M., Newman J., et al. 2003, in P. Guhathakurta ed., Society of Photo-Optical Instrumentation Engineers (SPIE) Conference Series Vol. 4834 of Presented at the Society of Photo-Optical Instrumentation Engineers (SPIE) Conference, Science Objectives and Early Results of the DEEP2 Redshift Survey. pp 161–172

Davis M., Geller M. J., 1976, ApJ, 208, 13

De Lucia G., Blaizot J., 2007, MNRAS, 375, 2

de Vaucouleurs G., 1948, Annales d'Astrophysique, 11, 247

Dekel A., Birnboim Y., Engel G., et al. 2009, Nature, 457, 451

Dickinson M., Giavalisco M., GOODS Team 2003, in R. Bender & A. Renzini ed., The Mass of Galaxies at Low and High Redshift The Great Observatories Origins Deep Survey. pp 324–+

Dressler A., 1980, ApJ, 236, 351

Eggen O. J., Lynden-Bell D., Sandage A. R., 1962, ApJ, 136, 748

Eisenstein D. J., Annis J., Gunn J. E., et al. 2001, AJ, 122, 2267

Eisenstein D. J., Weinberg D. H., Agol E., Aihara H., Allende Prieto C., Anderson S. F., Arns J. A., Aubourg É., Bailey S., Balbinot E., et al. 2011, AJ, 142, 72

Eisenstein D. J., Zehavi I., Hogg D. W., et al. 2005, ApJ, 633, 560

Elbaz D., Daddi E., Le Borgne D., et al. 2007, A&A, 468, 33

Ellis R. S., Treu T., Kneib J.-P., 2005, Highlights of Astronomy, 13, 327

Faber S. M., Jackson R. E., 1976, ApJ, 204, 668

Faber S. M., Willmer C. N. A., Wolf C., et al. 2007, ApJ, 665, 265

Feldmann R., Carollo C. M., Porciani C., et al. 2006, MNRAS, 372, 565

Ferraro F. R., Origlia L., Testa V., Maraston C., 2004, ApJ, 608, 772

Fioc M., Rocca-Volmerange B., 1997, AAP, 326, 950

Firth A. E., Lahav O., Somerville R. S., 2003, MNRAS, 339, 1195

Fitzpatrick E. L., 1986, AJ, 92, 1068

Fontana A., Santini P., Grazian A., et al. 2009, A&A, 501, 15

Förster Schreiber N. M., Genzel R., Bouché N., et al. 2009, ApJ, 706, 1364

Förster Schreiber N. M., van Dokkum P. G., Franx M., et al. 2004, ApJ, 616, 40

Fukugita M., Ichikawa T., Gunn J. E., Doi M., Shimasaku K., Schneider D. P., 1996, AJ, 111, 1748

Gallazzi A., Charlot S., Brinchmann J., White S. D. M., Tremonti C. A., 2005, MNRAS, 362, 41

Genzel R., Tacconi L. J., Eisenhauer F., et al. 2006, Nature, 442, 786

Giavalisco M., Ferguson H. C., Koekemoer A. M., et al. 2004, ApJL, 600, L93

Girardi L., Bertelli G., Bressan A., Chiosi C., Groenewegen M. A. T., Marigo P., Salasnich B., Weiss A., 2002, A&A, 391, 195

Girardi L., Bressan A., Bertelli G., Chiosi C., 2000, A&AS, 141, 371

Glazebrook K., the GDDS team 2003, ArXiv Astrophysics e-prints

González V., Labbé I., Bouwens R. J., Illingworth G., Franx M., Kriek M., Brammer G. B., 2010, ApJ, 713, 115

Gray M. E., Wolf C., Barden M., et al. 2009, MNRAS, 393, 1275

Grogin N. A., Kocevski D. D., Faber S. M., et al. 2011, ApJS, 197, 35

Gunn J. E., Carr M., Rockosi C., et al. 1998, AJ, 116, 3040

Gunn J. E., Siegmund W. A., Mannery E. J., et al. 2006, AJ, 131, 2332

Hatton S., Devriendt J. E. G., Ninin S., Bouchet F. R., Guiderdoni B., Vibert D., 2003, MNRAS, 343, 75

Heavens A. F., Jimenez R., Lahav O., 2000, MNRAS, 317, 965

Hogg D. W., Baldry I. K., Blanton M. R., Eisenstein D. J., 2002, ArXiv Astrophysics e-prints

Hopkins A. M., Beacom J. F., 2006, ApJ, 651, 142

Hubble E., 1926, Contributions from the Mount Wilson Observatory / Carnegie Institution of Washington, 324, 1

Hubble E., 1929, Proceedings of the National Academy of Science, 15, 168

Iben Jr. I., 1967, ARA&A, 5, 571

Iben Jr. I., 1974, ARA&A, 12, 215

Iben Jr. I., Renzini A., 1983, ARA&A, 21, 271

Ilbert O., Arnouts S., McCracken H. J., et al. 2006, A&A, 457, 841

Jimenez R., Bernardi M., Haiman Z., Panter B., Heavens A. F., 2007, ApJ, 669, 947

Kannappan S. J., Gawiser E., 2007, ApJL, 657, L5

Kauffmann G., Heckman T. M., White S. D. M., et al. 2003, MNRAS, 341, 33

Kennicutt R. C., 1986, in C. A. Norman, A. Renzini, & M. Tosi ed., Stellar Populations Star formation histories of galactic disks. pp 125–145

Kochanek C. S., Eisenstein D., Caldwell N., Cool R., Green P., AGES 2004, in American Astronomical Society Meeting Abstracts Vol. 36 of Bulletin of the American Astronomical Society, The AGN and Galaxy Evolution Survey. pp 1495–+

Koekemoer A. M., Faber S. M., Ferguson H. C., et al. 2011, ApJS, 197, 36

Komatsu E., Dunkley J., Nolta M. R., et al. 2009, ApJS, 180, 330

Kong X., Daddi E., Arimoto N., et al. 2006, ApJ, 638, 72

Koopmans L. V. E., Bolton A., Treu T., Czoske O., Auger M. W., Barnabè M., Vegetti S., Gavazzi R., Moustakas L. A., Burles S., 2009, ApJL, 703, L51

Kriek M., van der Wel A., van Dokkum P. G., Franx M., Illingworth G. D., 2008, ApJ, 682, 896

Kroupa P., 2001, MNRAS, 322, 231

Kuntschner H., 2000, MNRAS, 315, 184

Kurk J., Cimatti A., Zamorani G., et al. 2008, in T. Kodama, T. Yamada, & K. Aoki ed., Panoramic Views of Galaxy Formation and Evolution Vol. 399 of Astronomical Society of the Pacific Conference Series, A Spectroscopic Study of a z=1.6 Galaxy Overdensity in the GMASS Field. pp 332–+

Kurk J., Cimatti A., Zamorani G., et al. 2009, A&A, 504, 331

Lacy M., Afonso J., Alexander D., et al. 2008, in Spitzer Proposal ID #60024 SERVS: the Spitzer Extragalactic Representative Volume Survey. pp 60024–+

Lane K. P., Gray M. E., Aragón-Salamanca A., Wolf C., Meisenheimer K., 2007, MNRAS, 378, 716

Le Borgne J.-F., Bruzual G., Pelló R., Lançon A., Rocca-Volmerange B., Sanahuja B., Schaerer D., Soubiran C., Vílchez-Gómez R., 2003, A&A, 402, 433

Le Fèvre O., Vettolani G., Maccagni D., et al. 2003, ArXiv Astrophysics e-prints

Lee S., Idzi R., Ferguson H. C., Somerville R. S., Wiklind T., Giavalisco M., 2009, ApJS, 184, 100

Lejeune T., Cuisinier F., Buser R., 1997, A&AS, 125, 229

Lintott C. J., Schawinski K., Slosar A., Land K., Bamford S., Thomas D., Raddick M. J., Nichol R. C., Szalay A., Andreescu D., Murray P., Vandenberg J., 2008, MNRAS, 389, 1179

Longhetti M., Saracco P., 2009, MNRAS, 394, 774

Lupton R. H., Gunn J. E., Szalay A. S., 1999, AJ, 118, 1406

Madau P., 1995, ApJ, 441, 18

Madau P., Pozzetti L., Dickinson M., 1998, ApJ, 498, 106

Maraston C., 1998, MNRAS, 300, 872

Maraston C., 2005, MNRAS, 362, 799

Maraston C., 2011a, in C. Carignan, F. Combes, & K. C. Freeman ed., IAU Symposium Vol. 277 of IAU Symposium, Modelling Stellar Populations at High Redshift. pp 158–165

Maraston C., 2011b, in F. Kerschbaum, T. Lebzelter, & R. F. Wing ed., Why Galaxies Care about AGB Stars II: Shining Examples and Common Inhabitants Vol. 445 of Astronomical Society of the Pacific Conference Series, Why Galaxies Care about AGB Stars: Modeling Galaxies. p. 391

Maraston C., Daddi E., Renzini A., Cimatti A., Dickinson M., Papovich C., Pasquali A., Pirzkal N., 2006, ApJ, 652, 85

Maraston C., Greggio L., Renzini A., Ortolani S., Saglia R. P., Puzia T. H., Kissler-Patig M., 2003, A&A, 400, 823

Maraston C., Nieves Colmenárez L., Bender R., Thomas D., 2009, A&A, 493, 425

Maraston C., Pforr J., Renzini A., Daddi E., Dickinson M., Cimatti A., Tonini C., 2010, MNRAS, 407, 830

Maraston C., Strömbäck G., Thomas D., Wake D. A., Nichol R. C., 2009, MNRAS, 394, L107

Maraston C., Thomas D., 2000, ApJ, 541, 126

Masters K. L., Maraston C., Nichol R. C., et al. 2011, MNRAS, 418, 1055

Menéndez-Delmestre K., Blain A. W., Smail I., et al. 2009, ApJ, 699, 667

Meynet G., Maeder A., Schaller G., Schaerer D., Charbonnel C., 1994, A&AS, 103, 97

Mo H. J., Mao S., White S. D. M., 1998, MNRAS, 295, 319

Moustakas L. A., Casertano S., Conselice C. J., Dickinson M. E., Eisenhardt P., Ferguson H. C., Giavalisco M., Grogin N. A., Koekemoer A. M., Lucas R. A., Mobasher B., Papovich C., Renzini A., Somerville R. S., Stern D., 2004, ApJL, 600, L131

Muzzin A., Marchesini D., van Dokkum P. G., Labbé I., Kriek M., Franx M., 2009, ApJ, 701, 1839

Muzzin A., van Dokkum P., Franx M., Marchesini D., Kriek M., Labbé I., 2009, ApJL, 706, L188

Nelan J. E., Smith R. J., Hudson M. J., Wegner G. A., Lucey J. R., Moore S. A. W., Quinney S. J., Suntzeff N. B., 2005, ApJ, 632, 137

Noeske K. G., Weiner B. J., Faber S. M., et al. 2007, ApJL, 660, L43

Noll S., Burgarella D., Giovannoli E., Buat V., Marcillac D., Muñoz-Mateos J. C., 2009, A&A, 507, 1793

Noll S., Pierini D., Cimatti A., et al. 2009, A&A, 499, 69

Ocvirk P., Pichon C., Lançon A., Thiébaut E., 2006, MNRAS, 365, 46

Oemler Jr. A., 1974, ApJ, 194, 1

Oke J. B., 1974, ApJS, 27, 21

Pannella M., Carilli C. L., Daddi E., et al. 2009, ApJL, 698, L116

Panter B., Jimenez R., Heavens A. F., Charlot S., 2007, MNRAS, 378, 1550

Papovich C., Dickinson M., Ferguson H. C., 2001, ApJ, 559, 620

Papovich C., Dickinson M., Giavalisco M., Conselice C. J., Ferguson H. C., 2005, ApJ, 631, 101

Penzias A. A., Wilson R. W., 1965, ApJ, 142, 419

Percival W. J., Reid B. A., Eisenstein D. J., et al. 2010, MNRAS, 401, 2148

Pickles A. J., 1998, PASP, 110, 863

Pogson N., 1856, MNRAS, 17, 12

Popesso P., Dickinson M., Nonino M., et al. 2009, A&A, 494, 443

Pozzetti L., Bolzonella M., Lamareille F., et al. 2007, A&A, 474, 443

Pozzetti L., Bolzonella M., Zucca E., et al. 2010, A&A, 523, A13+

Press W. H., Schechter P., 1974, ApJ, 187, 425

Prevot M. L., Lequeux J., Prevot L., Maurice E., Rocca-Volmerange B., 1984, A&A, 132, 389

Prugniel P., Soubiran C., Koleva M., Le Borgne D., 2007, ArXiv Astrophysics e-prints

Quadri R. F., Williams R. J., 2010, ApJ, 725, 794

Reddy N. A., Steidel C. C., 2004, ApJL, 603, L13

Renzini A., 2006, ARAA, 44, 141

Renzini A., 2009, MNRAS, 398, L58

Renzini A., Buzzoni A., 1986, in ASSL Vol. 122: Spectral Evolution of Galaxies Global properties of stellar populations and the spectral evolution of galaxies. p. p. 195

Renzini A., Daddi E., 2009, The Messenger, 137, 41

Renzini A., Fusi Pecci F., 1988, ARA&A, 26, 199

Retzlaff J., Rosati P., Dickinson M., et al. 2010, A&A, 511, A50+

Rosenberg H., 1910, Astronomische Nachrichten, 186, 71

Rubin V. C., Burstein D., Ford Jr. W. K., Thonnard N., 1985, ApJ, 289, 81

Russell H. N., 1921, Popular Astronomy, 29, 541

Salaris M., Cassisi S., 1996, A&A, 305, 858

Salim S., Rich R. M., Charlot S., et al. 2007, ApJS, 173, 267

Salpeter E. E., 1955, ApJ, 121, 161

Sánchez-Blázquez P., Peletier R. F., Jiménez-Vicente J., Cardiel N., Cenarro A. J., Falcón-Barroso J., Gorgas J., Selam S., Vazdekis A., 2006, MNRAS, 371, 703

Schaller G., Schaerer D., Meynet G., Maeder A., 1992, A&AS, 96, 269

Schinnerer E., Smolčić V., Carilli C. L., et al. 2007, ApJS, 172, 46

Schlegel D. J., Finkbeiner D. P., Davis M., 1998, ApJ, 500, 525

Scoville N., Aussel H., Brusa M., et al. 2007, ApJS, 172, 1

Seaton M. J., 1979, MNRAS, 187, 73P

Serjeant S., Gruppioni C., Oliver S., 2002, MNRAS, 330, 621

Serra P., Trager S. C., 2007, MNRAS, 374, 769

Shapley A. E., Steidel C. C., Erb D. K., Reddy N. A., Adelberger K. L., Pettini M., Barmby P., Huang J., 2005, ApJ, 626, 698

Sitterly B. W., 1970, Vistas in Astronomy, 12, 357

Smoot G. F., Aymon J., de Amici G., Bennett C. L., Kogut A., Gulkis S., Backus C., Galuk K., Jackson P. D., Keegstra P., 1991, Advances in Space Research, 11, 193

Somerville R. S., Hopkins P. F., Cox T. J., Robertson B. E., Hernquist L., 2008, MNRAS, 391, 481

Somerville R. S., Lemson G., Sigad Y., Dekel A., Kauffmann G., White S. D. M., 2001, MNRAS, 320, 289

Springel V., White S. D. M., Jenkins A., et al. 2005, Nature, 435, 629

Stark D. P., Ellis R. S., Bunker A., Bundy K., Targett T., Benson A., Lacy M., 2009, ApJ, 697, 1493

Steidel C. C., Shapley A. E., Pettini M., Adelberger K. L., Erb D. K., Reddy N. A., Hunt M. P., 2004, ApJ, 604, 534

Stoughton C., Adelman J., Annis J. T., et al. 2002, in J. A. Tyson & S. Wolff ed., Society of Photo-Optical Instrumentation Engineers (SPIE) Conference Series Vol. 4836 of Society of Photo-Optical Instrumentation Engineers (SPIE) Conference Series, Data Processing Factory for the Sloan Digital Sky Survey. pp 339–349

Stoughton C., Lupton R. H., Bernardi M., et al. 2002, AJ, 123, 485

Strateva I., Ivezić Ž., Knapp G. R., et al. 2001, AJ, 122, 1861

Strauss M. A., Tyson J. A., Sweeney D., et al. 2010, in American Astronomical Society Meeting Abstracts #215 Vol. 42 of Bulletin of the American Astronomical Society, LSST Observatory System and Science Opportunities. pp 401.01–+

Tacconi L. J., Genzel R., Smail I., et al. 2008, ApJ, 680, 246

Thomas D., Maraston C., Bender R., Mendes de Oliveira C., 2005, ApJ, 621, 673

Thomas D., Maraston C., Schawinski K., Sarzi M., Silk J., 2010, MNRAS, 404, 1775

Tinsley B. M., 1972, ApJ, 178, 319

Tiret O., Salucci P., Bernardi M., Maraston C., Pforr J., 2011, MNRAS, 411, 1435

Tojeiro R., Heavens A. F., Jimenez R., Panter B., 2007, MNRAS, 381, 1252

Tojeiro R., Wilkins S., Heavens A. F., Panter B., Jimenez R., 2009, ApJS, 185, 1

Tonini C., Maraston C., Devriendt J., Thomas D., Silk J., 2009, MNRAS, 396, L36

Tonini C., Maraston C., Thomas D., Devriendt J., Silk J., 2010, MNRAS, 403, 1749

Toomre A., 1977, ARA&A, 15, 437

Toomre A., Toomre J., 1972, ApJ, 178, 623

Trager S. C., Faber S. M., Worthey G., González J. J., 2000, AJ, 119, 1645

Treu T., Ellis R. S., Liao T. X., van Dokkum P. G., Tozzi P., Coil A., Newman J., Cooper M. C., Davis M., 2005, ApJ, 633, 174

Tully R. B., Fisher J. R., 1977, A&A, 54, 661

Uomoto A., Smee S., Rockosi C., Burles S., Pope A., Friedman S., Brinkmann J., Gunn J., Nichol R., SDSS Collaboration 1999, in American Astronomical Society Meeting Abstracts Vol. 31 of Bulletin of the American Astronomical Society, The Sloan Digital Sky Survey Spectrographs. pp 1501–+

van der Wel A., 2008, ApJL, 675, L13

van der Wel A., Franx M., Wuyts S., van Dokkum P. G., Huang J., Rix H.-W., Illingworth G. D., 2006, ApJ, 652, 97

van Dokkum P. G., 2008, ApJ, 674, 29

Vanzella E., Cristiani S., Dickinson M., et al. 2008, A&A, 478, 83

Vázquez G. A., Leitherer C., 2005, ApJ, 621, 695

Wake D. A., Nichol R. C., Eisenstein D. J., et al. 2006, MNRAS, 372, 537

Walcher C. J., Lamareille F., Vergani D., et al. 2008, A&A, 491, 713

Walcher J., Groves B., Budavári T., Dale D., 2011, ApSS, 331, 1

Wang Y., Bahcall N., Turner E. L., 1998, AJ, 116, 2081

White M., Blanton M., Bolton A., et al. 2011, ApJ, 728, 126

White M., Song Y.-S., Percival W. J., 2009, MNRAS, 397, 1348

White S. D. M., Rees M. J., 1978, MNRAS, 183, 341

Wilkins S. M., Trentham N., Hopkins A. M., 2008, MNRAS, 385, 687

Williams R. J., Quadri R. F., Franx M., van Dokkum P., Labbé I., 2009, ApJ, 691, 1879

Wolf C., Dye S., Kleinheinrich M., Meisenheimer K., Rix H.-W., Wisotzki L., 2001, A&A, 377, 442

Worthey G., Faber S. M., Gonzalez J. J., 1992, ApJ, 398, 69

Wuyts S., Franx M., Cox T. J., Förster Schreiber N. M., Hayward C. C., Hernquist L., Hopkins P. F., Labbé I., Marchesini D., Robertson B. E., Toft S., van Dokkum P. G., 2009, ApJ, 700, 799

Wuyts S., Franx M., Cox T. J., Hernquist L., Hopkins P. F., Robertson B. E., van Dokkum P. G., 2009, ApJ, 696, 348

York D. G., Adelman J., Anderson Jr. J. E., et al. 2000, AJ, 120, 1579

Zwicky F., 1937, ApJ, 86, 217